UNIVERSITÀ DEGLI STUDI DI CATANIA
FACOLTÀ DI SCIENZE MATEMATICHE, FISICHE E NATURALI
DOTTORATO DI RICERCA IN FISICA - XXIV CICLO

ENRICA TROVATO

PERFORMANCE STUDY OF THE MUON PROTOTYPE DETECTOR AT THE PIERRE AUGER OBSERVATORY

PHD THESIS

TUTOR:
CHIAR.MO PROF. A. INSOLIA

CO-TUTOR:
DR. S. RIGGI

TRIENNIO 2009-2011

Contents

Chapter 1

Physics of Cosmic Rays

1.1 History of cosmic rays

Cosmic rays were first discovered by the austrian physicist Victor Hess, and since then have been an inexhaustible source of discoveries in astroparticle and subnuclear physics.
After the discovery of radioactivity by Henri Becquerel in 1896, it was generally believed that atmospheric electricity (ionization of the air) was caused only by radiation from radioactive elements in the ground or the radioactive gases (isotopes of radon) they produce. In 1910 Theodor Wulf developed an electroscope. He took it on the edge of the Eiffel Tower to measure the radiation, and observed a decrease of the radiation with respect to the sea level, but not as much as he expected.
Then, in 1912 V.F.Hess [1] carried three Wulf electroscopes at different altitudes during a balloon flight. He noted that the intensity of the ionizing radiation first decreased as the balloon went up, but above 1000 m the radiation started to increase, becoming 4 times greater at heights above 5000 m. This result did not conform with the idea that this ionization was caused by radioactive elements in the surface of the earth and Hess concluded that the observed radiation was of extraterrestrial origin and its intensity decreased with the interaction in atmosphere. R.A.Millikan [2], initially sceptical on the Hess' conclusions, finally confirmed his hypothesis and suggested that the formation of complex nuclei from protons and electrons in the universe produces a gamma radiation, that he called '*cosmic rays*'. The results of Hess were confirmed also by the experiments performed by Kolhörster in 1914-1919.
In 1929 Bothe and Kolhörster vertically disposed two Geiger counters and discovered a great number of coincidences. To test that a single charged particle passes through both counters, they disposed a golden block 4 cm high between them, discovering that 75% of the rays traversed also the block. This value of coincidence was comparable with that in the atmosphere and the measurement of the absorption coefficient was not compatible with the hypothesis of a gamma radiation at sea level [3].
That most of the incoming radiation consisted of charged particles was established first by Clay [4]. He showed that the ionization due to cosmic rays increased by 16% between the Equator and the geomagnetic latitude of Amsterdam, indicating that the cosmic rays were primarily charged as the lower energy component was progressively deflected by the geomagnetic fields at lower latitudes. In 1930 B. Rossi showed that if the cosmic rays were predominantly of one charge there should have been an 'east-west effect'. A 10% excess in cosmic rays in westerly directions was observed by Compton in the experiments performed in 1933-1937 [5] with about 70 ionization chambers located between the equator and a latitude of 50°. This evidence showed

that the cosmic rays are predominantly positively charged.
In 1934, Bruno Rossi [6] reported an observation of near-simultaneous discharges of three Geiger counters widely separated in a horizontal plane to form a triangle during a test of equipment he was using in a measurement of the east-west effect. He developed also a coincidence circuit to select only the events simultaneously hitting the 3 counters. The great number of observed coincidences showed for the first time the existence of a shower of secondary particles.
In 1938 Pierre Auger and R.Maze [7] detected the same phenomenon with counter separated by distances as large as 20 meters. Subsequent experiments in the Alps showed that the coincidences continued to be observed even at a distance of 200 meters. He concluded that cosmic rays, entering into the atmosphere and interacting with air molecules, produce a shower of secondary particles that reaches the sea level: he introduced the name '*Exstensive Air Showers*', or EAS. P. Auger and collaborators deduced that the primary energy was about 10^{15} eV and opened up a new way of exploring an energy regime far beyond direct measurement methods.
The studies with cosmic rays continued with extended array of Geiger counters. In 1962 J.Linsley and L.Scarsi [8] observed the first event of 10^{20} eV at the Volcano Ranch array in new Mexico [9]. In the following years many cosmic rays detectors with different detection techniques were developed: Haverah Park in UK [10], SUGAR in Australia [11], Yakutsk in Russia [12], AGASA in Japan [13], Fly's Eye [14], HiRes I [190] and HiRes II [16] in the Utah, and more recently the Pierre Auger Observatory [17] and TA [18].
Many discoveries are directly linked to the studies of cosmic rays, like the discovery of positrons by Anderson [19], muons by Anderson and Neddermeyer [20], pions by Powell and Occhialini [21] and first particles with strangeness by Rochester and Butler [22]. So it is evident the influence that cosmic ray discovery had on the particle physics development.
Many steps forward have been made in the understanding of the nature and properties of such radiation, but some essential questions, like the origin and the acceleration or their exact chemical composition, still remain unanswered or not totally clear. So, although cosmic rays were discovered a century ago, they are still subject to intensive and fascinate studies today.

1.2 Features of cosmic rays

1.2.1 The energy spectrum of cosmic rays

To understand the origin and nature of the cosmic rays we begin with the analysis of their overall energy spectrum. The cosmic ray spectrum extends over about 12 decades in energy with a flux which follows a power law $E^{-\gamma}$ and spans about 32 orders of magnitude.
The flux falls, at a rate of about 3 orders of magnitude per energy decade, from about one particle per m^2 per second at around 100 GeV to one particle per km^2 per year above 10 EeV. The total flux of particles over all energies amounts to about 1000 $m^{-2}s^{-1}$. The differential all-particle spectrum is shown in Figure 1.1(a), and in Figure 1.1(b) multiplied by a factor $E^{2.7}$ to recognize structures in the spectrum . The differential flux can be accurately described by a broken power-law function:

$$\frac{dN}{dE} \propto E^{-\gamma} \quad \text{with}\, \gamma \sim \begin{cases} 2.7 & E \leq 4 \times 10^{15}\,\text{eV} \\ 3.0 - 3.1 & 4 \times 10^{15}\,\text{eV} \leq E \leq 4 \times 10^{18}\,\text{eV} \\ 2.7 - 3.0 & E \geq 4 \times 10^{18}\,\text{eV} \end{cases} \tag{1.1}$$

We can divide the spectrum in the following energy regions:

- **Below 10^8 eV**: this region at lower energy is dominated by the contribution of the Sun, while the solar wind shields protons coming from outside the solar system. The low energy

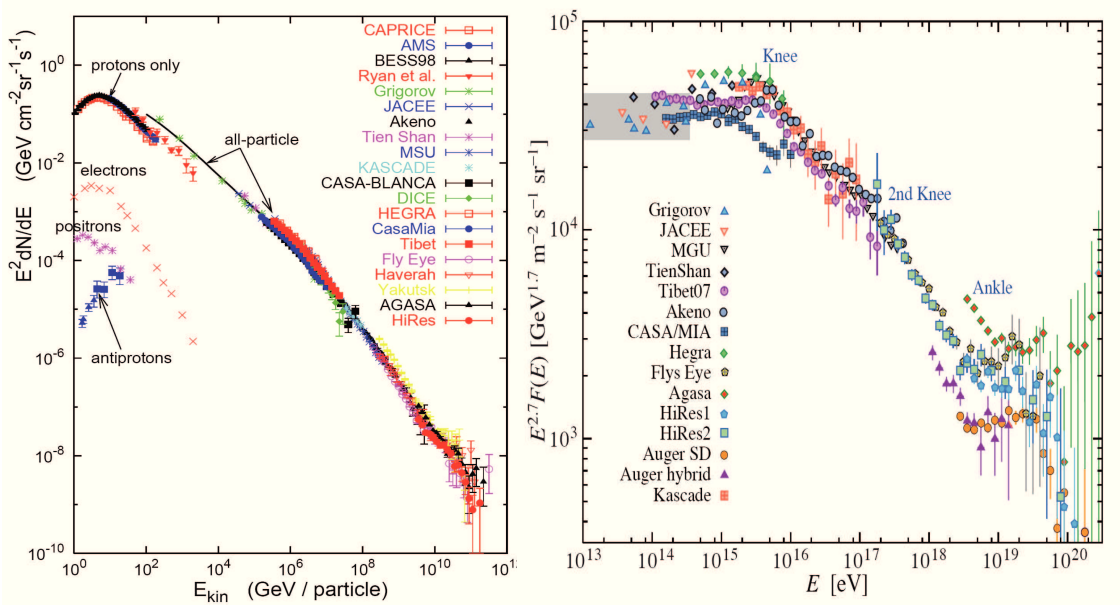

(a) (b)

Figure 1.1: 1.1(a): The all-particle spectrum from direct and air shower measurements multiplied by a factor E^2 (compilation from [23]); 1.1(b): The all-particle spectrum from air shower measurements multiplied by a factor $E^{2.7}$ (compilation from [24]). The shaded area shows the range of the direct cosmic ray spectrum measurements.

'solar' cosmic rays fade more or less smoothly into the galactic ones. Their intensity strongly depends on the solar activity and solar events such as flares.

- **Below (2-5)$\times 10^{10}$ eV**: the particles are modulated by the solar flux and a strong anti-correlation between solar activity and intensity of the cosmic rays is observed.

- **From 10^{10} eV to $\sim 4\times 10^{15}$ eV**: cosmic rays are originated within our galaxy. They reach the Earth's atmosphere because energy is not large enough to allow them to escape the magnetic field of our galaxy. The most plausible acceleration process is shock acceleration in supernovae remnants.

- **Around 10^{15}-10^{16} eV**: at these energies the spectrum becomes steeper and a sudden change of the power-law slope to E^{-3} appears. This region is called *knee* and might indicate a change in the source mechanism, and thus in acceleration processes of the cosmic rays. This is consistent with the idea that the galactic cosmic rays are accelerated by supernovae and the acceleration process becomes less efficient above 10^{15} eV. The knee can be interpreted as superposition of the energy spectra of the different elements, that exhibit their cutoff at different energies. It is still under investigation whether the exact shape of the knee can be described by a rigidity- or mass- dependent cutoff energy.

- **From 10^{16} eV to 10^{18} eV**: now the spectrum is again a power-law with spectral index 3.0-3.1. The existence of a second knee at around 4×10^{17} eV is discussed in Chapter 4.

- **Around $10^{18.5}$ eV**: this region, known as *ankle*, appears with a flattening of the spectrum. Debating interpretations are currently present in literature, dealing with the transition from galactic to extragalactic sources and with the source properties.

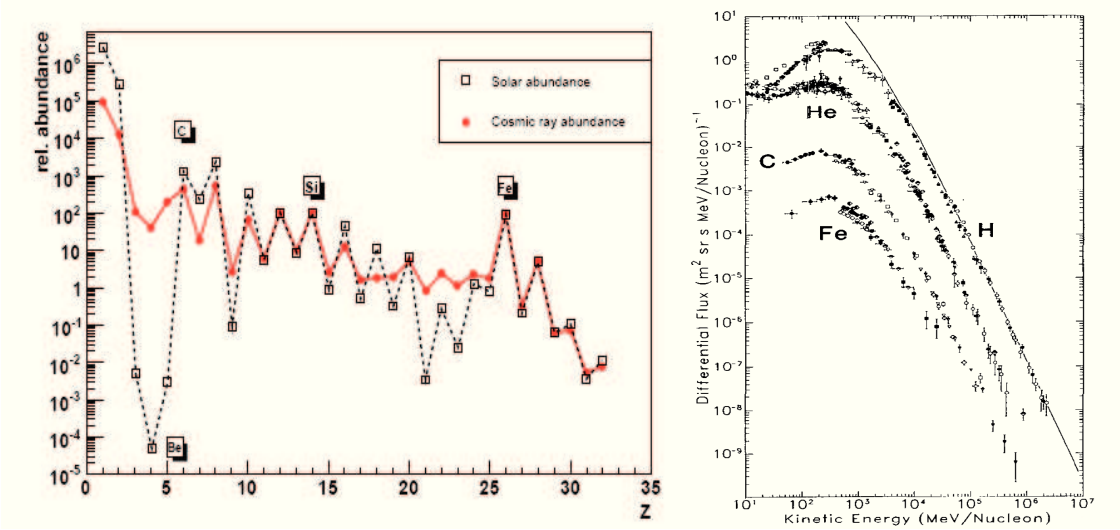

(a) (b)

Figure 1.2: 1.2: The abundances of various nuclei in the cosmic radiation compared to the abundances in the solar system. The nuclear charge scale refers to the elementary group H-Ni. The abundances are normalized to Si=1. (Compilation is based on [25]); 1.2(b): Cosmic rays energy spectra for the major components present in the primary radiation.

- **Above $10^{19.5}$ eV**: the experimental data of HiRes and Auger, put in evidence a cutoff in the spectrum, compatible with the suppression expected from the GZK effect (see section 1.2.4).

1.2.2 Mass composition

The composition of the cosmic radiation has been studied with the highest precision by satellite and balloon experiments up to energies of 10^{14} eV. Up to these energies CR are mainly composed by about 98% of hadrons and about 2% of electrons. Only $\sim 0.2\%$ is composed by photons and neutrinos. The hadronic component is dominated by protons (87%) and helium (12%), while the rest 1% corresponds to fully ionized nuclei of heavy elements. The predominance of protons and helium nuclei is due to the fact that the Earth's magnetic field and the solar wind shield heavy nuclei. Comparing the relative abundances of cosmic rays with those of Solar System elements, a similar trend with some exceptions is observable (Figure 1.2). The first is the lower abundance of hydrogen and helium in the cosmic radiation with respect to the abundance in our solar system. This is probably originate from their relatively high ionization energies and, since the most popular acceleration processes are only efficient for charged particles, it is assumed that only the ionized fraction of hydrogen and helium atoms is accelerated. The second exceptions concerns two groups of elements, Li, Be, B and Sc ,Ti ,V ,Cr ,Mn, that are more abundant in the cosmic ray composition than in the Solar System. This discrepancy is easily explained as a result of spallation. In fact the primary cosmic rays accelerated in their sources have to propagate through the interstellar medium to reach the Earth and in this process there are spallation phenomena between the cosmic rays and the ambient interstellar gas. The net result is that the common elements in the cosmic rays are chipped away and fragmented populating the nuclear channel with atomic and mass numbers just less than those of the common groups of elements. Those elements which are produced in large abundances in the sources are called

primary elements, while those mainly produced by spallation in the interstellar gas are called *secondary elements*. In Figure 1.2(b) the energy spectra for protons, helium, carbon and iron nuclei are plotted as a function of the kinetic energy per nucleon.

At energies around the knee, since it is not possible to perform a direct measurement of the cosmic radiation, the nature of primary particles is inferred from Extensive Air Shower studies. In the past years it has become obvious that the knee is not a sharp kink but more a continuous change of the slope and extends over a wider energy range between 3×10^{15} eV and 10^{16} eV. It can be understood in terms of the different elementary components having similar energy spectra, but different cutoff energies. In this energy region a shift towards a heavier nuclei composition is observed. The standard interpretation for the knee-feature is based on the escape from the galaxy of the lighter galactic component of cosmic rays. In fact, at energies above 10^{15} eV the galactic magnetic field is no more able to confine light particles, due to the high value of their magnetic rigidity.
However various scenarios to explain the knee are proposed in the literature. A category of models discuss astrophysical reasons (acceleration in supernovae remnants, diffusive propagation through the galaxy), arguing that the knee is an intrinsic property of the energy spectrum, while in other models new particle physics processes in the atmosphere are involved so that the knee does not exist in the primary energy spectrum, being only an effect of observing extensive air showers in the atmosphere. The basic idea of these theories is that a new type of interaction, with threshold in the knee region, transfers energy to a component not observable (or not yet observed) in air shower experiments. In the model by Kazanas and Nicolaidis the energy is transferred into techni-hadrons, lightest supersymmetric particles [26], and gravitons [27].
Although the current experimental data can not rule these alternative explanations for the knee (see [28–32]), extrapolations of the low energy cosmic ray data with a rigidity dependent cutoff can describe the existing data very well. Moreover, the deconvoluted galactic mass spectra measured with KASCADE show distinct knees for each elemental component, compatible with a rigidity dependent knee. A precise measurements of the average mass of cosmic rays as function of energy and the spectra of individual elements or at least of elemental groups is therefore a key point to distinguish among the proposed models.

The high energy cosmic rays above the knee have two crucial problems, both related to the explanation of the features observed in the energy spectrum. One is the transition from galactic to extragalactic cosmic rays and the nature of the ankle, and the other is the end of the spectrum and the presence of the GZK cutoff, discussed in section 1.2.4.
There is a debate on the transition from the galactic to the extragalactic cosmic ray component. The most popular models explaining this features are:

- *the ankle model* [193]: the ankle feature is reproduced as the intersection of a flat extragalactic component (proton injected with flat generation spectrum $\propto \mathrm{E}^{-2}$ valid for non-relativistic shock acceleration) with a steep galactic component of iron. The beginning of the ankle at $E \sim 10^{19}$ eV corresponds to equal fluxes of galactic and extragalactic cosmic rays at this energy. However, this model has a great difficulty: it requires another component of galactic cosmic rays with acceleration up to energy 100 times greater than maximum energy in the standard model, around the iron knee $\sim 8\times10^{16}$ eV.

- *the dip model* [34]: all extragalactic cosmic rays are assumed to be protons and the ankle can be explained by a propagation effect. While traveling through the cosmic microwave

background (CMB) over extragalactic distances, protons loose energy due to Bethe-Heitler e^+e^- pair production. This causes a suppression of the flux and a pile up at slightly lower energies. The model predicts a transition energy that is low enough to be compatible with current estimates of the maximum energy of galactic accelerators and can well reproduce spectral data. However, the hard injection spectrum at the source is problematic in terms of the overall energy luminosity of extragalactic sources if extrapolated to low energies.

- *the mixed composition model* [36, 194]: the composition of the extragalactic flux, as it arrives at Earth, is strongly altered during propagation over extragalactic distances, and thus must be very different from the original composition at the sources. Because of the required low flux of the extragalactic component, a new galactic component needs to be introduced (component B), which fills the gap between the vanishing galactic flux from component A and the observed all particle spectrum in the energy interval from the knee up to the ankle. It can be argued that the component B may be associated with special classes of supernova explosions [37, 38]. As the dip model, this model gives a good description of the existing spectrum data, but with a much softer extra-galactic source spectrum. The transition from galactic to extragalactic cosmic rays is at about a factor 10 higher energies close to 1 EeV and correspondingly, this model needs galactic sources with a higher maximum acceleration energy than the dip-model.

At present the experimental results are contradictory in some cases and do not point towards a common interpretation. The HiRes collaboration claims that above 1 EeV, the data are consistent with a light, mainly protonic composition if compared to the QGSJET prediction [39]. The conclusion is confirmed by recently analyzed stereo data, extending the elongation rate to nearly 100 EeV. On the contrary, the data from the Pierre Auger Observatory favors a mixed composition at all energies [40]. Therefore the problem of the cosmic rays mass composition is still open and debated, being one of the key point of study of the Pierre Auger Observatory.

1.2.3 Arrival directions

The question regarding the arrival direction of cosmic rays is not yet fully solved, depending on the energy regime.

- **Below 10^9 eV:** the flux of cosmic rays is significantly influenced by the process of solar modulation and hence information about the arrival direction of these cosmic rays at the Solar System is lost. An increase in the intensity of solar cosmic rays is followed by a decrease in all other cosmic rays, due to the fact that the solar wind is sweeping the cosmic rays further outward. This phenomenon is called *Forbush effect* [41].

- **Between 10^9 eV and 10^{17} eV:** above 10^9 eV the majority of detected particles originates from outside the heliosphere. The energies are small enough so that these particles can be trapped by galactic magnetic fields. Because of the deviation caused by the magnetic field, up to these energies the cosmic ray directions are completely isotropic. Measurements from the KASCADE experiment in the PeV-energy regime [42, 43] and L3-Cosmics in the multi GeV-energy regime [44] indicate that anisotropies larger than 1% can be excluded. Nevertheless, in the multi-TeV energy regime a small scale anisotropy has been observed by the Super-Kamiokande experiment [45, 46], and Tibet experiment [43, 47, 48]. The Tibet results are of the order of 0.01% and can be explained by the rotation of the Sun within the galaxy and the Earth's motion along its orbit [48]. One expects a sidereal-diurnal effect

of amplitudes. This effect is known as *Compton-Getting* effect and manifests as dipole. Additionally, the Super-Kamiokande experiment has measured additional higher harmonic small scale anisotropies [46].

- **Around 10^{18} eV:** at this energy the deflection of the magnetic field in our galaxy becomes smaller. An anisotropy is expected and the cosmic rays should point to their sources. Currently, there is an issue of plausibility of experimental data. Experiments like AGASA [49] and SUGAR [50] have reported an excess from the galactic center, as well as spacial multiplets, but it is excluded by the Pierre Auger Observatory [51].

- **Around 10^{20} eV:** the Larmor radius R and the angular deflection of a particle of charge Z from a straight line trajectory in a magnetic field can be estimated by [52]:

$$R_{kpc} \approx \frac{E_{18}}{Z\, B_{\mu G}} \qquad \Delta\Theta \approx 0.3^\circ\, Z\, \frac{L_{kpc} \times B_{\mu G}}{E_{20}} = 0.3^\circ\, Z\, \frac{L_{Mpc} \times B_{nG}}{E_{20}}$$

where, E_{18} and E_{20} are energy in units of 10^{18} and 10^{20} eV, B is the magnetic field strength in μG or nG, and L is the source distance in kpc or Mpc unites. The former case is typical for Galactic dimensions and fields, while the latter one is for extra-galactic paths. The exact strength of intergalactic field is rather vague, but it is plausible to assume that the fields are coherent on scales of about 1 Mpc. Interpreting the consecutive deflections along the regions of coherent fields in terms of multiple scattering, the average angular deviation from a straight line path can be approximated as $\sqrt{L_{Mpc}}$ times the angular deflection over 1 Mpc. The estimated angular deflection of a 10^{20} eV proton over Galactic distances is $\sim 0.3^\circ$, so that, if extragalactic deflections are negligible, we can locate the source with high precision with a detector angular resolution comparable to 0.3°. However, extra-galactic deflection are likely to exceed galactic deflection, even though the interaction with the background radiation limits the path to about 50 Mpc. This means that the arrival direction should be dispersed at maximum by $\sqrt{50} \times 0.3^\circ = 2.1^\circ$.
Recently the Pierre Auger Observatory claimed a correlation of the events with energies above $6{\times}10^{19}$ eV with the position in the sky of some known AGNs [53]. Although the AGN are currently considered the prime source candidates, up to now no definitive evidences of cosmic ray sources have been established.

1.2.4 The GZK cutoff

In 1965 Penzias and Wilson [54] discovered the existence of the Cosmic Microwave Background Radiation (CMBR), Big Bang remnants constituted by photons at 2.7° K permeating the whole Universe. The following year (1966) Greisen [55] and independently Zatsepin e Kuz'min [56] showed that the interaction of cosmic ray primaries with CMBR photons would have led to a cutoff in the cosmic ray spectrum at the highest energies. The cutoff in the spectrum became known as the *GZK-limit*, from the names of the three physicists. The interaction of primary protons and heavier nuclei with the CMB radiation determines a rapid degradation of their energy, originating the cut in the spectrum.
The main reactions occurring between protons and CMBR photons are photo-pion production and e^+e^- pair production:

$$p + \gamma_{CMB} \rightarrow \begin{cases} \pi^0 + p \\ \pi^+ + n \\ p + e^+ + e^- \end{cases} \tag{1.2}$$

Denoting with γ, m, E, θ the Lorentz factor, the mass, the energy and the reaction collision angle of the produced particle and with $E_{\gamma_{CMB}}$ the photon energy in the laboratory system, the energy threshold E_{thr} associated to the photo-pion can be derived from the following equation [57]:

$$E_{\gamma_{CMB}}(\gamma - \sqrt{\gamma^2 - 1}\cos\theta) = \Delta m\, c^2 \left[1 + \frac{\Delta m}{2m}\right]$$

with Δm mass difference between incoming and outgoing particles. The minimum threshold energy is found for head-on collisions ($\cos\theta$=-1) [1]:

$$\gamma_{thr}^{pion} \simeq \frac{m_\pi c^2}{2E_{\gamma_{CMB}}}\left[1 + \frac{m_\pi}{2m_p}\right] \simeq \frac{7.5\times10^7\text{eV}}{E_{\gamma_{CMB}}} \Rightarrow E_{thr}^{pion} \approx 6.8\times10^{19}\text{eV} \tag{1.3}$$

The mean free path L for a proton can be estimated as:

$$L = (\sigma\rho)^{-1} \sim 8Mpc \tag{1.4}$$

with a CMB photon energy density $\rho_{\gamma CMB}$ ~400 cm^{-3} and cross section of the process at the threshold energy $\sigma_{p\gamma}^{pion}10^{-28}$ cm^{-2}. The energy loss per interaction is $\sim$ 20%, thus giving an attenuation length of the order of some tenths of Mpc, beyond which the proton energy falls below the GZK threshold. This bring us to the conclusion that the sources of the highest energy observed events must be within a sphere of that size.
At lower energies the dominant process is the Bethe-Heitler pair production with a threshold energy, for the case of head-on collision, equal to:

$$\gamma_{thr}^{pair} \simeq \frac{m_e c^2}{E_{\gamma_{CMB}}}\left[1 + \frac{m_e}{m_p}\right] \simeq \frac{5.1\times10^5\text{eV}}{E_{\gamma_{CMB}}} \Rightarrow E_{thr}^{pair} \approx 4.8\times10^{17}\text{eV} \tag{1.5}$$

At higher energies this process is less significant as its inelasticity is $\sim$ 0.1%, much smaller compared to the energy loss for the pion photo-production. The mean free path, with a cross section of the order of 10^{-25} cm^{-2}, is in this case about ~1 Mpc. If enough energy is available, multi-pion production can also be important. Furthermore primary protons can produce pions through interactions with the infrared (IRB), optical and ultraviolet background.

In the case of nuclei, relevant mechanisms for the energy loss are pair production and photo-disintegration, both on IR and on CMBR:

$$A + \gamma_{CMB} \rightarrow \begin{cases} (A-1) + N \\ (A-2) + 2N \\ A + e^+ + e^- \end{cases} \tag{1.6}$$

The photo-pion production process is negligible, except for light nuclei at very high energies. Indeed, for a nucleus of mass number A and charge Z, the energy loss length for pion production is roughly the same one of a nucleon with identical Lorentz factor. This is due to the fact that the cross section for pion production is approximately proportional to the mass number A, while the inelasticity is proportional to $1/A$. Instead for the pair production, while the inelasticity is proportional to $1/A$ as before, the cross section is proportional to Z^2 resulting in an energy loss length lower by a factor A/Z^2 with respect to a proton with the same Lorentz factor. Since $Z \sim A/2$, the ratio of the photo-pair and photo-pion production increases roughly linearly with

[1] The assumption $\gamma \gg 1$ is used.

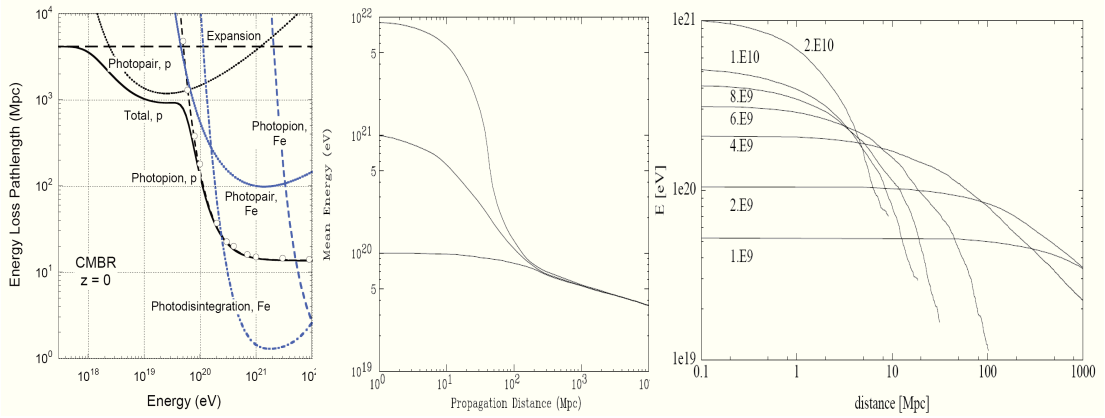

(a) (b) (c)

Figure 1.3: 1.3(a): Energy loss mean free path for UHECR protons (black) and Fe nuclei (blue) in the CMB at redshift z=0, as a function of the total particle energy (taken from [59]). The short-dashed black curve gives the analytical approximation for the UHECR proton photo-pion energy loss path length, in comparison with the numerical results, shown in open circles. Numerical results for the photo-pair energy-loss path length of UHECR protons and Fe are represented by the dotted curves. The blue dot-dashed curve gives the photodisintegration energy loss curve of Fe. Expansion losses are represented by the long-dashed line, with $c/H_0 = 4170$ Mpc; 1.3(b): Proton energy as a function of propagation distance through the CMB for the indicated initial energies (taken from [60]); 1.3(c): Iron energy as a function of propagation distance through the CMB for the indicated initial Lorentz factors (taken from [61]).

Z [58].
The photo-disintegration process in the CMB and IRB has a rate given by:

$$R_{A,Z,i_p,i_n} = \frac{A^2 m_p^2 c^2}{2E^2} \int_0^\infty \frac{n(\epsilon)}{\epsilon^2} d\epsilon \int_0^{2E\epsilon/Am_pc} \epsilon' \sigma_{A,Z,i_p,i_n}(\epsilon') d\epsilon' \tag{1.7}$$

where i_p and i_n are the numbers of protons and neutrons broken off from a nucleus in the interaction, $n(\epsilon)$ is the density of background photons of energy ϵ, and $\sigma(\epsilon')$ is the photo-disintegration cross section parameterized on the basis of current data. The cross section for nuclei is dominated by the giant dipole resonance (GDR), which peaks in the energy range $\sim 10-30$ MeV, while at higher energies the quasi-deuteron emission and the barionic resonances are the main processes, contributing to keep the nuclei attenuation length at their lowest values even at the very high energies, where the influence of the GDR decreases.
In Figure 1.3(a) the energy loss length in Mpc for proton and iron relative to the photo-pion, photo-pair production and photo-disintegration processes in the CMB as function of the primary energy is reported. The result of the described processes, together with the adiabatic energy loss due to the Hubble expansion, is the significant degrade of the initial energy of the primary at the source, leading to a different energy spectrum observed at the Earth with respect to the one injected at source. This is evidenced in Figures 1.3(b) and 1.3(c) in which the energy degradation is plotted as a function of the propagated distance for proton and iron primaries respectively. It can be seen that independently of the initial energy of the primary, after traveled distances of ∼100 Mpc, the energy reduces below 10^{20} eV. This imply that the universe is substantially opaque to nucleons with energy above $\sim 10^{20}$ eV on scales above ∼100 Mpc.
Regarding others primary particles, neutrons, even at the higher energies, decay into protons after a free fly of only ∼1 Mpc, so they could be ruled out.

In the case of high energy γ-rays, the dominant absorption process is pair production through collisions with the radiation fields permeating the Universe. On the other hand, electrons and positrons could produce new γ-rays via inverse Compton scattering. The new γ can initiate a fresh cycle of pair production and inverse Compton scattering interactions, yielding an electromagnetic cascade. The development of electromagnetic cascades depends sensitively on the strength of the extragalactic magnetic field B, which is rather uncertain. The threshold for the pair production process is given by:

$$E_{thr}^{pair} = \frac{m_e^2}{E_{\gamma_{CMB}}} \simeq \frac{2.6 \times 10^{11}}{E_{\gamma_{CMB}}} \text{eV}$$

Above 10^{20} eV , the most relevant interactions are those with radio background, which is almost unknown. Therefore, the GZK radius of the photon strongly depends on the strength of extragalactic magnetic fields. In principle, distant sources with a redshift $z > 0.03$ can contribute to the observed cosmic rays above $5{\times}10^{19}$ eV if the extragalactic magnetic field does not exceed 10^{-12} G [62].

The propagation of UHE neutrinos is governed mainly by their interactions with the relic neutrino background (RNB). Despite the smaller cross section with respect to neutrino-nucleon interactions, the neutrino-neutrino interactions are predominant because the RNB density, $\sim$100 cm^{-3} per family, is about 10 orders of magnitude larger than the baryon density. The $\nu\bar{\nu}$ annihilation mean free path is of the order of $\lambda_\nu{=}(\sigma_{\nu\bar{\nu}}\rho_\nu)^{-1}$ $\simeq 4{\times}10^{28}$ cm$\simeq$13 Gpc. Therefore they can travel over cosmological distances with negligible energy loss and could produce Z bosons. In that case, highly boosted decay products could be observed as super-GZK (above GZK-limit) primaries and they would point directly back to the source. This model of course requires very luminous sources of extremely high energy neutrinos through-out the Universe.

Finally, since the direct consequence of the GZK-limit is the impossibility for primaries of higher energies to travel through distances above $\sim$100 Mpc, and since at these energies primaries should not significantly suffer deflections due to galactic/extragalactic magnetic fields, these should point directly to their sources, allowing their individuation. Section 1.6.3 is dedicated to recent anisotropy results from the Auger experiment. Measurements of the presence of the GZK modulation made by experiments before the installation of the Pierre Auger Observatory have been inconclusive. Evidences for a steepening in the spectrum have been recently claimed by the Auger [63] and the HiRes [64] collaborations.

1.3 Origin of cosmic rays

Between 10^{10} eV and the knee at $3{\times}10^{15}$ eV it is widely accepted that the bulk of particles stem from galactic sources. Multi-wavelength observations of X-ray and TeV γ-rays favour that most of the CR particles are accelerated in supernovae remnants [65]. Integrating the flux over energy and assuming an isotropic and uniform distribution in space, the energy density is ρ_{sl} $\sim$0.3 eV cm^{-3}. This value is comparable to the energy density of the visible star light ρ_{sl} $\sim$0.3 eV cm^{-3}, the galactic magnetic fields $B^2/2\mu_0$ $\sim$0.25 eV cm^{-3}, or the microwave background ρ_{CMB} $\sim$0.25 eV cm^{-3}.

The power required to sustain a constant cosmic ray intensity can be estimated as

$$L_{CR} = \frac{\rho_{CR} V}{\tau_{esc}} \sim 10^{41} \ \ erg/s$$

where τ_{esc} is the residence time of cosmic rays in a volume V (the Galaxy, or the galactic halo). With a rate of about three supernovae per century in a typical Galaxy the energy required could

be provided by a small fraction (∼10%) of the kinetic energy released in supernova explosions. The region between knee and ankle is still matter of discussion.

1.3.1 Acceleration models

There are basically two kinds of acceleration mechanisms considered in connection with CR acceleration: the direct acceleration of charged particles by an electromagnetic field and the statistical acceleration in a magnetized plasma (Fermi acceleration).

Single-shock models

These models focus basically on rotating magnetized neutron stars, called pulsars. Other models focus on accretion discs around black holes, that are threaded by magnetic fields. One of the major disadvantages of direct acceleration models is that most models do not reproduce the observed power-law spectrum. Moreover, direct acceleration can be excluded to explain the origin of the UHECR. Pulsars or stellar black holes cannot produce a field strong enough to accelerate particles up to 10^{20} eV. Galactic black holes, like the core of a rotating radio galaxy, would give rise to an electromagnetic field large enough to accelerate the particles up to 10^{20} eV, but these objects are shielded by dense pair plasma and intense radiation, which would cause energy losses. The crab pulsar might have the capacity to accelerate a proton up to a few 10^{16} eV and iron into the 10^{18} eV range but it is not expected that the complete electric field is available to accelerate particles.

The Fermi acceleration model

One of the earliest theories on the acceleration of cosmic rays was proposed by Enrico Fermi in 1949 [66]. It became known as the *Second Order Fermi Mechanism*. In this model, particles collide stochastically with magnetic clouds in the interstellar medium. This mechanism naturally predicts a power law energy spectrum, but the power index depends on the details of the model and would not give rise to a universal power law for cosmic rays arriving from all directions. This mechanism is also too slow and too inefficient. So, a more efficient version of Fermi Acceleration was proposed, in witch particles are accelerated by strong shock waves propagating through interstellar space [67–70]. A scheme of the process is described below.
A shock-front moves with the velocity v_{shock} through a stationary interstellar medium. Starting in the shock-front's rest frame, the upstream fluid is approaching the shock-front with v_{shock} and flowing away with v_{down}. Using the continuity equation we derive $v_{shock}/v_{down} = \rho_{down}\rho_{ISM}$. For a mono-atomic or fully ionized gas using the adiabatic constant for specific heats of an ideal gas $\gamma = 5/3$ we obtain $v_{shock}/v_{down} = 4$. The idea is that a particle in the upstream rest frame sees the downstream gas approaching with $3/4v_{shock}$. When crossing the shock-front a small amount of energy is transferred to the particle. The turbulences in the downstream region isotropize the particles again and in the downstream rest frame the interstellar medium approaches with $3/4v_{shock}$. When crossing the shock-front again, they encounter gas moving towards the shock front with $3/4v_{shock}$. Therefore, the particles are expected to be accelerated by exactly the same process when crossing from the upstream to the downstream region and vice versa. A particle that repeatedly crosses the shock front can gain energy rapidly. Consequently, this model is referred to as the *First Order Fermi Mechanism*.
The predicted energy gain is $\propto \beta$, with $\beta = \mathrm{v}_{shock}/\mathrm{c}$. After a time T the maximum energy

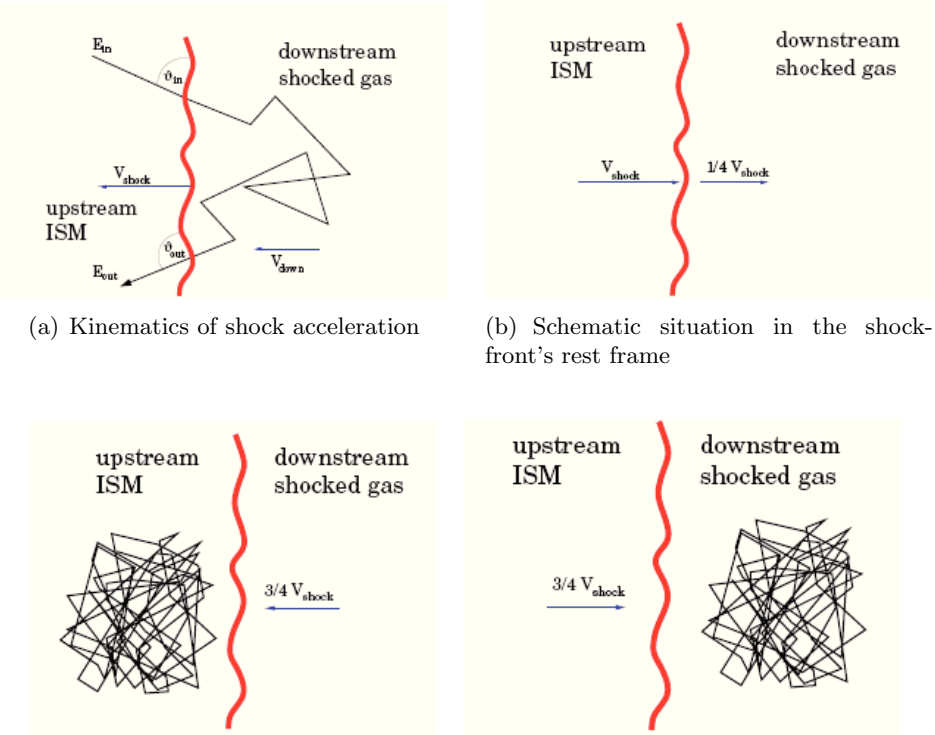

(a) Kinematics of shock acceleration

(b) Schematic situation in the shock-front's rest frame

(c) Schematic situation in rest frame of downstream fluid

(d) Schematic situation in rest frame of the upstream ISM

Figure 1.4: Schematic illustration of the 1st order Fermi acceleration in strong shock winds.

attained is

$$E_{max} \sim Ze\beta BTv_{shock}$$

This results in an upper limit, assuming a minimal diffusion length equal to the Larmor radius of a particle of charge Ze in the magnetic fields B behind and ahead of the shock. Using typical values of type II supernovae exploding in an average interstellar medium yields E_{max} ∼Z×100 TeV [71]. More recent estimates give a maximum energy up to one order of magnitude larger for some types of supernovae $E_{max} \sim Z{\times}5$ PeV [72–74]. As the maximum energy depends on the charge Z, heavier nuclei can be accelerated to higher energies. This leads to consecutive cutoffs of the energy spectra for individual elements proportional to their charge Z, starting with the proton component.

1.3.2 Sources of high energy cosmic rays

The question on the possible sources of the ultra high energy cosmic rays is one of the most challenging in the astroparticle field. On the theoretical side, models have been proposed to solve this question. We will briefly summarize here the two possible scenarios:

- The *bottom-up* scenario in which particles are accelerated from low energies to higher energies in astrophysical environments;

- The *top-down* scenario in which exotic particles, from early universe, decay producing cosmic rays.

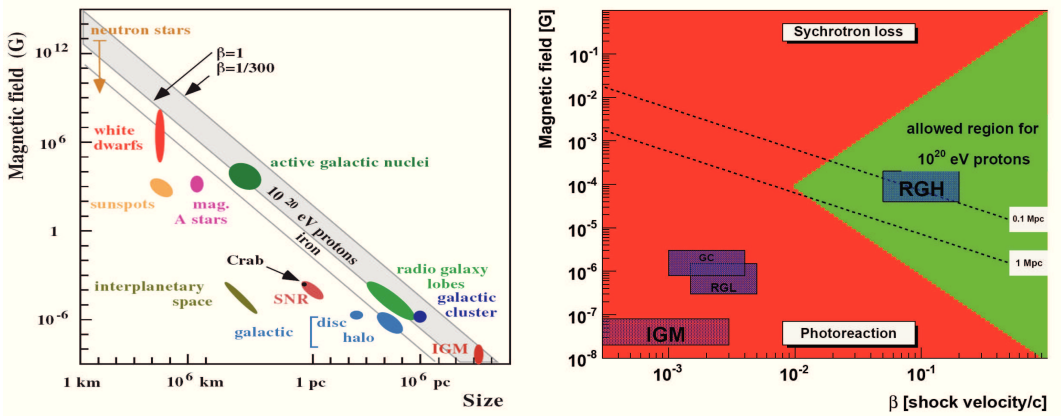

(a) (b)

Figure 1.5: 1.5(a): Hillas plot. Magnetic field strength and size of possible acceleration sites are drawn; 1.5(b): Additional limits in the Hillas plot drawn from synchrotron loss processes and photo-pion dissipation (compilation from [52]). Magnetic field strength and shock velocity of possible acceleration sites are drawn. Only the green region allows acceleration of protons up to 10^{20} eV. Candidate accelerators must also lie above the dashed lines appropriate to their characteristic size. RGH: Radio Galaxy hot spots, RGL: Radio Galaxy Lobes, GC: Galactic Cluster, IGM: intergalactic medium.

Bottom-up scenarios

Bottom-up scenarios can be classified into models that assume a single-shock acceleration of particles in an electromagnetic field or statistical acceleration via Fermi acceleration in magnetized plasma.
The maximum energy attainable in diffusive shock acceleration depends on the size and on the magnetic field strength of the object where the acceleration takes place. Large sizes and strong fields are required to accelerate particles up to 10^{20} eV , since particles with a Larmor radius exceeding the size of the astrophysical objects are able to escape from the acceleration region. This condition is summarized in the following expression [193]:

$$E_{max} \propto \beta\, Ze\, B\, R \tag{1.8}$$

where β is the velocity of shock waves in case of stochastic acceleration or the efficiency of the acceleration in case of a single-shock acceleration scenario.
This is known as *Hillas criterion*. The *Hillas criterion* allows to classify different sources, as summarized in the form of the popular *Hillas diagram* shown in Figure 1.5(a). The possible sources are represented according to their size and magnetic field strength. For a fixed acceleration energy and particle type the possible sources have to lay above a straight line. Usually, these objects are not expected to achieve the maximum energy predicted by the Hillas equation due to processes of energy loss occurring at the source. The main energy loss mechanisms are the synchrotron emission of the accelerated charged particles and the photo-pion production on the CMB or more realistic with local radiation at the source, having an energy loss rate of $-\frac{dE_{sync}}{dt} \propto B^2E^2$ and $-\frac{dE_{pion}}{dt} \sim const.$ Acceleration ceases when the loss rate excesses the energy gain rate. This condition leads to the exclusion zones plotted in Figure 1.5(b). Until now, no clear astrophysical source could be identified to be the source of the UHECR, nevertheless the list of possible candidate sites is long [75]. The characteristics of some of them are summarized below:

- *Active Galactic Nuclei* (AGN): are one of the most favored sources for cosmic rays at the

highest energies. AGNs are powered by the accretion of matter onto a supermassive black hole of $10^6 \div 10^8$ solar masses. Typical values in the central engine are $R \sim 10^{-2}$ pc, and $B \sim$5 G, which make possible the containment of protons up to 10^{20} eV. The main problem here is the large energy loss in a region of high field density, which would limit the maximum energy achievable for protons and forbid the escape for heavy nuclei. Neutrons could eventually escape the central region and then decay to protons with maximum energy around 10^{18} eV. Another solution is that the acceleration occurs in AGN jets where particles are injected with Lorentz factors larger than 10, and where energy losses are less significant;

- *Radio-galaxies hot spots*: Fanaroff-Riley II galaxies are the largest known dissipative objects (non-thermal sources) in the Universe. Jets from the central black-hole of an active galaxy end at a termination shock where the interaction of the jet with the intergalactic medium forms radio lobes and localized regions of intense synchrotron emission, known as 'hot spots'. For typical hot-spot conditions $B \sim 300$ μG and $\beta \sim 0.3$. Assuming that the magnetic field of the hot spot is limited to the observable region ($\sim$ 1 pc), one obtains $E_{max} < 5{\times}10^{20}$ eV;

- *Clusters of galaxies*: galaxy clusters are reasonable sites to consider for ultra-high energy cosmic rays acceleration, since particles with energy up to 10^{20} eV can be contained by cluster fields (~ 5 μG) in a region of size up to 500 kpc. However losses due to interactions with the microwave background during the propagation inside the clusters limit UHECRs in cluster shocks to reach at most 10 EeV;

- *Gamma Ray Bursts* (GRBs): collapse of massive stars or mergers of black holes or neutron stars could explain the origin of the detected bursts of gamma rays up to GeV energies. The observed gamma-rays are emitted by relativistic electrons via synchrotron radiation and inverse Compton scattering. Acceleration of electrons and protons to the highest energies is then necessary. The duration of the detected GRB signal extends over 5 orders of magnitude ($10^{-3} \div 10^2$ s) with an energy release up to 10^{51} erg/s. This is consistent with the luminosity required for cosmic rays above 10^{19} eV, but the large estimated GRBs distances cannot account easily for the UHECR flux;

- *Neutron stars*: for direct acceleration in compact objects, for example in rotating neutron stars or pulsars, the relation (1.8) becomes $E_{max} = \omega/cZB_sR_{ns}^2$, where ω is the pulsar angular velocity, B_s the surface magnetic field and R_{ns} the neutron star radius.
  If $B_s \sim 10^{12}$ G, $r_{ns} \sim$10 km, and $\omega \sim$200 Hz (values refer to the Crab pulsar), this is equivalent to an electromagnetic force of $\sim 10^{18}$ V.

Top-Down scenarios

An alternative to acceleration models, introduced to explain the highest energy cosmic rays, are the so called top-down models, which involve the decay or annihilation of exotic particles. These can be: topological and non-topological solitons, X-particles, cosmic defects, microscopic black-holes, fundamental strings, basically decaying in quarks and leptons. The quarks produce jets of hadron, mainly pions and a few percent of nucleons. The pions decay then to photons, muons, neutrinos (anti neutrinos) and electrons (positrons). The general characteristic of these models is a photon domination of the spectrum at the highest energies. This signature makes the hypothesis testable.

In order to detect the produced UHECR, the X-particle must be super-massive (>10^{11} GeV). The density and the rate of decay must be large enough to account for an observable cosmic rays flux. Moreover, to avoid energy loss during the propagation from the source, the decays must take place within a limited distance (∼100 Mpc). To explain the UHECR one commonly classifies between two cases :

- **Decay Top-Down Scenarii:** in this case unstable particles decay and, among their decay products the UHECR are produced. An unified formula for the quantum decay rate of all these objects was provided in [76]. For all relics one has to fine tune the lifetime of these objects to be the age of the universe and the value of their mass that must be adjusted to be larger than 10^{20} eV. Heavy relics could have been formed by the end of inflation at typical GUT's energy scales.
- **Annihilation Top-Down Scenarii:** other models proposed that stable heavy relics can produce UHECR through annihilation by pairs [77]. In this scenario, the relics are assumed to have masses around M_X ∼10^{12} GeV and produce UHECR through annihilation when they collide. Here, the lifetime free parameter is replaced by the annihilation cross section. These super-heavy particles are assumed to be produced during reheating.

A signature of top-down scenarios is that the spectra of the particles generated in the top-down models are typically flatter than the bottom-up ones. Contrary to the acceleration mechanisms the top-down generated spectra do not follow a power-law.

1.3.3 Propagation model

The propagation of cosmic rays, up to 10^{18} eV is supposed to be related to the structure of our galaxy. In fact, after their acceleration cosmic rays are transported along magnetic field lines and several physical processes take place. These are diffusion on the irregularities of the magnetic field, spallative reactions with the interstellar gas and radioactive decay. Following the diffusive transport equations which govern both, acceleration and propagation of cosmic rays can be written as [78]:

$$\begin{aligned}\frac{dN_i(E)}{dt} &= \underbrace{\nabla\cdot(D_i\nabla N_i)}_{\text{diffusion}} - \underbrace{\frac{\partial}{\partial E}(b_i(E)N_i(E))}_{\text{acceleration}} - \underbrace{\nabla\cdot\mathbf{v_c}N_i(E)}_{\text{convection}} \\ &+ \underbrace{Q_i(E,t)}_{\text{source}} - \underbrace{p_iN_i}_{\text{loss}} + \underbrace{\sum_i\int_E^\infty N_j(E_j)f_{ji}(E,E_j)dE_j}_{\text{fragmentation}} \end{aligned} \tag{1.9}$$

where D is the diffusion coefficient (D=$1/3\lambda_D v$, with v particle velocity and λ_D diffusion mean free path), $b_i(E) \equiv dE/dt$ is the mean rate at which a particle gains energy (either energy loss or acceleration), v_c is the convection velocity, $Q_i(E,t)$ is a source term representing the number of injected particles of type i per volume, time and energy interval dE, p_i gives the collision and decay probability and f_{ij} gives the probability that a particle j with energy E_j is converted to a particle i with energy E_i.
More simple approximate models are also used in the investigations of cosmic ray propagation. The most popular is the *Leaky-box Model* (e.g. see [79]) where the transport of energetic particles is described by introducing the mean escape time of cosmic rays from the Galaxy that is function of particle energy. In this model the diffusion term of 1.9 is replaced by $-N/\tau_{esc}$. In the absence

of collision and other energy changing processes, and without convection, the solution for a delta function source $Q(E,t)=N_0(E)\delta(t)$ is

$$N(E,t) = N_0(E)\exp(-t/\tau_{esc}) \tag{1.10}$$

Thus, τ_{esc} is interpreted as the mean time spent in the Galaxy and $\lambda_{esc} \equiv \rho\beta c\tau_{esc}$ as the mean amount of matter traversed by a particle of velocity βc. In the equilibrium condition (dN_i/dt=0) the transport equation have been used with success to describe the composition data of low energy galactic cosmic rays under the assumption that all nuclei have the same propagation history, as a function of interaction length λ_{esc}. If the fragmentation of higher nuclei is neglected the solution is:

$$N(E) = \frac{Q(E)\tau_{esc}(R)}{1+\frac{\lambda_{esc}(R)}{\lambda}} \tag{1.11}$$

This approximation gives good results up to 10^{15} eV, while the situation changes around the knee, where the gyro-radius of the particles exceeds the size of the galactic disk and it is assumed that the galactic fields cannot longer bind the particles. Here, it is supposed, that the diffusion of the galaxy becomes dominant and one would expect to see a rapidity dependent cutoff in the energy spectra of the different components. In these cases, the full transport equation is solved typically employing sophisticated numerical simulations like the GALPROP code [80]. Monte Carlo codes are used also to study the extragalactic propagation of high energy cosmic rays.

1.4 Extensive Air Showers

When high energy cosmic ray particles hit the atmosphere, they interact with molecules of the air. These interactions at the highest energies initialize the formation of *Extensive Air Showers* (EAS). The atmosphere acts as a huge calorimeter, since the primary energy is related to the energy deposited in the atmosphere by the produced particles. The number of particles $N(X)$ produced in successive interaction generations at a given traversed atmospheric depth X (usually expressed in $\mathrm{g\,cm^{-2}}$) grows up reaching a maximum $N_{max}(X_{max})$, then it begins to decrease, because the energy carried by secondary particles becomes lower than the energy needed to produce a new generation. Figure 1.6(a) is an image of the particle tracks produced by a proton of 10 GeV entering a cloud chamber. The proton interacts with the lead layers (1.3 cm thick) producing a cascade of secondary particles.
If the cosmic ray primary is a nucleon or a nucleus, the shower begins with a hadronic interaction that produces a large number of shortlived mesons (mainly pions) of which many decay into muons, electrons and photons. It is convenient to group the particles of an EAS into three main groups: hadronic, muonic and electromagnetic. In Figure 1.6(b) a scheme of the interactions occurring during the development of an EAS is shown. A typical interaction is

$$p + p \rightarrow p + p + N(\pi^+\pi^-\pi^0)$$

Inelastic collisions of hadrons with air nuclei of the atmosphere produce usually high energetic hadronic secondaries which again interact or decay. This component is mostly dominated by mesons, like π or K. The charged pions decay according to $\pi^\pm \rightarrow \mu^\pm + \nu_\mu(\bar{\nu}_\mu)$ contributing, together with the decay of kaons ($K^\pm \rightarrow \mu^\pm + \nu_\mu$ or $K^\pm \rightarrow \pi^\pm + \pi^0$) to form the flux of muons and neutrinos at ground level.
The electromagnetic cascade is initiated and fed principally by the π^0, but other particles like the

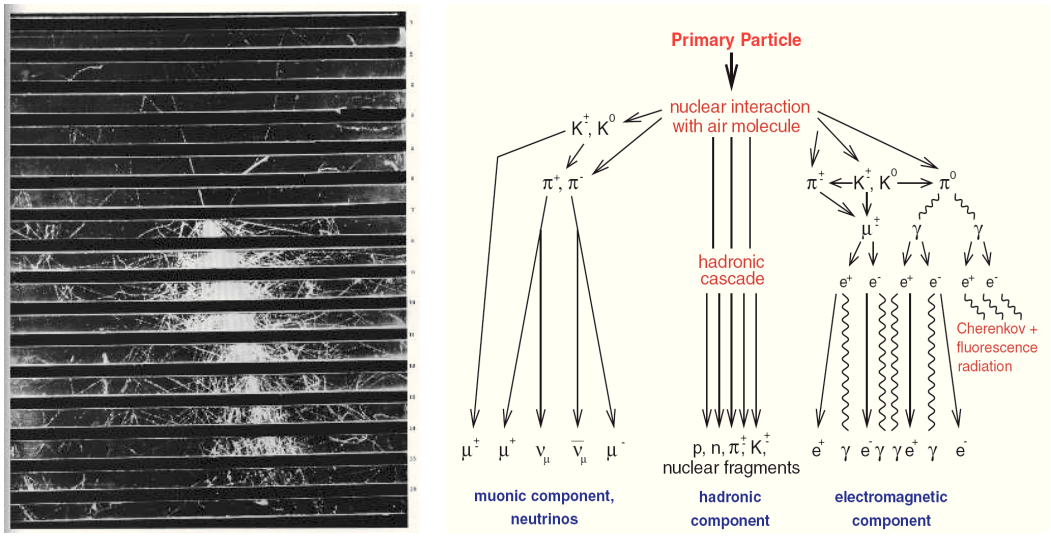

(a) (b)

Figure 1.6: 1.6(a): Particle tracks generated by a 10 GeV proton entering a cloud chamber; 1.6(b): A scheme of the particle interactions involved in EAS generations.

η mesons are involved. The π^0 can decay in $\gamma\gamma$, that can produce $e^{\pm}$ via pair production. The electrons can recreate γ via bremsstrahlung and the process continues. This process ceases when the electrons have reached the critical energy ε_c at which the ionization loss in air dominates over the loss due to bremsstrahlung [81]:

$$\varepsilon_c = \frac{710}{Z + 0.92}\,\text{MeV} \sim 86\text{MeV}$$

where Z=7.3 is the effective charge number of the atmosphere.
Electromagnetic particles are by far the most abundant and they carry the largest fraction of the total energy. Globally about 90% of the primary energy is dissipated in the electromagnetic channel by ionization. The remaining energy is kept by muons and neutrinos produced by the decay of charged pions. In addition, there are particles not contributing much to the total energy balance, i.e. UV-photons (fluorescence and Cherenkov) and radio emission, or which are not detectable and are therefore called invisible component (neutrinos and very low energy particles).

1.4.1 The electromagnetic component

The processes involved in the development of the electromagnetic component of the cascade have been extensively treated by Rossi and Greisen [81, 82]. Before recalling the basic results of their 'cascade theory', it is instructive to consider a simpler model, the *Toy Model* developed by Heitler in 1944 [83]. This model, although certainly not realistic, allows to catch some basic properties of the shower, e.g. the number of produced particles as function of the atmospheric depth (longitudinal profile), to be compared with more sophisticated predictions. It neglects multiple scattering and Compton scattering effects and considers only the bremsstrahlung and pair production, assuming equal interaction lengths for the two processes. It is assumed that the photon energy in pair processes is shared between both leptons. Furthermore, the energy of an electron in a bremsstrahlung process is shared between the photon and outgoing electron.

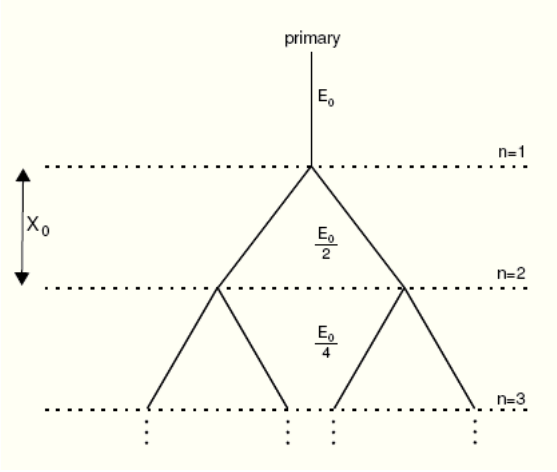

Figure 1.7: Heitler model for an effective electron-photon shower.

Figure 1.7 displays the electromagnetic Heitler model, where electromagnetic means high energy e^-, e^+ and γ with an energy larger than their critical energy.
Denoting with X_0 the radiation length of air, it is assumed that after exactly one splitting length

$$\lambda = X_0 \ln 2$$

an interaction occurs and the energy of the initial particle is distributed equally onto the two interaction products. The total number of particles doubles after every λ and the total energy E_0 is subdivided equally onto the particles of the cascade

$$N_n = 2^n \qquad E_n = E_0/2^n$$

When the energy per particle drops below the critical energy ε_c they are assumed to stop producing new particles, but loose their remaining energy by ionization (collisional energy loss). At this point the cascade reaches its maximum in particle number and suddenly dies out:

$$N_{max} = E_0/\varepsilon_c \qquad X_{max} = \lambda \frac{\ln(E_0/\varepsilon_c)}{\ln 2} = X_0 \ln(E_0/\varepsilon_c)$$

Although the assumptions of the Heitler model are quite crude, which is reflected in the predicted unrealistic end of the particle cascade, it reproduces the average trends in the longitudinal shower development, the fact that the depth of maximum has a logarithmic dependence on the primary energy, while the number of particles at maximum scales linearly with the energy.
In the work of Rossi and Greisen the development of the shower is described by the cascade equations:

$$\frac{dN_\gamma}{dX} = -\frac{N_\gamma(E,X)}{\lambda_{pair}} + \int_E^\infty N_e(E',X)\frac{dn_{e\to\gamma}}{dEdX}dE' \tag{1.12}$$

$$\frac{dN_e}{dX} = -\frac{N_e(E,X)}{\lambda_{brems}} + \int_E^\infty N_e(E',X)\frac{dn_{e\to e}}{dEdX}dE' + 2\int_E^\infty N_\gamma(E',X)\frac{dn_{e\to\gamma}}{dEdX}dE' \tag{1.13}$$

where $N_\gamma(E,X)$ and $N_e(E,X)$ are the number of γ and $e^\pm$ of energy E at depth X. In the so-called *Approximation* A[2][79] the solution for the number of charged particles N_e is:

$$N_e(X) = \frac{0.31}{\beta_0^{1/2}} e^{X(1-\frac{3}{2}\ln s)}$$

where β_0=ln(E_0/ε_c) and $s \simeq \frac{3X}{X+2\beta_0}$ is the *shower age* (s=0,1 at the shower beginning and at maximum respectively and s>1 beyond the maximum). The depth of maximum and number of particles at maximum are given by:

$$X_{max} = 1.01\left[\ln\left(\frac{E_0}{\varepsilon_c}\right) - \frac{1}{2}\right] \qquad N_{max} = \frac{E_0}{\varepsilon_c}\cdot\frac{0.31}{[\ln(E_0/\varepsilon_c) - 0.18]^{1/2}}$$

As can be seen, the predictions made by the Toy Model are confirmed by a more detailed description.

The above description refers to an average behavior of the shower. Actually the fluctuations in the first interaction point, as well as along the entire cascade, has to be considered. The former can be parameterized assuming an exponential interaction probability $P(X_1)$=$\sigma_0 \exp(-\sigma_0 X_1)$, with X_1 first interaction depth, and corresponding fluctuation in the number of particles is $\delta \ln N \sim 9/14(s - 1 - 3\ln s)$. The fluctuations due to the stochastic behavior of the interactions occurring along the shower development cannot be modeled analytically, hence a Monte Carlo numerical simulation is employed.

Furthermore, during the longitudinal development of the air shower, the electromagnetic component spreads laterally due to Coulomb scattering. The determining factor for the lateral spread is the Moliére radius[3] r_0=E$_s$X$_0$/ε_c ≈9.3 g cm^{-2}.

The lateral extent of the electromagnetic component is described by the NKG-function (J.Nishimura, K.Kamata and K.Greisen) [55, 84]

$$\rho(r) = C(s)\frac{N_e(X)}{r_0^2} f\left(\frac{r}{r_0}\right) = C(s)\frac{N_e(X)}{r_0^2}\left(\frac{r}{r_0}\right)^{s-2}\left(1+\frac{r}{r_0}\right)^{s-4.5} \tag{1.14}$$

where $C(s)$ is a normalization parameter and the Lateral Distribution Function (LDF) $\rho(r)$ represents the density of shower particles (particles/m^2) as a function of the distance r from the core, computed in the shower plane (perpendicular to the shower axis). The previous parametrization is valid in the range 0.6≤ s≤1.8 with $s \simeq \frac{3X}{X+2\ln(E_0/\varepsilon_c)+2\ln(r/r_0)}$. More recent analysis and results from Monte Carlo simulations show that the LDF is steeper with respect to the NKG form, however, this parametrization or slight modifications of it are proved to be adequate to describe the lateral distribution observed in the data.

It is worth to consider that electromagnetic cascades can produce also a muon component at ground. This is essentially determined by interaction processes, like $\mu^+\mu^-$ production and photonuclear reactions, that have smaller cross sections compared to other electromagnetic interactions. The $\mu^+\mu^-$ cross section is $\sigma_{\mu^+\mu^-} = \sigma_{e^+e^-} m_e^2/m_\mu^2$, obtained by simply replacing m$_e$ →m$_\mu$ (details about muons in EAS are reported in Chapter 2).

[2]In the *Approximation A* the energy loss by ionization is neglected together with photoelectric and Compton effects, the radiation length is independent of energy and the inclusive cross sections for pair production and bremsstrahlung scale.

[3]The Moliére radius r_0 is defined as the lateral distance travelled by electrons at the critical energy traversing 1 radiation length X_0.

1.4.2 The hadronic component

An EAS induced by a primary nucleus is made up of two components, the hadronic and the electromagnetic cascade. The two cascades cannot be treated separately as the latter is continuously fed by the former. In the first interaction a considerable fraction of the primary energy (∼50%) is transferred to the produced mesons, while the remaining energy is carried by the leading nucleons, that initiate other generations of mesons according to the interaction length. With a mean free path of 84 $\mathrm{g\,cm^{-2}}$ for a vertical incoming particle typically 12 interactions occur. The majority of secondary hadronic particles are neutral and charged pions, followed by kaons, baryons like protons and neutrons and nucleonic fragments.
The development of the hadronic component is essentially determined by two observables: the inelastic cross section σ_{in} of the primary particle and of the secondaries with air, and the inelasticity κ of the collision [4].
The total nucleon-nucleon cross section (elastic+inelastic) is ∼ 40 mb at center of mass energies of 3 GeV< $\sqrt{s}$ <100 GeV. It has been measured experimentally up to a nucleon momentum of 1000 GeV/c in the laboratory system, corresponding to 44.7 GeV in the center of mass. For higher momenta the cross section is extrapolated using an empirical fit of the inelastic proton-antiproton cross section (a detailed discussion can be found in [85] and the most recent parameterizations in [24]). The corresponding inelastic part, determined by subtracting the measured elastic cross section from the total one, is ∼ 30 mb.
The inelasticity combines the multiplicity and the energy of the secondaries, thus describing how much of the energy of the incoming particle is transferred onto secondary particles. Therefore it is more relevant than the particle multiplicity alone. High inelasticity means that the energy is dissipated quickly and the shower develops fast, i.e. it reaches its maximum higher up in the atmosphere. Low inelasticity means that the leading particle carries off most of the energy, leading to slow developing and long showers.

Primary nuclei have been treated according to the *superposition model* with the assumption that a nucleus of mass A and primary energy E_0 is just equivalent to a superposition of A free nucleons of energy E_0/A.
Although very simplified, this model allow to understand some basic differences of the showers initiated by nucleons and by nuclei. The interaction cross section for nuclei is higher than for nucleons so that the first interaction occurs higher in atmosphere and the shower development is ruled by the energy per nucleon rather than by the total energy. This means that the available energy per nucleon is smaller with respect to a primary nucleon of the same initial energy. For this reason the showers induced by nuclei develop faster in the atmosphere, i.e. they reach the maximum at smaller depths. Moreover, the observed fluctuations for nuclei are smaller than for nucleons, as the interaction fluctuations are averaged over all the constituent nucleons.
Denoting with λ_N the interaction length of the nucleons in air, the prediction for the depth of maximum reached by a primary nucleus of mass A is:

$$X_{max} \propto \lambda_N \ln\left(\frac{E_0}{A\varepsilon_c}\right) \tag{1.15}$$

More realistic descriptions of nucleus-nucleus collision properties are developed (for example with the Glauber theory [86]), but again the numerical solutions of the cascade equations describe

[4] The inelasticity is defined as the fraction of the energy of the parent particle transferred to the secondary particles

the 'average' behavior of the shower and a full Monte Carlo approach is needed to reproduce shower fluctuations.
Finally, it should be stressed that, whereas electromagnetic interactions are rather well understood within perturbative QED, hadronic multiparticle production cannot be calculated within QCD from first principles. Phenomenological models have to be used to describe the final states of hadronic interactions. The parameters of these models are determined by comparing the model predictions with accelerator measurements. Reflecting the different methods for describing data, low- and high-energy interaction models are distinguished. The former ones are typically based on the picture of intermediate resonance formation and decay as well as parametrizations of data. The latter ones are involving the production of color strings and their fragmentation.

1.5 Detection techniques

The rapid decrease of the integral flux makes extremely difficult the direct observation of primaries of energy $E > 10^{15}$ eV . For this reason the study and detection of cosmic rays uses different techniques depending on the energy region of interest. Instruments as calorimeters, emulsion chambers, and others can be used to detect primaries up to $E = 10^{14}$ eV . At these energies the cosmic ray flux is high enough to use compact devices connected to balloons or satellites launched in the higher part of the atmosphere, allowing a direct detection of the primaries. At energies $E > 10^{15}$ eV the study is necessarily performed detecting the shower of secondary particles that originates from the interactions of the primaries with the atmosphere: this is named *indirect* detection technique.
The indirect detection technique spans an energy range from 10^{12} eV to the highest detectable energies. Several detection techniques allow to complementary measure both the longitudinal development of the shower traversing the atmosphere and the lateral distribution and composition of the footprint, that is produced by the shower front on ground. While fluorescence telescopes can see the longitudinal shower evolution, water Cherenkov detectors and muon counters arranged in coincidence in a large arrays can see the lateral footprint. A relatively new technique allows also the detection of EAS by their radio emission. A scheme of the different and complementary techniques employed in cosmic ray detection is sketched in Figure 1.8.

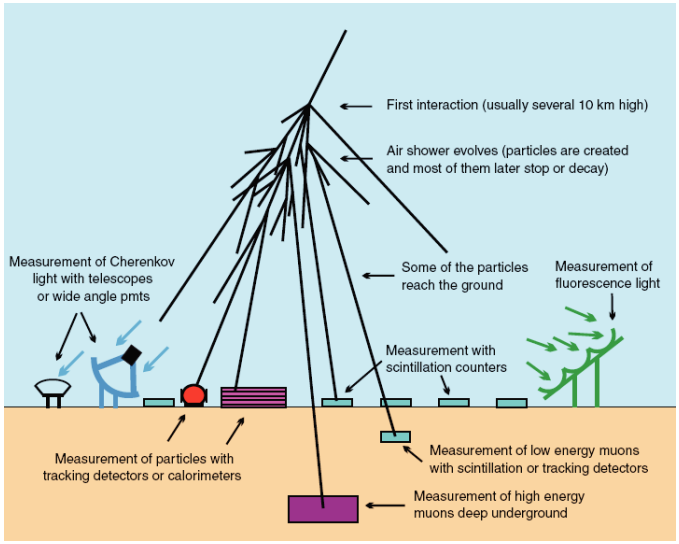

Figure 1.8: Sketch of the current detection techniques employed for EAS measurements.

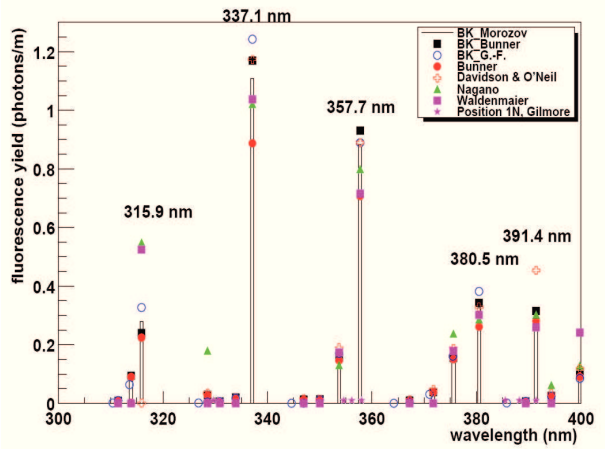

Figure 1.9: Fluorescence yield spectra, measured and calculated for 0.85 MeV electrons as exciting particles (taken from [87]).

1.5.1 Air Fluorescence Detection

Most of the particles' energy is lost via ionization and excitation of the atmospheric molecules by the electromagnetic cascade. Using the atmosphere as calorimeter one can obtain the longitudinal profile of an EAS, visible in UV-fluorescence light of excited molecules. The requirement to detect an EAS by its fluorescence light is the capability to detect a very weak signal of a few photons on a noisy night sky background within a few microseconds. Thus, this detection technique is limited to operate only during clear nights. Furthermore, the pure fluorescence signal from the EAS is contaminated by direct and scattered Cherenkov light. In the following the fluorescence light emission, the Cherenkov contribution and the light propagation through the atmosphere are described.

Fluorescence Light Emission

The electrons of the electromagnetic cascade loose their energy via continuous ionization and excitation of the air molecules, while the excited molecules itself dissipate the energy gain via non-radiative collisions or internal quenching. The fluorescence emission spectrum of the exited nitrogen molecules is shown in Fig 1.9 and covers the UV range between 300 nm up to 400 nm. The emission is isotropic and proportional to the number of charged particles in the shower. Also Argon and Oxygen can be exited but in the following we focus on the effect of electron excitation of the N_2 molecules, as this is the dominant process in air-showers.
The main fluorescence light is emitted by the second-positive (2P) band system of N_2 and the first-negative (1N) system of N_2^+. In air, the optical emission of the prompt radiative return from the upper states of the 2P and 1N system of nitrogen will be affected by some competing processes. The most important process is the *collisional quenching*: an excited nitrogen electronic-vibrational state can also become de-activated by non-radiation processes such as rotational, vibrational or translational energy transfer during collisions with other molecules [88]. These quenching processes strongly depend on the number density (pressure) and the velocity (temperature) of the colliding molecules.
The fluorescence yield Y_λ defines the number of fluorescence photons emitted per unit length and number of charged particles and can be described by [89]:

$$Y_\lambda = \varepsilon_\lambda(p,T)\frac{\lambda}{hc}\frac{dE}{dX}\rho_{air} \quad [\text{photons/m}]$$

where ρ_{air} is the atmospheric density, dE/dX is the energy deposit and $\varepsilon_\lambda(p,T)$ is the fluorescence efficiency defined as the ratio between the energy deposit into radiation and the total energy deposit, function of the air pressure and temperature.
The fluorescence yield is altitude- and humidity-dependent. From ground level to altitudes around 10 km, Y_λ increases slowly. Above 10 km, the yield decreases disclosing the sensitivity to temperature and pressure variations. Additionally to the altitude dependence, there is also a seasonal dependence: e.g. during winter the lower temperatures induce a higher yield below 9 km, while up to 17 km, the temperatures are comparatively high leading to a reduced fluorescence yield. The humidity dependence is due to the fact that in actual atmospheric conditions there is sometimes a considerable fraction of water vapor inducing quenching effects. Two experiments have recently begun to investigate the effect of water vapor.
The measurement of the fluorescence yield is not straightforward and its knowledge is currently uncertain. Experiments to provide it are however ongoing, as well as theoretical calculations to be compared to data. In Figure 1.9 a comparison of the Y_λ values at sea level in the US Standard Atmosphere is shown for calculations as well as for direct measurements [90–92]. In the former case the yield is calculated choosing 0.85 MeV electrons as exciting particles, so that the ionization energy deposit is $dE/dX = 1.677$ MeV/[g cm^{-2}]. Typical values for the yield, after summing over all wavelengths (300-400 nm), are 3.001 ph/m, 3.490 ph/m, 3.698 ph/m respectively for the measurements of Bunner [90], Davidson and O'Neil [91] and Nagano et al. [92], e.g. compared to the calculated value of 3.672 ph/m by Bunner [90].
Further fluorescence yield measurements, however without spectral resolution, can be found in literature. Kakimoto et al. provide a formula to calculate the fluorescence yield between 300 and 400 nm, which gives at sea level 3.275 ph/m [93]. The HiRes Collaboration uses a value of about 5 ph/m per charged particle in an air shower [94]. For these charged particles, an average energy deposit of 2.2 MeV/[g cm^{-2}] is assumed at 5 km a.s.l [90], which leads to a corresponding fluorescence yield at sea level of 3.811 ph/m for a 0.85 MeV electron.

Cherenkov Light Emission

Nearly all charged particles in an EAS carry enough energy to emit Cherenkov light. In a region between the shower axis and 25° off-axis the direct Cherenkov light emission dominates above the fluorescence light emission. The number of Cherenkov photons can be estimated as follows:

$$\frac{dN_\gamma}{dl} \sim 33\, N_e F(1.57\, E_s)\, e^{-\frac{h}{H_0}} \text{ photons/m}$$

where N_e is the number of electrons, F the fraction of electrons with energy above the Cherenkov threshold, H_0 is an atmospheric factor and h the production height. At an angle $\theta > 25°$ away from the shower axis the Cherenkov contamination can be estimated by folding the Cherenkov production rate with the angular distributions of the electrons:

$$\frac{d^2N_\gamma}{dl\,d\Omega} = \frac{dN_\gamma}{dl}\,\frac{e^{-\frac{\theta}{\theta_0}}}{2\pi\sin\theta}$$

where the characteristic angle θ_0 is a function of the Cherenkov threshold energy and scales with the primary energy approximately as $\theta_0 \sim 0.83/\mathrm{E}^{0.67}$.

Light Propagation through the Atmosphere

While propagating through the atmosphere the emitted light undergoes multiple scattering processes and is attenuated. A key role of air fluorescence detectors is to measure each of these

processes in order to precisely derive the light emitted along the shower track starting from that detected at the diaphragm. The involved physical processes are:

- **Rayleigh scattering**: It describes the scattering of light from the molecules of the air and particles up to about a tenth of the wavelength of the light. For the energy regime of Cherenkov and fluorescence light (∼400 nm) the interaction length of UV photons in air at sea level has been measured to be 2.3×10^4 m. The amount of light scattered out of a beam of N_γ photons is [14]:

$$\frac{dN_\gamma}{dl} = -\rho\frac{N_\gamma}{x_R}\left(\frac{400}{\lambda}\right)^4$$

  where ρ is the molecular air density, λ is the wavelength of the scattered light and x_R is the mean free path (e.g. x_r=2874 g cm^{-2} as reported by Bucholtz [95]). Taking into account the angular distribution estimated for the Rayleigh scattering, the total amount of light diffused by this process is:

$$\frac{d^2N_\gamma}{dld\Omega} = \frac{dN_\gamma}{dl}\frac{3}{16\pi}(1+\cos^2\theta)$$

- **Mie scattering**: In contrast to Rayleigh scattering, Mie scattering occurs when the light is scattered out of objects of the order of the wavelength, e.g. while the light propagates through aerosols. The amount of fluorescence light diffused out of a beam of N_γ photons due to Mie scattering is [14]:

$$\frac{dN_\gamma}{dl} = -\frac{N_\gamma}{L_{Mie}}e^{-h/H_{Mie}}$$

  where L_{Mie} and H_{Mie} are the aerosol horizontal attenuation length and scale height. These parameters have to be adjusted to the night conditions. The angular distribution is strongly peaked in the forward direction, but not as much as for the Cherenkov light. Approximately, for angles between 5° and 60° the amount of light diffused is given by:

$$\frac{d^2N_\gamma}{dld\Omega} \approx \frac{dN_\gamma}{dl}\,0.80\,e^{\theta/\theta_M}$$

  where θ_M ∼26.7°.

The light intensity I_λ at a detector observing an angular interval of $\Delta\Omega$ can be estimated by using the transmission coefficients of both processes, $\mathcal{T}_\lambda^{Rayleigh}$ and $\mathcal{T}_\lambda^{Mie}$, to correct for attenuation:

$$I_\lambda = I_{\lambda_0}\mathcal{T}_\lambda^{Rayleigh}\mathcal{T}_{lambda}^{Mie}(1+f)\frac{\Delta\Omega}{4\pi}$$

where f refers to higher order corrections, due to multiple scatterings.
Cherenkov photons undergo also multiple scattering and it is common to distinguish between the direct and indirect Cherenkov contribution. The indirect Cherenkov light is emitted at higher altitudes and can significantly dominate over the fluorescence light that is emitted deeper in atmosphere, where the electromagnetic component starts attenuating.

1.5.2 Surface detection

Surface detectors sample the extensive air shower at ground by means of an array of particle detectors. The shower is essentially a disc of particles moving at speed of light. When it strikes the ground, the particles are spread away from the shower axis (defined by the direction of the primary) due to the combined effect of multiple Coulomb scattering and traverse momentum in shower interactions. The particle distribution is symmetric around the axis and its density falls with the distance to the core. Although the density distribution is characterized by the Molière radius, about 100 meters at ground level, in the higher energy events it is possible to detect particles some kilometers away from the core. Surface detectors measure essentially the lateral distribution of the density of particles in the shower. The energy of the primary is determined in surface detectors (in an indirect manner) from the measured lateral distribution. Essentially, a Monte Carlo program is used to simulate high energy showers in the atmosphere, predicting the relation between energy and particle density. At the ground, one of the main indicators of the primary mass is the shower muon content. Its also possible to study the primary mass using the timing of the shower front: since muons suffer less scattering they tend to arrive earlier than the electromagnetic component [96] . Surface detectors use generally scintillators or water Cherenkov tanks as their detector stations.

1.5.3 Muon counters

Additionally, some UHECR experiments use muon counters, like the KASCADE experiment and now the Pierre Auger Observatory. This allows to quantify the number of electrons and muons separately for most showers, representing a useful information for the composition determination (see Chapter 4).

1.5.4 Radio detection

A very young experimental technique to detect air shower properties is radio detection of EAS. The radio emission was originally predicted by Askaryan [97] in 1962 and experimentally discovered by Jelley [98] in 1965 for dense transparent media like ice. The idea for coherent radio emission of air showers is the following: the electrons and positrons of the electromagnetic cascade are deflected by the Earth's magnetic field and emit synchrotron radiation, often referred to as geosynchrotron radiation [99]. The radio signal can be detected by an array of dipole antennas and the air shower can be reconstructed. The frequency belt is between a few up to 100 MHz and can be measured by standard RF techniques. The advantage of this technique is that the radio antennas can operate with 100% duty cycle, similar to the water Cherenkov detectors.

1.6 Results from the Pierre Auger Observatory

Two complementary techniques are used at the Pierre Auger Observatory to study extensive air showers initiated by ultra-high energy cosmic rays (UHECR): a surface detector array (SD) and a fluorescence detector (FD).
The Observatory started collecting data in January 2004 and the construction operations (both SD and FD detectors) ended in March 2008. The exposure is now 20905 km^2 sr yr. Significative results have been obtained and released, concerning the UHECR energy spectrum, mass composition and arrival direction.

1.6.1 Energy spectrum and GZK cut-off

In Fig. 1.10 the SD and hybrid spectrum reported at the ICRC 2011 [100] are shown together with the event numbers in each energy bin. Only the statistical errors are indicated. Fig. 1.10(a) shows the energy spectrum based on the surface detector data using the period between 1 January 2004 and 31 December 2010. The event selection requires energies above 3 EeV (energy range in which the array is fully efficient) and a reconstructed zenith angle smaller than 60°. (The Horizontal Air Shower (HAS) spectrum, obtained with data having zenith angles between 60° and 80°, is reported in [101]).

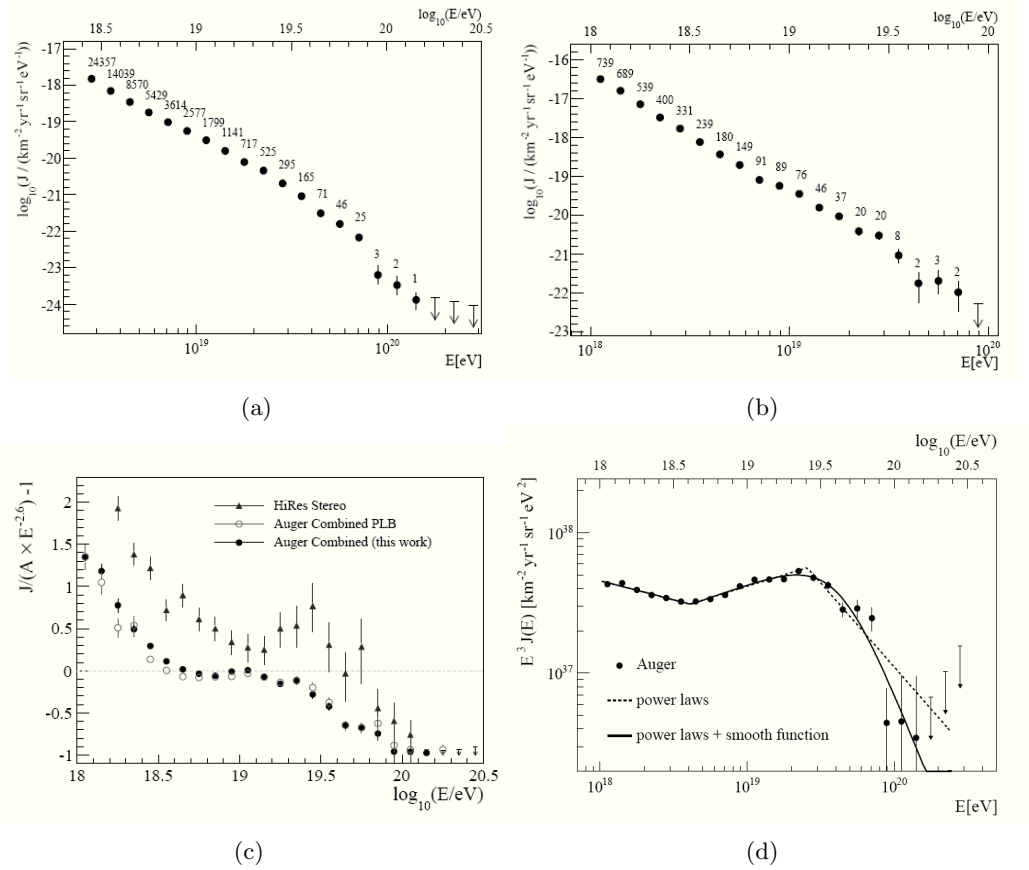

(a) (b)

(c) (d)

Figure 1.10: 1.10(a), 1.10(b): The energy spectrum measured by the Pierre Auger Observatory using surface detector and hybrid data respectively; 1.10(c): Fractional difference between the combined energy spectrum of the Pierre Auger Observatory and a spectrum with an index of 2.6. Data from HiRes stereo measurements [102] are shown for comparison; 1.10(d): the spectrum is multiplied by a factor E^3. (taken from [100])

The total number of events above 3×10^{18} eV fulfilling the selection criteria is about 64000. The number of events with energy greater than 10^{19} eV is about 5000. The calibration of the energy estimator of the surface detector is based on events measured in coincidence with the fluorescence detector. The procedure is affected by a systematic error of 22% due to the uncertainty on the fluorescence energy assignment. The total systematic uncertainty of the flux for the derived spectrum is 6% and is obtained by summing in quadrature the exposure uncertainty (3%) and that due to the forward-folding assumptions (5%).
The energy spectrum for hybrid events, from data taken between 1 November 2005 and 30

September 2010, is shown in Fig. 1.10(b). To ensure good energy reconstruction only showers with geometries that would allow the observation of all primaries in the range from proton to iron are retained in the data sample. The main systematic uncertainty is due to the energy assignment which relies on the knowledge of the fluorescence yield, choice of models and mass composition, absolute detector calibration and shower reconstruction. The total uncertainty is estimated to be about 22%.
Combining the two measurements above, the complete energy spectrum is obtained. The combination procedure uses a maximum likelihood method which takes into account the systematic and statistical uncertainties of the two spectra. The fractional difference of the combined energy spectrum with respect to an assumed flux $\propto E^{-2.6}$ is shown in Fig. 1.10(c) with the measurements in stereo mode from the HiRes experiment [102] for a comparison. A modest systematic energy shift applied to one or both experiments could account for most of the difference between the two. In Fig. 1.10(d) the spectrum is multiplied by a factor E^3. Two spectral features are evident: an abrupt change in the spectral index near 4 EeV (the ankle) and a more gradual suppression of the flux beyond about 30 EeV. The position of the ankle at $\log_{10}(E_{ankle}/\mathrm{eV}) = 18.61 \pm 0.01$ has been determined by fitting the flux with a broken power law $E^{-\gamma}$. An index of $\gamma = 3.26 \pm 0.04$ is found below the ankle, while above the ankle $\gamma = 2.55 \pm 0.04$. Moreover the spectrum is suppressed by a factor two at $\log_{10}(E_{1/2}/\mathrm{eV}) = 19.61 \pm 0.03$ with a significance larger than 20 [103]. The suppression is similar to what is expected from the GZK effect for protons or nuclei as heavy as iron, but could in part also be related to a change of the shape of the average injection spectrum at the sources.

1.6.2 Mass composition

Elongation Rate

The depth of maximum and its fluctuations as function of the primary energy have been measured using hybrid events, in which at least the information of a tank is available. Results from data taken between December 2004 and September 2010 are shown in Fig. 1.11(a) and 1.11(b), compared to predictions from air shower simulations. A broken line fit describes the elongation rate and yields a break-energy of $10^{18.38}$ eV. The small elongation rate at high energies could be interpreted as a change in composition of cosmic rays, from lighter primaries to heavy [104].

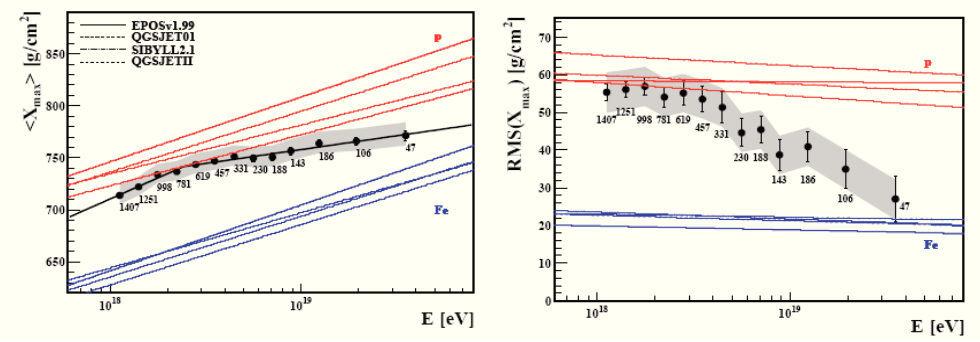

(a) (b)

Figure 1.11: The mean X_{max} (a) and its RMS (b) as a function of the primary energy from hybrid data recorded by the Pierre Auger Observatory. The number of events in each bin is indicated. The results are compared to the predictions given by the current hadronic models (QGSJET01, QGSJETII, SIBYLL, EPOS), shown with dashed lines (taken from [104]).

Photon limit

A large fraction ($\sim$ 50%) of photons in the cosmic-ray spectrum at the highest energies is predicted within several "top-down" models to explain the origin of cosmic rays. The Pierre Auger Observatory has reported a suppression of the cosmic ray energy spectrum beyond $10^{19.6}$ eV [100] which is consistent with the predicted GZK cut-off for protons but could also be due to the photon disintegration of heavy nuclei or due to a limit in the maximum particle energy reached at the sources. The observation of a photon flux compatible with this theoretical prediction could provide an independent proof of the GZK process. The Auger Collaboration recently reported a limit to the photon fraction of the cosmic radiation, independently measured with hybrid data [105] and with ground array only data [106].
The direct measurement of X_{max} contained in the hybrid data has been used to discriminate between photonic and nucleonic UHE primaries, since photon induced showers are expected to develop deeper in the atmosphere compared to hadrons. Taking into account the systematic uncertainties related to the X_{max} determination and the photon shower simulations employed, the Auger hybrid analysis provide an upper photon fraction limit of 0.4%, 0.5%, 1.0%, 2.6% and 8.9% above 1, 2, 3, 5 and 10 EeV [107]. They are shown in Fig. 1.12 compared to previous experimental results. The bounds corroborate previous results disfavoring exotic models also in the lowest energy region.

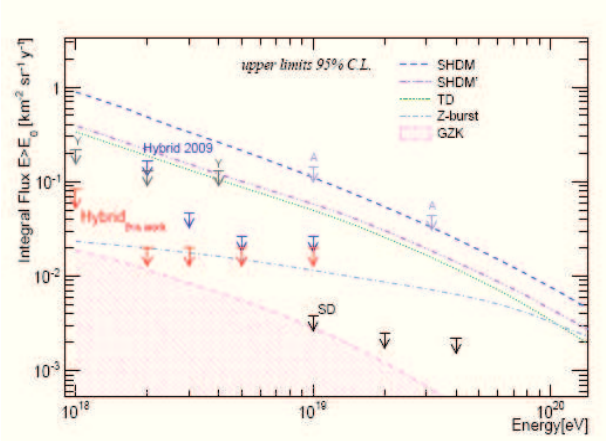

Figure 1.12: Upper limits on the photon flux above 1, 2, 3, 5 and 10 EeV derived from [107] (red arrows) compared to previous limits from Auger (SD [106] and Hybrid 2009 [105]),from AGASA (A) [108] and Yakutsk (Y) [109]. The shaded region and the lines give the predictions for the GZK photon flux [110] and for top-down models (TD, Z-Burst, SHDM from [110] and SHDM' from [111]). The Hybrid 2009 limits on the photon fractions are converted to flux limits using the integrated Auger spectrum [100])

Neutrino limit

With the surface detector of the Pierre Auger Observatory it is possible detect and identify UHE neutrinos in the 0.1 EeV range and above [112]. Two different neutrino detection channels can be used: the '*Earthskimming*' [113] tau neutrinos are expected to be observed through the detection of showers induced by the decay products of an emerging τ lepton, after the propagation and interaction of a ν_τ inside the Earth; the '*Down-going*' [112] neutrinos of all flavours can interact in the atmosphere and induce a shower close to the ground. The point for the indentification is to exploit the feature that neutrinos can penetrate large amounts of matter and generate a *young* shower close to the observation level, exhibiting shower fronts extended in time. In

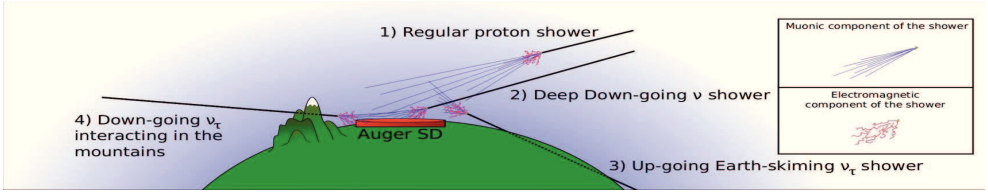

(a)

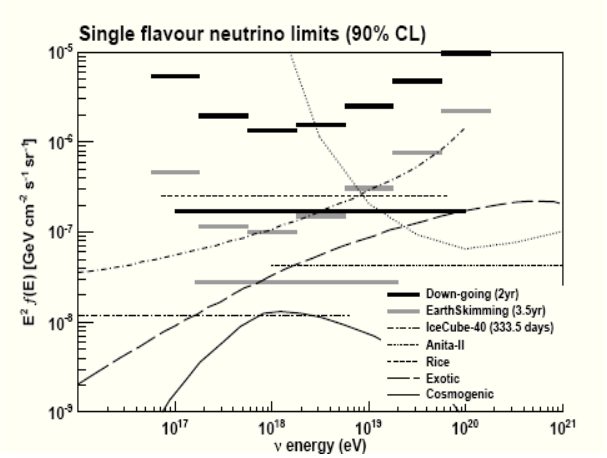

(b)

Figure 1.13: 1.13(a): Sketch of different inclined showers which can be detected by the Pierre Auger Observatory. (1) An inclined shower induced by a proton interacting high in the atmosphere whose electromagnetic component is absorbed and only the muons reach the detector. Inclined showers presenting significant electromagnetic component at the detector level: (2) a deep down-going ν shower; (3) an Earth-skimming ν_τ shower; (4) and a ν_τ interacting in the mountains; 1.13(b): Differential and integrated upper limits (90% C.L.) from the Pierre Auger Observatory [114] for a diffuse flux of down-going ν (2 yr of full Auger) and Earth-skimming ν_τ (3.5 yr of full Auger). Limits from other experiments are also plotted (IceCube [115], ANITA [116], RISE [117]). Expected fluxes are shown for cosmogenic neutrinos [118] and for a theoretical exotic model [119].

contrast, UHE particles such as protons or heavier nuclei interact within a few tens of $\mathrm{g\,cm^{-2}}$ after entering the atmosphere, producing *old* showers with shower fronts narrower in time. In Fig. 1.13(a) we show a sketch of these two kinds of showers together with an Earth-skimming shower and a ν_τ interacting in the Andes, which can also be identified.
Both types of neutrino interactions can be identified through the broad time structure of the signals induced in the Auger Surface Detector stations. Two independent sets of identification criteria were designed to search for Earth skimming and down going neutrinos in the data collected from 1 Jan 2004 to 31 May 2010, and from 1 Nov 2007 to 31 May 2010, respectively [114]. The obtained neutrino limit is shown in Fig. 1.13(b) compared with other limits: this result represents at present the most sensitive bound on neutrinos at EeV energies, where the fluxes of GZK neutrinos are predicted. Over 20 years of Auger operation the limit should improve by over an order of magnitude if no neutrino candidate is found.

1.6.3 Observation of Anisotropy

The search for anisotropies in the arrival directions of UHECRs has been a goal since their discovery. Since at GZK energies they are not expected to be confined by magnetic fields in the disk of our galaxy, it is likely that they originate outside the Galaxy. Furthermore, the

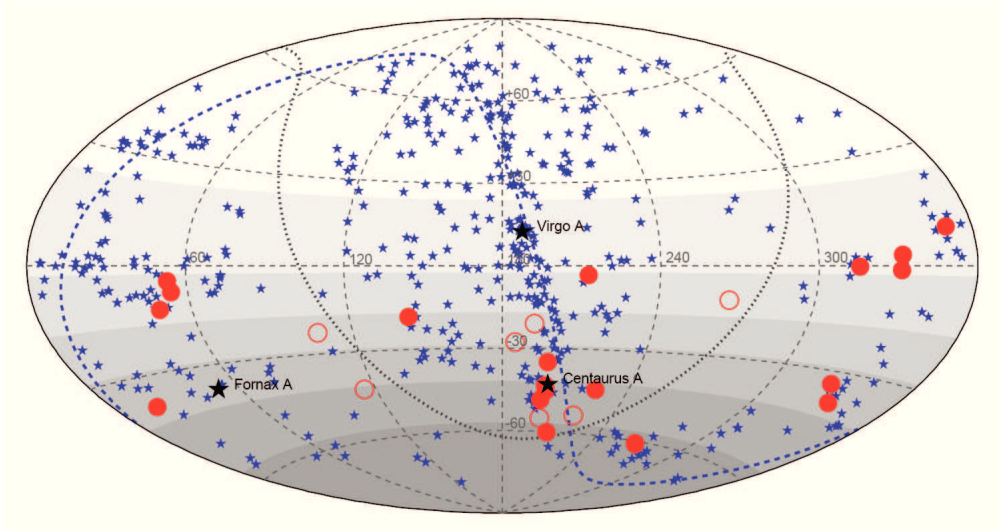

Figure 1.14: Arrival direction of 27 events recorded at the Pierre Auger Observatory with energies above 57 EeV (circles) and the position of close-by AGN objects (stars) with redshift z≤0.018 (D<75 Mpc) as classified in the 12th edition of the catalog of quasars and active nuclei. The plot is given in Earth-bound equatorial coordinates, while the projection of the galactic plane is represented by the dotted line and that of the supergalactic plane by the dashed line. The shaded areas denote the integrated exposure of the Auger detector. The full circles denote the events, which are located within an angular distance of 3.1° from the next AGN. Events not correlating are shown as open circles. All the open circles are located not far from the galactic plane, where the used AGN catalog is known to be incomplete and the expected cosmic ray deflections are the largest. The three strongest AGNs (Centaurus A, Fornax A, Virgo A) are marked as black stars.

existence of the GZK cutoff imposes that they must have been produced relatively nearby. Since light particles with energies above EeV range are expected to not be largely deflected from their original path, they should point back to the source. The AGASA Collaboration claimed an excess of clustering at small angular scale respect with the isotropic expectation [49], later contradicted by the HiRes data [120]. Analysis of data recorded by several cosmic ray experiments revealed a general correlation with the supergalactic plane [121], but with limited statistical significance. Recently, the Pierre Auger Collaboration reported the observation of of a correlation between the arrival directions of cosmic rays with the highest energies measured by the Pierre Auger South Observatory and the positions of nearby AGN [53, 122]. The most recent analysis dealing with astrophysical source search are detailed in [123]. The departure of the arrival direction distribution from an isotropic one has maximum significance for cosmic rays with energy above 6×10^{19} eV, in correlation with AGN lying within ∼75 Mpc. The Pierre Auger Collaboration analysis confirmed the anisotropy hypothesis and the correlation with a confidence level of more than 99%.

The used parameter values are those corresponding to the minimum of the probability P for a set of N events from an isotropic flux to contain k or more events at a maximum angular distance ψ from any member of the collection of candidate point sources, as obtained from an exploratory scan done with data collected from 1 January 2004 through 27 May 2006. The parameters used in the exploratory scan are the lower energy threshold E_{th} for the cosmic ray events, the maximum source redshift z_{max} and the maximum angular separation ψ. The minimum of P is obtained with $E \geq E_{th} = 56$ EeV, $z_{max}=0.018$ ($\leq$75 Mpc) and $\psi \leq 3.1°$. Applying the analysis to the full data set, the Auger Collaboration found that 20 out of 27 cosmic rays events correlate

with at least one of the 442 selected AGN, while only 5.6 were expected for an isotropic flux. The sky map in Fig. 1.14 shows the arrival directions of the 27 events detected from 27 May 2006 to 31 August 2007 with energies above 57 EeV (circles of radius 3.1°). The 442 AGN (within 75 Mpc and with redshift lower than 0.018) from the Véron-Cetty and Véron [124] catalog are marked as asterisks. It is clear that with the present statistic is not possible to unequivocally identify the sources, but the Auger Observatory will gather a larger statistic in a few years.

Chapter 2

Muons in EAS

The interest in muon results has changed during along 50 years. In the beginnings muons were used to study geomagnetic effects. Muon measurements and the muon charge ratio were then interpreted in terms of the primary cosmic ray spectrum and composition. Even though the geomagnetic field is now very well known, the interest in the primary cosmic ray spectrum still continues and it is expected that muons may play an important role in understanding both the primary energy and composition. Muons may act as well as the best messengers of the hadronic shower development while helping to constrain the high energy hadronic models used in the Monte Carlo simulations of EAS.

2.1 Muon flux in atmosphere

Most shower muons are the decay product of mesons (pions and kaons). The production spectrum is the sum of all contributions of particle of type i that decay in particle of type j at energy E and depth X

$$P_j(E,X) = \sum_i \int_{E_{min}}^{E_{max}} \frac{dg_{ij}(E,E')}{dE} D_i(E',X)dE' \tag{2.1}$$

where the first term is the spectrum of secondary particles and D_i is the spectrum of decaying mesons of energy E'. Gaisser [79] assumes a proton spectrum of $1.8\mathrm{E}^{-2.7}$ $\mathrm{cm}^{-2}\mathrm{s}^{-1}\mathrm{sr}^{-1}\mathrm{GeV}^{-1}$ and, accounting for the two-body decay of pions and kaons, finds the muon spectrum

$$\frac{dN_\mu}{dE_\mu} \simeq 0.14 E_\mu^{-2.7} \left[\frac{1}{1 + \frac{1.1 E_\mu \cos\vartheta}{115 GeV}} + \frac{0.054}{1 + \frac{1.1 E_\mu \cos\vartheta}{850 GeV}} \right] \tag{2.2}$$

where the first fractional term is the contribution from pions and the second one is the contribution from kaons. This equation does not account for the muon energy loss, being valid only at high energy where this contribution is small.
We note that pions decay more easily in nonvertical showers so muons have a flatter energy spectrum at larger angles. In Fig. 2.1 the comparison between two data set of muons is shown: one by *Allkofer* [125], for vertical muons, and the other by *Jokisch* [126], for muons with an angle of 75°. Gaisser's formula fits well the data for high energy, while at low energy overshoots the two measured fluxes. This is due to the fact that the treatment of Gaisser does not account for the energy lost by muons, that is relevant at low energy.
Moreover the comparison between the two data sets shows how the spectrum changes at different angles. Due to the loss of energy, at low energy the flux for the data set at 75° is lower , while

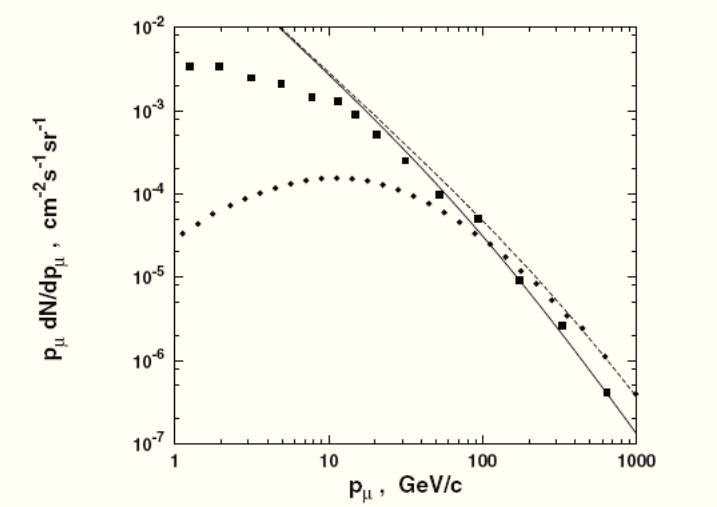

Figure 2.1: The muon flux of Eq. (2.2) (solid line for vertical, dashed line for 75° muons) is compared to the vertical muon flux measured by *Allkofer et al.* (squares) and the 75° muon flux measured by *Jokish* et al. (diamonds).

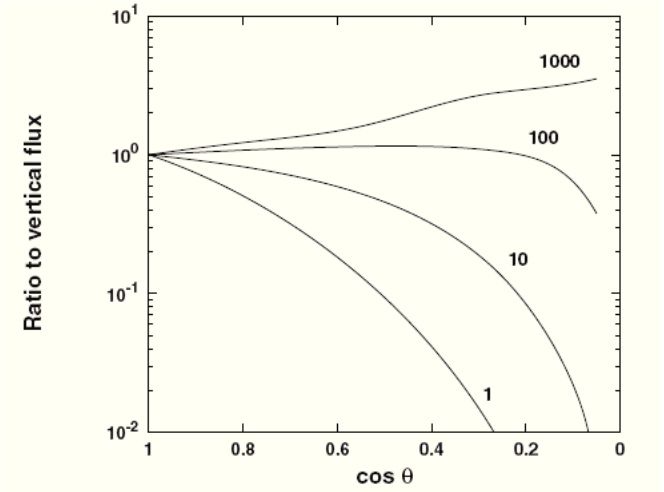

Figure 2.2: The ratio of the inclined to the vertical muon flux as a function of $\cos\theta$. Each curve is labeled according to muon momentum, given in GeV/c.

at high energy becomes flatter than the vertical one. Fig. 2.2 gives a quantitative impression of this effect by a Monte Carlo simulation [127]: at $E = 1$ GeV/c the flux decreases drastically at 60°, while at $E = 100$ GeV/c it is almost flat up to $\cos\theta$ =0.2. Instead at $E = 1000$ GeV/c the flux increases with the zenith angle.
Fig. 2.3(a) shows collections of muon data taken at ground level by different experiments [128] compared to calculation; Fig. 2.3(b) emphasizes the muon fluxes at high energy. From 100 GeV/c to 1000 GeV/c the data show a flux slightly flatter than prediction. To explain this effect we observe that the calculations are one-dimensional, so we assume that all secondary particles move in the direction of the primary cosmic ray particle. This is true at high energy where all secondaries are emitted in a narrow forward cone in the lab. system.

Another important result is the ratio between charged muons $R = F_{\mu^+}/F_{\mu^-}$. The dominance of protons in the primary cosmic ray flux makes R greater than unity and its value can be

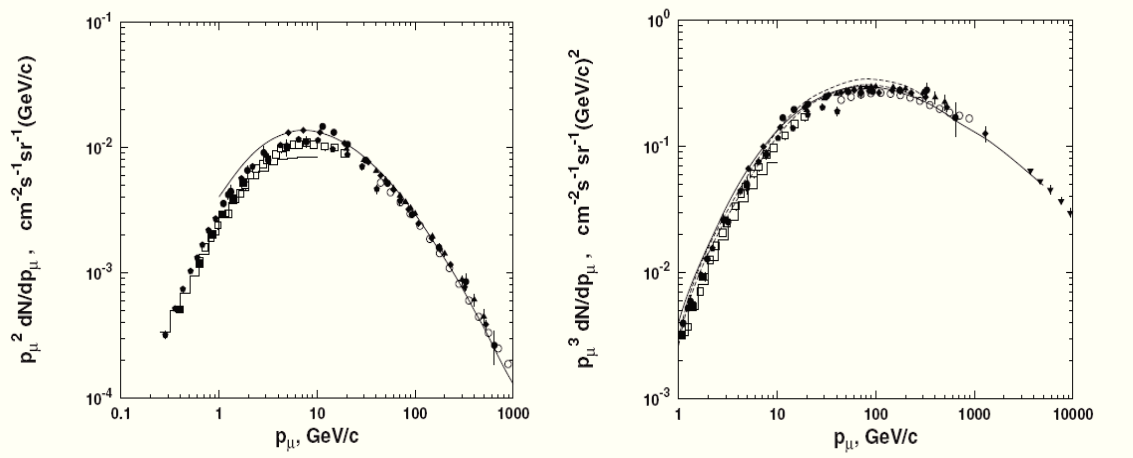

(a) (b)

Figure 2.3: 2.3(a): Muon differential energy spectra measured at sea level by different experiments. Data are weighted by p_μ^2. The data are from *Allkofer et al.* [125], *Ayre et al.* [129], *Ivanenko et al.* [130], *Rastin* [131], *DiPascale et al.* [132], *Boezio et al.* [133], *Motoki et al.* [134], *Achard et al.* [135]; 2.3(b): the same spectra weighted by p_μ^3.

interpreted in terms of the average p/n ratio in the cosmic ray flux.
Fig. 2.4 shows the data of BESS [136], L3C [135] and MINOS [137]. In the GeV range the charge ratio gradually increases, while in the energy range from 10 to 100 GeV it becomes approximately constant at ≈1.27; at energies greater than a few hundred GeV several competing processes can affect the charge ratio. Thus, the fraction of muons seen from kaon decays increases because the longer-lived pions become more likely to interact before decaying than the shorter-lived kaons. Consequently, kaon decays begin to give an increasingly important contribution to the muon charge ratio at these energies. Since strong interaction production channels lead to a muon charge ratio from kaon decays that is greater than that from pion decays, the measured charge ratio increases to 1.4 at TeV energy [137].

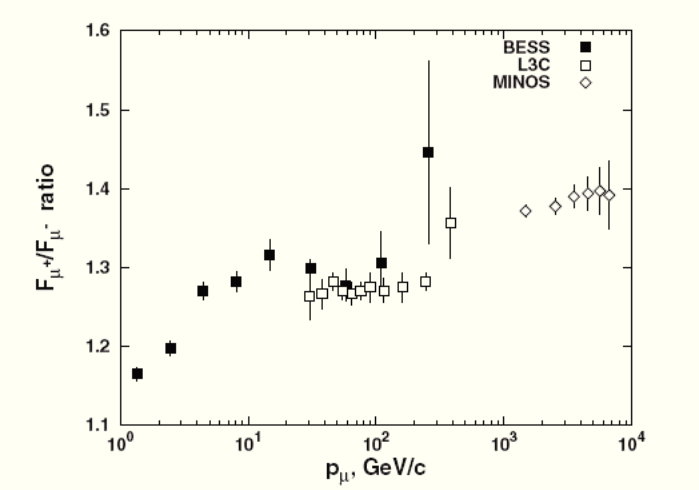

Figure 2.4: Muon charge ratio as a function of the muon momentum, according to values reported by several experiments.

2.2 Underground cosmic rays

Primary cosmic rays almost never reach sea level. Secondary particles do. But only very high energy muons (E_μ >500 GeV) can penetrate deep underground, while other particles as hadrons, electrons and γ-rays interact immediately with rock and are absorbed. So high energy muons can be detected by underground detectors. They can measure the muon flux for a very long time and provide reliable information on the primary cosmic ray spectrum. To interpret these measurements we need a good description of the muon production spectrum and also we have to know very well the muon energy loss at high energy and the thickness and composition of the rock above the detector.

2.2.1 Interaction processes

For muons in the GeV energy range the only essential energy loss process is ionization, while for the muons underground other processes become important:

- *Bremsstrahlung* : this is the electromagnetic radiation produced by the acceleration of a charged particle when deflected by another charged particle, such as an atomic nucleus. The bremsstrahlung cross section for muons is

$$\frac{d\sigma_{Br}}{du} = \alpha(2Zr_e\frac{m_e}{m_\mu})^2\frac{1}{u}\left[\frac{4}{3}(1-u)+u^2\right]\xi(\delta) \tag{2.3}$$

  where u is the fraction of energy transferred to the photon and the screening function $\xi(\delta)$ depends on the minimum momentum tranfer to the nucleus $\delta = m_\mu^2 u/[2E(1-u)]$. The screening function has been parametrized with the form

$$\xi(\delta) = \ln\left[f_n\frac{m_\mu}{m_e}\frac{189Z^{-1/3}}{1+(\delta/m_e)\sqrt{e}189Z^{-1/3}}\right] \tag{2.4}$$

  where f_n is the nuclear form factor [138].

- *Pair Production* : in this process the muon emits a virtual photon that produces an electron-positron pair. Because of the two electromagnetic vertices the cross section is proportional to α^2 and not to α as for the bremsstrahlung. In general form the cross section can be written as

$$\frac{d\sigma_{pair}}{dv} = \frac{2\alpha^2 r_e^2}{3\pi}Z^2\frac{1-v}{v}\int[F_e(r)+\frac{m_e^2}{m_\mu^2}F_\mu(r)]dr \tag{2.5}$$

  where v is the fractional energy loss of the muon and r is $(E_{e^+}-E_{e^-})/v$. (For the parametrizations of functions F_e and F_μ see ref [139]). The cross section for pair production is higher than the bremsstrahlung one, however the energy losses of the two processes are of the same order.

- *Photoproduction* : in this case the muon emits a virtual photon that, interacting hadronically with matter, generates secondary hadrons. Only higher energy photons are important, so the cross-section for muon energies in the GeV range is very small. The photoproduction cross-section for muons is given by

$$\frac{d\sigma_{ph}(E_\mu)}{dv} = \frac{A\alpha}{2\pi}\sigma_{\gamma N}(vE_\mu)v\times F[E_\mu, v, \sigma(vE_\mu)] \tag{2.6}$$

where v is again the fractional energy loss of the muon and $\sigma_{\gamma N}$ is the interaction cross-section of a real photon with nucleons. (For the parametrization of functions F see ref. [140])

In Fig. 2.5 the relative energy loss is reported for the three processes in standard rock (an artificial material with atomic mass $A = 22$, atomic number $Z = 11$ and density 2.65 g/cm^3).

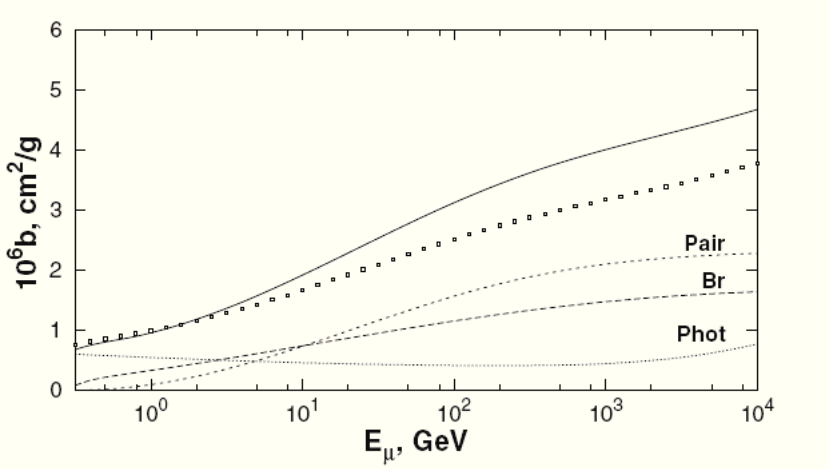

Figure 2.5: Relative energy loss in standard rock. Solid line shows the sum of the three processes. Circles show the energy loss for clean ice with density 0.93 g/cm^3.

2.2.2 Energy loss

Ionization energy loss depends weakly on the muon energy so we can consider it as a constant, with a value of about 2 MeV per g/cm^2. The processes described above, instead, are proportional to the muon energy so the total muon energy loss becomes

$$\frac{dE_\mu}{dx} = -a - bE_\mu \tag{2.7}$$

where b is the sum of the three contributions related to radiation processes

$$b = b_{br} + b_{pair} + b_{ph} \tag{2.8}$$

For standard rock it assumes a value of $4{\times}10^{-6}$.
The energy at which the energy loss by radiation is equal to the one by ionization is the critical energy $\epsilon = a/b \simeq$500 GeV. When $E_\mu \gg \epsilon$ radiation processes dominate, while when $E_\mu \ll \epsilon$ ionization process dominates, as showed in Fig. 2.6.

Now we can calculate the average energy E_μ of a muon with initial energy E_μ^0 after propagating through a material of thickness X expressed in (g/cm^2):

$$E_\mu = (E_\mu^0 + \epsilon) \times \exp(-bX) - \epsilon \tag{2.9}$$

and the reverse quantity

$$E_\mu^0 = (E_\mu + \epsilon) \times \exp(bX) - \epsilon \tag{2.10}$$

So, from 2.10 we can obtain also the minimum energy for a muon to penetrate at depth X

$$E_\mu^{min} = \epsilon[\exp(bX) - 1] \tag{2.11}$$

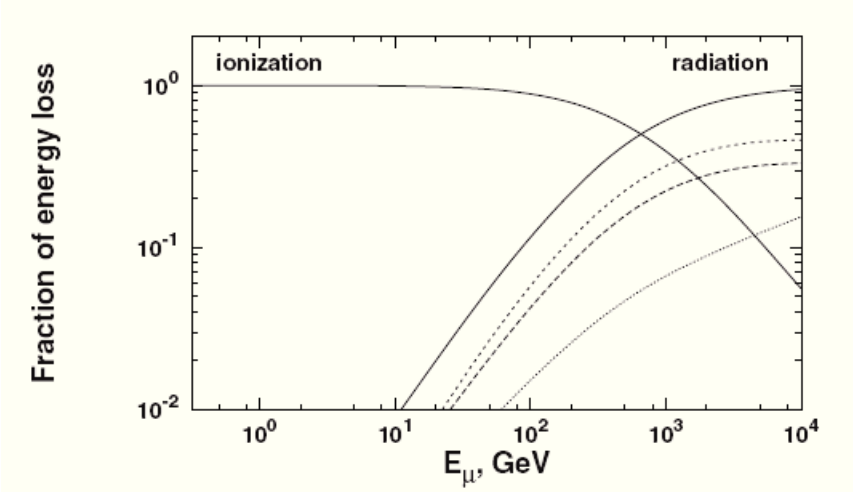

Figure 2.6: Relative importance of different energy loss processes as a function of the muon energy normalized to the total energy loss per g/cm^2.

At small depth ($X \ll 1/b$ g/cm^2) muons lose energy mostly by ionization and $E_\mu^{min} \simeq aX$. The muon spectrum underground reflects the surface spectrum with a flattening under $E_\mu \simeq aX$. Instead at big depths ($X \gg 1/b$ g/cm^2) the spectrum has an almost constant shape up to $E_\mu \simeq \epsilon$ and steepens above this energy.

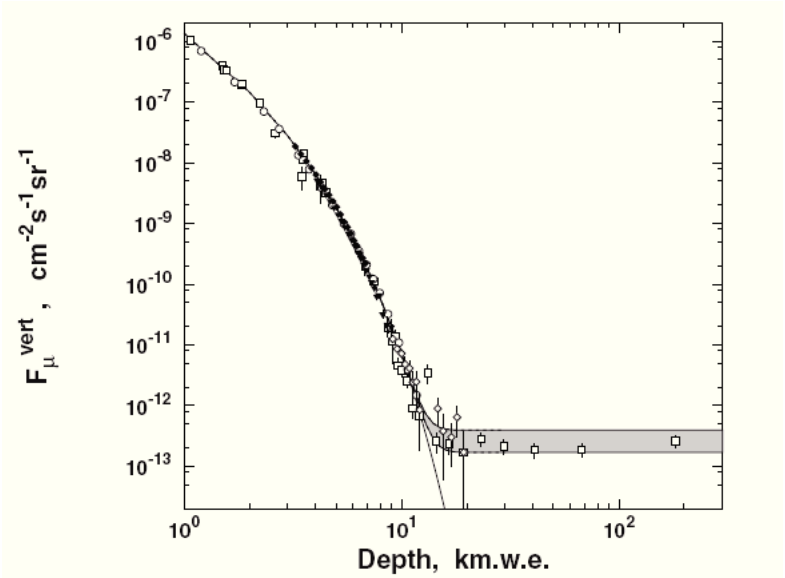

Figure 2.7: The integral muon flux measured at different angles and converted to vertical muon flux is compared to prediction as a function of depth.

In Fig. 2.7 different measures of underground muons are compared. The data are from the compilations of M.Crouch [141], Baksan [142], LVD [143], MACRO [144] and Frejus [145]. To compare data taken at different zenith angles, the fluxes are converted to vertical direction using muon production models, and the various depths are converted to standard rock [128]. Assuming a power law muon energy spectrum at the ground and accepting the definition of the minimum

muon energy to reach a depth X, the relation between the intensity and the depth becomes

$$F_{\mu}^{vert} = \frac{K\epsilon^{-\alpha+1}}{\alpha-1} \times \exp(-(\alpha-1)bX) \times (1-\epsilon^{-bX})^{-\alpha+1} \tag{2.12}$$

where the first term is a constant and reflect the muon energy spectrum at the ground, the second term determines the depth intensity curve, and the third term is always larger than 1, reaching a value $\simeq$1 at large depths. Finally from 2.11 we obtain the range of a muon of energy E_{μ}

$$R(E_{\mu}) = \frac{1}{b} \ln\left(\frac{E_{\mu}}{\epsilon} + 1\right) \tag{2.13}$$

This expression is true if we consider that muons lose energy continuously and in equal amount through the track. But this assumption is valid only for energy up to 100 GeV (when ionization is the main energy loss process), while at higher energy muons occasionally interact and lose a large fraction of their energy. Fluctuations are inherent to the radiative processes and they replace the range $R(E_{\mu})$ with a distribution of ranges. Muons that did not radiate propagate much further than the range $R(E_{\mu})$, but the majority of muons did radiate and cannot reach this depth. So we can compare the average range distribution $\langle R_{\mu}\rangle$ to R to estimate the survival probability in standard rock for muons as shown in Fig. 2.8. The ratio $\langle R_{\mu}\rangle/R$ is energy

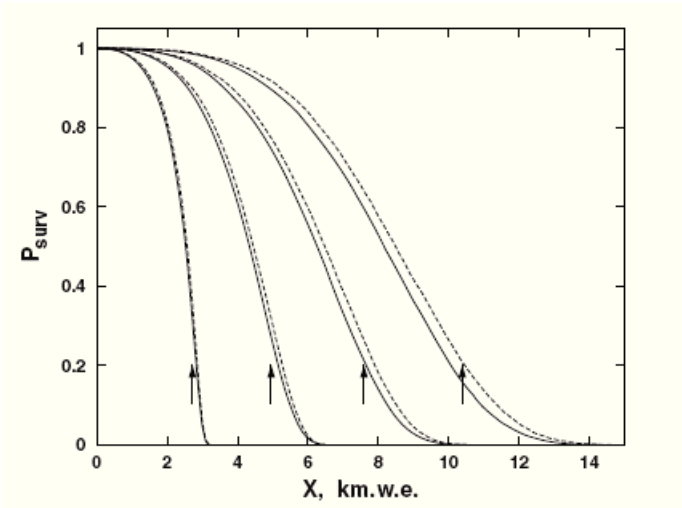

Figure 2.8: Survival probability of muons with energy 1, 3.16, 10 and 31.6 TeV in standard rock. The two curves for each energy indicate the uncertainties in the bremmstrahlung. The arrows show the average depth for muon survival calculated from Eq. 2.11.

dependent. For high $\langle E_{\mu}\rangle$ the radiation processes are dominant and the fluctuations are more important. The range distribution becomes wider and $\langle R_{\mu}\rangle/R$ decreases.

2.3 Muonic component in EAS

Muons in the shower are created from the decay of charged pions, where the probability of decay is a balance between the interaction cross section with atomic nuclei and the decay time of the particle. The lifetime of the pion in the observer frame increases with energy as does the interaction cross section, and muon production becomes prevalent as the pion energy drops. Pion decay also depends on the density of air at the given height, $\rho(h)$, and the probabilities of

decay and interaction become equal when:

$$\gamma\tau c = \frac{\lambda}{\rho(h)} \tag{2.14}$$

where γ, τ and λ are the Lorentz factor, lifetime in the rest frame and mean free path for interaction of the pion respectively.
Matthews [146] had adjusted Heitler's approach to hadronic showers by the introduction of physical parameters. In his approach he considers the relation between the number of muons (N_μ) and the total number of decaying pions (N_π)

$$\ln N_\mu = \ln N_\pi = \beta \ln(E_0/\epsilon_\pi) \tag{2.15}$$

where E_0 is the energy of the primary cosmic ray, ϵ_π is the energy associated with the competition between decay and interaction for the pions and β reflects the fraction of the multiplicity in charged pions. The number of generated muons is

$$N_\mu = (E_0/\epsilon_\pi)^\beta \tag{2.16}$$

To describe realistically the total number of muons, Matthews proposes a value ϵ_π =20 GeV, and β given by

$$\beta = \frac{\ln \frac{2}{3}\langle m\rangle}{\ln\langle m\rangle} = 0.85 \tag{2.17}$$

To extend the theory to heavier nuclei we can apply the *superposition approximation* in which a shower initiated by a nucleus of mass A and energy E_0 corresponds to A showers initiated by nucleons of energy E_0/A. In this approximation the average depth of the shower maximum becomes

$$X^A_{max} = X^p_{max} - X_0 \ln A \tag{2.18}$$

Air showers initiated by He, O, and Fe nuclei of the same total energy will reach maximum 50, 100 and 150 g/cm^2 earlier than proton showers. As a consequence, showers induced by heavy primaries generate more secondary particles, each of smaller energy and leading to an earlier attenuation of the electromagnetic component (after the shower maximum). This reduces the average pion energy in the early stages of the cascade relative to a proton shower of the same energy. As a result, the number of muons is larger and becomes

$$N_\mu = A\left(\frac{E_0/A}{\epsilon_\pi}\right)^\beta = A^{1-\beta}N^p_\mu \tag{2.19}$$

The muon excess over proton showers is 23%, 52% and 83% respectively for He, O and Fe showers.
Gaisser [79] gives the following approximate expression for the total number of muons N_μ with energies above 1 GeV:

$$N_\mu(>1\text{GeV}) \approx 2.8A\left(\frac{E}{A\varepsilon_\pi}\right)^{0.86} \tag{2.20}$$

Measuring the ratio N_e/N_μ, where N_e is the number of the electrons at ground, can thus provide an estimation of the primary composition. The sensitivity to the primary mass of the correlation between shower size N_e and number of muons N_μ is explained by the earlier longitudinal development of showers induced by heavy primaries combined to the weak dependence of the multiplicity

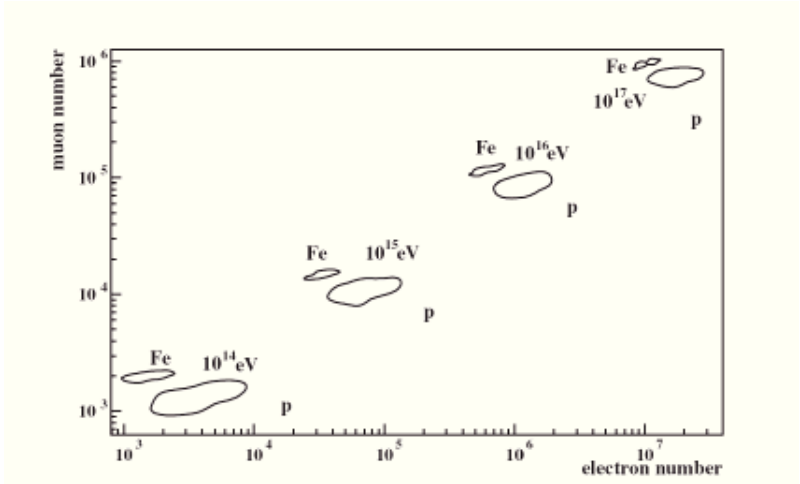

Figure 2.9: The (N_μ,N_e)-correlation from MC simulations shown for proton and iron primaries at various energies. The lines represent the half-width maxima of the distributions.

n of the secondaries on the energy of the interacting nucleon, i.e. $n_A(E) \propto A\ln(E/A)$, leading to more secondary particles for heavy primaries. Due to the shorter interaction length and the smaller energy per nucleon and because of the reduced attenuation of the muon component, the electromagnetic component of a heavy-particle induced shower has progressed more on average at the observation level, and the shower carries more muons than a proton induced shower of the same energy. A quantitative example of such N_e-N_μ correlation is shown in Fig. 2.9 by MC simulations for proton and iron primaries at various energies. As it is evident, iron showers have more muons and less electrons at all energies.
In this treatment we have not taken into account the muon decay and its energy loss. A realistic value of β is a function of the muon energy; for example low energy muons are less likely to decay so β increases by an amount $\delta\beta$ depending on the muon energy. Fig. 2.10 shows the dependence of the number of produced shower muons as a function of the primary energy for a proton shower using Monte Carlo simulations [147]. There is a slight variation of the power law index β with the muon threshold energy. These variations are due to the different hadronic interaction models. The number of produced muons increases with the energy of the primary cosmic ray. This increase however does not scale linearly with the primary energy. Simulations show that in a proton induced shower the factor which reflects the number of produced muons β grows with the primary energy by $E^{0.85}$.
Moreover, depending on the angle at which the primary cosmic ray enters the atmosphere the shower can suffer more or less attenuation. Showers with high zenith angles have to traverse a higher amount of air, thus they are more absorbed. In these cases charged pions find a denser mean and usually decay into low energy muons which are more likely to decay.

2.4 Muons experimental arrays

As it was already mentioned above, the muonic component of the shower can help to discriminate between different primary cosmic ray masses. Throughout this section we will give a brief description of the High-Res - MIA, AGASA and KASCADE-Grande experiments, where a muon array has been used over the past years to provide experimental data on the problem under discussion.

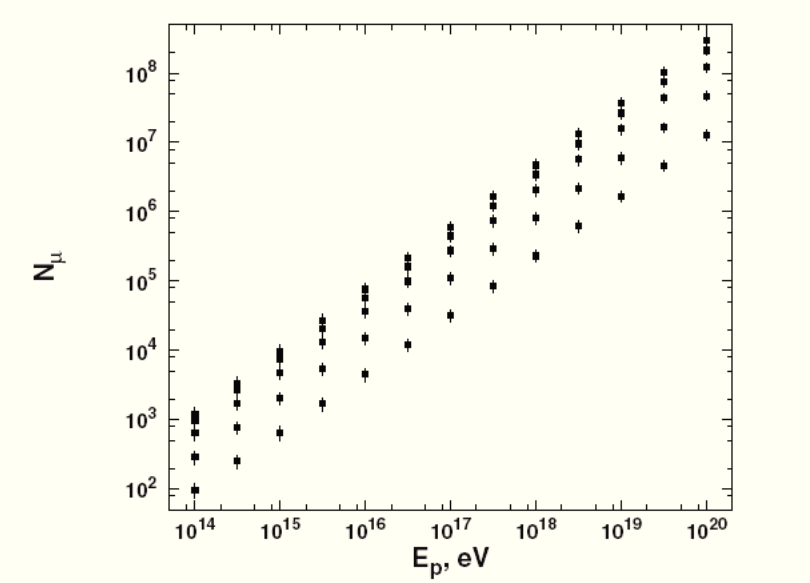

Figure 2.10: Average number of muons at sea level in vertical proton showers as a function of the primary energy and for different values of the muon energy threshold. From top to bottom the thresholds are 0.3, 1, 3, 10 and 30 GeV.

2.4.1 Hight resolution Fly's Eye - MIA

Located on the western desert of Utah, the High Resolution Fly's Eye - MIA (Michigan Muon Array) experiment, combined both fluorescence telescopes and buried muon detectors. The High Resolution Fly's Eye was constituted by 14 optical reflector telescopes. Their field of view was about 3° to 70° in elevation and 64° in azimuth at the top and 32° at the bottom of the field of view. MIA used 16 patches of 64 scintillator muon counters buried at approximately 3 m depth covering an effective area of 2500 m^2 and a total area of 370 m × 370 m. The muon array records both the arrival times and the muon counts within a 4μ s interval for each triggered detector. The muon detectors present an average energy threshold of $E_\mu^{Th} \approx 850$ MeV for vertically incident muons. The muon density was estimated at 600 m from the shower core based on a fit to the triggered counters for each event [148, 149].

2.4.2 Akeno-AGASA

The Akeno experiment measured muons with energies $E \geq 1$ GeV from showers belonging to the energy range of $10^{16.5}$eV $-10^{19.5}$eV. The experiment comprised a set of shower arrays of 1 km^2, 20 km^2 and 100 km^2. The array of 1 km^2 consisted of 156 scintillation counters having an area of 1 m^2 each and 8 muon detectors of 25 m^2 each. The muon detectors were shielded by a 2 m thick concrete layer yielding a muon energy threshold of 1 GeV. The muon lateral distribution function was determined at a range distance of 50 m to 800 m from the shower core. The 20 km^2 array was composed by 19 scintillator counters of 2.2 m^2 each and 4 scintillators of 1 m^2 each placed at 1 km spacings apart from each other. This array also implemented 8 muon detectors of 25 m^2 from the 1 km^2 array. Finally, the 100 km^2 array, also denominated AGASA, was composed by 111 scintillators each one covering an area of 2.2 m^2. Additionally there were also 14 muon detectors whose shielding was either made of concrete or by a mixture of iron and lead, both presenting a muon threshold energy of 0.5 GeV. Twelve muon detectors had an individual area of 2.8 m^2 while the remaining two had an individual area of 10 m^2 . For all the three arrays

the energy of the primary, the core position and the arrival directions were calculated by the scintillators. The muon densities were calculated from the mean of all the events. Fig. 2.11(a) show a view of the Akeno Observatory and a scheme of the 100 km^2 array.

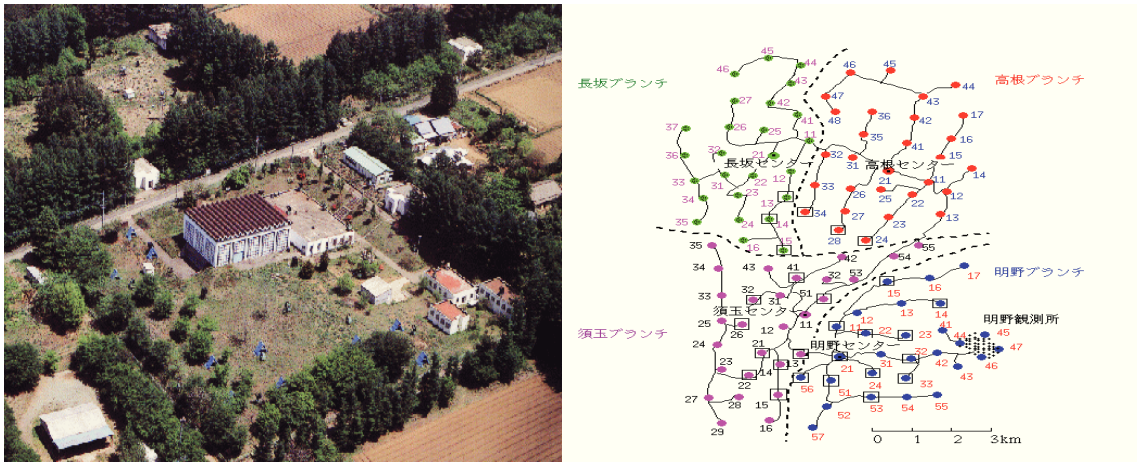

(a) (b)

Figure 2.11: 2.11(a): A view of the Akeno Observatory; 2.11(b): The scintillators array of AGASA.

2.4.3 KASCADE

The KASCADE experiment (KArlsruhe Shower Core and Array DEtector) is placed at the laboratory site of the Forschungszentrum Karlsruhe at 110 m a.s.l. and takes data continuously since 1996. In April 2009 the collaboration officially celebrated the closure of the activities: the array will continue to record data, with limited maintenance.
The KASCADE array studies the energy region between 10^{14}eV and 10^{16}eV and covers an area of 40000 m^2 composed by 252 scintillator counters to measure the electromagnetic component. The experiment measures the muonic component by scintillators and by the Muon Tracking Detector (128 m^2 with E_μ >800 MeV) at four different energy thresholds and the hadronic component by a 300 m^2 iron sampling calorimeter [155]. Fig. 2.12(a) and 2.12(b) show the detector arrangement of the KASCADE array at the Karlsruhe Forschungszentrum with the three main components: detector array, central detector and muon tracking detector on a surface of 200×200 m^2. A scheme of the scintillator station is shown in Fig. 2.12(c).
In 2003 the KASCADE experiment was upgraded with the addition of 37 detector stations, forming the Grande Array. Each of the stations consists of 10 m^2 plastic scintillator which is sensitive both to the electromagnetic component and to muons with energies above 5 MeV. The whole installation covers an area of 0.5 km^2 with spacings of about 130 m allowing air shower measurements up to 10^{18} eV. To provide a fast trigger to KASCADE a compact array of 8 stations with 11 m^2 plastic scintillator each, named Piccolo Array, has been added to the Grande Array over an area of 360 m^2.

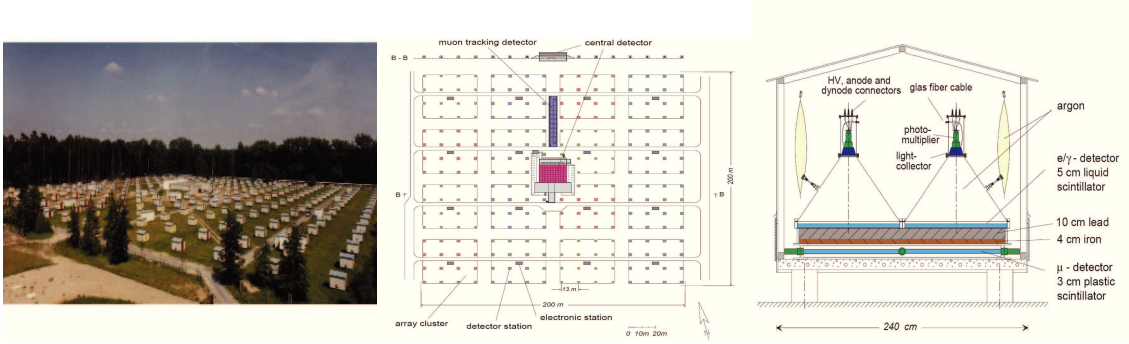

(a) (b) (c)

Figure 2.12: 2.12(a): A view of the KASCADE array at the Karlsruhe Forschungszentrum; 2.12(b): The detector layout of the KASCADE array; 2.12(c): A sketch of a scintillator station of KASCADE.

2.5 Experimental results on muons

2.5.1 Muon LDF

The particle lateral distribution function (LDF) of extensive air showers is the key quantity for cosmic ray ground observations, from which most shower observables are derived. The lateral distributions of electrons and muons in EAS not only contains information on the nature of the primary cosmic ray particle, which is related to astrophysical questions, but it also carries information relevant to particle physics. While the electromagnetic interactions are thought to be well understood, this is not true for the high energy hadronic interactions. A parameter commonly used to describe the form of the lateral density distribution is the lateral form parameter in the Nishimura Kamata Greisen (NKG) function, as it was already mentioned in Chapter 1, that describes the particle density at the ground as a function of its distance to the shower core. For the shower muons Greisen proposed the following function :

$$\rho_\mu(R) = N_\mu \left(\frac{C_\mu}{R_0^2}\right) r^{-\alpha}(1+r)^{-\beta} \tag{2.21}$$

where $\rho_\mu(R)$ is the density of muons measured at a distance R from the shower core, $r = R/R_0$, R_0 is a characteristic distance and C_μ is a normalization factor. The value of α was fixed to be 0.75, while β and R_0 were determined for vertical showers by fitting $\rho_\mu(R)$. The best fitted values are $\beta = 2.52 \pm 0.04$ and $R_0 = 266 \pm 32$ m [150]. Equation 2.21 seems to describe well the muon distribution for small distances from the shower core, within 800 m from the core. However for $R > 800$ m the data show significantly lower values than the extrapolated values of 2.21 . In order to get a better reproduction of the observed data the Akeno group proposes the following muon lateral distribution of muons up to 2000 m

$$\rho_\mu(R) = N_\mu \left(\frac{C'_\mu}{R_0^2}\right) r^{-\alpha}(1+r)^{-\beta} \left\{1 + \left(\frac{R}{800}\right)^3\right\}^{-\delta} \tag{2.22}$$

where $\delta \sim 0.6$. The average ρ_μ obtained from AGASA are plotted as a function of core distance in Fig. 2.13(a) for different energy ranges. The thick solid curve are those expected from 2.21; it can be seen that the agreement with data is good only within 800 m from the core, while in the range 800-2000 m the modified LDF proposed fits very well the data. In Fig. 2.13(b) more recent data are shown [151].

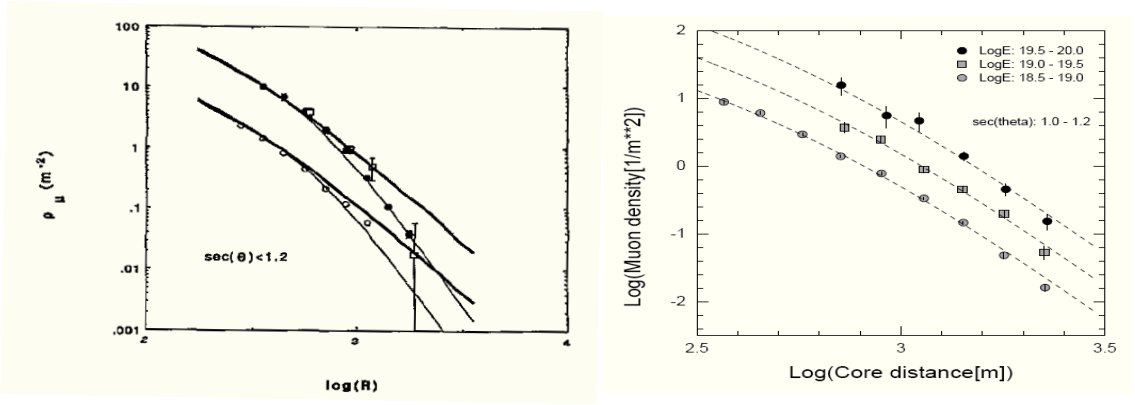

(a) (b)

Figure 2.13: 2.13(a): Lateral distribution of muons obtained by Agasa for vertical showers ($\langle \sec\theta \rangle = 1.09$) in $10^{17.5} \leq E < 18^{18}$ eV (open circles) and $10^{18.5} \leq E < 18^{19}$ eV (full circles). The Greisen LDF represented by 2.21 and the modified LDF represented by 2.22 are shown by thick and thin solid curve; 2.13(b): The lateral distribution of muons in air showers with energy $10^{18.75}$ eV, $10^{19.25}$ eV, $10^{19.75}$ eV.

Instead, KASCADE-Grande proposes the following lateral distribution for the distance range of 275 m to 625 m from the shower core:

$$\rho_\mu(R) = N_\mu \left(\frac{C'_\mu}{R_0^2}\right) r^{p_1}(1+r)^{p_2} \left\{1 + \left(\frac{R}{10R_0}\right)^2\right\}^{p_3} \tag{2.23}$$

where $p_1 = -0.69$, $p_2 = -2.39$, $p_3 = -1.0$ and $C_\mu = 0.28$ were obtained from a fit of the function for simulated proton and iron showers in the energy range of 10^{16} eV - 10^{17} eV [152]. As before $r = R/R_0$ where R is the distance to the shower core, and $R_0 = 320$ m is based on CORSIKA simulations using the interaction model QGSJet01.

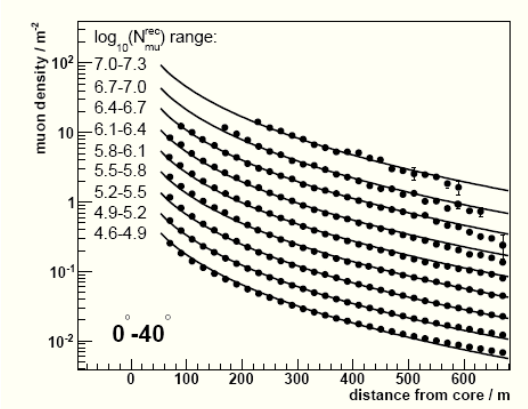

Figure 2.14: Lateral density distributions of muons measured with KASCADE-Grande.

Fig. 2.14 shows a comparison of mean muon lateral distributions from simulations with the measured data. The showers are binned in intervals of total muon number, being a good estimator of primary energy. The lateral distribution obtained from the data agrees relatively well with the simulations. The lines shown correspond to the equation 2.23 where N_μ is set to the measured mean muon number obtained in each interval.

2.5.2 The conversion between N_μ and E

The number of muons, N_μ, is expressed as a function of N_e and $\sec\theta$ by

$$N_\mu = (2.6 \pm 1.4) \times 10^{5+a}(N_e/10^7)^b \tag{2.24}$$

for $10^7 \leq N_e < 10^{8.5}$ and $\sec\theta \leq 1.6$, where $a = (1.07 \pm 0.13)(\sec\theta - 1)$ and $b = (0.77 \pm 0.02) - (0.17 \pm 0.02)(\sec\theta - 1)$. The average N_μ is plotted in Fig. 2.15 as a function of N_e for vertical showers measured by AGASA.

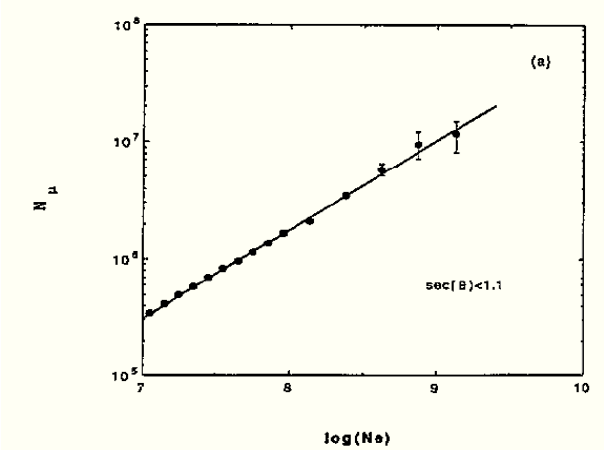

Figure 2.15: The average N_μ as a function on N_e for vertical showers ($\langle\sec\theta\rangle = 1.05$) by AGASA.

Now, using the relation between N_e and E proposed by *Nagano et al.* [153]

$$E = 3.9 \times 10^{15}(\frac{N_e}{10^6})^{0.9} eV \tag{2.25}$$

combined with the Eq. 2.24, AGASA obtains the energy of the primary particle as a function of N_μ:

$$E = 2.16 \times 10^{18}(\frac{N_\mu}{10^7})^{1.19} eV \tag{2.26}$$

2.5.3 Primary composition

The muon content of a shower reflects its primary composition. For the same energy, showers initiated by heavy nuclei tend to be richer in muons than proton initiated ones.
Based on this assumption, MIA uses the muon density measured at a distance of 600 m from the shower core as an indicator of the primary composition. Assuming the validity of the *superposition model* for the development of showers initiated by nuclei MIA defines a parameter β, the 'muon content index' for a shower of primary energy E, calculated as:

$$\beta = \frac{d\log\overline{\rho(600m)}}{d\log E} \tag{2.27}$$

where $\overline{\rho(600m)}$ is the mean muon density at 600 m from the shower core. To evaluate an eventual change in composition of cosmic rays, MIA used the following expression:

$$\frac{d\log A}{d\log E} = \frac{\beta - \beta_0}{1 - \beta_0} \tag{2.28}$$

where A is the mass number of the primary, E the primary energy and β_0 is the estimated value of the 'muon content index' for a pure beam of primary nuclei of mass A. On the performed simulations both the primary energy E and β_0 were found to be model dependent; however A was quite insensitive to the chosen hadronic model. In the studied energy range, 10^{17} eV$\leq E \leq 10^{18}$ eV, QGSJET simulation results yielded a value of $\beta_0 = 0.83 \pm 0.01$/decade both for a pure proton and a pure iron primary composition [148]. The measured value of the 'muon content index' was $\beta = 0.73 \pm 0.03$/decade which is consistent with a composition change, from a predominantly heavy to a light one, at $\sim 3 \times 10^{17}$ eV. So they conclude that the HiRes-MIA hybrid experiment confirms the Fly's Eye experiment result that the primary composition changes towards a lighter mix of nuclei from 10^{17} to 10^{18} eV [149].
The value of the mean muon density at 600 m from the shower core obtained from data was $\overline{\rho(600m)} = 0.24 \pm 0.02/\mathrm{m}^2$ which is quite similar with the results obtained by AGASA which measured $\overline{\rho(600m)} = 0.25/\mathrm{m}^2$ despite of the very different hadronic models used by both experiments [150].

The AGASA experiment provided a composition measurement by comparing the number of muons at 1000 m from the core $\rho_\mu(1000)$ with model predictions in the energy range $10^{17.5}$-10^{19} eV [154]. Figure 2.16 shows the results for observed events (circles). The events with no muon detection are plotted at the bottom. The expected $\pm\sigma$ distribution bounds are indicated for proton (dashed curves), iron (dotted) and gamma-ray initiated showers (solid). The average mass decreases gradually as the energy increases. The composition is predominantly light around 10^{19} eV, with an iron fraction upper limit of 40% above 10^{19} eV at a 90% CL.

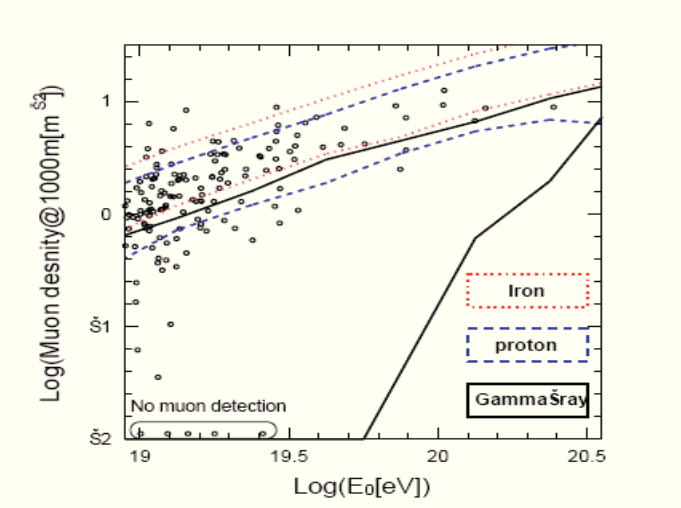

Figure 2.16: $\rho_\mu(1000)$ vs E_0 plots for observed events above 10^{19} eV by AGASA. The events without muon detection are ploted at the bottom. Curves denote $\pm 1\sigma$ distribution bounds for proton (dashed curve), iron (dotted) and gamma-ray (solid) initiated showers.

The $N_e - N_\mu$ correlation stands again at the basis of KASCADE composition results [156, 157]: using data from the field array it was possible to determine the electron number $\lg N_e$ and the truncated muon number $\lg N_\mu^{tr}$ (number of muons with shower core distances between 40 m and 200 m) to form a two-dimensional shower size spectrum. An example of such spectrum for an interval of zenith angles of 0°-18° is shown in Fig. 2.17(a). The content N_j of each histogram

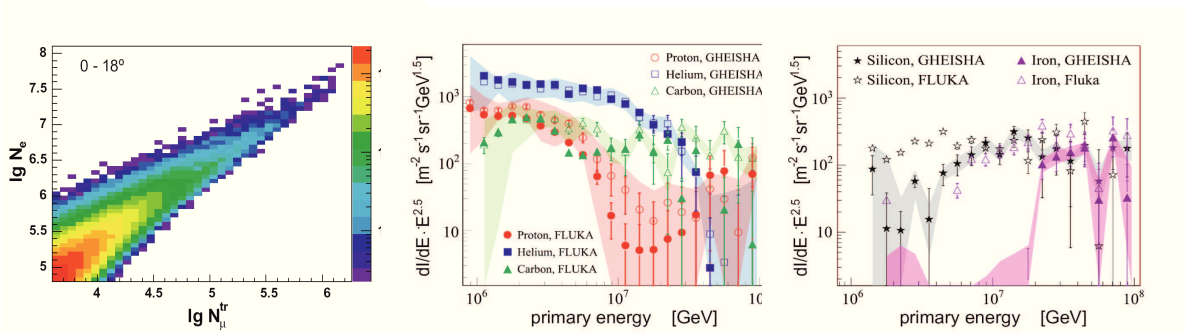

(a) (b) (c)

Figure 2.17: 2.17(a): Two-dimensional shower size spectra as measured by KASCADE for a zenith angle range of 0°-18°; 2.17(b),2.17(c): Energy mass spectra of H, He and C (left) and of Si and Fe (right) as reconstructed by KASCADE. The comparison between QGSJET/FLUKA-based and QGSJET/GHEISHA-based results is shown. Shaded bands correspond to estimates of the systematic uncertainties for the QGSJET/GHEISHA solution.

cell j is related to the single mass spectra and can be written as:

$$N_j = C \sum_{A=1}^{N_A} \int_{-\infty}^{\infty} \frac{dJ_A}{d\lg E} p_A d\lg E \tag{2.29}$$

where C is a normalization constant, containing measurement time and aperture, and the functions $p_A = p_A(\lg N_{ej}, \lg N^{tr}_{\mu j} | \lg E)$ include shower fluctuations, efficiencies and reconstruction resolution, thus giving the probability for a shower with energy E and mass A to be measured and reconstructed with shower sizes N_{ej} and $N^{tr}_{\mu j}$. The two-dimensional shower size spectrum is regarded as a set of coupled integral equations that can be solved for the mass group energy spectra (H, He, C, Si and Fe) through unfolding methods, in this case Gold deconvolution. The results obtained from the unfolding, adopting QGSJET01 as high energy hadronic model, are shown in Fig. 2.17(b) for the light groups (H, He and C) and in Fig. 2.17(c) for the heavy components (Si and Fe). In both figures the mass spectra obtained using two different low energy hadronic model, GHEISHA (describing the interactions for laboratory energies below 80 GeV) and FLUKA (describing the interactions up to 200 GeV), are compared: above the thresholds the low energy models are replaced by QGSJET01.
The helium component is found the most abundant below the knee, followed by proton and carbon components: in the H and He cases the spectrum shows a change of slope, that is absent in the carbon component. On the contrary the trend of Si and Fe spectra appear to be almost flat with energy.
Moreover, due to the very different shower development for high energy and heavy primary CR particles, another parameter that KASCADE uses to discriminate the primary composition is the mean muon production heights, as shows the CORSIKA [158] simulation in Fig. 2.18.

In the high energy domain, above the knee in the all particle spectrum, many others experiments recorded data, like Haverah Park, Volcano Ranch, witch terminated their operations, or Yakutsk, Hires and the Pierre Auger Observatory that are still in data taking. In Fig. 2.19 a compilation of experimental results for the iron abundance as measured by the experiments Akeno/AGASA, Fly's Eye, Volcano Ranch and Haverah Park is reported . The results obtained by different experiment are controversial and do not lead to a firm conclusion. Moreover a comparison among them is not easy, as they rely on different hadronic models.

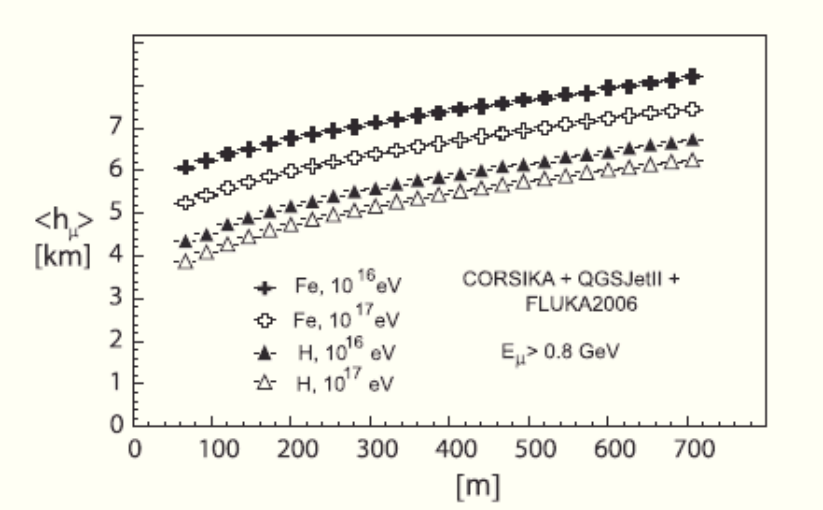

Figure 2.18: Mean muon production heights observed at different distances from the shower core in CORSIKA simulated vertical showers for proton and iron primaries at two fixed primary energy values by KASCADE.

As can be seen, the Haverah Park results are not in agreement with those from Volcano Ranch. The two analysis are based on the QGSJET98 moded, but the observed discrepancy is statistically significant (more than 2σ at 10^{18} eV) and not understood. A disagreement is observed also between HiRes and Haverah Park measurements: the first experiment finds a change in the composition towards light species in the range 0.1-1 EeV, against a composition dominated by heavy nuclei, as found in the Haverah Park data. AGASA and HiRes results are also contradictory, but they are obtained with different models. An attempt to compare the two results has been carried out in [159] adopting the same model SIBYLL 1.5 for both data sets.
These arguments demonstrate the difficulty encountered when comparing results coming from different experiments. The measurements are in most cases not taken in the same period and

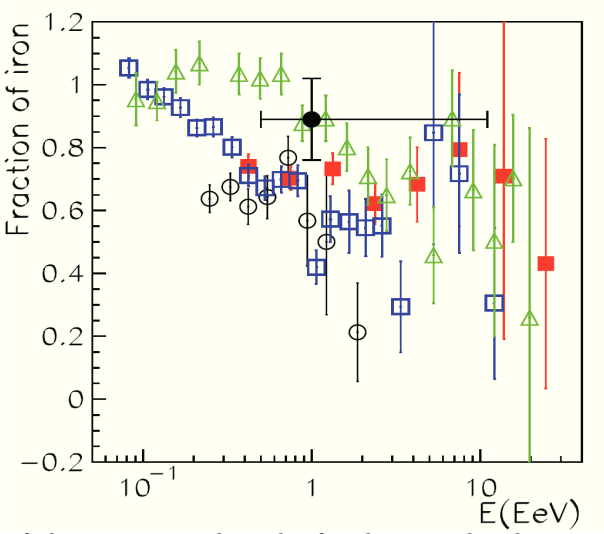

Figure 2.19: A compilation of the experimental results for the iron abundance as obtained by Fly's Eye (△), AGASA A100 (□), AGASA A1 (■), using SIBYLL 1.5 as hadronic model, Haverah Park (○) and Volcano Ranch (●), using QGSJET98 as hadronic model.

the predictions change according to the hadronic model chosen to describe the data. Some basic conclusions can be drawn: the photons are not dominating the cosmic ray radiation, no matter what type of model is chosen, and a certain percentage of heavy nuclei seems to be present even at the highest energies. However, the experimental results are contradictory in some cases and do not point towards a common interpretation. The problem of the cosmic rays mass composition is therefore still open and debated, being one of the key point of study of the Pierre Auger Observatory. In this way The Pierre Auger Observatory intends to dedicate a line of investigation on the muon content of EAS and compare its results with other experiments. Its main bet resides on AMIGA, an upgrade which is being built consisting on the addition of a smaller surface array of Cerenkov water tanks and buried muon detectors that will be buried at a depth high enough in order to avoid a heavy punch-through effect due to the electromagnetic component of the shower which constitutes the major drawback in experiments like AGASA and KASCADEGrande.

Chapter 3

The Pierre Auger Observatory

The Pierre Auger Project is the result of an international effort to measure properties of cosmic rays at the highest energies by detecting Extensive Air Showers with unprecedented statistics and precision: 17 countries, about 70 Research Institutes and Universities from all over the world, involving more than 300 physicists, are taking part in the construction and data analysis of the Auger Observatory. The observatory has been optimized to answer all the open questions on UHECR: the spectrum and the mass composition in the GZK-region, the observation of point-like sources of cosmic rays and the observation of large scale anisotropy.
The concept of the experiment was guided by the following requirements [52]:

- **Large aperture**: as previously mentioned the flux of cosmic rays in the GZK regime is extremely low. The rate of particles with an energy larger than 10^{19} eV is about 1 $\mathrm{km}^{-2}\mathrm{yr}^{-1}$. Thus, it is necessary to instrument a sufficiently large area to achieve significant statistics in a reasonable measurement time. The Observatory covers an area of about 3000 km^2 with surface detectors. So the array allows to detect up to 3000 cumulative events per year above the energy region of the ankle, while about 30 cumulative events per year is the rate in the region beyond the predicted GZK cutoff. This would lead to a sufficient statistics over the activity years in order to draw physical conclusions with a reasonable significance.

- **Precision**: on each site the ground area will be equipped with water Cherenkov detectors(SD) to measure the distribution of particles at ground and by four fluorescence stations (FD) to observe the development of the shower in atmosphere. The array can measure all the time, providing a 100% duty cycle, while the FD can operate with about 10% duty cycle. This allows to gain a subset of events with hybrid information. The combined use of these two detection techniques will provide a cross-calibration and better event reconstruction accuracy. Moreover the collaboration is actually enhancing the original design, with high elevation telescopes, an infill area with finer granularity of tanks in a sub-array to achieve low energy extension, as well as muon counters to be placed underground and a radio antenna array, a technique that provides a cheap and full duty cycle way to measure a shower [160].

The Auger Observatory is built in the Argentinian Pampa Amarilla, near the small town of Malargüe (69° W, 35° S) in the Department of Mendoza [161], in an uplands at an altitude between 1300 m and 1500 m above sea level. This corresponds to a vertical atmospheric depth of about 870 $\mathrm{g\,cm}^{-2}$, needed to observe the shower maximum above ground for air showers at highest energies with the fluorescence telescopes.

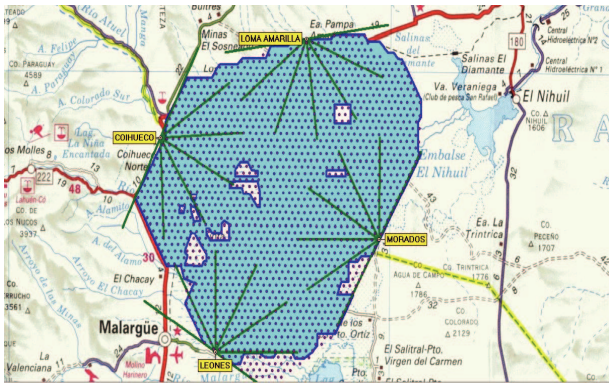

Figure 3.1: Current status map of the Southern Pierre Auger Observatory in the province of Mendoza. Each dot is a deployed surface detector tank, while the green lines represent the operational FD telescopes.

The choice of this experimental site was motivated by physical considerations and practical concerns related to the advantageous characteristics of the local environment. The landscape provides an area of more than 3000 km^2 for instrumentation, that is mostly flat (average slope of 0.5%). Furthermore, vegetation and topology allow feasible deployment of tanks as well as construction and maintenance of infrastructure although some difficulties are related to the absence of adequate roads within the field. The fluorescence eyes are situated at the edges of the area, optimized to observe the atmosphere above the ground array. The cloud coverage less than 15% provides good measuring conditions. Moreover population in the region of the experimental site is small and thus, light levels due to civilization are small.
The installation of detectors started in 2002 and the Observatory started collecting data in January 2004. In the following sections we focus on the two main detector systems, the Fluorescence Detector telescopes (FD) and the Surface Detector array (SD). All fluorescence telescopes are fully operational since February 2007, while the surface array has been completed in March 2008.

3.1 The Surface Array

The surface detector array is a triangular grid of 1660 Cherenkov water tanks, extending over an area of 3000 km^2, with 1.5 km spacing between detectors [162]. The final configuration of the array is shown in Fig. 3.1. The station spacing is the result of a compromise due to the need of limiting the cost of the apparatus and the aim of reaching an adequate particle sampling especially far from the core. With a spacing of 1.5 km the number of triggered stations at the very highest energies is large enough (15 to 20 units) to allow high quality and unambiguous event reconstruction.
The water Cherenkov detection technique has been selected mainly from cost considerations: the production and assembly of the water tanks is relatively cheap, the tanks can be brought out in the field without deionized water and filled afterwards. In addition the water tank offers a natural way to optimize muon pulse heights with respect to the electromagnetic component and can provide a good response to inclined showers.
Each surface detector station is a 3.6 m diameter tank containing a sealed and diffusively reflective Tyvec liner. It is filled with 12 m^3 of ultra-high pure water which is expected to maintain its quality without degradation for the lifetime of the experiment, estimated at 20 years. The tanks are made of high-density polyethylene: such material allows a good resistance to atmospheric and corrosive agents (very strong wind, rain, snow, extreme temperature oscillations from -15°C

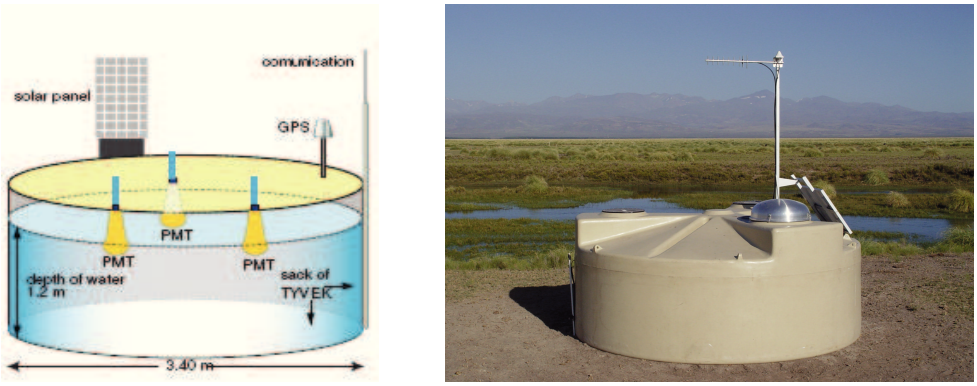

Figure 3.2: 3.2(a): A scheme of the adopted tank design;3.2(b): A surface detector station deployed in the field.

to 50°C,...) and possible animal attacks.
Three nine-inch-diameter photomultiplier tubes(XP1805/D1 Photonis PMTs) are mounted facing down and look into the water to collect the Cherenkov light produced by the transit of relativistic charged particles. The water height of 1.2 m makes it also sensitive to high energy photons, which convert to electron-positron pairs in the water volume. A tank and its components are shown in Figures 3.2(b) and 3.2(a) .
The station electronics is made up of the front-end electronics (FE), a station controller composed of a microprocessor performing local software processing, a slow control module, a GPS receiver and a time tagging unit. On the FE-board, the PMT signals are filtered and fed to a 10-bit ADC which samples at 40 MHz: the signal recorded by the FADC is referred to in units of channels (ch), with a range of 0-1023, corresponding to an input range of 0-2 V. Each FADC bin corresponds to 25 ns.
The surface detector station is self-contained. A solar power system provides the electrical power for the PMTs and the electronics package. The electronics assembly possesses a Tank Power Control Board (TPCB) which also monitors the charging and discharging of batteries and sets the system to hibernation mode if necessary.
Moreover, in order to correlate data taken at different detector stations, a common time base is established by using the GPS system. The intrinsic resolution of the GPS system is about 8 ns, corresponding to an accuracy of 1 m in the reconstruction of the shower core.

3.1.1 Surface detector calibration

The calibration is designed to establish the signal sizes in each station, to set the high voltages of the PMTs, to give the amplification factor of the anode with respect to the last dynode and to set the trigger levels. The signal produced in a station depends on variable parameters like water quality, liner reflectivity, the coupling of the PMT to the water, the gain of the PMT, the gain of the last dynode, the electronic gain of dynode and anode amplifiers. Thus the calibration has to be independent on the number of PMTs functioning and on differences from station to station. The basic physics calibration [163] information needed by the SD is the average charge produced by a vertical and centrally through-going muon. It is named vertical equivalent muon (VEM) and is the signal unit in the water tanks. The conversion to this unit is done to provide a common reference level between tanks. Therefore the calibration goal is to obtain the value of 1 VEM in electronic units for each individual station.
The surface detector in its normal configuration cannot distinguish the vertical from the inclined

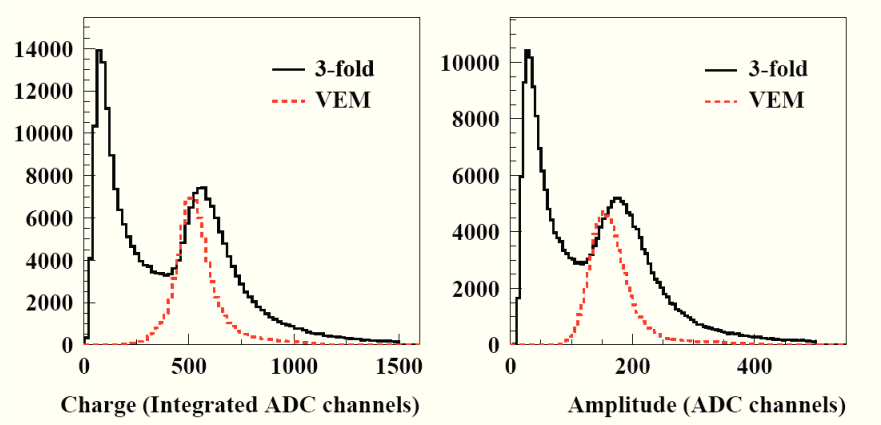

Figure 3.3: Charge and pulse height histograms from an SD station, triggered by a 3-fold coincidence between all 3 PMTs at a trigger level of 5 channels above baseline, with the signal from all PMTs summed. The dashed histogram is produced by an external muon telescope providing the trigger to select only vertical and central muons. The first peak in the black histogram is caused by the convolution of the trigger on a steeply falling distribution from low-energy particles. The second peak is due to vertical through-going atmospheric muons.

atmospheric muons passing constantly through. However the distribution of light from atmospheric isotropic muons produces a peak which has to be related to the VEM. The sum of the PMTs is a measure of the total signal deposited in the tank, whereas the individual PMTs are sensitive only to a fraction of the signal, deposited in the proximity. Thus this peak is at ≈ 1.09 VEM for the first case and ≈ 1.03 VEM for individual PMTs. These values were measured in a reference tank [164], a special setup consisting of a station equipped with two centered scintillators, one on top and the other underneath the station, the trigger requiring coincidences within the two scintillators (see the charge and pulse height histogram in Fig. 3.3)
The calibration to VEM units includes three main steps and is done only on the peak produced by the omnidirectional muons:

- **The PMTs gains set up**: the PMTs voltage is set at the deployment time and it determines the dynamic range of each PMT. Each PMT can be re-calibrated on request from the Central Data Aquisition System (CDAS). The initial value is chosen in such a way that a single vertical muon produces a peak of about 50 FADC counts, meaning a gain of 3.5×10^5 for 94 photoelectrons per VEM per muon. The gains of the three PMTs are set up by matching a point in the event distribution to a measured rate from the reference tank. The latter is calibrated by obtaining a charge histogram and adjusting the three PMTs until the peak of the histograms agree. The gains of the PMTs are set such that the single rates at 150 channels above baseline are 100 Hz.

- **The online local calibration**: to maintain a uniform trigger condition of the array, the station must be able to get to a common trigger threshold. Therefore the online calibration has to compensate for possible drifts in the gain of the PMT. This allows a tank independent analysis of the array response. The trigger levels are set on a minute by minute basis and compensate the drifts of the peak for each detector. Detectors which have drifted significantly (>20 ch) from the nominal value of I_{VEM}^{peak} of 50 ch are re-inizialized. For each station some quantities (charge for each PMT and for the sum of all 3 PMTs, pulse height for each PMT and baseline of each FADC channel) are collected every minute, stored in histograms and sent to the CDAS. During data analysis, the second peak of individual

charge histogram is used to obtain the value of Q_{VEM} necessary to convert the integrated signals into units of VEM.

- **Dynode to anode ratio**: large shower signals are measured on the anode channel, when the dynode channel is saturated. However, the absolute energy scale using muons is determined from the dynode channel, as single muon signal on the anode is too small to be useful for calibration. Consequently, the relative gain between these two channels must be measured. One way to measure this relative gain is from moderately large signals of 20 to 50 VEM. These signals do not saturate the dynode channel, and at the same time they are well above the noise level on the anode channel. Comparing the signal in this overlap region allows us to extract the relative gain of the two channels.

3.1.2 Trigger levels

The surface detector triggering system [165] can be seen as a chain, from the low level trigger received from the single tank (T1, T2) to the array trigger (T3) and to the physical events trigger (T4 and T5). The T2 and T3 conditions allow to detect the cosmic rays in a wide range of energies with an efficiency $> 95\%$ for cosmic rays with energies above 10^{18} eV.

Station Trigger (T1 - T2)

- **T1 trigger**: the first level can operate in two different modes: The TOT (Time Over Threshold) trigger is a simple time over threshold trigger for each PMT, triggering with about 1.6 Hz. The condition required is that at least 13 bins in a 120 bin interval are above a threshold of 0.2 I_{VEM} in coincidence with at least two of the tank's PMTs. The TOT trigger allows muon background rejection from low energy showers and to select small and time spread signals coming from very high energy showers in stations far from the core.
  The single-bin trigger requires a coincidence of all three PMTs having a signal above 1.75 I_{VEM} in just one single bin. The rate of this condition is about 100 Hz. The two configurations are shown in Figures 3.4(a) and 3.4(b).

- **T2 trigger**: the T2 trigger is a software trigger analyzing the full FADC trace of each PMT. All T1-TOT promoted directly to the T2 trigger, while the T1-single-bin triggers are required to have a signal peak above 3.2 I_{VEM} for one bin in all 3 PMTs. The rate is 20 Hz. The concept of not directly requiring a threshold of 3.2 I_{VEM} and combine T1 and T2, is to trigger T1 with high rate to monitor the tank and calibration stability.

Central Data Aquisition System (CDAS) trigger (T3)

This trigger identifies time coincidences between the signals in different tanks that could be associated with a real air shower. It does not guarantee that the data are physics events while a large number of chance coincidences in accidental tanks is expected due to low energy showers and to single cosmic muons. It considers any of the following requests:

- **T3-3TOT**: the 3 TOT mode requires at least 3 tanks satisfying the T2-TOT condition, with at least two of the tanks being in direct neighbours and one being at least second neighbour (Figure 3.4(c)). This configuration is very sensitive to vertical showers and fires for 90% of all T3 events .

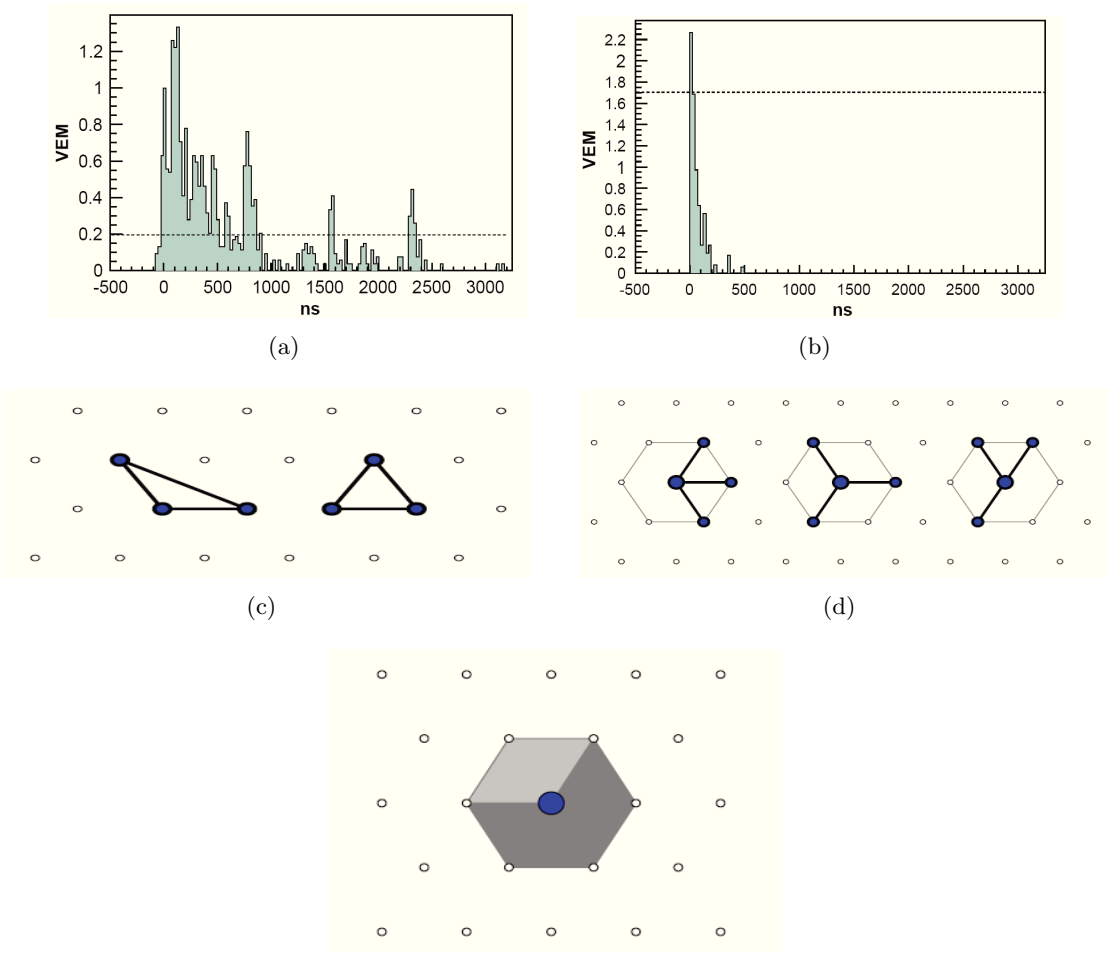

(a) (b)

(c) (d)

(e)

Figure 3.4: The SD trigger schema. 3.4(a): The first operation mode of the T1 trigger, requiring a 2-fold PMT coincidence with 13 bins in 120 bins window above 0.2 VEM. An example of a PMT trace is shown together with the 0.2 VEM threshold; 3.4(b): The second operation mode of the T1 trigger, requiring a 3-fold PMT coincidence in a single bin above 1.75 VEM. An example of a PMT trace is shown together with the 1.75 VEM threshold; 3.4(c): Two possible 3TOT compact configurations; 3.4(d): The three (minimal) 4C1 configurations; 3.4(e): The T5 configuration: the central station with the largest signal is surrounded by 6 functioning stations.

- **T3-4C1**: the T3-4C1 mode is a trigger on 4-fold coincidence of tanks having any T2 trigger. The required compactness is moderate, that means, that one triggered tank of four can be up to 6 km far away from the others in a certain time window (Figure 3.4(d)). Although only 2% of these triggers are real events this configuration is of importance for inclined showers, that produce wide spread patterns.

Physical trigger (T4 - T5)

- **T4 trigger**: the aim of this trigger is to select physical EAS events. The current configuration is applied to all data used for analyzes and studies of events below 60° zenith angle. Actually it is implemented offline and requires either a compact 3TOT-T3 trigger, or a compact configuration 4C1 with one tank being surrounded by at least three triggered tanks in direct neighbourhood. The 3TOT-T4 trigger selects about 95% of all events below

60°, while the 4C1-T4 rejects about 98% of all previous triggers.

- **T5 trigger**: the T5 trigger is a quality cut on data, requiring that at least five of the six neighbouring stations surrounding the station with the hottest signal have triggered and that the reconstructed core is located in an equilateral triangle of working stations (Figure 3.4(e)). This assures a good and unbiased reconstruction of the event.

Hybrid trigger

In addition the SD-array can be triggered by the FD-telescopes with the FD-T3 trigger. This is an external trigger from the Fluorescence Data Acquisition System (FDAS). The aim is to look for single triggered tanks, out of the general SD trigger scheme, and use the tank information to reconstruct the event in a hybrid mode.

3.2 The Fluorescence Detector

The fluorescence telescope detection is provided by 24 telescopes. Such system is fully operational since February 2007, when the last detector site was completed. The design requirements include a wide field of view to overlook the whole area instrumented by the SD tanks, a good signal to noise (S/N) ratio, and minimal deployment and operational costs.
The fluorescence detector consists of four stations (Los Leones, Coihueco, Los Morados, Loma Amarilla) called *Eyes*, each one hosting 6 telescopes. The telescopes are mounted in the same housing, separated by large canvases dividing the telescope buildings in so called *bays*. Each telescope covers a field of view of $30° \times 30°$ in azimuth and elevation and located on small hills at the array vertex, as shown in Figure 3.1 [166]. The combination of the six telescopes provides full 180° coverage in azimuth, thus the fluorescence detectors cover the complete ground array. Fig. 3.5 shows pictures of all four stations. The first completed station was Los Leones, going into operation in May 2001, followed by Coihueco in April 2002, Los Morados in November 2004 and finally Loma Amarilla in February 2007.
With the telescopes placed at the edges of the ground array pointing inside the surface detection field, it is also possible to trigger EAS by more than one telescope. These so called multi-fold events form a high quality subset of data, that can be used to cross check FD-performance with real data.
Figure 3.6(a) shows the arrangement of the six telescopes inside the FD building. Figure 3.6(b) represents a scheme of an individual FD telescope. Each telescope is built with Schmidt optics partially correcting spherical aberration and eliminating coma aberration. The basic elements of the optical system are a UV transmitting filter, placed at the entrance window, a circular aperture, a corrector ring, a mirror and a camera with photomultipliers. The optical filter is a planar window made of Schott M-UG6 glass, which reduces the background light and provides protection from outside dust. It exhibits good transmissivity in the wavelength range 300-400 nm, containing all the fluorescence emission bands of molecular nitrogen.
The circular diaphragm with a radius of 1.1 m is located at the center of curvature of the spherical mirror. The size of the aperture is optimized to limit paraxial rays such that the spot size[1] due to spherical aberration is kept within a diameter of 15 mm, corresponding to an angular spread of 0.5°. In order to enhance the FD aperture and the light collection capability, a corrector

[1]The spot is the image of the point source at infinity on the focal surface of the optical system. The size of the spot characterizes the quality of the optical system.

(a) Los Leones site, in operation since May 2001.

(b) Coihueco, in operation since April 2002

(c) Los Morados, in operation since November 2004

(d) Loma Amarilla, in operation since February 2007

Figure 3.5: The fluorescence telescopes of the Pierre Auger Observatory.

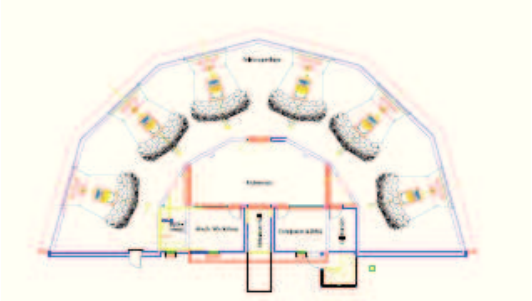

(a)

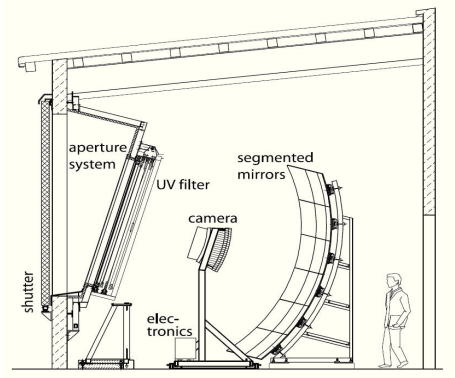

(b)

Figure 3.6: 3.6(a): The scheme of a fluorescence detector building, hosting 6 telescopes; 3.6(b): The layout of a telescope inside the FD building.

ring, between radii 0.85 m and 1.1 m, is also used in each telescope. The analysis of real shower data proved that the corrector ring indeed increase the FD aperture roughly by a factor of 2. Each telescope comprises a large 3.5 m×3.5 m spherical mirror, with a curvature radius of 3.4 m, which reflects the UV light from the aperture system onto a camera of 440 hexagonal pixels, arranged to form a matrix of 22 rows by 20 columns (see Figure 3.6(b)). The camera body covers only 0.1 m^2 in the field of view of the mirror. The matrix was optimised in order to find a good compromise between resolution and minimum visible spot, that is reached for a PMT distance of 45.6 mm (corresponding to an angular aperture of 1.5°, to be compared with a typical spot size of 0.5°). To achieve a good covering a hexagonal structure was chosen. A significant amount of insensitive area is still present. On the one hand there is need of space between the PMTs for

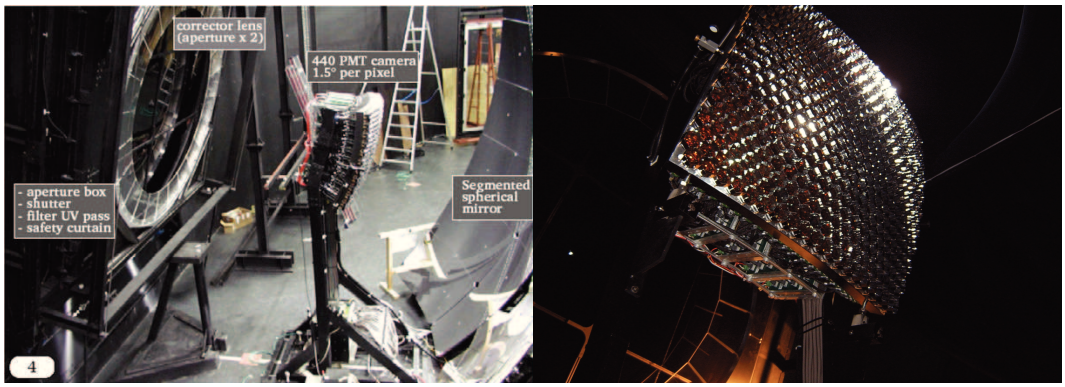

(a) (b)

Figure 3.7: 3.7(a): A picture of a fluorescence detector telescope. The telescope aperture, the segmented mirror, as well as the PMT camera are visible; 3.7(b): A picture of the PMTs matrix.

safe mechanical mounting in the mask, on the other hand, the effective cathode is smaller than the area of the glass envelope. In order to maximize light collection, avoiding the dead zones in between the hexagonal PMTs, they are complemented by light collectors. The basic element for the pixel light collector is a Mercedes star, with three arms oriented 120° apart, positioned on each pixel vertex. Six Mercedes co-rotate one PMT and guarantee a collection efficiency of 94% (without the light collectors, the collection efficiency decreases to 70%). A picture of a single FD telescope is shown in Figure 3.7.
The photomultipliers are 8-stage PMTs (Photonis XP3062) with a hexagonal window (40 mm side to side), diameter 2″ and standard bialkaline photocathode of quantum efficiency around 25% in the wavelength range 350-400 nm. The nominal gain for standard operation is set to $5{\cdot}10^4$.
The PMT readout is digitized by a 12-bit FADC. The sampling rate of 10 MHz and wide dynamic range allows good geometry and profile reconstruction of the detected showers. In fact a sample duration of 100 ns corresponds to a profile sampling of 4 g/cm2.

3.2.1 FD Calibration

The reconstruction of air shower longitudinal profiles and the ability to determine the total energy of a reconstructed shower depend on being able to convert ADC counts to a light flux at the telescope aperture for each channel that receives a portion of the signal from a shower. It is therefore necessary to have some method for evaluating the response of each pixel to a given flux of incident photons from the solid angle covered by that pixel, including the effects of aperture projection, optical filter transmittance, reflection at optical surfaces, mirror reflectivity, pixel light collection efficiency and area, cathode quantum efficiency, PMT gain, pre-amp and amplifier gains, and digital conversion. While the response could be measured for each of these effects independently, the FD calibration system provides a single end-to-end calibration measuring the cumulative effect.
The absolute calibration of the FD is made in three different mode:

- **Absolute calibration with Drum**: this type of calibration requires the use of a portable 2.5 m diameter, 1.4 m deep, calibrated pulsed light source, generally called *drum*, mounted on the exterior of the FD aperture in order to have a uniform illumination of the whole room (Figure 3.8(a)). Inside the drum, illumination is provided by a pulsed UV LED at

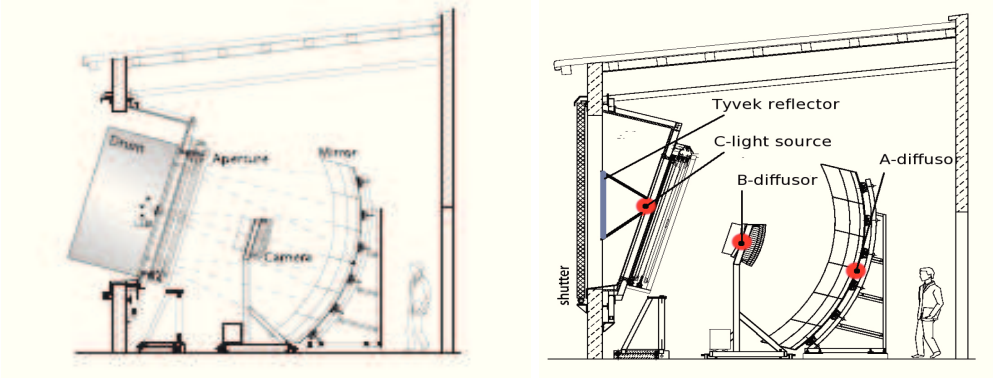

(a) (b)

Figure 3.8: 3.8(a): A schematic view showing the drum mounted in a telescope aperture; 3.8(b): Schematic drawing of the relative calibration system.

375 nm, mounted against the face of a 2.5 cm diameter × 2.5 cm long Teflon cylinder. The Teflon cylinder is mounted in a 15 cm diameter reflector cup, which is mounted flush to the center of the drum front surface, illuminating the interior of the drum. A silicon detector attached to the opposite end of the teflon cylinder monitors the relative light output for each pulse of the LED. The side and back surfaces of the drum interior are lined with Tyvek, which diffusively reflects the light in the UV. The absolute calibration of the drum light source intensity is based on UV-enhanced silicon photodetectors, calibrated at NIST. Studies were made of uniformity of emission across the surface and as a function of viewing angle using a CCD, viewing the emitting surface of the drum from a distance of 14 m. The measured drum non-uniformities are small, less than 1%, indicating that the FD pixels see similar intensities integrated over the drum surface.

- **Absolute calibration using vertical laser shots**: the drum technique for absolute calibration has been checked for some pixels using remote laser shots at 337 and 355 nm. A laser pulse is shot vertically into the air with a known intensity. As the laser energy is known, once accounting for the light propagation from the laser to the FD, the light flux at the aperture can be derived. Using the ADC traces induced by the laser in the camera and the drum calibration constants it is therefore possible to compare the number of predicted to measured photons. The uncertainties of this technique, estimated to be around 12%, are dominated by the laser calibration and atmospheric effects.

- **Multi-wavelength calibration**: the drum device mounts at the back a xenon flasher, with a filter wheel containing 5 filters for selection of those wavelengths spanning the FD acceptance. It is therefore possible to investigate also the wavelength dependency of the absolute calibration.

At the begin and the end of each night of data taking three additional relative calibration procedures are executed. The purpose of relative calibration is to monitor possible changes in the response of the PMTs between drum calibrations. Three positions (A, B, and C) are illuminated for each camera, monitoring different groups of detector components, as shown in Figure 3.8(b). Light is distributed through optical fibers, from permanently installed light sources.

- **Relative Calibration A**: a 470 nm led, positioned in the center of each mirror, illuminates

the camera. Led pulses are splitted in 7 fibers at the source: 6 fibers run to 1 mm thick Teflon diffusor located at the center of each mirror in the FD building, illuminating the camera face, and the remaining fiber provides light for an output monitoring photodiode at the source.This calibration monitors the PMT behavior and provides relative calibration constants on a nightly base, needed to correct the reference absolute calibration.

- **Relative Calibration B**: a xenon light source is mounted at the focus of a f/1.5 lens, with downstream optics including a beam splitter (for a source monitoring fiber), a filter wheel, and an f/2.4 lens focusing onto a 7:1 splitter. The 7 fibers run to each fluorescence telescope, and to a monitor for each output, as for the A fiber. The B source fibers terminate at 1 mm thick Teflon diffusors located at the sides of the camera, with the light directed at the mirror. The Johnson-U filter approximates the full wavelength acceptance of the fluorescence telescopes. This calibration checks the reflectivity of the mirror and the behavior of PMTs.

- **Relative Calibration C**: in this case a xenon light source is mounted as in the case of calibration B. The C source fibers are also split, and terminate outside the aperture with the light directed outwards. Tyvek sheets are mounted on the inside of the aperture shutters. The sheets are positioned such that they are opposite the fiber ends when the shutters are closed, and the diffuse light scattered off the Tyvek enters the aperture. The C source filter wheel containing interference filters is centered at wavelengths of 330, 350, 370, 390 and 410 nm, for monitoring detector stability at wavelengths spanning the spectral acceptance. This calibration checks the whole chain inside the telescope enclosure (the filter, the mirror and the camera).

3.2.2 FD Electronics and triggering system

The organization of the electronics follows the structure of the FD detector. Each of the 24 telescopes is readout by one front-end sub-rack through its associated Mirror-PC. Each sub-rack covers 22×20 pixels and contains 20 Analog Boards (AB), each board serving 22 channels for the signals coming from the pixels of one camera column, 20 First Level Trigger (FLT) boards and one Second Level Trigger (SLT) board.
The AB is responsible for adjusting the gain of each channel and adapting the dynamical range of 15 bits to the 12-bit ADCs. For that purpose a *virtual channel* scheme is adopted. Every channel is configured with a high and low gain of about 20 and 1 respectively. The high gain is optimized for the most frequent small and intermediate pulses and is digitized pixel by pixel. The signal of the low gain is first summed with signals from 10 other channels and then processed by a virtual channel with a gain of about unity. When a high energy shower falls very close to the eye, only one channel out of the group of 11 pixels saturates at the same time and the signal can be recovered from the virtual channel.
The First Level Trigger (FLT) module is the heart of the digital front-end electronics. It discriminates the fluorescence light above a certain threshold from night sky fluctuations and generates a pixel trigger for each channel, digitizes continuously the signals from the analog board and store the raw data in memory for later readout. The hit rate, actual threshold, offset, and especially the variance measured by the hardware are periodically read out and stored in a database for monitoring purpose. Then, the pixel triggers generated for each channel in the 20 FLT boards of a camera are read into the Second Level Trigger (SLT) board.
The electronic boards have been designed to satisfy some precise requirements, among which a

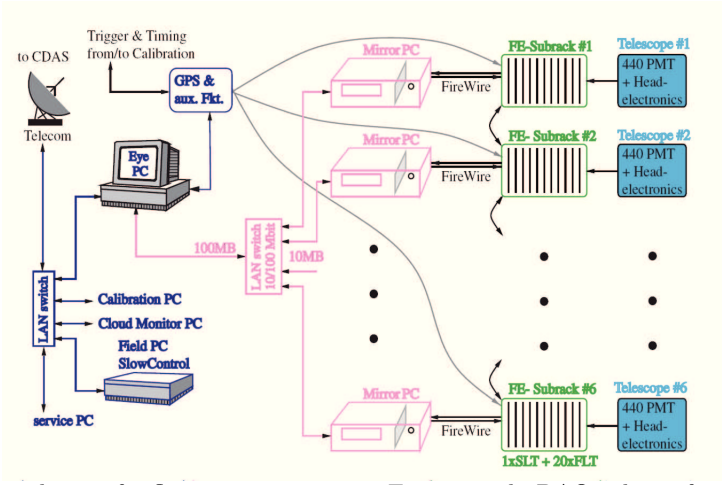

Figure 3.9: Readout scheme of a fluorescence stations: Eye network, DAQ subnet, front-end, and camera.

large dynamic range of 15 bits with 7 bit relative resolution, time resolution of 100 ns, absolute time correlation with the SD smaller than 120 ns, low production and operation cost, remote control for the DAQ.
Moreover, a DAQ-subnet links the six MirrorPCs with a central EyePC via a LAN switch, and the Eye Network links the readout system with the telecommunication tower and the slow control PC. The system is synchronized by a clock module which is based on the same GPS receiver used to synchronize the SD array. A scheme of the FD redout is shown in Figure 3.9. The FD trigger scheme consists of two hardware triggers, the first level trigger (FLT) and second level trigger (SLT) followed by a software trigger, the third level trigger (TLT). In addition the so called T3-trigger acts as external trigger for the ground array to enhance the hybrid event rate.

- **First Level Trigger (FLT)**: the ADC values are integrated by calculating the moving sum of the last n samples, where n is a programmable integration length ($5< n <16$), and this trigger fires if the signal of a PMT passes over a certain threshold. The threshold is adjusted dynamically. A feedback system monitors the trigger rate and changes the signal threshold in such a manner that the trigger rate is constantly at 100 Hz.

- **Second Level Trigger (SLT)**: the aim of the SLT is to discriminate if the FLT was induced by a shower track or from noise. Therefore, the matrix of PMTs in each camera is scanned for certain patterns. The trigger algorithm searches for five pixel track segments using the fundamental patterns shown in Figure 3.10 as well as those created by rotation and mirror reflection of these patterns. In some cases the track does not pass through the pixel center, hence the PMT may not record enough light to trigger. In other cases some pixels may be defective or not properly working. For that reasons the algorithm requires only 4 triggered pixels out the 5 pattern pixels. This requirement leaves a final number of 108 possible configurations. Technically, the grid of the camera is analyzed in a smaller 5×20 sub-matrices. Each scan takes about 1 μs. An additional task of the SLT board is to provide a time stamp for each event using synchronization signals from the GPS module. During good atmospheric conditions the SLT detects about 1 or 2 events per minute, but only a few events per night represent real showers where the reconstruction of direction and energy is successful. However, quite frequently the telescopes observe distant lightning (especially in austral winter) that cause a large area of the camera to trigger in bursts of up to 100 Hz; this effect may lead to congestion of the 64 event buffers and finally to a

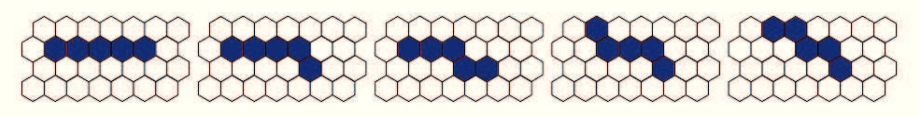

Figure 3.10: Fundamental types of pattern regarded as straight track segments by the SLT.

high dead time. To solve this problem and to refine the event selection, the Third Level Trigger(TLT) software trigger stage was implemented.

- **Third Level Trigger (TLT)**: the TLT is designed as software trigger to discriminate non-physical events. It was optimized for a fast rejection of lightning, of events caused by muons hitting the camera, and of random triggered pixels. A first step consist in the rejection of events not surviving to applied cuts on some signal parameters (number of dips, the number of steps in the signal waveform, and the integral over the 100 μs event window) and on the total number of triggered pixels. Roughly 99% of all lightning events can be rejected in this step. Then it works with the T2-triggered pixel list and their closest neighbours, discarding pixels far off from the group forming the light track. The light arrival times measured in the remaining pixels are compared with the expected times coming from a fit procedure. In this way accidental events with random triggered pixels and events caused by muons are identified and rejected with high efficiency.

- **Hybrid Trigger T3**: as the TLT trigger is implemented on the MirrorPC it can make use only of single telescope data. An Event Builder software collects all events of the same FD site through the DAQ subnet. Concurrent events from adjacent telescopes are merged to jointed events.
  As discussed previously , a special feature of the hybrid design is the possibility of the FD system to interact with the SD stations by sending a T3 hybrid trigger with a rough reconstruction of the shower direction and impact time at ground to the CDAS. There, the DAQ performs the readout of SD tanks in that direction and time.

3.3 Atmospheric Monitoring System

Experiments based on fluorescence detection use the atmosphere as a huge calorimeter, whose properties vary with altitude and time. To obtain a precise estimate of the amount of the fluorescence light emitted by the cosmic ray shower, a detailed knowledge of the atmospheric conditions is required. In fact its condition influences the shower development, the production of particles at ground and of fluorescence and Cherenkov photons and may affect the trigger of both SD and FD detectors. Moreover the light is scattered by aerosol and molecules during its propagation and clouds may strongly attenuate the UV light. Thus, the constantly changing conditions demand a sophisticated monitoring with several instruments deployed at the Pierre Auger Observatory [167]. In Figure 3.11 the Auger map with the position of all the atmospheric monitoring devices is shown.

Weather stations
Molecular conditions at ground level are measured by a network of weather stations at each FD site and in the center of the SD; these record the temperature, pressure, relative humidity and wind speed at ground-level every five minutes. The pressure and temperature data from

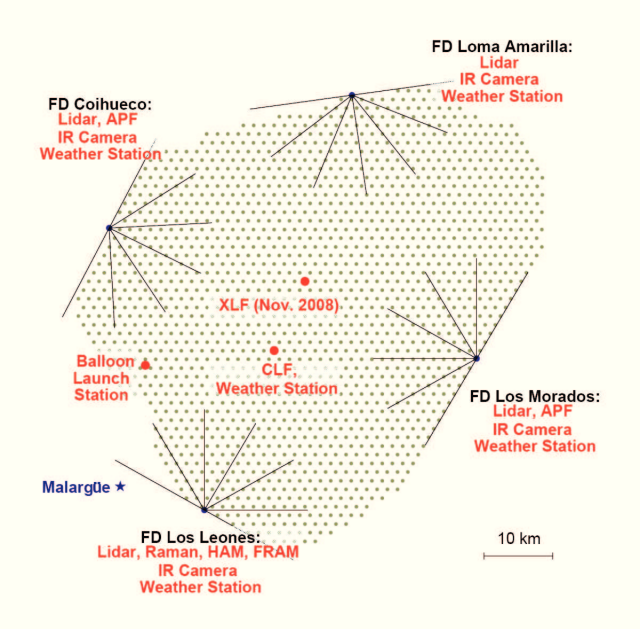

Figure 3.11: The surface detector stations and fluorescence detectors of the Pierre Auger Observatory, shown with the locations of Malargüe and the atmospheric monitoring instruments operating at the site.

these monitors are primarily used to correct for the weather-based efficiency of the SD water Cherenkov stations.

Balloon radio soundings

In order to obtain an air density profile, essential to transform atmospheric depth to geometrical altitude and viceversa, the atmosphere is continuously investigated with radiosondes fixed at helium balloons (one or two l per week) equipped with standard meteorological instruments to measure pressure, temperature, humidity and wind data about every 20 m up to an average altitude of 25 km, with a GPS receiver on board to determine the geometrical height.
Depending on the launching site and wind directions these measurements represent various slices of the atmosphere above the experiment. In connection with local weather stations located at each telescope site a three dimensional model has been developed representing the Malargüe-monthly atmospheric profiles above the surface array. The atmospheric model is stored in a MySQL database and can be accessed by the reconstruction software to guarantee time dependent atmospheric parameterization.

LIght Detection and Ranging (LIDAR)

The atmospheric monitoring campaign includes also a system of four elastic LIDAR stations located next to each FD-site. In each LIDAR station a high repetition UV laser fires short light pulses in the atmosphere. The backscattered light is detected by PMTs mounted in the foci of three parabolic mirrors. Both laser and mirror system are mounted on a steering frame and allow full sky pointing feasibility. The LIDAR operates during FD data taking periods. Each hour the LIDAR scans the sky above each FD site in north-south and east-west direction to monitor the local aerosol scattering and absorption properties of the atmosphere. It is also possible to detect height and optical depth of clouds above each site and estimate a local cloud coverage.
Moreover, when a very high energy event is detected by FD and SD, the Lidar provides an addi-

tional monitoring of the aerosol and clouds content (*Shoot the Shower*) by inspecting the region of the expected arrival direction of the shower. In addition, the Lidar located near Los Leones site is also equipped with a vertical Raman system, detecting the inelastic Raman back-scattered light.

Horizontal Attenuation Monitors
The Horizontal Attenuation Monitors (HAM) is used to measure the attenuation length at ground level and its dependence on wavelength. It consists of a Xenon lamp located at FD-Coihueco that is observed by a CCD camera placed at Los Leones, about 45 km distant. This configuration allows the HAM to measure the total horizontal atmospheric attenuation across the Observatory. A filter in front of the CCD allows the monitoring at different wavelength (365, 404, 436 and 542 nm).

Aerosol Phase Function
The Aerosol Phase Function (APF) devices are designed to measure the aerosol differential scattering cross section ($d\sigma/d\omega$). Two devices are located several km from the FD buildings of Coihueco and Los Morados. Each APF uses a collimated Xenon flash lamp to fire an hourly sequence of 350 nm and 390 nm shots horizontally across the FD field of view. The shots are recorded during FD data acquisition, and provide a measurement of scattering at angles between 30° and 150°.

Central Laser Facility (CLF)
The central laser facility is located in the middle of the surface array, between 26 and 39 km from the FD telescopes. It produces calibrated UV laser beams every 15 minutes during FD data taking. A similar system (eXtreme Laser Facility, XLF) was set up in November 2008 at a symmetric position with respect to the CLF. Both systems produce vertical and inclined laser beams at 355 nm with a nominal energy of 7 mJ (approximately equivalent to 10^{20} eV). The laser beam is observed by all the FD sites. The number of photons reaching the telescopes depends on the atmospheric conditions between the laser and the detector. The aerosol transmission and the presence of clouds within the laser site and FD can then be estimated. The CLF is also connected through an optical fiber to a nearby station allowing the study of SD-FD time synchronization.

Cloud monitors
Although CLF and LIDAR are sensitive to the presence of clouds, they don't provide a detailed all-sky map of cloud distributions. Thus an infrared camera, mounted on the roof of each FD site and operating with a spectral range 7-14 μm, allows to measure the temperature differences between clouds and clear sky. The camera has a field of view of 46°×35° and is mounted on a steerable frame to observe the full sky around each site. During data-taking these cameras provide a full sky image every 15 minutes, used by the FD shift crew to remotely examine the weather conditions at the telescope site. However the cloud cameras are not able to detect the absolute distance of clouds. Information from the CLF, Lidars and clouds cameras are store in a database for crossing all the available information.

Stars monitors
On top of the Los Leones telescope building the Auger Star Monitor (ASM) is installed. The system consists of a CCD, that continuously images the night sky through a wide-field lens

(105°) and a Johnson U-band filter. The ASM is designed to take simultaneous photometric measurements of the stars. Variations between the expected apparent brightness of the stars and their observed brightness as a function of their instantaneous zenith angles give the total extinction of the atmospheric overburden. Also information about the cloud cover can be obtained from the images. The ASM is working remotely and fully automated all nights during the operation time of the fluorescence detectors.

3.4 Enhancements

Instrumental enhancements are currently being installed close to the Coihueco FD station. These include underground muon detectors, additional water Cherenkov detectors, highelevation fluorescence telescopes for a larger field-of-view and radio antenna to detect the geo-synchrotron emission of air showers.

3.4.1 HEAT

The energy threshold of the baseline Auger South detectors can be lowered considerably by additional fluorescence telescopes with an elevated field of view. At energies below 10^{18} eV the fluorescence light of the air showers is detected only at distances up to 10 km. In addition, at these energies, the showers reach their maximum rather high in the atmosphere. Consequently, a large part of the shower profiles falls outside the field of view of the FD telescopes, which is limited to about 30° above the horizon. Therefore, in these cases a reliable reconstruction of the shower profile is often not possible. On the other hand, the energy range between 10^{17} eV and 10^{19} eV is of special interest for a detailed investigation of the spectrum and composition. In this energy range the transition from galactic to extra-galactic cosmic rays is supposed to take place. A number of different theoretical predictions for these processes are available and need conclusive experimental testing (see Chapter 4). To lower the energy threshold for high quality shower data to about 10^{17} eV three additional telescopes are installed near to the FD building of Coihueco (Figure 3.12(a)). These telescopes are similar in design to the other 24 telescopes but can be tilted upwards by 29° to cover the upper part of the nearby atmosphere while the telescopes of Coihueco measure the tails of the low energy air showers. For high reconstruction quality the additional (timing) information of at least one SD array detector is required. To reduce the dependence of the hybrid mode trigger efficiency on primary mass and zenith angle a higher local density of surface detectors (infill array) is needed for the low energy domain.

3.4.2 AMIGA

The AMIGA upgrade is described in details in Chapter 4.

3.4.3 Radio Array

The detection of extensive air showers by their radio emission has revived a few years ago [168–170] after the initial measurements made in the 1960's [171]. There is now evidence that the emission mechanism is an effect of the Earth's magnetic field. Close to the core the thickness of an air-shower is less than about 5 m and the radio emission will be coherent up to frequencies of about 100 MHz. The LOPES [172] and CODALEMA [173] collaborations have shown that the radio signal exceeds the noise level even in radio-loud environments for cosmic rays with energies above 10^{17} eV. The advantages of radio detection of UHE cosmic rays are: radio signals are not

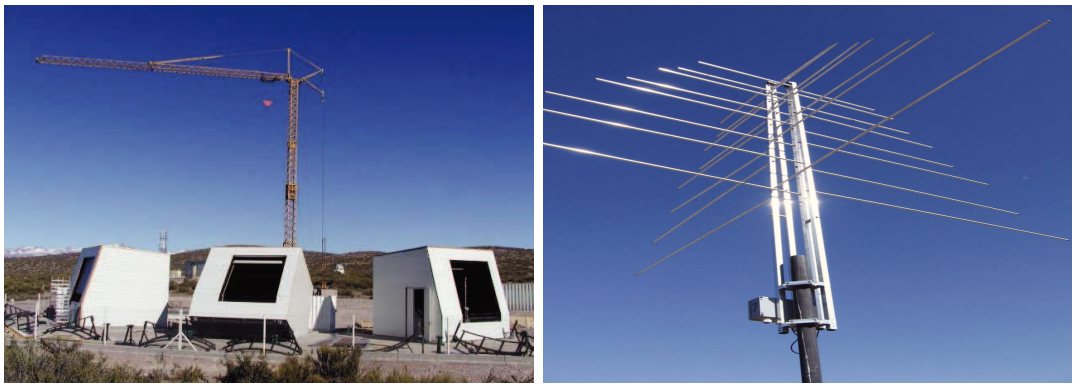

(a) (b)

Figure 3.12: 3.12(a): Three individual enclosures for the HEAT telescopes during hardware installation in May 2008. The central enclosure is shown in the tilted-up position to be used in the low energy measurements later; 3.12(b): A radio antenna tested in the field.

absorbed or deflected on their path and the amplitude of the signal is proportional to the energy of the incoming event. In addition, radio detection can operate at 100% duty cycle, about seven times higher than fluorescence detection. The technique may provide additional information which is complementary to that from SD and FD, as it determines directly the evolution of the electromagnetic properties of the shower in the atmosphere. This complementary information will open the possibility to identify the primary particle. In addition, if one measures radio pulses with receivers distributed over a grid with a pitch size of many hundreds meters, a high angular resolution better than one degree for the arrival direction of the event can be obtained. The technology is potentially inexpensive, if the receivers can be deployed at large enough distances and if the data transmission challenges are solved. The southern Auger Observatory provides an excellent test bed to study the radio detection of extensive air showers as an alternative, cost-effective, and accurate tool for cosmic-ray physics. The data from the radio setup can be correlated with those from the well-calibrated baseline detectors of the Pierre Auger Observatory. A picture of a Radio antenna is shown in Figure 3.12(b)

3.5 Event Reconstruction

As already pointed out, the Pierre Auger Observatory uses two independent techniques that can be used in a complementary way. Events with at least 3ToT stations can be reconstructed using only the information of the surface array. In the same way also a pure FD reconstruction can be performed for events detected by the fluorescence detector. In the hybrid mode the FD information are combined with SD, improving the geometry determination and taking advantages of the calorimetric measurement of the energy from FD.

3.5.1 SD-events Reconstruction

Several experiments have proved successful in measuring extensive air shower parameters by use of a surface array. The concept of this technique is illustrated in Figure 3.13. In a simplified description, the geometry of the shower can be reconstructed by fitting the time and space information of the hit detector at ground [174]. Moreover from the signal recorded in each detector, the lateral distribution function (LDF) or the particle density as a function of the

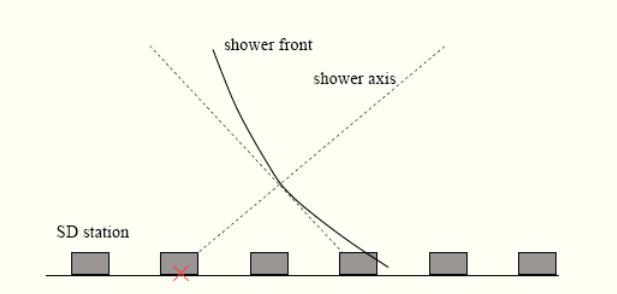

Figure 3.13: Schematic view of the SD reconstruction technique. The geometry of the showers and the lateral distribution function (LDF) are derived from the position, the time and the signal of the triggered stations.

distance from the core can be derived.

Geometry Reconstruction

The signal-weighted and time-weighted barycenters of the stations are set as the distance and time origins. A shower track is described by the following equation:

$$-\widehat{a}(\vec{x}(t)-\vec{b}) = c(t-t_0)$$

where $\vec{x}(t)$ is a point moving with the speed of light along the straight shower track of normalized axis $\widehat{a} \equiv (u, v, w)$, passing the origin at time t_0.
The shower axis can be determined by minimizing the squares of the time differences between the measured signal start t_i (with variance $\sigma^2_{t_i}$) and the model time prediction $t_{\vec{x}_i}$ for each station:

$$\chi^2 = \sum_i \frac{[t_i - t(\vec{x}_i)]^2}{\sigma^2_{t_i}} = \sum_i \frac{[ct_i - ct_0 + \vec{x}_i\widehat{a}]^2}{c^2\sigma^2_{t_i}} = \sum_i \frac{[ct_i - ct_0 + x_iu + y_iv + z_iw]^2}{\sigma^2_i}$$

with $\vec{x}_i$=$\vec{x}_i$-$\vec{b}$ the position, σ_i=cσ_{t_i} and u, v z satisfying the constraint $u^2 + v^2 + z^2$=1. The axis determination is thus a non-linear problem. Nevertheless from a simplified linear model an approximate solution can be obtained and used as a starting point to more elaborate fitting procedures.

LDF Reconstruction

The surface array detects only a sample of the particles arriving at ground therefore a fit of the lateral distribution has to be performed [175]. The lateral dependence of the signal measured in stations is modeled as:

$$S(r) = S_{1000} f_{LDF}(r)$$

where $f_{LDF}(r)$ is a shape parametrization normalized in such a way that $f_{LDF}(1000\,\mathrm{m})$=1.
The energy is estimated using the procedure given in [176, 177]. As a result of a Constant Intensity Cut (CIC) analysis, S_{1000} is converted into a reference signal size, S_{38} , independent of the zenith angle by

$$S_{38^\circ} = \frac{S_{1000}}{1 + 0.92x - 1.13x^2}$$

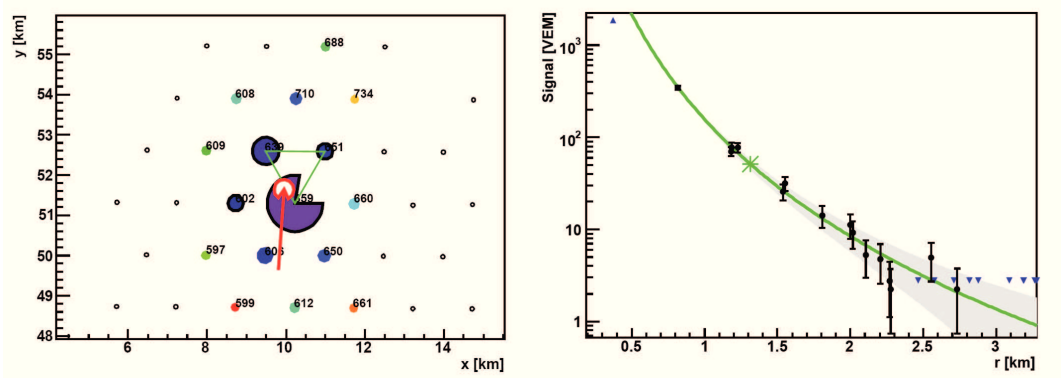

(a) (b)

Figure 3.14: 3.14(a): Array layout of a real SD event measured at the Pierre Auger Observatory (ID 1153192). See text for explanations relative to station colors; 3.14(b): Reconstructed lateral distribution function.

with $x = \cos^2\theta$-$\cos^2 38°$. The energy conversion is provided by samples of golden hybrid events. For these events the S_{38} parameter is compared to the FD energy estimate and a calibration curve is derived, yielding the desired conversion:

$$E = 0.149[S_{38°}]^{1.078}\,\mathrm{EeV}$$

In such a way the dependence of the energy measurement on the predictions given by the hadronic interaction models is extremely reduced.
Typical results of this procedure are shown in Figure 3.14 for a real event (SD id=1153192) measured by the surface detector. In Figure 3.14(a) the array layout is shown: candidate stations are represented with filled circles (in bluish colors for on-time stations, in reddish colors for delayed stations), with size proportional to the square root of the signal. Zero-signal (or silent) stations are denoted by small black opaque circles. Candidate stations with black-rimmed circles have saturation in the high gain channel. The core position is shown with a red circle with an arrow indicating the shower azimuth. In Figure 3.14(b) the LDF fit of this event is shown: the signal of the candidate stations are plotted with black dots, while the LDF fit and the corresponding 1σ confidence band is shown in green and gray. Zero signal stations are plotted here as downward pointing blue triangles, while saturated-signal stations are represented as upward pointing blue triangles.

3.5.2 FD-events Reconstruction

SDP Reconstruction

In the FD a cosmic ray shower is detected as a sequence of triggered pixels. This pattern defines the 'shower detector plane' (SDP) that is the plane containing the shower axis and a point representing the center of the telescope (see Figure 3.15). The normal vector $\vec{n}$ of the SDP can be obtained with a signal-weighted χ^2 fit using the pointing directions r_i of the triggered PMTs:

$$\chi^2 = \sum_i (\vec{n} \cdot \vec{r_i}) w_i \tag{3.1}$$

where the weights w_i are proportional to the signal amplitude $\propto \sqrt{S_i}$.
In the second phase of geometry reconstruction, the timing information of the pixels are used for

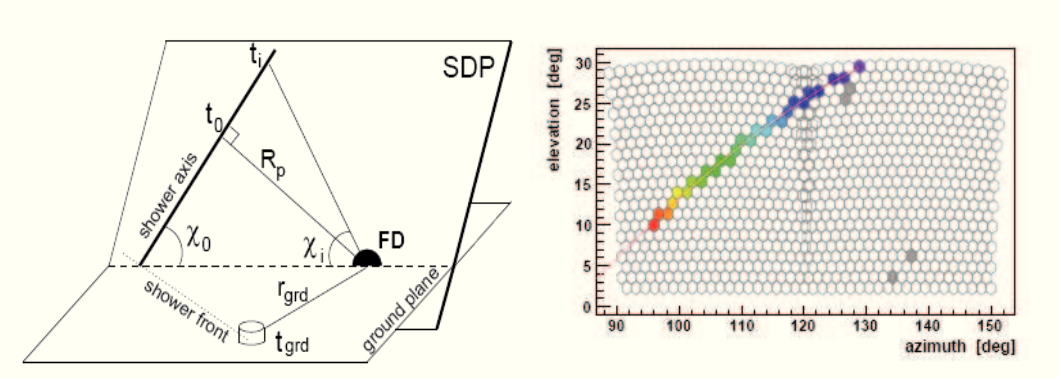

(a) (b)

Figure 3.15: 3.15(a): Illustration of the hybrid reconstruction concept. The shower-detector plane (SDP) and the geometrical parameters relevant to reconstruction are shown; 3.15(b)The pattern of illuminated pixels at the fluorescence camera.

reconstructing the shower axis within the SDP. Assuming instantaneous emission of light and straight propagation with vacuum speed, the expected arrival time of light at pixel i identified by its elevation angle χ_i is given by:

$$t_i = t_0 + \frac{R_p}{c} \tan\left(\frac{\pi - \chi_0 - \chi_i}{2}\right) \tag{3.2}$$

where R_p is the distance of closest approach, t_0 is the time at which the shower front reaches the distance R_p and χ_0 is the angle between the shower axis and the horizontal. These parameters are estimated from a best-fit to data points, by minimizing the sum of the squared differences between measured and predicted times, averaged with their uncertainties:

$$\chi^2_{time} = \sum_i (t_i - t_{meas})^2 / \sigma^2_{t_i} \tag{3.3}$$

This procedure is the one used for monocular FD. However the accuracy on the orientation of the shower axis degrades when the measured angular speed $d\chi/dt$ remains quite constant over the observation time (i.e for short tracks or showers close to FD). In this case, the function given in (3.2) degenerates to a line and the fit parameters become correlated, leading to large uncertainties in the determination of shower geometry. A significant improvement in resolution can be achieved with the hybrid reconstruction. In this case the shower's footprint on ground is known from at least one tank information. This can be used as additional data point for the time fit. This improvement is shown in Figure 3.16(a), where the red ellipse encompasses the results of the monocular reconstruction for a real event. Figure 3.16(b) shows the reconstructed time fits with FD mono and hybrid procedure.
In Figure 3.17(a) and 3.17(b) the 3D view of a FD mono event (Auger event id=200434100694 - SD id=1099363 - FD eye 4,run 683, event 10 - date 2004/12/07) and a hybrid event (Auger event id=200513500999 - SD id=1364365 - FD eye 1, run 895, event 981 - date 2005/05/16) are shown.

An additional possibility to improve the geometry determination, offered by the current detector layout, is the stereo mode: a subset of the available events is measured by two or more FD eyes at the same time. In such cases, the SDP are determined separately for each single FD eye and then the shower axis is found by the intersection of these SDPs, without the timing

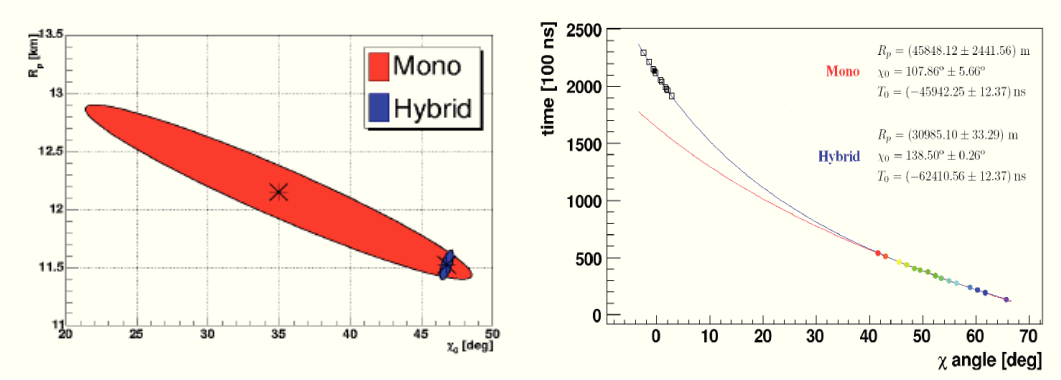

(a) (b)

Figure 3.16: 3.16(a): FD monocular reconstruction uncertainty (red) versus hybrid uncertainty (blue) [178]; 3.16(b) Functional form that correlates the time of arrival of the light at each pixel with the angle between the pointing direction of that particular pixel and the horizontal line within the shower-detector plane. FD data (color points) and SD data (squares) are superimposed to the monocular (red line) and hybrid (blue line) reconstruction fits. The full square indicates the SD station with the highest signal. This is a typical event in which the monocular reconstruction does not work well.

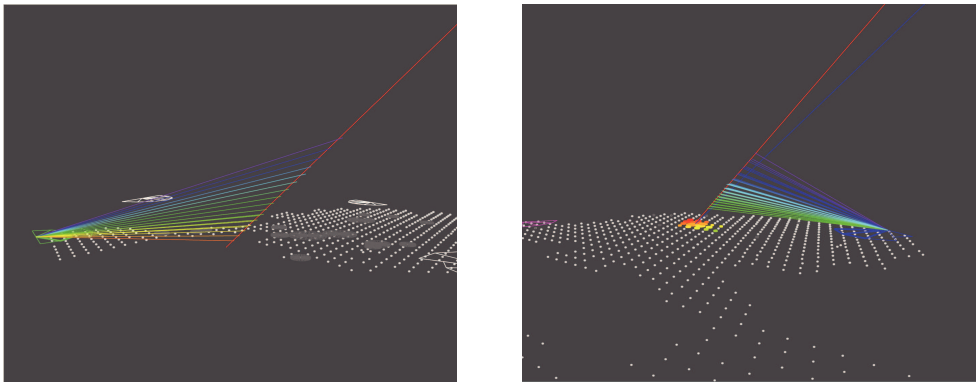

(a) (b)

Figure 3.17: The shower geometry in the SDP in the FD-mono scheme (Figure 3.17(a)) and in the FD-hybrid scheme (Figure 3.17(b)).

information. The achieved resolution depends on the accuracy with which the single SDPs are determined and on the intersection angle among the SDPs.

Profile Reconstruction and Energy determination

Once the geometry is known, the total energy of each event can be reconstructed by combining the knowledge of detector response with monitor data describing the atmosphere properties. The number N_γ^i of emitted fluorescence photons [179–181] is proportional to the energy released by charged particles propagating through the atmosphere.

$$N_\gamma^i = \frac{dE}{dX_i} \times Y_{fl}^i \times \Delta X_i \times A/4\pi r_i^2 \times T_{atm}^i$$

$$N_{FADC} = \alpha_{cal} \times N_\gamma$$

where Y_{fl}^{i} is the efficiency of fluorescence light production, dependent on pressure, temperature and humidity, ΔX_i is the transversed atmospheric depth within a given observation time-window, A the mirror effective area, T_{atm}^{i} the coefficient that takes into account the atmospheric attenuation (Rayleigh scattering and Mie scattering), r_i is the distance of the shower track slice to the telescope and N_{FADC} and α_{cal} are the ADC counts and the detector calibration constants.
The attenuation of light during its propagation to the detector needs to be corrected. In addition to fluorescence light, also the direct and scattered Cherenkov light hit the camera. The method used to take into account the fraction of forward emitted and scattered Cherenkov light is described in details in [182]. Moreover, due to the lateral extent of air showers, a small fraction of shower light is not contained within the optimal light collection area. This is corrected by taking into account the universal lateral fluorescence [183] and Cherenkov light [184] distributions.
The calorimetric energy, E_{cal} of a shower is given by the integral over the longitudinal energy deposit profile,

$$E_{cal} = \int_0^\infty \frac{dE}{dX}(X)dX \tag{3.4}$$

The determination of the total energy requires that the observed profile is extrapolated along the entire shower path, beyond the boundaries of the telescope field of view. Therefore, a Gaisser-Hillas function in slant depth X is fitted to the observed profile:

$$f_{GH} = (\frac{dE}{dX})_{max} \left(\frac{X - X_0}{X_{max} - X_0} \right)^{\frac{X_{max}-X_0}{\Lambda}} e^{\frac{X_{max}-X_0}{\Lambda}} \tag{3.5}$$

where X_{max} is the position of the shower maximum, $(dE/dX)_{max}$ is the maximum energy deposit and Λ and X_0 are two shape parameters. A 'calorimetric' measurement of the primary energy is then provided by the integral of the function given in Eq. 3.5.
An example of the reconstructed light at aperture and reconstructed longitudinal profile is shown in Figure 3.18.

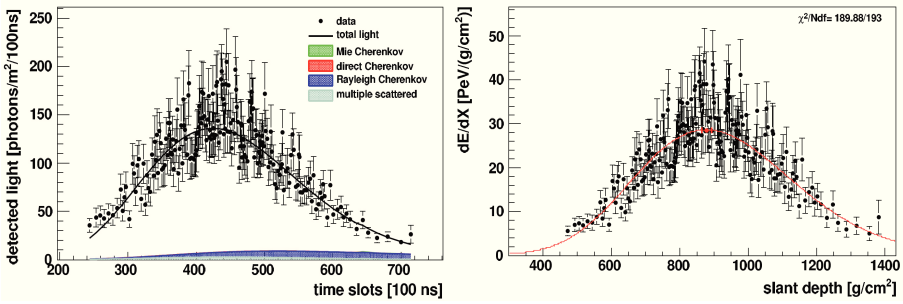

(a) (b)

Figure 3.18: 3.18(a): Reconstructed light at aperture. Different contributions to the light profile (fluorescence, direct and scattered Cherenkov) are shown in different colors; 3.18(b): Reconstructed longitudinal profile. The red line represents the Gaisser-Hillas fit to data.

The position of the shower maximum is determined with an uncertainty of about 20 g cm^{-2} and the energy is reconstructed with an accuracy of about 8% - 10%, improving with energy.
The overall uncertainty on the hybrid energy determination is about 22% and the several contributions are discussed in details in [185]. The largest uncertainty (∼14%) is given by the absolute scale of the fluorescence yield [179]. The absolute calibration of the fluorescence telescope contribute for about 9%. An additional uncertainty of about 5% is due to the measurement of

atmospheric pressure, humidity and temperature and 4%-8% (depending on energy) is related to the attenuation of the light [186]. Moreover, in the algorithm used to reconstruct the longitudinal profile of the shower, an important aspect is the collection of light (including that due to the full lateral width) in the focal plane of the telescope. Systematic uncertainties in these and other steps of the reconstruction method contribute for about 10% to the total uncertainty in the measured energy. Finally the invisible energy (neutrinos and high energy muons) correction has a systematic uncertainty of 4%.

Chapter 4

Detector upgrades to the Auger Observatory: the AMIGA and BATATA muon detectors

The Pierre Auger Observatory, now completed in its original design, has an energy threshold of $\sim 3 \times 10^{18}$ eV for the surface events, and $\leq 10^{18}$ eV for the fluorescence events; these energies correspond to the middle of the ankle. Now the Pierre Auger Collaboration intends to extend the energy range for high quality data from 0.1 to 3 EeV and determine the muon component of showers. In fact in the region from 10^{17} to $10^{19.5}$ eV the spectrum is reported to show two further traits: a break, called the *second-knee*, and a broad feature known as the *ankle*. The second-knee feature has been suggested to be a realization of the knee for the heaviest stable elements as Fe.

The extensions to the existing setup plan the addition of three fluorescence telescopes with a more elevated field of view (HEAT) and a nested surface array, with 750 and 433 m spacing respectively, with additional muon detection capabilities (AMIGA). Such extension will allow the complete inclusion of the ankle and the second knee inside the observation range of Auger. Figure 4.1 show the energy range covered by Auger and the range that will cover with the new extension.

At the energies of the upgrades, $10^{17} - 10^{19}$ eV, there is a change in the origin, acceleration and propagation regime of primary cosmic rays. As explained in Chapter 1, above the knee the primary chemical composition becomes heavier which is consistent with supernova remnants failing to accelerate lighter nuclei any further; up to energies $\sim 10^{17}$ eV the Galaxy is the source of cosmic rays, while at higher energies the galactic acceleration become inefficient. Therefore, it is expected that the cosmic ray flux detected between the second knee and the ankle of the spectrum is a mixture of the Galactic and extragalactic components, highlighting the astrophysical richness and complexity of the region. There are two main physical interpretations of the ankle depending on where the transition from galactic to extragalactic sources takes place. If it occurs at the second knee, then the ankle is reported to arise from the photo-production of electron-positron pairs in interactions of extragalactic protons with the microwave cosmic background radiation [191, 192]. On the other hand, if it occurs at the ankle, then the ankle would arise from the different spectrum indexes of the galactic and extragalactic components [193, 194]. Therefore several effects could contribute to this feature: the end of the Galactic cosmic ray component, the pile-up from pair creation processes due to proton interactions with the cosmic microwave background radiation during propagation in the intergalactic medium or

a combination of both effects: the evolution of the spectrum through the second knee and ankle, and corresponding predicted changes in composition, are crucial to the understanding of the end of Galactic confinement and the effects of propagation on the lower energy portion of the extragalactic flux, that is related to the cosmological distribution of sources and to the composition of the injected spectrum.

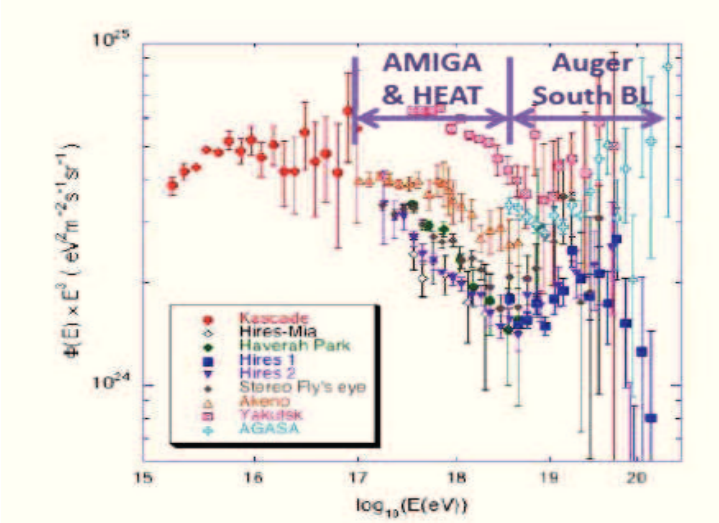

Figure 4.1: Cosmic ray energy spectrum and its main features: knee (few PeV), second knee (0.5 EeV) and ankle (EeV to few tens of EeV). The energy regions covered by Auger baseline design and that added by the upgrades AMIGA and HEAT are shown [195].

Although several experiment like Akeno [187], Fly's Eye [188], Yakutsk [189] and HiRes [190] had observed the second knee in the vicinity of 4×10^{17} eV , its physical interpretation is not still clear. So, the upgrade are designed to operate in the energy region where the superposition of the Galactic and extragalactic spectra takes place. The two main requirements are good energy resolution in order to settle the current discrepancies among different experiments and primary type identification (statistical discrimination over this energy range will suffice) since as mentioned above the transition from galactic (heavy elements) to extragalactic (light elements) sources is directly linked to primary composition. This is a theoretically challenging region where the smooth matching of the two rapidly varying spectra has yet to be explained. The shape of the spectrum is by far insufficient to decipher the underlying astrophysical model, thus variation of the composition as a function of energy turns then into the key to discriminate both fluxes and to select among a variety of theoretical options [195]. So, the determination of the composition and its energy dependence inside the transition region is a primordial objective of these upgrades.
AMIGA, covering a larger detection area than all other experiments will be able to gather a set of this low energy events in a short period of time. Such an extension would allow:

- to make a reliable measurement with low reconstruction uncertainty of the energy spectrum from the second knee to the ankle;

- to make more accurate anisotropy measurements at lower energies avoiding the many spurious effects like the temperature dependence of the event rate and the composition dependent efficiency;

- to bridge with a sizeable overlap the data between KASCADE-Grande and Auger, thus

increasing the reliability of the results obtained.

4.1 The AMIGA array

AMIGA is the acronym of Auger Muons and Infill for the Ground Array. AMIGA covers a small area of the surface array and was designed to study, with a higher resolution, cosmic rays in the energy region 10^{17} eV - 10^{19} eV. The AMIGA array (~ 25 km^2) is located 6 km away from the fluorescence detector at Coihueco and consists on the addition of 85 new stations. Each station will be composed of a water-Cherenkov surface detector and a 30 m^2 muon detector buried about 2.25 m underground. AMIGA will work in hybrid mode both with the FD and the HEAT telescopes.
In order to assess the impact of such upgrade, extensive simulations have addressed, the dependence of the resolution for different shower parameters (arrival direction, core position, lateral distribution of shower particles, energy, etc.) on detector spacing, for different primary energies, composition, and zenith angles. The results from such simulations demonstrated that to reach the above mentioned energy range with unitary efficiency, a graded infill is required, i.e, an array with a 750 m-grid and, in an even smaller area, an infill of this infill, with a spacing of 433 m between SDs as shown in Fig. 4.2(a). The first array covers an area of 23.5 km^2 with 61 pairs

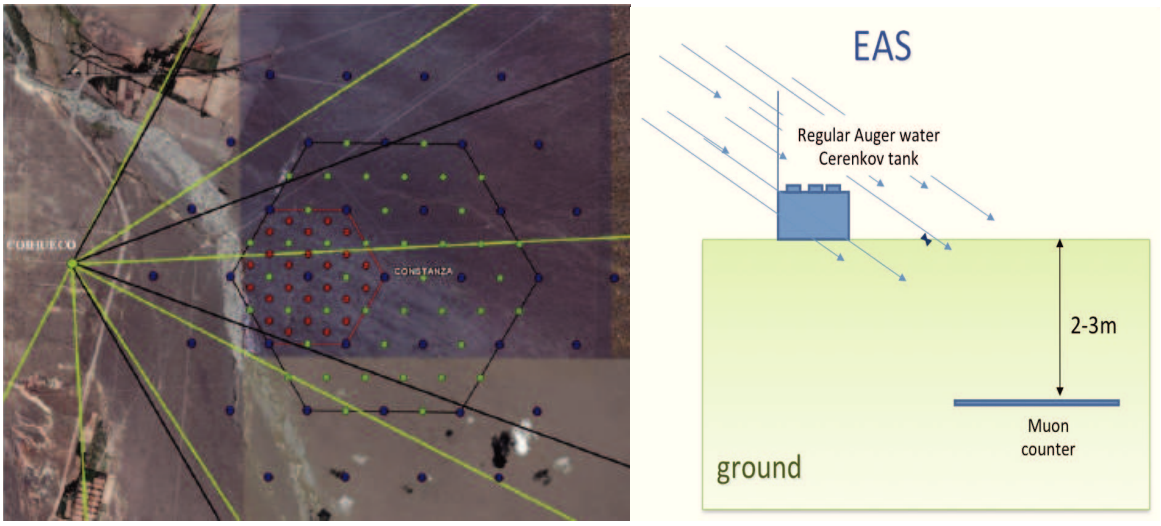

(a) (b)

Figure 4.2: 4.2(a): The Graded Infill Array of the Southern Auger Observatory. The bigger hexagon highlights the 750 m spaced SDs (green spots). The next smaller hexagon highlights the denser 433 m spaced SDs (red spots). The blue spots indicate the SDs that are part of the Auger original array; 4.2(b): Scheme of a tank-muon station.

of SD tanks and muon counters arranged in a triangular grid. It will become fully efficient at $E > 3.5 \times 10^{17}$ eV. The second array covers an area of 5.9 km^2. It will reach its full efficiency at $E > 10^{17}$ eV.
From Fig. 4.3 we can observe that a separation of 750 m between detectors guarantees a detection efficiency of 95% for proton showers with an energy of 3.6×10^{17} eV, and for iron with an energy of 1.8×10^{17} eV. Instead, with the denser infill a similar acceptance can be obtained for showers of as low as 9×10^{16} eV for proton primaries and 4×10^{16} eV for iron [196].

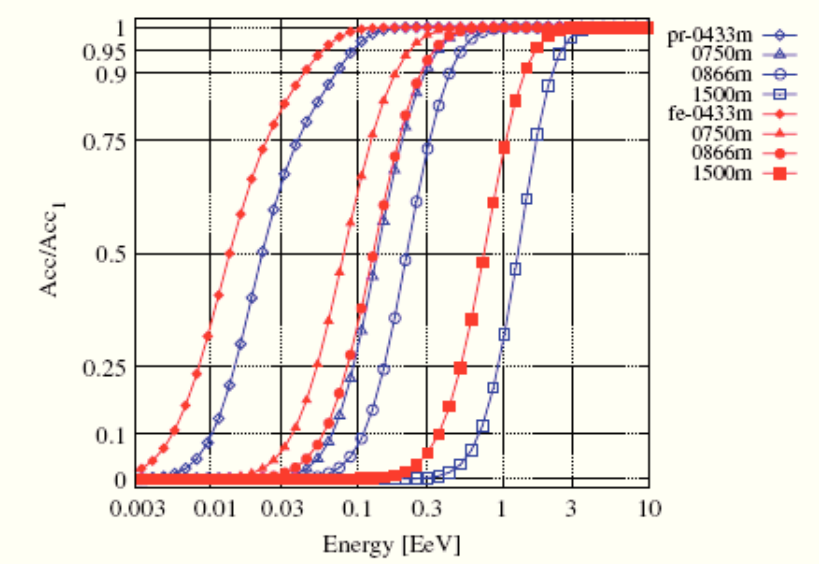

Figure 4.3: Relative acceptance for proton and iron in different infill configuration.

The muon counters of both arrays will be buried located at a given horizontal displacement from the SD tank (see Fig. 4.2(b)) in order to avoid shadowing effects from it while maintaining a uniform shielding. However, the muon detector displacement will be small enough in order to share the same physical point at the shower front, the GPS time signal and telecommunication system provided by the SD tank. At present a smaller prototype was installed.

4.1.1 The Infill capabilities

This infill array uses the same technology of Auger SDs and benefits from the existing knowledge and infrastructure at the site. The AMIGA infill will allow the trigger of a higher number of SD tanks for the lower energy EAS than the original 1500 m array. In particular, the 750 m array will act as the superposition of 3 Auger grids allowing the study of fluctuations and reconstruction errors of the Auger grid. According to [197] the spectral index of the differential flux of cosmic rays at the target energy range of AMIGA is -2.84. The differential cosmic ray flux $d\phi/dE$ can be thus expressed as

$$E\frac{d\phi}{dE} = 30.9\left(\frac{E}{EeV}\right)^{-1.84} km^2 yr^{-1} sr^{-1} \tag{4.1}$$

From equation 4.1, the number of expected events with energy above E_0 and a zenith angle below $\theta_{max} = 60°$ in one year for a detector of area A is given by:

$$N = 795 \cdot \left[\frac{A}{20km^2}\right]\left[\frac{t}{yr}\right]\left[\frac{E_0}{1EeV}\right]^{-1.84} \tag{4.2}$$

yielding about 4300 events for the 750 m array, considering $E_0 = 3.5 \times 10^{17}$ eV, and about 10800 events for the 433 m array if an energy of $E_0 = 10^{17}$ eV is considered. So, an infill with an effective area of $\sim$ 20 km^2 (for well-contained events), which would comprise a total of 64 SDs separated by 750 m, could accumulate a statistically significant number of events with a relatively small effort: only 44 detectors beyond the regular Auger array would be required,

which amounts to less than 3% of the full Auger Observatory [196].

To determine the angular resolution we define the angle Θ as the relative angle between the real ($\widehat{R}_{real}$) and reconstructed ($\widehat{R}_{rec}$) direction, from which $\cos(\Theta) = (\widehat{R}_{real}) \cdot (\widehat{R}_{rec})$. Such quantity is represented in Fig. 4.4 as a function of the detector spacing and for different shower energies at 68% confidence level. On the left we show the results for iron initiated showers, while on the right the results for proton showers. We can see that, for both iron and proton showers with energy 10^{18} eV, the 750 m (433 m) yields an angular resolution close to 1° (0.5°) which means an improvement of a factor 2 with respect to the actual angular resolution achieved by the Auger grid [196]. Comparing these results with other experiments, Akeno achieves a pointing accuracy of 3° [198], while, at 10^{17} eV, Kascade−Grande [199] is expected to have an angular resolution of 0.3° and IceTop [200] claims an accuracy of 0.6° (in this energy region the 433 m-infill will have an angular resolution smaller than 0.7°).

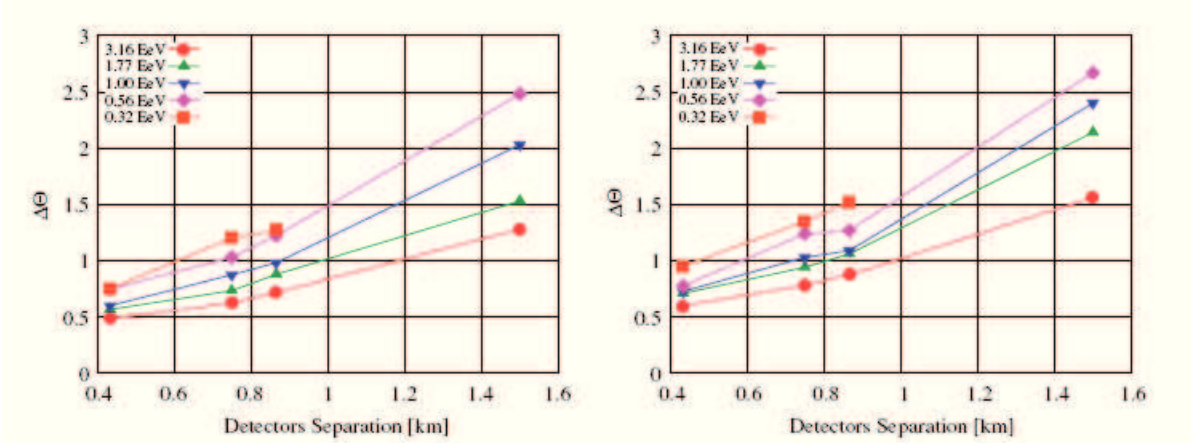

Figure 4.4: AMIGA angular resolution as a function of the detector spacing and the primary type and energy. Detector spacings of 433 m, 750 m, 866 m and 1500 m on the Auger grid were considered. On the left side are displayed the results for iron showers and on the right side for proton showers with $\theta = 30°$.

Another important parameter of the reconstruction process is the core position, that is calculated, as a first estimate, by the barycenter of the 3 stations which present the highest signal. The expected uncertainty for the reconstruction method depends on the array configuration and was estimated by the expression [196]:

$$\Delta Core = \sqrt{(x_{rec} - x_{real})^2 + (y_{rec} - y_{real})^2} \tag{4.3}$$

where x_{rec} and y_{rec} are the shower core coordinates obtained by the reconstruction process, and x_{real} and y_{real} are the real shower core coordinates on the array plane of the simulated showers. Since the lateral distribution function decreases rapidly with distance, the presence of stations near the core plays a fundamental role in its position determination, and, since both AMIGA arrays present a smaller spacing than the Auger grid, more tanks will be triggered thus achieving a better resolution. As shown in Fig. 4.5 the core position reconstruction uncertainty for the 433 m-infill yields a value of ∼15 m and it is rather insensitive both to the primary composition and energy. Regarding the 750 m-infill it is seen that the core position resolution improves by a factor of ∼4, with a slight dependence on the primaries energy, with respect to Auger. This will have an important impact on the reconstruction, giving a better angular and energy resolution.

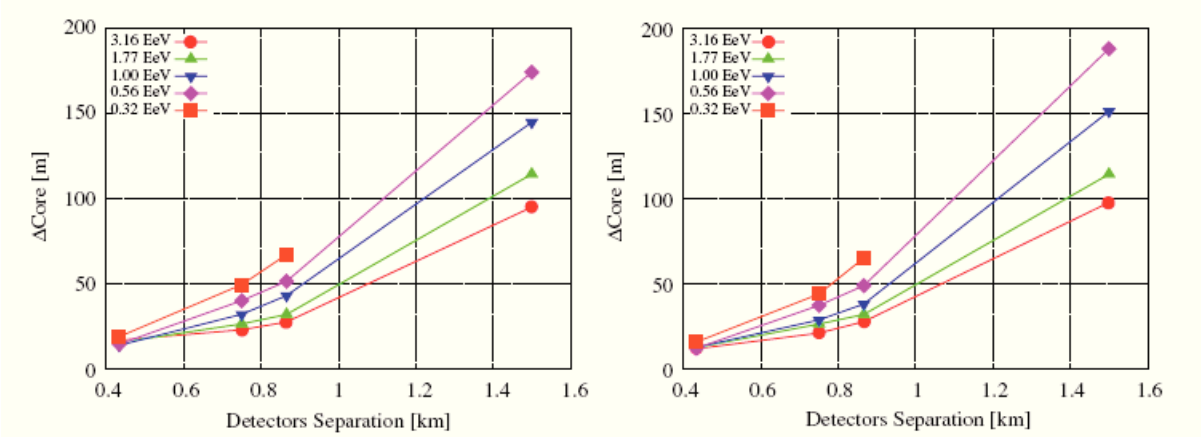

Figure 4.5: AMIGA core position resolution as a function of the detector spacing and the primary type and energy. The same detector spacings as in figure 4.4 were considered. On the left side are displayed the results for iron showers and at the right side are displayed the proton showers for $\theta = 30°$.

Finally the LDF parametrization chosen for the reconstruction is:

$$LDF(r) = S(r_0)\left(\frac{r}{r_0}\right)^{-\beta+\gamma\log(r/r_0)} \tag{4.4}$$

Auger uses for r_0 a value of 1000 m, but in the case of AMIGA that want to reach lower energies with a smaller detector spacing, the best parameter is instead S(600), i.e., the time integrated signal expected in a detector at 600 m from the shower core. Figure 4.6 shows the ratio $\sigma_{S(600)}/S(600)$, where $\sigma_{S(600)}$ is the dispersion of the reconstructed S(600) distribution, as a function of energy for iron and proton shower injected in the 750 m-infill. In this configuration the accuracy of the new energy parameter S(600) for $E = 10^{18}$ eV is $\sim 10\%$ for iron primaries whereas for protons this value is about 13% [196].

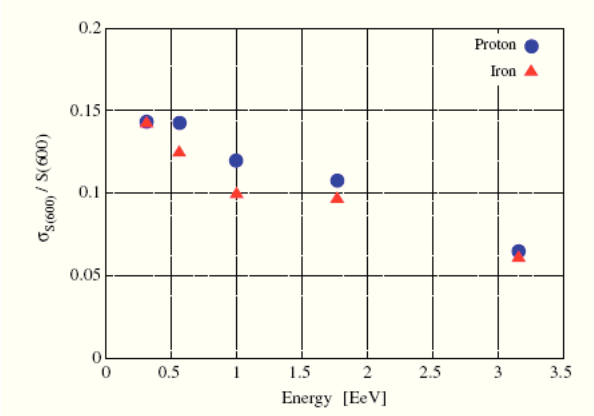

Figure 4.6: Relative dispersion on S(600) defined as $\sigma_{S(600)}/S(600)$ for iron (triangles) and proton (circles) as function of input energy for 750 m spacing and for $\theta = 30°$.

4.1.2 The Muon Counters

The muon detector acts only as a muon counter, i.e. as a detector providing a signal whenever it is crossed by a muon. The detector segmentation will reduce the pile-up effect. For each segment and in a given time bin, only the presence or not of a muon will be recorded.
Each muon detector is made by three modules lodged in a PVC casing. Each module is highly segmented into 64 plastic scintillator strips (density of 1.060 g/cm^3). Each strip is 400 cm long, 4.1 cm wide and 1.0 cm thick, made of extruded polystyrene doped with fluor and co-extruded with a TiO_2 reflecting coating. The 64 strips are placed in two groups of 32 at each side of a central dome where the electronics is lodged and each strip is placed next to another without any gap between them. A wave-length shifter (WLS) optical fiber crosses a groove on the top side and, at one extremity it is connected to a 64 channel multi anode Hamamatsu H8804-200MOD photomultiplier tube (PMT) for the signal readout [203]. Therefore a muon counter will be composed of three of these modules buried alongside a water Cherenkov tank, i.e. 192 independent channels. In Fig. 4.7 the detector assembly and a diagram of a scintillator module are shown.

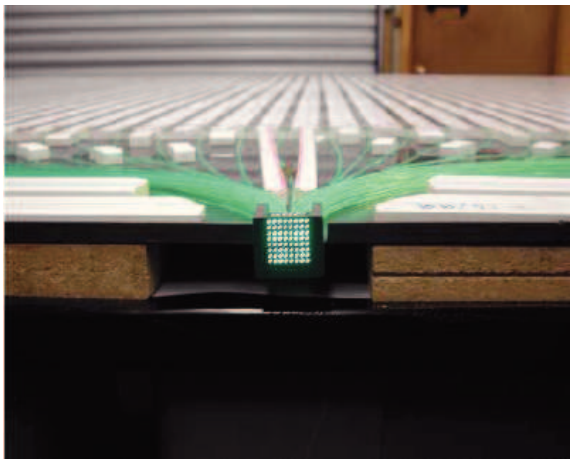

(a)

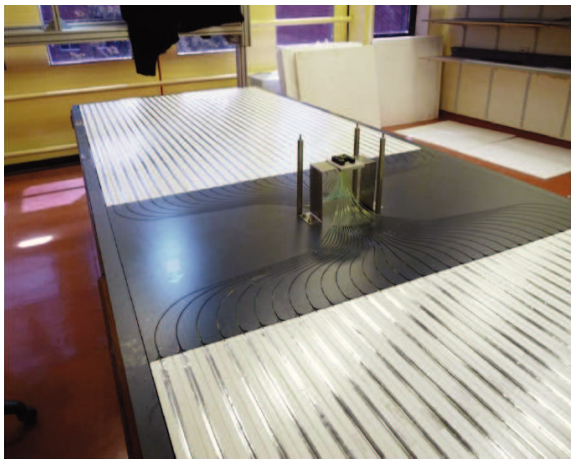

(b)

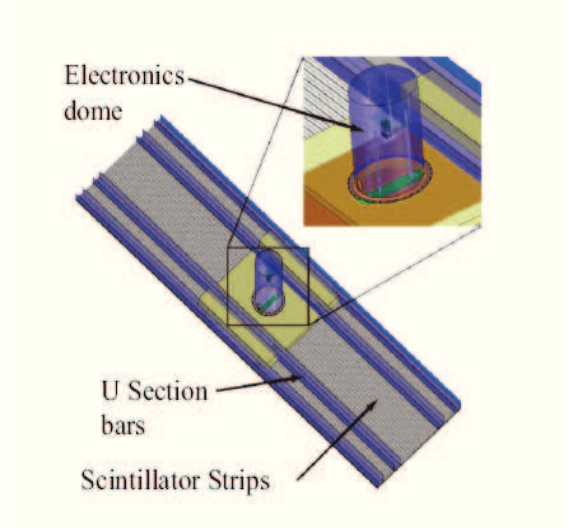

(c)

Figure 4.7: 4.7(a),4.7(b): The assembly of the muon counter.4.7(c): A scheme of a scintillator module.

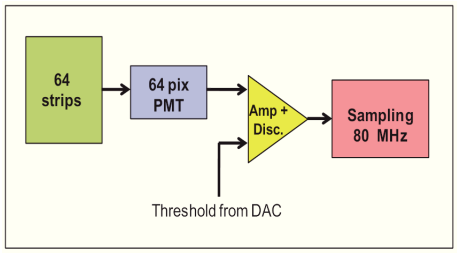

Figure 4.8: A simple scheme of electronic.

When EAS muons hit a segmented muon detector there is the possibility that more than one muon crosses the same segment. The pile-up effect occurs whenever two or more muons cross the same segment within the same time interval. When this happens, the number of counted muons is under-estimated. Thus a detector constituted by a high number of segments is the way to overcome this problem. With this segmentation a pile-up uncertainty can be estimated for the closest counter to the core which is at a mean distance of 230 m for a 750 m grid assuming a 25 ns electronics: for 90 muons (as expected for $\theta = 30°$ and 1.0 EeV iron shower at 200 m from the core arriving in the first 25 ns bin) the uncertainty is just increased by 15% on top of the Poisson fluctuations [204].
To test the baseline design, an engineering array also called Unitary Cell (UC) was built at 7 of the 61 surface detector stations locations in the 750 m infill array, forming an hexagon around the "Los Piojos" central SD. In order to assess the effects of muon pile-up near the core of a shower each muon counter of the UC is composed by 4 modules 200 cm long to have 256 independent channels. Each muon counter of the UC will be buried at 2.25 m deep [205].

AMIGA electronics will have both an underground and a surface section powered by solar panels which provide a total of 20W, 24V DC supply to the buried muon counter on each SD pair. A simple scheme of the electronics is shown in Fig. 4.8. Each PMT is connected with a set of printed circuit boards (PCBs) that allow to filter and amplify the PMT pulse. The output is sampled and transformed in digital data by a Field Programmable Gate Array (FPGA). The discrimination level can be controlled independently for each of the 64 channels using 8 units of 8-channel programmable 12 bit digital-to-analog converters which are driven by the FPGA. After laboratory experiments, the threshold was set at $\sim$ 30% of the pixel mean single photo electron (SPE) amplitude ($\sim$ 15 mV after amplification). After discrimination, for each a tank trigger signal, the output of each strip will be 0 or 1. A circular buffer allows to store this output and to sent it to the surface electronics. Here another data handling FPGA sends the received data to a microcomputer, which upon a request from the central data acquisition system at the Auger Campus, transmits both tank and muon counter data by radio link.
AMIGA will communicate using an 802.11 standard wireless network, widely known as WiFi, taking advantage of the low cost and wide availability of this technology. As a plus, the high communication bandwidth will allow for the recollection of high amount of data at the early stages of the experiment.
PMTs will be tested in a dark box built in the AMIGA laboratory at CAC before transportation to the Auger Observatory. The relevant parameters to be checked for each PMT are: relative quantum efficiency, gain uniformity between pixels, crosstalk, overall dark-rate (sum of 64 channels) and the SPE mean amplitude.

4.1.3 Status and firsts results from AMIGA

Infill

On September 2011 the 61 surface stations planned for the 750 m infill have been deployed. For the smaller 433 m grid 24 new detectors will be installed in the next months. Data taking with the AMIGA detector has now started with the SD 750 m infilled area. Here are presented some preliminary results for the events with zenith angle $\theta < 60°$. Integrating the instantaneous effective infill aperture over the time when the detector was stable, the exposure between August 2008 and September 2011 amounts to 35.7 km^2 sr yr. The trigger requirement is that each event is well constrained within the infill, i.e. with the six SDs of the hexagon enclosing the highest signal SD in its center active.
Figure 4.9(a) shows the distribution of the differences between angles of arrival directions with and without the infill measurement. A large fraction (68%) of the events turns out to be within 1.4° [201]. This means that there is a good compatibility between the two arrays, and it is mostly

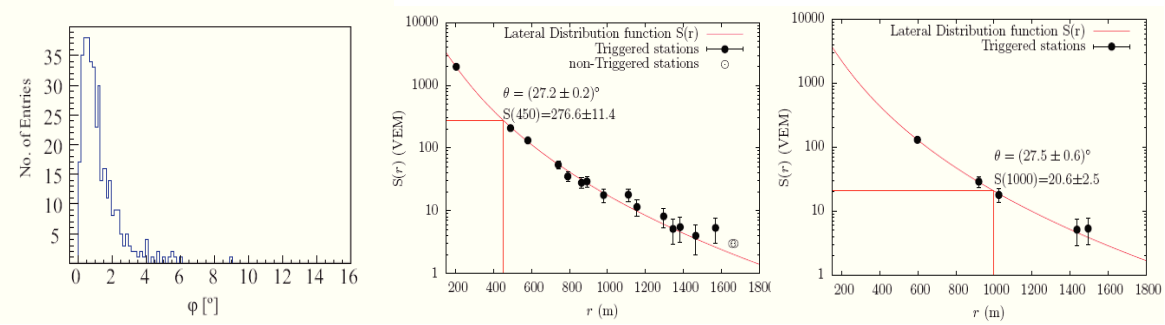

(a) (b) (c)

Figure 4.9: 4.9(a)Reconstruction of arrival direction with and without infill SDs. φ represents the difference between angles of arrival of the reconstructed shower with minus without the infill measurements; 4.9(b),4.9(c): The same event reconstructed with the infill (left) and the regular (right) array. Solid and open circles are triggered and non-triggered station respectively

related to the uncertainty of the Auger regular reconstruction due to the expected better infill accuracy being a denser array. An other check on the compatibility between the regular and the AMIGA arrays is the LDF reconstruction. As an example the LDF of a well-contained infill event of 2.7×10^{18} eV impinging with zenith angle of 27° is shown in Figure 4.9(b). The same event reconstructed using stations from the regular array alone is illustrated in Figure 4.9(b). Both reconstructions are compatible [206].

Another result concerns the study of the preliminary energy calibration performed from the analysis on the events simultaneously detected by the infill and the FD. The infill and regular array calibrations are both extracted from FD energy measurements, but we have to remember that the results have to be optimized for different energy ranges. Moreover infill signals are more attenuated with zenith angle, and the infill shower ground parameter is taken at 600 m instead of 1000 m. In figure 4.10(a) is shown the correlation between the constant intensity cut corrected shower ground parameter $S_{600}(38°)$ and the FD assigned energy fitted with an exponential function [201].
Finally Figure 4.10(b) represents a very preliminary energy spectrum [202]. The infill is fully efficient at $log(E/eV) \approx 17.5$.

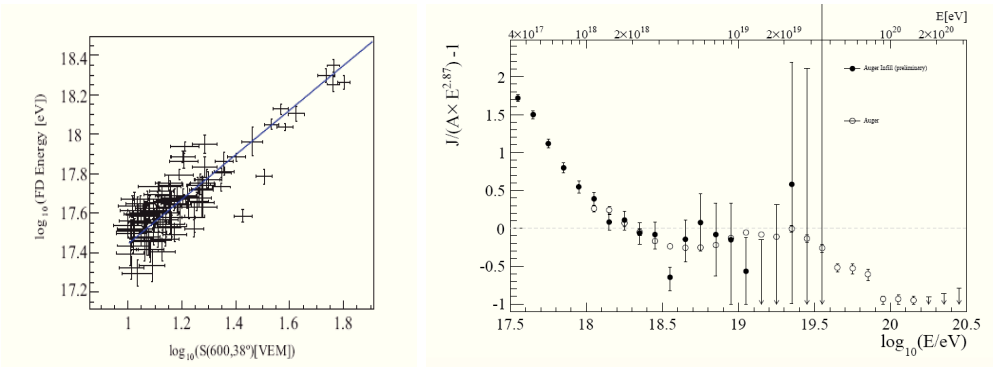

(a) (b)

Figure 4.10: 4.10(a): Correlation between $S_{600}(38°)$ and the FD energy; 4.10(b)A preliminary energy spectrum obtained by the first infill events.

Muon counters

The muon detector is currently in its prototype phase, named the Unitary Cell (UC). At present, three 10 m^2 detectors have been deployed in the positions shown in Figure 4.11 with prototype electronics sampling every 12.5 ns (80 MHz). At the hexagon centre, an additional 5 m^2 module was also installed. The analysis of the events is on-going.

(a) (b)

Figure 4.11: 4.11(a): Surface infill SD station with its associated muon counter already buried. Once instrumented, the access pipe is filled with bags containing soil from the installation site. 4.11(b): Photomontage to depict the detector concept: any impinging muon with energy $\geq$ 1 GeV propagates in the soil and is capable of reaching the buried scintillator.

4.2 BATATA

4.2.1 The detector setup

As a prototype of the AMIGA muon counters an additional detector was constructed: BATATA. Its main objective is to quantify the electromagnetic contamination and measure the ratio between muonic and electromagnetic component coming from cosmic ray showers as a function of undergroung depth. The detector has to be installed at the center of the AMIGA array and EAS of around 10 PeV are selected with a small triangular array of 200 m side composed by 3+2 Auger surface Cherenkov stations. A schematic view of the tracking hodoscope and its working principle are shown in fig 4.12.

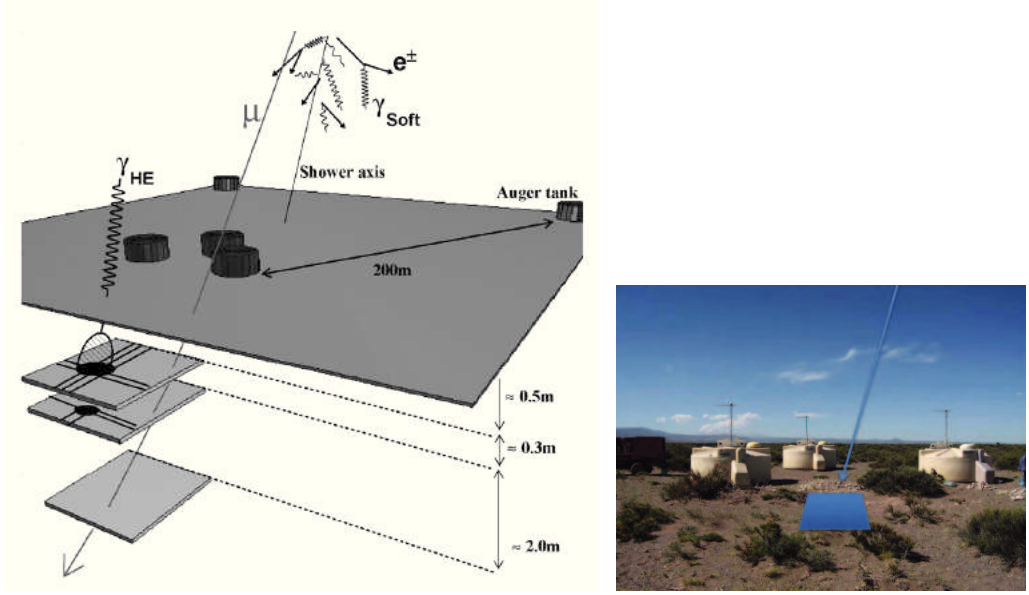

(a) (b)

Figure 4.12: 4.12(a): Auger-like tanks on surface and buried plastic scintillators of the hodoscope and its working principle. 4.12(b): A photo of the BATATA location.

The detector is composed by three horizontal dual-layer scintillator planes buried at different depths. Each layer in a plane consist of 49 rectangular strips 2 m long, 4 cm wide and 1 cm thick. The two layers of a plane are rotated by 90° in order to produce an effective x-y plane with 4.1 cm × 4 cm pixels covering an area of 4 m^2. The scintillators are MINOS extruded polystyrene strips with one embedded Bicron BC92 fiber of 1.5 mm diameter. The scintillator light coming from each layer is collected by a 64 pixel photo-multiplier tube H7546B. The front-end(FE) electronics works in counting mode and signals are transmitted to the surface DAQ stage using low-voltage differential signaling (LVDS). Each x-y plane is fitted inside an individual casing made of fiber glass. It was designed to be water- and light-tight and to withstand handling during shipping and burying. Two caps allow the access to the corresponding front-end boards and optical couplings between PMTs and optical fiber cookies. The caps can be dismounted for inspection and servicing. Moreover the casing and sealing are versatile enough to allow addition of new components and cabling not specifically foreseen in the original design. Figures 4.13 and 4.13(b) shows a scheme of one x-y plane inside the casing and the detector lateral view.
The power consumption of BATATA is $\leq$ 200 W. This power is supplied by an array of 20 solar panels with their corresponding batteries, ensuring continuous operation even during low

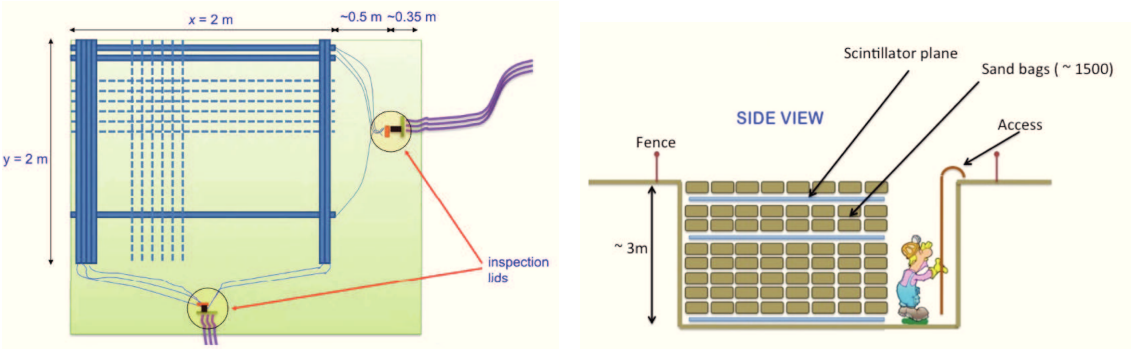

(a) (b)

Figure 4.13: : Schematic view of the layout of scintillators, optical fibers, PMTs and front-end electronics inside the casing for any one of the three hodoscope planes; 4.13(b): Schematic lateral view of the detector layout.

insolation winter months.
In July 2011, one of the three planes, the deepest, was installed.

4.2.2 The Scintillator

Solid scintillators have been used extensively in many particle physics detectors and in particular these have frequently been the active detectors of choice for sampling calorimeters. Some features are required in the choice of the scintillator:

- *Good energy resolution*: the light output must be sufficient so that the detection efficiency for muons crossing a strip is greater than 90%;
- *Uniformity*: in order to ensure that it is possible to correct for position dependence of showering events, the light output of the scintillator strips should vary by no more than 30% with respect to a nominal response at that location (after correcting for attenuation in the WLS fiber);
- *Attenuation*: the light observed from the near and far side of a strip should differ by no more than a factor of 5;
- *Fast timing*: scintillation detectors have the intrinsic property of permitting nanosecond timing;
- *Flexibility in readout*;
- *Simple and robust construction*: assembly of solid scintillator strips into detector modules requires little hardware and experience;
- *Long-term stability*: the light output of the scintillator system should have long term stability with an expected decay time of at least 10 years;
- *Low maintenance*: we expect the system to be quite robust and to require little maintenance;

- *Reliability*: there are no catastrophic failure modes for solid scintillator which cannot be externally repaired. A possible long term decrease in light output can be corrected using calibration data. Because there is little to go wrong, the detector is likely to achieve its intrinsic measurement capabilities.

The scintillator strips are MINOS type [207]. They are made of polystyrene, doped with the fluors PPO(1%) and POPOP(0.030%). This compound is melted and extruded in the shape of a rectangular bar with a narrow groove along the center of one of the wide sides, as shown in Fig. 4.14. The groove depth is sufficient to contain a 1.5 mm diameter wavelength shifting fiber. A thin outer layer of $Ti0_2$ (0.25 mm) surrounds the entire scintillator bar except for a small region near the groove and the lateral extremes, in order to prevents the light from escaping and increases the capture probability by the optical fiber. Each scintillator strip is 4.1 cm wide, 1 cm thick, and 2 m long.

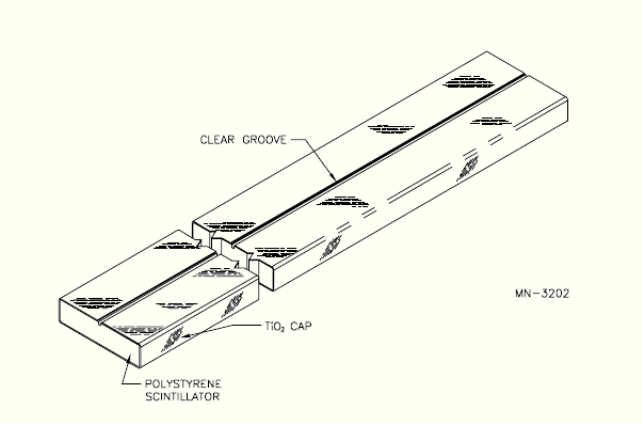

Figure 4.14: Schematic view of a scintillator strip with groove and reflective coating.

4.2.3 The WLS Fiber

To guarantee an acceptable light output, optical fibers produced by Bicron and Kuraray were tested in laboratory [208]. The final choice was for the Bicron BC92 wavelength shifting (WLS) fibers. When a charged particle goes through the scintillator bar, a fraction of the produced light is collected by the optical fiber and re-emitted at a different wavelength. Each one of the BATATA's x or y layers needs at least 141.4 m of optical fiber, therefore the overall detector's optical fiber requirement is 848.4 m.
The coupling of the fibers to the PMT requires a fine polishing of the surface that touches the glass on top of the photocathode. For this purpose the use of a razor blade knife provides an efficient cut, although a lot of care is needed to avoid cladding chiping . After the cutting a fine polishing is required to assure a flat and perpendicular tip with respect to fiber axis. This step is very important because a slant or dirty tip can never be well coupled to the PMT photocathode resulting in considerably light loss. Therefore the surface of the fiber is refined using subsequently a 2000-grit, 3 μm and finally a 0.3 μ sandpaper. Figure 4.15 shows the fiber tips after each step [209].

Several tests were performed on the optical fibers.
Its spectrum was measured by using a spectrometer and a blue LED. Figure 4.16 shows the results. The spectrum of the LED has a maximum at around 475 nm which slightly depends on

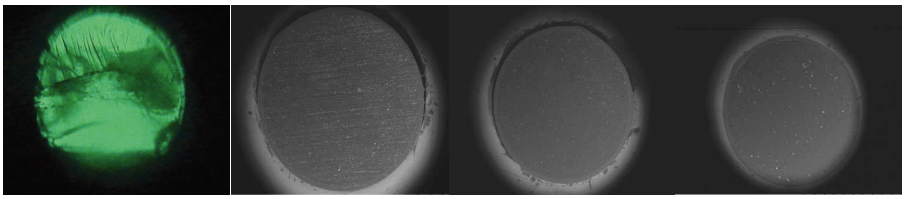

(a) (b) (c) (d)

Figure 4.15: Front view of a fiber obtained from an electronic microscope for different polishing steps: 4.15(a): after cutting; 4.15(b): after polishing with 2000-grit sandpaper; 4.15(c): after polishing with 3 μm sandpaper; 4.15(d): after polishing with 0.3 μm sandpaper.

the voltage used. As expected the light emitted by the fiber after injecting the light of the LED is shifted from blue towards the green (510 nm approximately) [210].
The attenuation length of the fibers was measured using a moving LED with a hole specially drilled in order to let the testing fiber move in it. A fiber of 380 cm long was fixed by its extremes inside a black box of 4 m long and one of the extremes was put in contact with a phototransistor optically coupled with optical grease. The attenuation lenght was extracted from a fit to the measured phototransistor voltage as a function of the LED position over the fiber (which, in turns, is proportional to the amount of light transmitted). To fit the curve it was used a double exponential function [210]

$$A_{tt}(x) = ae^{-x/\lambda_1} + (1-a)e^{-x/\lambda_2} \tag{4.5}$$

The obtained values are ≈ 40 cm and ≈ 600 cm for short (λ_1) and long (λ_2) attenuation length respectively. The amount of light absorbed within λ_1 is $a \approx 30\%$.
The light collection in the PMTs strongly depends on the care taken in the manipulation and cleaning of the optical fibers and grooves of the strips and on the uniformity with which the glue is distributed along the groove. A clean room was arranged in order to keep the fibers and the strips free of dirt. The fibers and bars are washed with peroxide by using a medical gauze; then the glue is poured very carefully by using a syringe filling the empty space left by the fiber in the groove. This process is done slow enough and pouring continuously the glue in order to prevent air bubbles formation which again can affect the light collection. Finally, the extreme which does not go onto the PMT pixel is painted with white paint to increase the amount of light that reaches the PMT.

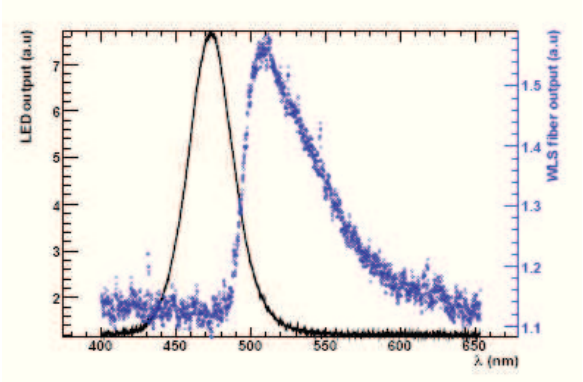

Figure 4.16: Blue LED spectrum (solid black line) shifted towards green by the WLS fiber (open gray circles).

4.2.4 Electronics and trigger

The scintillator light coming from each layer is collected by multi-anode PMTs of 64 pixels (H7546B). The electronics works in counting mode and signals are transmitted to the surface DAQ stage using low-voltage differential signaling (LVDS). A logical signal is produced only when the height of the analog pulses are greater than a given threshold and the thresholds for each channel can be adjusted independently in real time. Any strip signal above threshold opens a GPS-tagged 2 μs data collection window. Data, including signal and background, are acquired by a system of FPGA Spartan boards and a TS7800 single board computer. The code controlling the data flux at the FPGA level was written in VHDL (VHSIC -Very High Speed Integrated Circuits-hardware description language). The front end boards are $12.3'' \times 9.3''$ and comprise 64 channels, but at present only 49 of them are used. The multi-anode PMT and its high-voltage supply are located on the board. Each channel contains:

- an amplification stage which uses an AD8009 operated at amplification factor ~ 6;
- a discrimination stage, which uses a MAX9201 high-speed, low power, quad comparator with fast propagation delay (7ns typ at 5mV overdrive) connected in bipolar mode;
- a digital-to-analog converter TLC7226C to independently setup the discrimination voltage of each channel;
- a high-speed differential line driver SN55LVDS31 to transform the discriminator output into a differential signal.

The detector has six of such boards enclosed and buried in the same casing as the scintillator planes. It has be experimentally determined that, under the most unfavorable conditions, the equilibrium temperature at the surface of the board never exceeds 40°C, which is well within the working range of the electronic components.
A schematic view of the electronic board corresponding to a single layer is shown in Fig. 4.17 where its main components are indicated. When a shower events reach the detector it can trigger at least tens of channels in a time scale of a microsecond, that is a rate much higher than the ∼kHz background of the detector due to low energy cosmic rays and natural radioactivity. So, to detect an EAS event a simple trigger scheme is implemented at the FPGA level. In order to ensure the stability of the trigger rate, background events are also recorded at fixed time intervals during each run and are used to re-calibrate the discriminator thresholds at the end of each run [212].
Moreover to limit the data acquisition in a defined energy range and distance between shower axis and detector, BATATA will be combined with a triangular array of water cerenkov detectors on the surface. The surface detectors will be 200 m apart from each other in order to produce a GPStagged threefold coincidence signal for quasi-vertical showers in the vicinity of 10 PeV. The separation of the background from the signal coming from showers will be performed offline.

4.2.5 PMT, strip and front-end characterization

Regarding the PMTs, BATATA uses Hamamatsu multianode photomultipliers H7546B tubes [213]. The main features of these devices are:

- 8×8 multianode with 2 mm × 2 mm anode size;
- effective area of 18.1 mm × 18.1 mm;

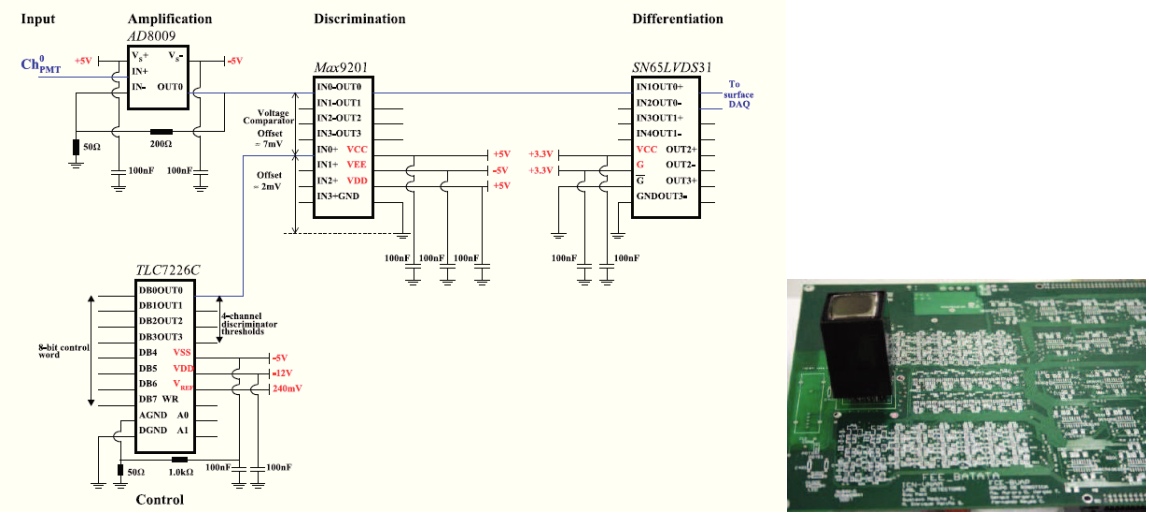

(a) (b)

Figure 4.17: 4.17(a): Front-end channel diagram: excepting the amplifier, each device controls 4-channels. Therefore in one FE board there are 16 of such components and 64 amplifiers. 4.17(b): General view of the front-end board with the multi-anode PMT.

- high speed response;
- low cross-talk (2% typical);
- high cathode sensitivity.

To find the optimal operational voltage for the PMTs, the single photo-electron (SPE) spectrum as a function of the supplied voltage was checked with a controlled LED pulse . 50,000 output pulses for each supplied PMT voltage ranging from 825 V to 950 V were recorded. Finally the selected operational voltage was 950 V. Figure 4.18 shows the gain curve obtained and the pulse charge distribution for the final chosen voltage. The Gaussian peak around zero in the figure is the charge distribution of the baseline, while the shoulder peak on its right is the single

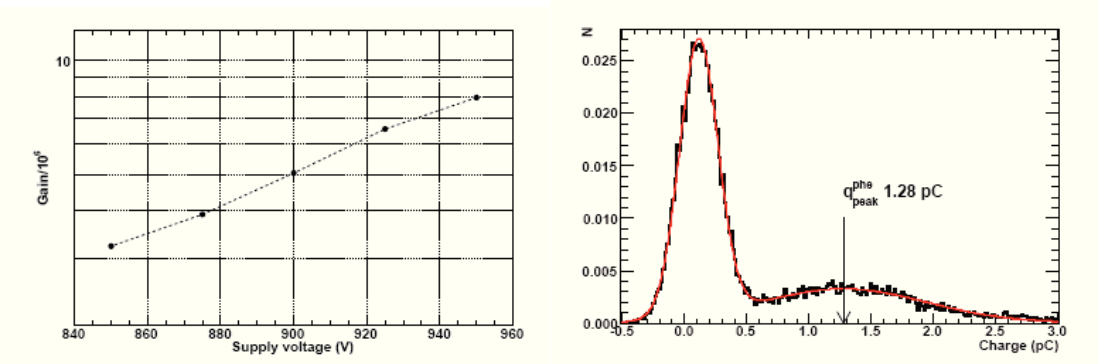

(a) (b)

Figure 4.18: 4.18(a): PMT gain as a function of supplied voltage. 4.18(b): Single photo-electron spectra for 950V supplied PMT voltage with its fit result superimposed.

photo-electron charge distribution. The charge histogram were fit with [214]

$$\sum_{n}^{n_{tot}} \sum_{m}^{m_{tot}} P(n|N_{phe}) \times P(m|n\epsilon) \times N(q - q^{m}_{peak}, \sigma^{m}) \tag{4.6}$$

where $P(n|N_{phe})$ is the Poisson probability of having n photo-electrons pulled out from the photo-cathode if the mean is N_{phe}; $P(m|n\epsilon)$ is the Poisson probability of emitting m secondary electrons from the first dynode if the efficiency is ϵ; $N(q - q^{m}_{peak}, \sigma^{m})$ represents the contribution of each one of the m electrons after being multiplicated by the consecutive dynodes. The last term is a Gaussian whose peak position is q^{m}_{peak} and whose dispersion is σ^{m}. Using this equation we found the single photo peak position for each PMT voltage and from the $q^{m=1}_{peak}$ the gain G is extracted.
The typical anode response variations, specified by the manufacturer over the whole PMT pixel grid, ranges from 5% to 30% approximately, being the pixels on the edge the most sensitive. The anode uniformity has been checked over 8 pixels illuminating them with the same strip in order to avoid strip-to-strip intrinsic fluctuations. The results are shown in Fig. 4.19. It can be seen that, in completely agreement with factory specifications, the pixels on the edge are the most sensitive and non-uniformities can reach $\sim 30\%$ in the center of the grid.

Figure 4.19: PMT relative pixel uniformity: non-uniformity can be as high as 30% in the center of the PMT pixel grid.

Cross talk features have several implications on detector efficiency and therefore must be very well known and characterized, in fact trigger as well as physics analysis strategies depend on a good understanding of cross talk. To find the BATATA cross talk, the scintillator light of a strip was injected in a single PMT pixel recording the output from that pixel and two neighbouring pixels. The measurements were performed at 160 cm away from the PMT. We are specially interested here in the pulse height distribution of the muon signals because the BATATA first level trigger (FLT) works on amplitude signals, not on charge signals. The results obtained can be seen in Fig. 4.20 [215] where the pulse height probability distribution of the three measured pixels (4.20(a)) and the cross talk matrix (4.20(b)) are shown. The results are summarized in Table 4.1 for 15 mV and 20 mV discrimination threshold. For example, for a threshold of 15 mV ∼6% of the muonic signals will be lost (i.e., the efficiency will be reduced to 94%) and 95% of the fake cross talk signals in one adjacent pixel will be avoided.
To test the scintillator strip it was measured the number of photo-electrons pulled out from the photo-cathode when scintillation light is produced by muons depositing energy in the strips at varying distances from the PMT. A coincidence signal in detectors P1 and P2, located X centimeters away from the PMT, triggers the readout system (see scheme in Fig. 4.21) Complete

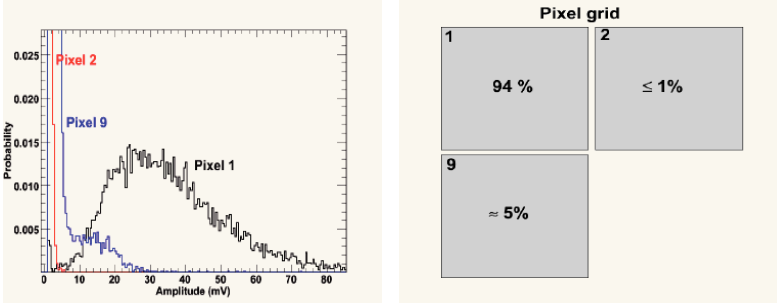

(a) (b)

Figure 4.20: Cross talk features. Input signal was injected only in pixel 1 while output was recorded also in its adjacent pixels 2 and 9; 4.20(a): Pulse height probability distribution; 4.20(b): cross talk matrix at 160 cm with a FLT threshold of 15 mV (NB: the value for pixel 1 is considered as the corresponding efficiency).

Table 4.1: Efficiency (pixel 1) and cross talk (pixel 2 and 9) for two different discrimination threshold.

Pixel	**Prob**$(h \geq h_{thr})$	
	$\mathbf{h_{thr} = 15\ mV}$	$\mathbf{h_{thr} = 20\ mV}$
1	≈94%	≈83%
2	≪1%	≪1%
9	≈5%	≤2%

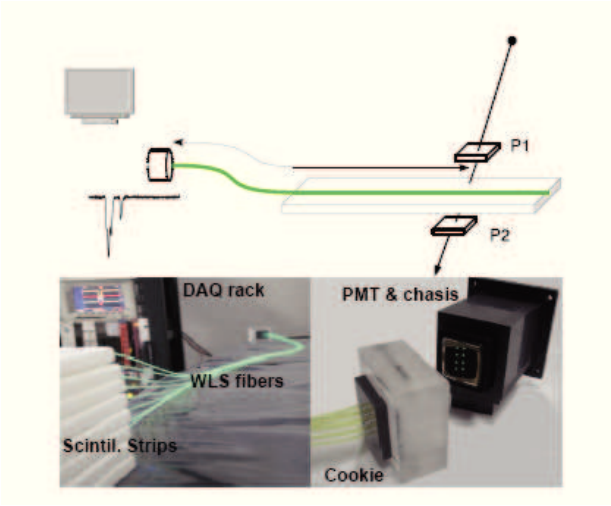

Figure 4.21: Top: experimental setup to record real muon signal at a given X distance from the PMT. A coincidence between detectors P1 and P2 triggers the data acquisition. Bottom: strips, fibers and DAQ rack used in the test.

waveform pulses were stored in the PC through a Tektronix TDS3014B oscilloscope using a NI-GPIB interface. Additionally signals were sent to a CAMAC CMC080 module to measure their charges. The interface towards the PC was a CC32 Wiener crate controller.
Figure 4.22 shows some waveform pulses obtained 160 cm away from the PMT. We can note that the multiple peaks seen in a single signal are randomly distributed in amplitude, i.e., first peaks could be either the lowest. Moreover individual peaks in the signals are very sharply lasting for no more 10 ns [215].

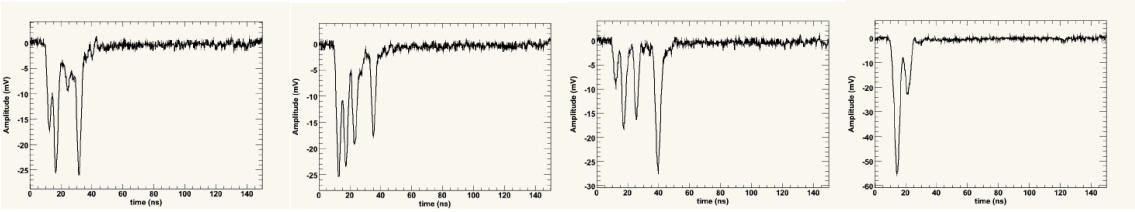

(a) (b) (c) (d)

Figure 4.22: Typical pulses at 160 cm from the PMT.

On the other hand, it was studied the longitudinal response of the assembled strips. This measurement is very important because the hodoscope will read out signals from one edge of the scintillator strips, so we have to characterize the typical non-unifromity along the longest side of the strips. The shortest and farthest distances were 180 and 380 cm (it is worth to note that both lengths are in the long attenuation regime of the WLS fiber). It is found that the scintillator light at 380 cm produces, in average, around five photo-electrons in the PMT, while the light at 180 cm produces a number close to 7 phe (Fig. 4.23(a) shows this result). This attenuation of 25% between extreme edges of the strips depends mainly on 2 factors: the reflection that can be achieved at the edges of the strip (where there is no $Ti0_2$ coating and the fiber tips and scintillator strip ends are covered by a white paint), and the extra fiber length needed to join the strip end with the PMT (which is linked to strip position in the x-y plane). The charge distribution spectra for background muons crossing eight strips at 185 cm away from the PMT are shown in Fig. 4.23(b) where the histograms are normalized to the less efficient PMT pixel (i.e. pixel 19 close to the center of the pixel matrix). The measured average amplitude of the muon pulses was 35 mV and the half time and total width were ∼6.5 and 40 ns, respectively.

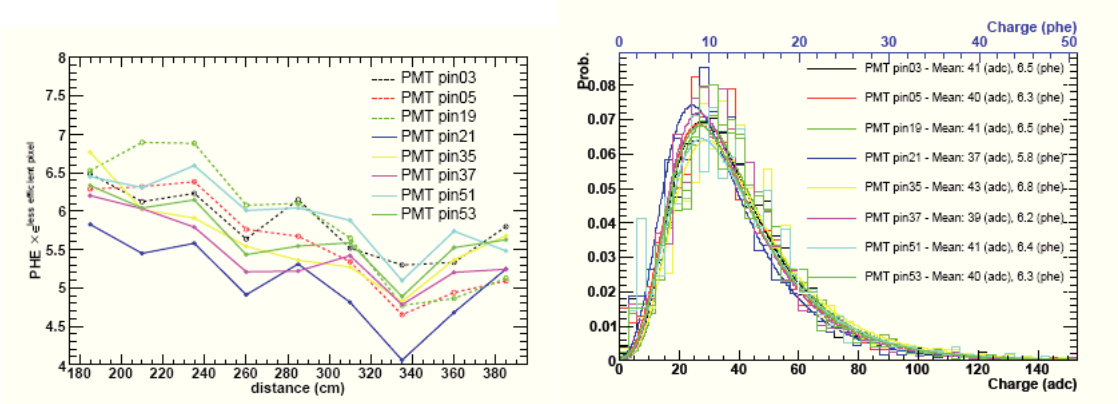

(a) (b)

Figure 4.23: 4.23(a): Mean values of the photo-electron spectra per strip. 4.23(b): Charge distribution spectra at 185cm from the PMT.

Finally each stage of the FE board has been tested with controlled square pulses of 50 mV height and ∼ 10 ns width, injected at a frequency of 1 kHz. The average pulse shapes at each stage (amplification and differentiation) are shown in Fig. 4.24(a) On the other hand the rates of all 64 channels were studied as a function of the FE discriminator threshold voltage. As an example,the output rates of 16 channels are shown in Fig. 4.24(b) where the corresponding offsets were taken into account.

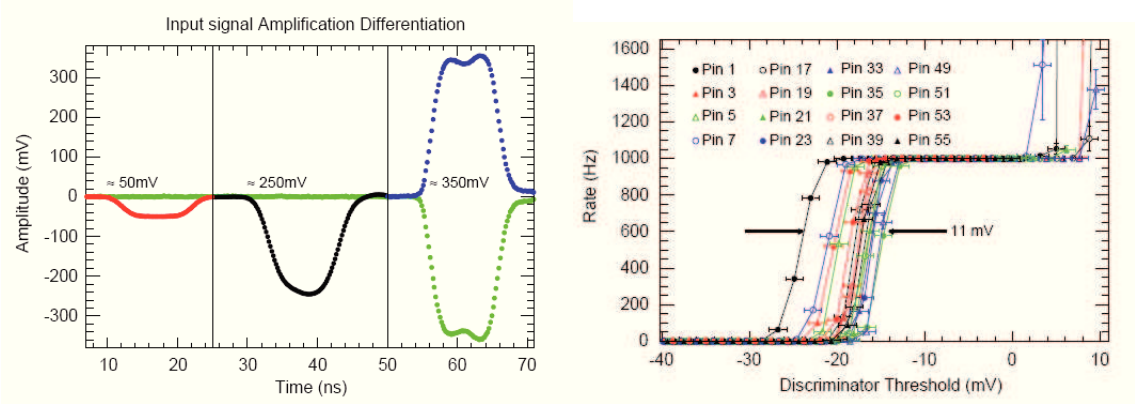

(a) (b)

Figure 4.24: Front-end characterization:4.24(a) the amplification and differentiation stages; 4.24(b): the FE rates of 16 different channels with controlled square pulses.

It should be noticed that the above rates were measured imposing a gain of one at the amplification stage. As it can be observed, there is a channel-to-channel difference of around 10 mV arising from the offset between the two comparator input terminals (indicated as IN+ and IN- in 4.17(a)), needed to obtain a TTL logic at the discriminator output [216].

4.2.6 BATATA & AMIGA soil study

The punch through as a function of depth is strongly correlated with the chemical composition of the soil in which the detector is buried. Therefore, it is extremely important to know how representative the soil above the BATATA planes is of the soil above the other muon counters of the AMIGA array that are located at several km of distance from the former. In order to be able to answer this basic question, a minerological, geochemical and grain size characterization of the whole AMIGA area and, particularly, of the BATATA site was performed. 24 sediment samples were studied, deposited in the alluvial plain of Cuenca Amarilla in Malargüe, considered as representative of the sediments of all the studied area, although slight changes in grain size are expected. Several tests were performed: density measurements, grain size analysis, grain shape characterization, major elements geochemistry by X-ray fluorescence, mineral composition by X-ray diffraction [217].
Chemically, the sand are very homogeneous upto a few meters of depth, showing high contents in silica (58.80 wt. % SiO_2), aluminum (15.39 wt. % Al_2O_3), iron (6.40 wt. % $Fe_2O_{3(T)}$) and calcium (5.82 wt. % CaO). The average composition of sand approaches the composition of granite.
The average measured density is 1.7 g/cm^3 for sands and 2.1 g/cm^3 for gravels. In water saturation conditions, the density rises up to 25 % in sandy sediments. The calculated effective porosity for the sand is ∼34 %, and about 25 % for gravels.
The average atomic number Z and weight A of the sediments, stoichiometrically deduced from the average major element composition, are 10.04 and 20.25 respectively.

Chapter 5

Simulation studies with the BATATA device

The aim of this work is to evaluate, through simulation, the performance of the BATATA muon detector. We performed an end-to-end simulation of such device with the aim of evaluating its muon-background discrimination capabilities. Although this constitutes its main goal, BATATA naturally offers also the possibility of measuring the arrival direction of muons, including those coming from low-energy showers ('background muons'). Such measurements are indeed interesting, not only for calibration or alignment studies, but also for anisotropy studies, i.e. searches of muon excesses in the sky, and comparison of angular distribution with those predicted by current hadronic models. For this additional goal, the knowledge of the angular reconstruction accuracy is a primary need.
The simulation framework is based on CORSIKA and Geant4. CORSIKA was used to perform a detailed simulation of the particle cascade development in the atmosphere up to the ground level. At this stage information about the shower particles (particle type, energy, momentum and number of secondary particles generated for a given energy threshold), the zenithal and azimuthal angle and the shower core position are available. In the following step, the shower particles have to be first resampled to take into account the thinning procedure applied in the shower simulation phase and then injected into a detector layout. These steps have been implemented in modules fully integrated in the official Auger $\overline{\text{Off}}\underline{\text{line}}$ tool used for event simulation and reconstruction. The tracking stage and interaction with the detector is done with the Geant4 Toolkit, which is encapsulated inside the main $\overline{\text{Off}}\underline{\text{line}}$ framework. Finally, the produced data, containing the hits in the detector, PMT traces, etc, have to be treated to reconstruct the physical information.

5.1 Simulation Framework

5.1.1 Shower Simulation with CORSIKA

Analyzing experimental data on Extensive Air Showers (EAS) or planning corresponding experiments requires a detailed theoretical modelling of the cascade which develops when a high energy primary particle enters the atmosphere. This can only be achieved by detailed Monte Carlo calculations taking into account all knowledge of high energy strong and electromagnetic interactions.
CORSIKA (COsmic Ray SImulations for KAscade) [218] is a detailed Monte Carlo program to study the evolution of EAS in the atmosphere initiated by photons, protons, nuclei, or any other

particle up to 10^{20} eV. The particle transport takes into account both the energy deposited on the atmosphere and particle decay. All secondary particles are tracked explicitely along their trajectories and their parameters are stored when reaching an observation level. This allows a detailed analysis of all features of simulated showers.
The most serious problem of EAS simulation programs is the extrapolation of hadronic interaction to higher energies and into rapidity ranges which are not covered by experimental data. Therefore one has to rely on extrapolations based on theoretical models. To study the systematics of such models, five different hadronic interaction models are available in CORSIKA to simulate the hadronic interactions at high energies: the VENUS [219], QGSJET [220], and DPMJET [221] models are based on the Gribov-Regge theory, while SIBYLL [222, 223] is a mini-jet model. The NEXUS model [224] extends far above a simple combination of QGSJET and VENUS routines. The most recent EPOS model [225] is based on the NEXUS framework but with important improvements concerning hard interactions and nuclear and high-density effect. HDPM [218] is inspired by findings of the Dual Parton Model [226] and tries to reproduce relevant kinematical distributions being measured at colliders.
Hadronic interactions at lower energies are described either by the GHEISHA [227] interaction routines, by a link to FLUKA [228], or by the microscopic URQMD model [229]. All decay channels with a branching ratio above 1% are taken into account.
For electromagnetic interactions a taylor made version of the shower program EGS4 [230] or the analytical NKG [55, 84] formulas may be used. It is also possible to explicitly simulate Cerenkov light on the atmosphere and to handle both electronic and muonic neutrinos and anti-neutrinos. This Monte Carlo simulation implies a 3D tracking of particles in an atmosphere with changing density and in the magnetic field of the Earth as well as a detailed implementation of particle decays and interactions over up to 14 orders of magnitude in energy. Since the number of shower particles grows proportionally to the energy, the number of particles that needs to be simulated increases by the same orders of magnitude as the energy. A standard method to drastically reduce the computation demands is particle "*thinning*" [231]. By this technique not each individual particle is tracked any more: all particles with energy E below an adjustable fraction of the primary energy E_0 (called "thinning level" $\varepsilon_{th} = E/E_0$) which emerge from an interaction are exposed to the thinning algorithm. Only one of these particles is followed and an appropriate weight is given to it, while the other particles below the thinning level are dropped. At extreme particle densities (several 1000-10000 per m^2), it is very efficient to track only few high weighted particles instead of all the individual particles. A thinning algorithms provides a reliable important sampling, keeping the few relevant particles and removing the very abundant particles that are predicted not to give an important contribution to the total extensive air shower. By using a typical weight limitation of 100-10000 the computation demands are reduced almost correspondingly. Unfortunately thinning does remove relevant information from the shower, leading to artificial fluctuations. An improvement to reduce undesired statistical fluctuations of particle densities far from the shower core uses a limitation of the weights [232]. Particles emerging from an interaction which would exceed a specified weight limit are excluded from the thinning algorithm. Different weight limits can be assigned to electromagnetic and hadronic (including muonic) particles. Also the reverse procedure of thinning, usually called "*un-thinning*", needed for subsequent detector simulation is a delicate process with its limitations. In conclusion, it should be mentioned that thinning is always a compromise between computation speed and simulation quality.
Another strategy, needed to save space on disks, reduces the number of particles close to the shower core where anyway the detectors would saturate. Particles arriving at the detector level

within a selected core distance r_{max} are selected randomly with a probability $\propto r/r_{max}$ and, when surviving, their weight factor is multiplied with the inverse of this probability, irrespective of exceeding the weight limit.

5.1.2 The GEANT4 Toolkit

Geant4 [233] is the acronym of GEometry ANd Tracking and it is a Monte Carlo tool kit based on C++ language which simulates the passage of particles through matter. Geant4 is specially designed to simulate the detector response, geometry, run event, track management, visualization and user interface.
According to the user needs, the Geant4 Toolkit allows the simulation of complex detectors composed by an arbitrary number of smaller components which can act as independent detectors. This components may have different shapes, sizes or materials with different particle production thresholds. The geometry module provides a large variety of solid volumes and the capacity of performing boolean operations on the existing solids to create new ones. The volumes can be rotated, translated or replicated along symmetry axis. The solids may be made of several materials on which several properties or particle production thresholds may be defined. If a solid is defined as a sensitive detector it is possible to take snapshots of the particles as they cross through it and record the information of each particle such as it's energy, momentum, position, etc.
With the Geant4 Toolkit it is also possible to simulate a wide variety of physical processes in order to provide a more realistic description of the particle interaction in the detector for a large range of energies. When applicable, the particle decay can be considered. In this case, the resulting secondary particles obey to the several branching ratios of the primary particle. A large variety of decays are considered, from the simplest case of a two-body decay to a multiple-body decay. Secondary particles may also be generated by the interaction of the primary particle with the surrounding medium. Here the processes of bremsstrahlung, Compton, ionization or the photoelectric effect may be accounted. The energy threshold for a particle to generate secondaries can be lowered in order to increase the simulation precision or increased to prevent some or all secondary particles to be generated. If the production of secondary particles is suppressed by the user, the simulated particles will only propagate through the medium or detector and undergo some scattering through the interactions with the material or, for instance, by the interaction with an external electromagnetic field. Several hadronic processes accounting with different models can also be implemented. It is possible to simulate the propagation of a wide variety of fundamental particles and register their track along the detector as well as it's physical processes and interactions for a wide range of energies. According to the passage of the particles of interest through the detector, the user may choose among a pure model of electromagnetic interactions or a pure model of hadronic interactions or even look at a model which contemplates both kinds of interactions.
Finally, Geant4 provides a graphical user interface which allows the user to access an interactive visualization and check the detector's geometry or the particle's tracks and interactions as it propagates on the detector.

5.1.3 The $\overline{\text{Off}}\underline{\text{line}}$ Framework

Most of the offline activities within the Pierre Auger Observatory are performed using the Auger $\overline{\text{Off}}\underline{\text{line}}$ Framework, developed by the Auger collaboration members and described in details in [234]. This tool is responsible for the simulation and reconstruction of events using surface,

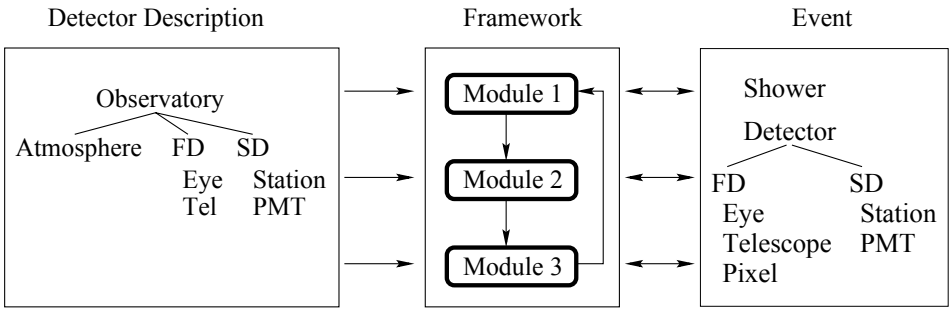

Figure 5.1: Simulation and reconstruction tasks are broken down into modules. Each module is able to read information from the detector description and/or the event, process the information, and write the results back into the event. Communication between modules occurs only through the event.

fluorescence and hybrid methods, as well as simulation of calibration techniques and other tasks such as data preprocessing.
It has been written entirely in C++ trying to satisfy these needs:

- handling several data formats (generally ROOT, ascii and binary format), from the simulated showers produced by different air shower simulation codes (CORSIKA, AIRES, CONEX, SENECA) to the real and simulated data produced by the Auger detectors (CDAS, FDAS, OFFLINE, IOAUGER);

- accessing to information on the detector configuration and performance as a function of time, including data stored in MySQL databases;

- possibility for the user to develop his own physical algorithms.

The main working scheme of the $\overline{\text{Off}}\underline{\text{line}}$ framework is shown in Fig. 5.1. It consists of three principal parts:

- a series of *modules* (C++ classes), responsible for the simulation and reconstruction tasks, which can be assembled and sequenced through instructions provided in a XML file. Each of these modules is able to read information from the detector description and/or the event;

- an *event* structure through which modules can relay data to one another and which accumulates all simulation and reconstruction information. It contains all raw, calibrated, reconstructed and Monte Carlo data. A series of utilities supports the multi-format reading and writing;

- a *detector* structure describing the configuration and performance of the observatory as well as atmospheric conditions as a function of time.

The simulation of events observed by the Auger detectors typically involves the creation of a shower using a Monte Carlo generator (CORSIKA, AIRES, CONEX and SENECA are supported), the simulation of the response and triggering of the surface tanks hit by the particles arriving at ground level, and the simulation of the response and triggering of the fluorescence telescopes hit by the light emitted along the shower track. Finally, event building and export to various formats can be performed.
Detector simulations can be broken down into a sequence of steps, each of which is generally encapsulated within a separate module. All these steps are executed sequentially as listed in a

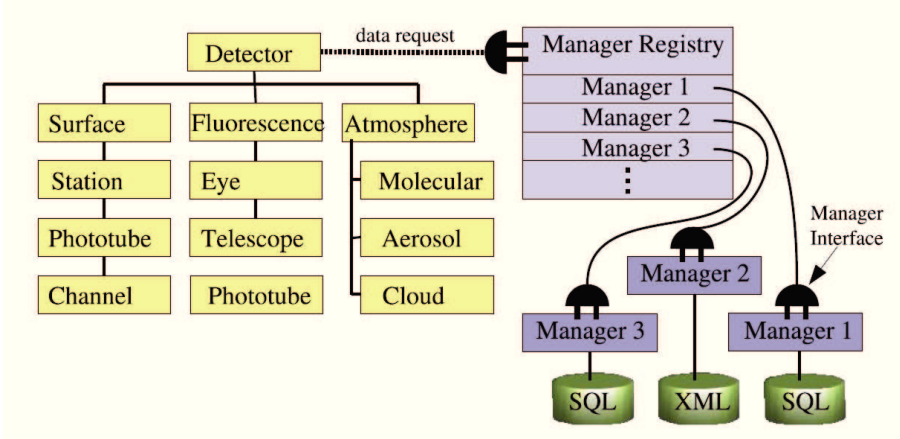

Figure 5.2: Schematic design of the Offline detector interface.

so-called *Module Sequence*. Run-time control over the module sequence is afforded through a run controller which invokes the various processing steps within the modules according to a set of externally provided instructions.
The detector interface is organized following the natural hierarchy of the Auger detectors, as depicted in Fig. 5.2. It allows to retrieve information about the detector configuration and performance at a particular time. These data are typically stored in XML files [235] for static detector information, and in MySQL databases [236] for time-varying info, such as monitoring and calibration data. The data queries are passed by this interface to a registry of so-called *managers*, each of which is capable of extracting a particular sort of information from a particular data source.
The detector interface is also equipped to support a set of plug-in functions, called *models*, which can be used for additional processing of data retrieved through the detector. These are used primarily to interpret atmospheric monitoring data.
The Offline is provided with a collection of utilities (some of them are external tools, others are developed inside the Auger collaboration), including a XERCES-based XML parser [237], an error logger, various mathematics and physics services, testing utilities, a geometry package and a set of foundation classes to represent objects such as signal traces, tabulated functions and particles.

5.2 A module to simulate the Batata detector

We developed an Offline module (implemented in the C++ class *G4BatataSimulatorSCG*) to track particles in the Malargüe soil and simulate their interaction with the Batata detector[1]. The implementation scheme strictly follows what is currently used for the GEANT4 simulation of the surface detector tanks. The modules used for the resampling of the shower particles (*CachedShowerRegeneratorOG*) and for the injection of single particles (*ParticleInjectorOG*) were adapted as from the existing modules to the muon counter simulation needs.
The module sequence used to simulate and reconstruct events in the Batata detector is shown in Fig. 5.3. The *EventFileReaderOG* module reads the profile and ground particle data of a previously generated shower from an EAS simulation program (CORSIKA in this case). The *EventGeneratorOG* module injects the generated shower in the Auger detector, assigning an

[1] A stand-alone version of the tool, entirely based on GEANT4, is also available.

```
<!-- A sequence for a Muon Counter simulation -->

<sequenceFile>
  <enableTiming/>
  <moduleControl>

    <loop numTimes="1" pushEventToStack="yes">

      <module> EventFileReaderOG         </module>

      <loop numTimes="1" pushEventToStack="yes">

        <module> EventGeneratorOG          </module>

        <loop numTimes="unbounded" pushEventToStack="no">
          <module> ShowerRegenerator </module>
          <!-- <module> G4MuonCounterParticleInjector </module> -->
          <module> G4BatataSimulatorSCG  </module>
        </loop>

        <module> G4BatataReconstructorSCG  </module>

        <module> EventFileRecorder  </module>

      </loop>
    </loop>

  </moduleControl>

</sequenceFile>
```

Figure 5.3: Module sequence used for BATATA event simulation and reconstruction in the Offline framework.

event time and a core location. Several possibilities are left to the user for the choice of the event core, that can be assigned close to a particular tank, distributed over all the array size, in the eye/telescope field of view (suited for FD and hybrid simulations). This module sets also the event data structure to be used in the simulation (SD, FD or hybrid structure). The *ShowerRegenerator* module performs the shower unthinning. A statistical procedure is applied (see [238]) to resample particles over a specified detector area. Shower particles outside these areas are not simulated. In the case of surface detector tanks the resampling is applied over all surfaces (top and lateral), while in this case the considered area is the Batata detector plane size (2×2 m^2) at ground level. The module *G4BatataSimulatorSCG* is responsible for the particle simulation in the detector and will be described with more details in the next section. The *G4BatataReconstructorSCG* module accesses to the simulation output produced by the first module and performs the reconstruction of the simulated event (event identification, muon tracking, ...). The algorithm used for track reconstruction will be detailed in Section 5.5.
Eventually the *ParticleInjector* module is a service module that can be used to inject single particles in Batata, i.e. for debug or parametrizing or fast simulation studies. The *EventFileRecorder* is used at the end of the sequence chain to store simulation and reconstruction info to file.

5.2.1 *G4BatataSimulatorSCG* module

This module is implemented in a series of C++ classes responsible to build the detector geometry (material properties and shapes), define the relevant physical processes, track shower particles underground, create hits in the detectors, simulate the PMT response and the event digitization.

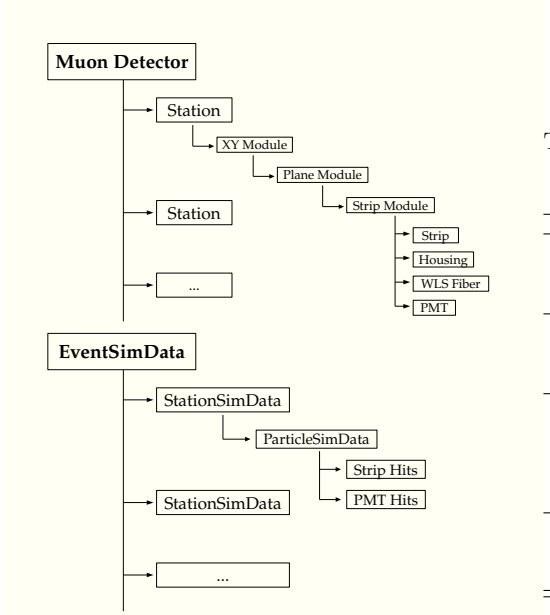

Figure 5.4: Scheme of detector and event structure organization in the simulation module.

Table 5.1: Detector parameters adopted in the simulation.

BATATA	
Plane	n^{xy}_{plane}= 3, n_{strip}= 49 Size(cm): 200×200×6, Depth(m): (0.5,0.8,2.8)
Casing	Thickness(cm): 3 PVC
Scintillator	Size (cm): 200×4×1, ρ_{scint}(g/cm^3): 1.05 PS+PPO(1%)+POPOP(0.03%)
Coating	Thickness (mm): 0.25, ρ_{coat}(g/cm^3): 1.046 PS+TiO_2
BC92 Fiber	Radius(mm): 1.5 PMMA+Polyethylene+Fluor. polymer $\rho_{core,clad1,clad2}$(g/cm^3): (1.19,1.20,1.43) $n_{core,clad1,clad2}$: (1.60,1.49,1.42)
Groove	Size(cm): 200×0.17×0.17, ρ_{glue}(g/cm^3): 1.19 Epoxy TEK glue
Soil	ρ_{soil}(g/cm^3): 1.8 SiO_2(63.3%)+Al_2O_3(15.4%)+Fe_2O_3(6.4%) CaO(5.8%)+Na_2O(3.7%)+MgO(2.3%)+K_2O(2.0%) TiO_2(0.8%)+P_2O_5(0.1%)+MnO(0.1%)

Detector Geometry

The detector geometry is organized in hierarchical layers as shown in Fig. 5.4.
The inner element is the strip module, hosting the scintillator strip, surrounded by a reflective coating layer. A groove is machined along the strip surface to accomodate the double-clad WLS fiber. The scintillating strips, put side-to-side, form a detector plane module. Two detector planes, rotated by 90° one with respect to the other, are joined to form a X-Y superplane module. Three of these modules are buried underground at given depths from the surface (in this work we assumed 50, 80, 280 cm) forming a muon counter station. The station is replicated over the array according to the same layout of the AMIGA muon counters. This is done both to speed-up simulations, i.e. by using the same simulated shower in different position at ground in the same run without re-doing the particle reading and resampling, and also to study the final results as a function of the distance from the core, in particular sampling at the same positions where the AMIGA counters are planned to be placed.
The soil was modelled according to the measured characteristics reported in [217] and discussed in Section 4.2.6.
The adopted detector geometry settings (sizes, material bulk properties, ...) are summarized in Table 5.1. Eventually these can be customized in a straightforward way.

Physics Processes

All relevant physical processes (electromagnetic and hadronic) are defined for each particle and can be included in the simulation. The optical processes, such as scintillation light generation, Cherenkov emission, bulk absorption, Rayleigh scattering, boundary processes (reflection, refraction, absorption), WLS emission, can be included as well or eventually switched-off to speed-up the simulation.
Indeed, including the optical processes in the simulation results to be extremely cpu-consuming,

particularly the WLS emission. For instance, $\sim 1.2 \times 10^5$ scintillation photons are produced per MeV of deposited energy in each hit strip, each suffering many reflections before reaching the photocathode or being absorbed in the detector medium. If we consider the expected particle densities from air showers we realize that the full simulation approach is unfeasible. Moreover, a number of relevant parameters needed to perform a full simulation, such as the light absorption coefficients in the scintillator and in the fiber or the optical coupling effects, are poorly known. For this reasons, using a parametrization of the photoelectron yield as a function of the energy deposition in the strip and eventually distance from the PMT would be more feasible. For our studies we decided to switch-off the optical processes in all performed simulations. The PMT response may be anyway calculated afterwards in a fast way as discussed below.

Detector Hits

Particles depositing energy in the strips generate hits and, if optical processes are included in the simulation, the production of scintillation and Cherenkov photons, eventually create WLS photons in the fiber medium. Hits are created also in the photomultiplier when the generated photons reach the photocathode. A number of useful information can be stored for each kind of hit, such as track info (type, energy deposition, vertex, time, ...), number of photons produced per process and reaching the photocathode, etc.
The scheme used to store the relevant info produced in the simulation is shown in Fig. 5.4 : a top-layer structure contains the data at the event level, such as shower generated info and the collection with simulated data for all triggered stations. Each station data structure contains the data collection for the injected particles as well as geometrical information. At the bottom-layer, the particle data structure keeps the collection of all hits produced in the scintillators or in the PMTs by that particle, plus other useful information (collection of track points, number of particles reaching each detector planes, strip multiplicity, ...).
A minimum energy deposit threshold of 300 keV was considered for strip triggering and hit production. When a strip is above threshold a gate of 2 μs width is opened to collect the hit information from all strips, sampled with a t_{sampl}=10 ns width [239]. Moreover to reproduce somehow the effect of the pile-up in the strips, we considered a veto time interval of t_{veto}= 20 ns, preventing a triggered strip to trigger again within t_{veto}. We anyway kept stored the full hit information to eventually re-process the simulated data, for instance using different threshold/veto conditions.

PMT response

When the PMT has hits, a signal at the anode can be fully simulated in the following way, already discussed in [210, 240]. A number n_{pe} of photoelectrons is generated at the PMT cathode according to the specified quantum efficiency with timings t_i^{cath} corresponding at the arrival time of photons on the cathode surface. The pulse at the anode $V(t)$ is given by the superposition of all single photoelectron pulses (SPEs) $V_{spe}(t_i)$:

$$V(t) = \sum_{i=1}^{n_{pe}} V_{spe}(t_i) \tag{5.1}$$

where t_i is the photoelectron time at the anode. This can be obtained by summing the arrival time at the cathode t_i^{cath} and the transit time $t_i^{transit}$ in the dynode chain. The latter is of the order of few ns and assumed to fluctuate according to the specified PMT transit time spread.

When the optical processes are switched-off, n_{pe} and timings t_i^{cath} are not directly available and need to be calculated from a parametrization and tuned with laboratory data. The number of photoelectrons n_{pe} can be expressed as:

$$n_{pe} = k \times A \times E_{dep} \tag{5.2}$$

where k is a calibration factor, A is the double-exponential function describing the attenuation of the signal in the WLS fiber[2] and E_{dep} is the strip deposited energy in MeV, directly accessible in fast simulations.
The timings can be calculated by summing the delay times t_i^{delay}, due to scintillation and WLS emission, and the propagation times t_i^{prop}. As derived in [240], t_i^{delay} arises from the combination of two poissonian processes and therefore can be generated according to $(e^{-t/t_s} - e^{-t/t_f})/(t_s - t_f)$, with t_s and t_f decay times in the scintillator and fiber respectively. These are determined from data-simulation tuning, yielding t_s=1 ns and t_f=6.5 ns. The propagation times can be determined assuming a meridional approximation inside the fiber $t_{prop} = x \times n_{core}/(c \times \cos\phi)$, with the emission angle ϕ uniformly distributed.
The single photoelectron signal has been measured and reported in [210] and can be parametrized assuming the PMT internal circuit is a $C_1R_1 - (R_2C^2)^\alpha$ network, i.e. a single high-pass filter (a differentiator with time constant $\tau_1 = C_1R_1$) followed by α low-pass filters (integrators with $\tau_2 = C_2R_2$). Assuming all filters with the same time constant $\tau = \tau_1 = \tau_2$ the single photoelectron voltage is given by:

$$V_{spe}(t) = \frac{QR}{\tau\Gamma(1+\alpha)} \left(\frac{t}{\tau}\right)^\alpha e^{-t/\tau} \tag{5.3}$$

where Q is the characteristic single photo-electron charge and R is the circuit load resistance.

5.3 Simulated data samples

We produced two sets of simulated data. The first data set, denoted as 'single-particle sample', consists of a large sample of particles at ground (e, μ, γ, p, n) injected in a given station using the *ParticleInjector* module with fixed energies in the range (0.001-100) GeV and fixed zenith angles in the range 0-60 degrees. These were tracked underground until eventually reaching the muon counter detector. This data set is essentially used to understand the main event footprints produced in the detector by different kind of particles, as well as candidate observables for the muon-background discrimination.
Then, to evaluate the muon-background identification and tracking capabilities of Batata, we have to consider particles from simulated air showers. For this study we used a set of Corsika protons showers (QgsjetII hadronic model) generated with a flat energy spectrum in the range 10^{16}-10^{20} eV, then resampled to a E^{-3} spectrum, and a zenith distribution $\propto \sin\theta\cos\theta$ in the range 0°-60°.
As discussed before, the muon counter device was replicated and buried over the array to form the same layout of the Amiga infill. Shower particles were resampled in a sampling area at ground having size equal to that of the detector plane (2×2 m^2) and then tracked underground to the detectors. The shower cores were distributed randomly around a fixed station at the infill center. This data set is denoted as 'EAS sample'.

[2]The attenuation constants λ_1= 40 cm, λ_2= 6.0 m have been determined when characterizing the WLS fibers with LED pulses.

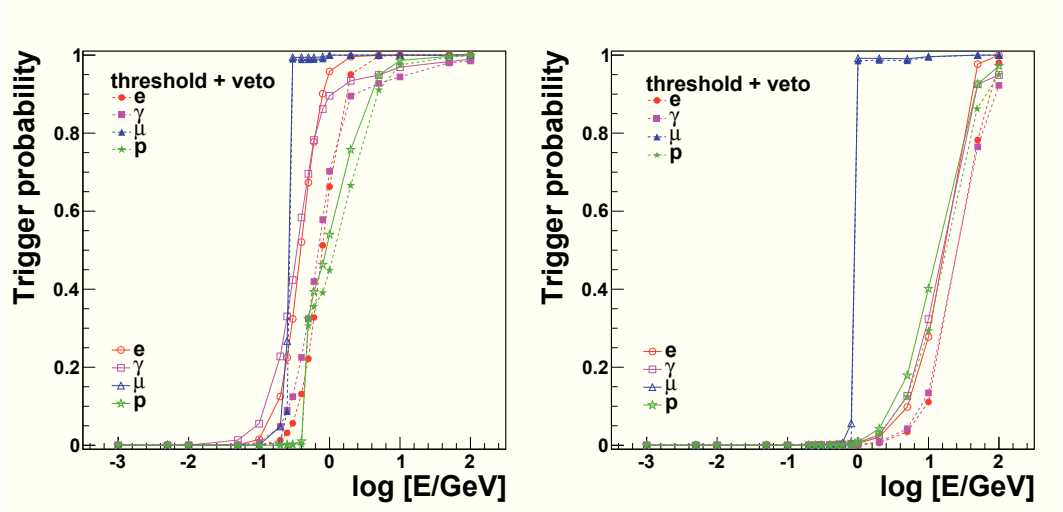

(a) 2-fold (b) 3-fold

Figure 5.5: 2-Fold and 3-Fold trigger probabilities as a function of energy for different particles ($\mu^{\pm}$,$e^{\pm}$, γ, p) when applying a strip energy threshold of 300 keV and a veto of 20 ns (filled dots, dashed lines) and without these conditions (empty dots, solid lines).

To speed-up the simulation, and reduce the number of tracked particles that would not anyway reach the detectors, we increased the energy threshold used in the resampling with respect to the chosen settings currently adopted for the tank simulation. In particular an energy threshold of 50 MeV was set for electrons and gammas, while leaving unchanged the threshold for muons, hadrons and mesons (10 MeV). Infact, at 50 MeV the calculated probability to get electromagnetic particles triggering at least two planes is almost zero (see for instance Fig. 5.5).
Furthermore, to avoid tracking a huge number of particles when the core falls very close to a station, we introduced a safe inner cut in the station-core distance of 100 m above 10^{17} eV and 50 m below, excluding in this way the closest station from saturation.
Eventually the energy and angular distributions in the shower sample from each particle type may be extracted and given to the *ParticleInjector* module to produce realistic simulated sample in a faster way.

5.3.1 Single-particle data sample

We report in Fig. 5.6 a sample vertical electron, muon and proton track of energy 1 GeV, from left to right panels respectively, seen from the detector side (upper panels) and top (lower panels) view. The hit strips are indicated in red. The different propagation behavior in the soil can be appreciated: while muons propagate ballistically with little angular deviation, electrons, gammas and protons develop underground sub-showers. Although most of the energy of these sub-showers is concentrated within the Moliere radius (which is ∼5 cm in our case), it is expected that the signatures left by impinging γ or $e^{\pm}$ are broader than the corresponding muonic signatures. However, the exact features will depend on the initial energy of the particles hitting the ground and the depth of the considered detector plane. Since the mean energy of muons at ground, for cosmic primaries of PeV energies is a few GeV, they are expected to cross the three scintillator planes triggering one strip per layer. Therefore, their signature will be an xy-cross of triggered strips per plane. On the other hand, γ, $e^{\pm}$ and protons are much less penetrating and are likely to trigger more than one adjacent strips per layer. Moreover unlikely they will reach the third

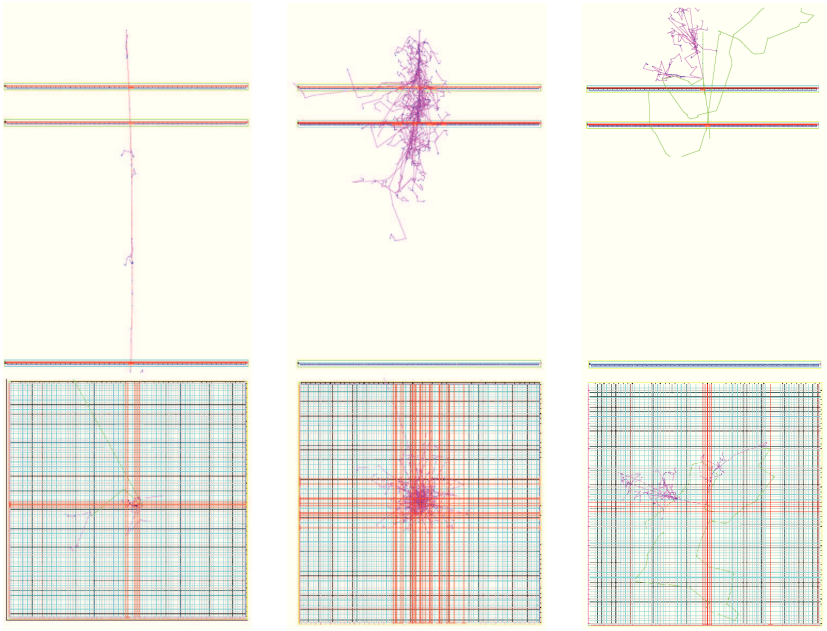

(a) μ^- track side and top view

(b) e^- track side and top view

(c) p track side and top view

Figure 5.6: A sample tracked vertical muon, electron and proton of energy 1 GeV (respectively from left to right) seen from the detector side (up panel) and top (low panel) view.

plane.
In Fig. 5.7 and 5.8 we report the distributions of energy deposited by electrons, gammas, muons and protons in the three X planes of energy 1 GeV and 10 GeV and zenith angle of 0°, 30°. Similar results are observed for the Y planes. As expected, the average energy deposit for muon has a peaked distribution around $\sim$ 1.5-2.0 MeV, no matter what detector plane and primary energy we consider. On the contrary, the other particles manage to reach only the first two planes and the observed energy deposit distribution is broader. Obviously, the larger the traversed track length, the larger the energy deposit.
The strip multiplicity corresponding to the same conditions of Figs. 5.7, 5.8 is reported in Fig. 5.9, 5.10. The muons multiplicities is around 1-2 for all planes. Significantly larger multiplicities are instead expected on average for the other particles on the basis of their different propagation, as discussed above. Moreover, due to the produced electromagnetic cascades it is expected that on average the hit strips are found to be not adjacent one to the other as in the muon case.
In Fig. 5.5(a) and 5.5(b) we evaluated the detection probability for different particles (e, γ, μ, p) as a function of the generated energy by counting the simulated particles triggering at least one strip in each X- and Y-module. Fig. 5.5(a) corresponds to events triggering the first two XY-planes, denoted as '*2-fold*', while 5.5(b) to those triggering all XY-modules, denoted as '*3-fold*'. Filled dots and dashed lines refer to simulated data where we applied an energy deposit threshold in the strips of 300 keV and a veto of 20 ns, empty dots and solid lines to simulated data where we do not apply such conditions. As can be seen, muons reach full efficiency below 1 GeV with a very sharp trend as compared to other particles. At such energies the probability to get a three-fold event not due to muons is below 1%. As obvious, the strip threshold + veto conditions has the effect of moving the trigger probability towards higher energies. As discussed above, these computed probabilities result to be very useful to optimize the simulation procedure in the case of particles generated from real showers.

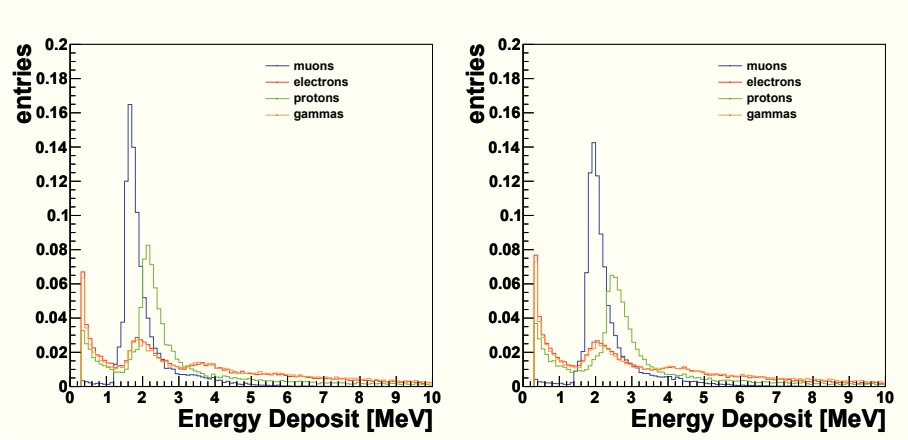

(a) plane 1X, θ=0° (b) plane 1X, θ=30°

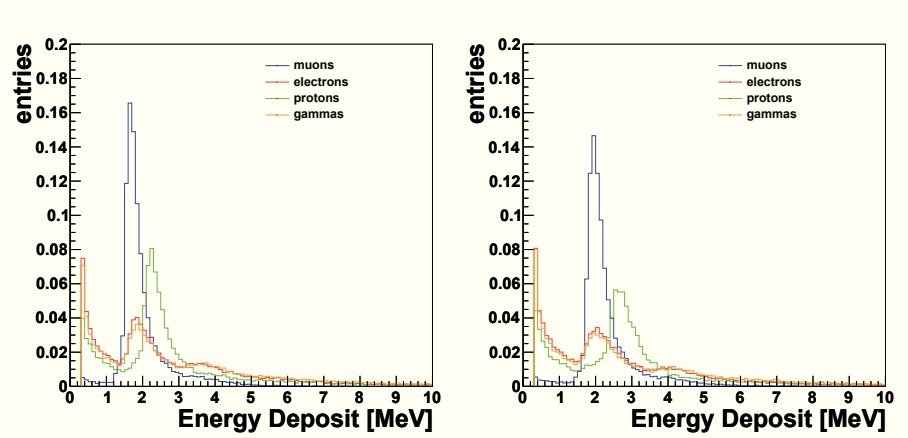

(c) plane 2X, θ=0° (d) plane 2X, θ=30°

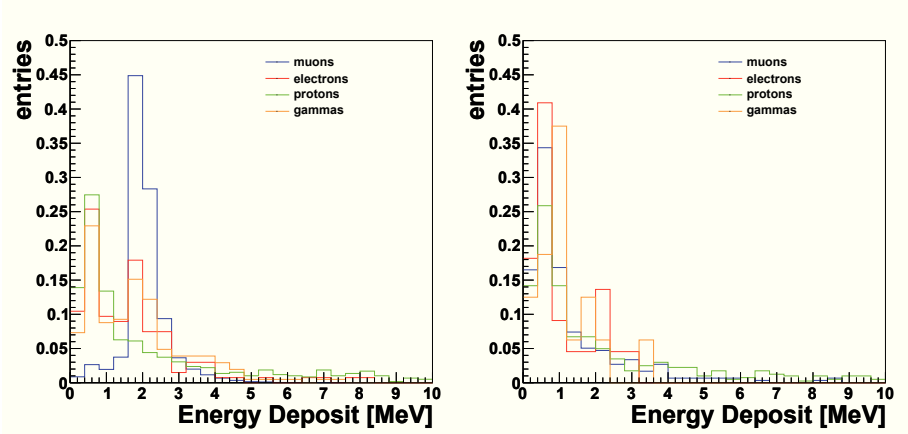

(e) plane 3X, θ=0° (f) plane 3X, θ=30°

Figure 5.7: Energy deposit distribution in strips for different particles of energy 1 GeV and zenith angle 0° (left panels), 30° (right panels) for the three detector planes X (from top to bottom).

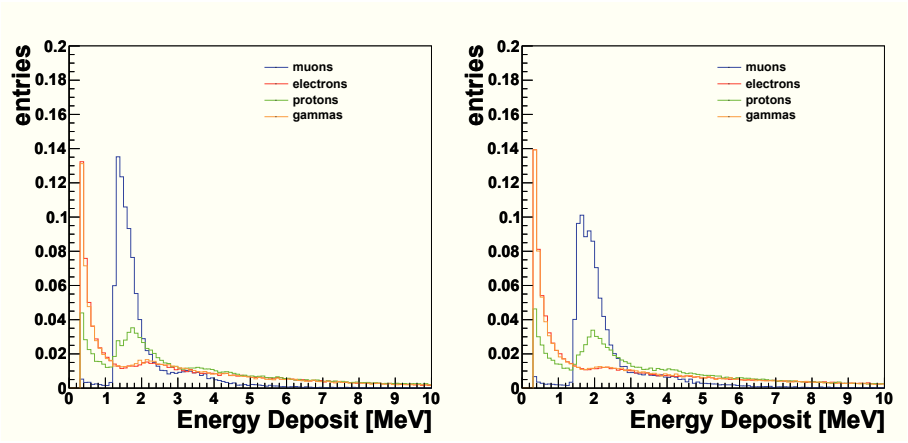

(a) plane 1X, θ=0° (b) plane 1X, θ=30°

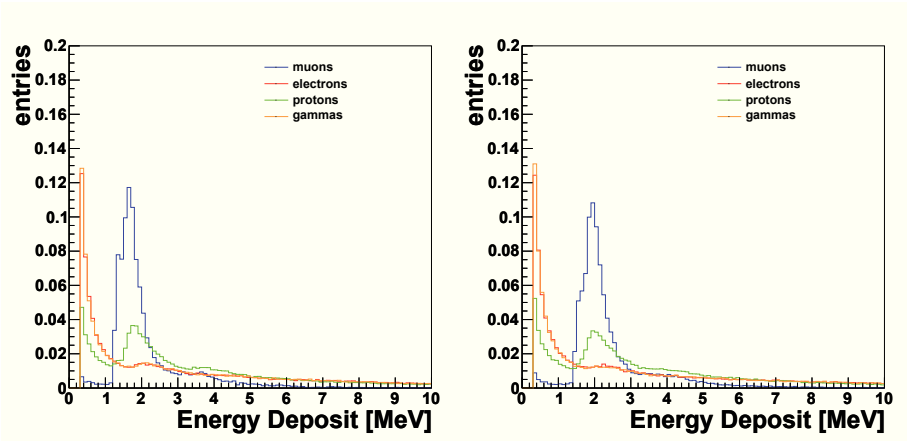

(c) plane 2X, θ=0° (d) plane 2X, θ=30°

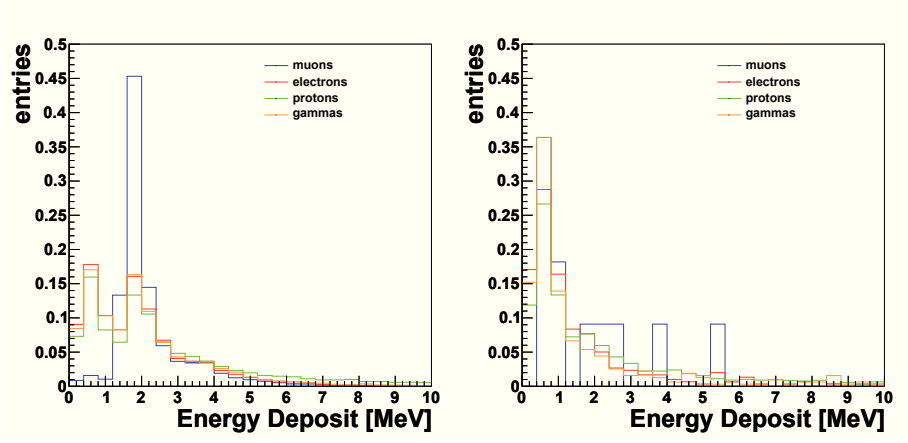

(e) plane 3X, θ=0° (f) plane 3X, θ=30°

Figure 5.8: Energy deposit distribution in strips for different particles of energy 10 GeV and zenith angle 0° (left panels), 30° (right panels) for the three detector planes X (from top to bottom).

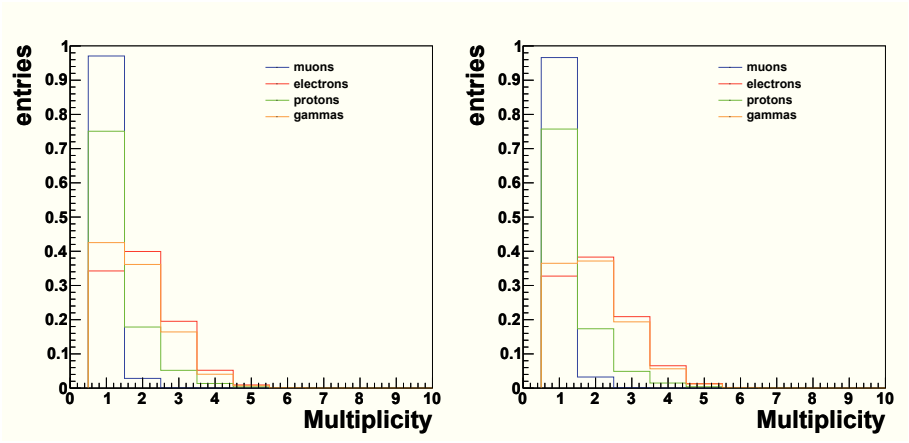

(a) plane 1X, θ=0° (b) plane 1X, θ=30°

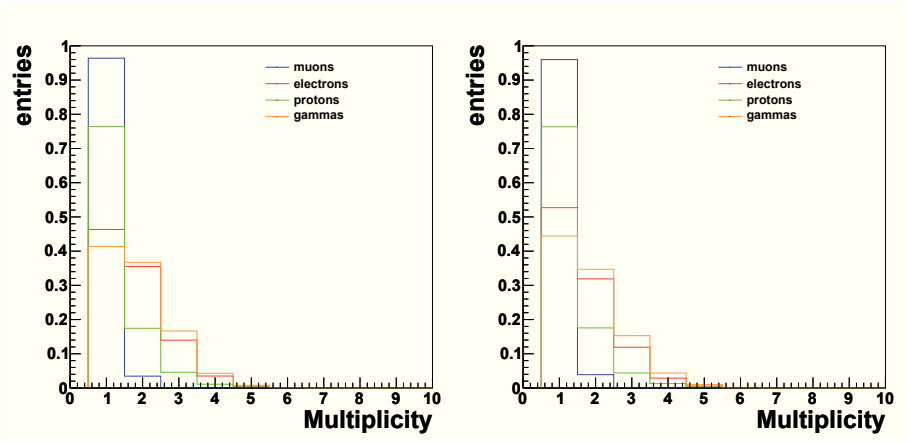

(c) plane 2X, θ=0° (d) plane 2X, θ=30°

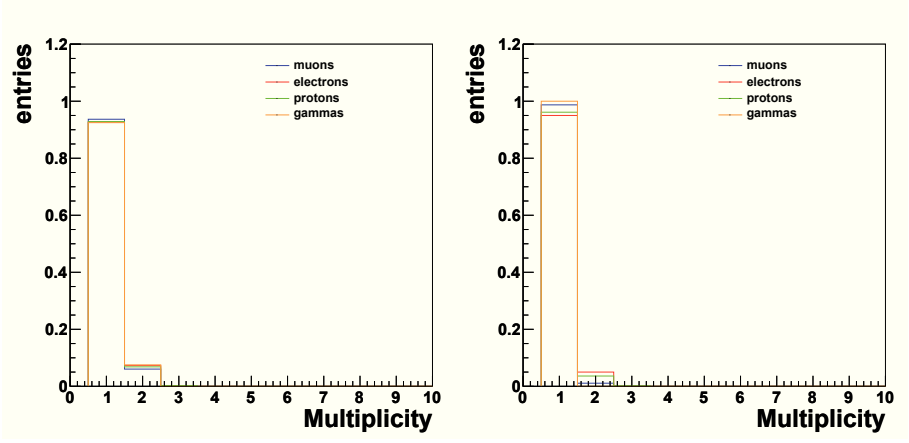

(e) plane 3X, θ=0° (f) plane 3X, θ=30°

Figure 5.9: Multiplicity of hit strips for different particles of energy 1 GeV and zenith angle 0° (left panels), 30° (right panels) for the three detector planes X (from top to bottom).

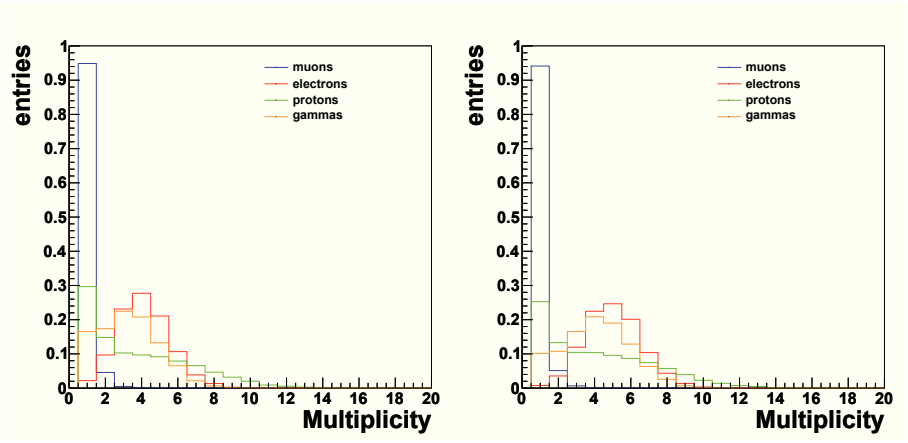

(a) plane 1X, θ=0° (b) plane 1X, θ=30°

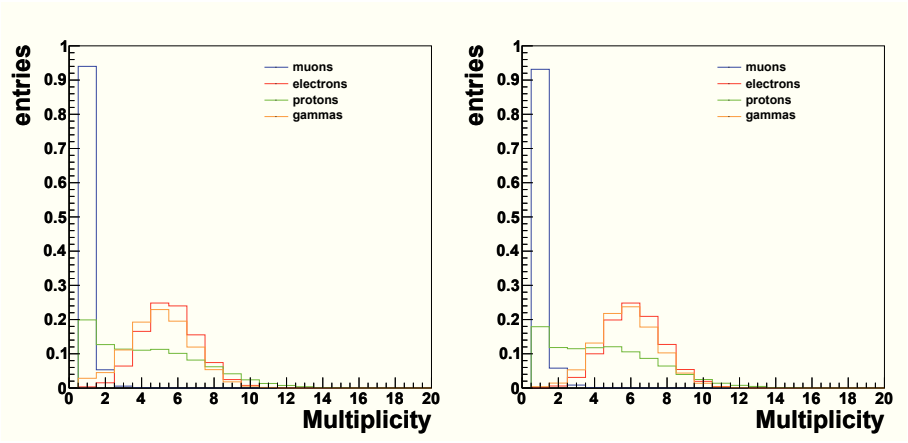

(c) plane 2X, θ=0° (d) plane 2X, θ=30°

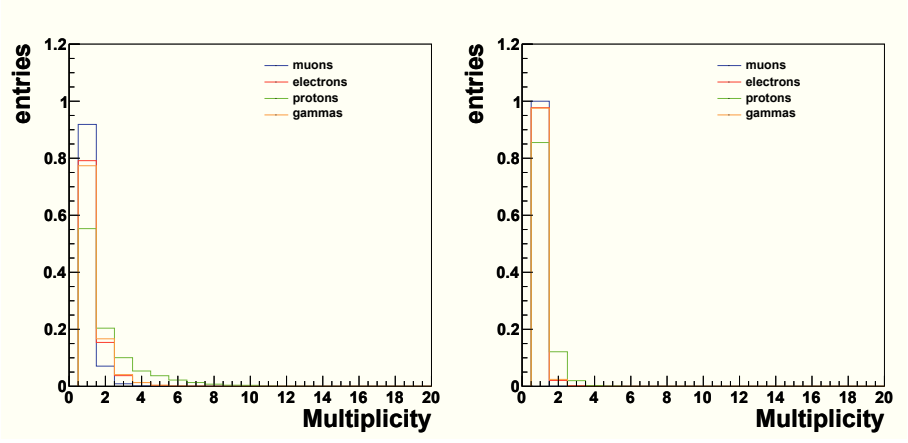

(e) plane 3X, θ=0° (f) plane 3X, θ=30°

Figure 5.10: Multiplicity of hit strips for different particles of energy 10 GeV and zenith angle 0° (left panels), 30° (right panels) for the three detector planes X (from top to bottom).

5.3.2 EAS data sample

An array view of a sample shower event of energy $10^{17.2}$ eV and zenith 9° is shown in Fig. 5.11. The core position is represented with a black star. Each numbered open dot represents a station position, while the filled coloured dots indicate the stations with injected particles, being the marker size proportional to the particle density.

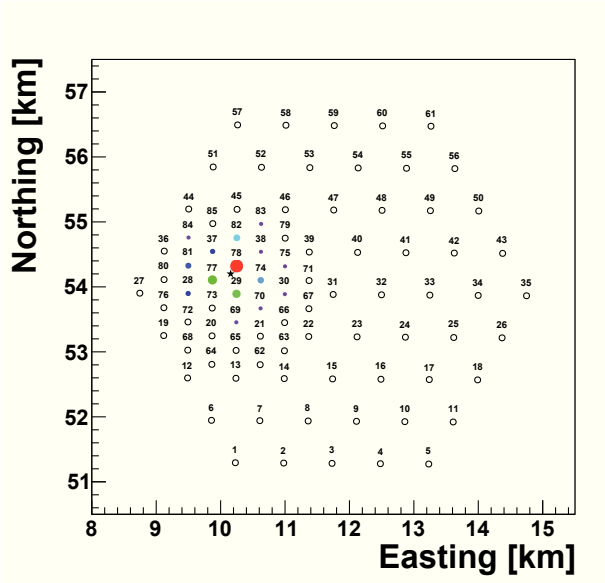

Figure 5.11: Array view of a sample shower event of energy $10^{17.2}$ eV and zenith 9°.

In Fig. 5.12 we report the distribution of energy deposit in strips for the three detector planes for muons and background particles. The minimum applied threshold of 300 keV is visible in the plots. Background particles deposit energy mainly in the first and second planes. The shape of their energy deposit distribution from 10 keV to 1 MeV is produced by particles that stop at the detector loosing their energy via ionization process. For high particle energies electromagnetic showers are produced in the soil and radiation losses play a dominant role. The peak observed at ~ 2 MeV mainly reflects the minimum ionization plateau of secondary particles coming out from the shower. This behavior can be seen also in Fig. 5.7, where the initial particle energy was set to 1 GeV. Muons, on the other hand, deposit almost the same amount of energy in the three planes.

To quantify the expected background contamination we report in Fig.5.13 the number of particles resampled and injected underground in the detector within the discriminator sampling time interval (10 ns) for two different distance from the core, $r = 100$ m for left panels and $r = 200$ m for right panels. We report the results obtained for two different shower energy $\log E$=17 (5.13(a),5.13(b)), and $\log E$=18 (5.13(c),(5.13(d)). As can be seen, when the core falls close to the station the expected background contamination in the first timing bins is around one order of magnitude larger than the muon component. Far from the core or after ~ 50 ns the expected signal and background are comparable.

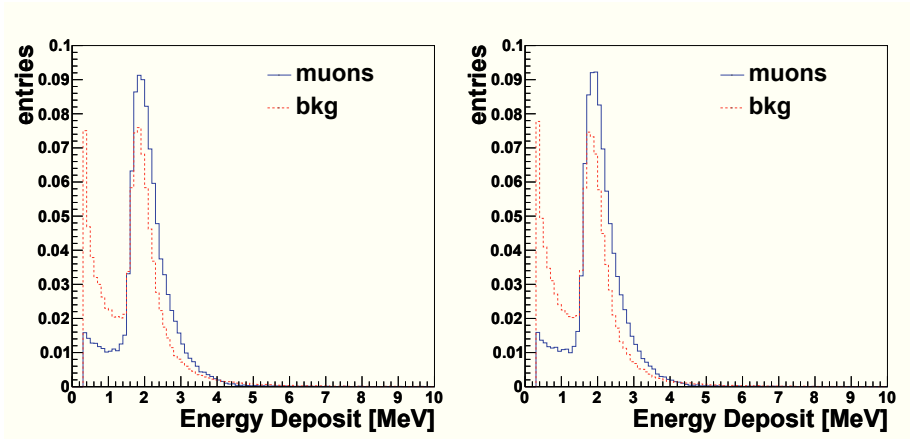

(a) plane 1X (b) plane 1Y

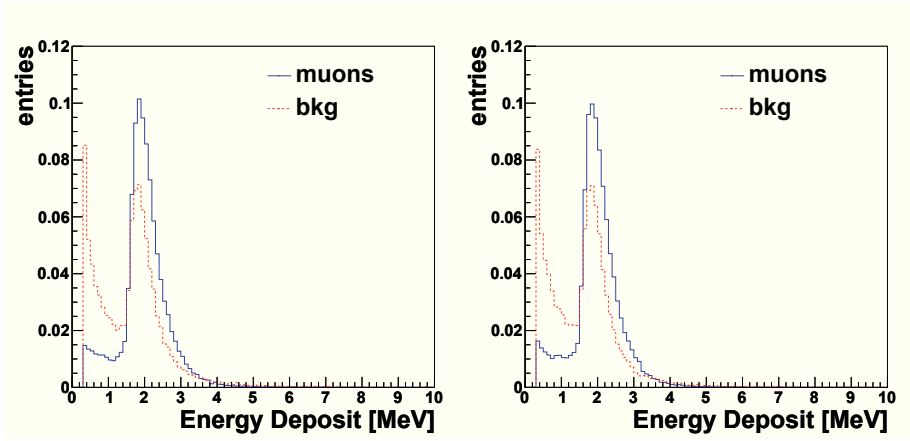

(c) plane 2X (d) plane 2Y

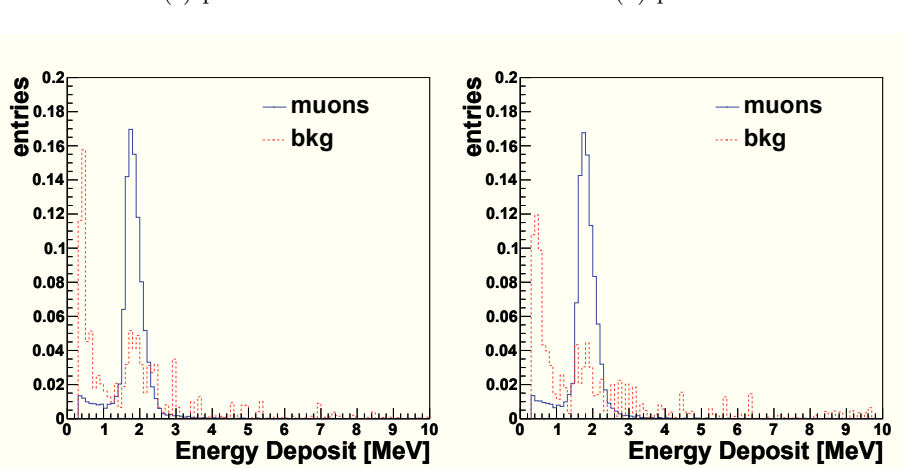

(e) plane 3X (f) plane 3Y

Figure 5.12: Distribution of energy deposit in strips of muons (solid lines) and background particles (dashed lines) from the shower data sample.

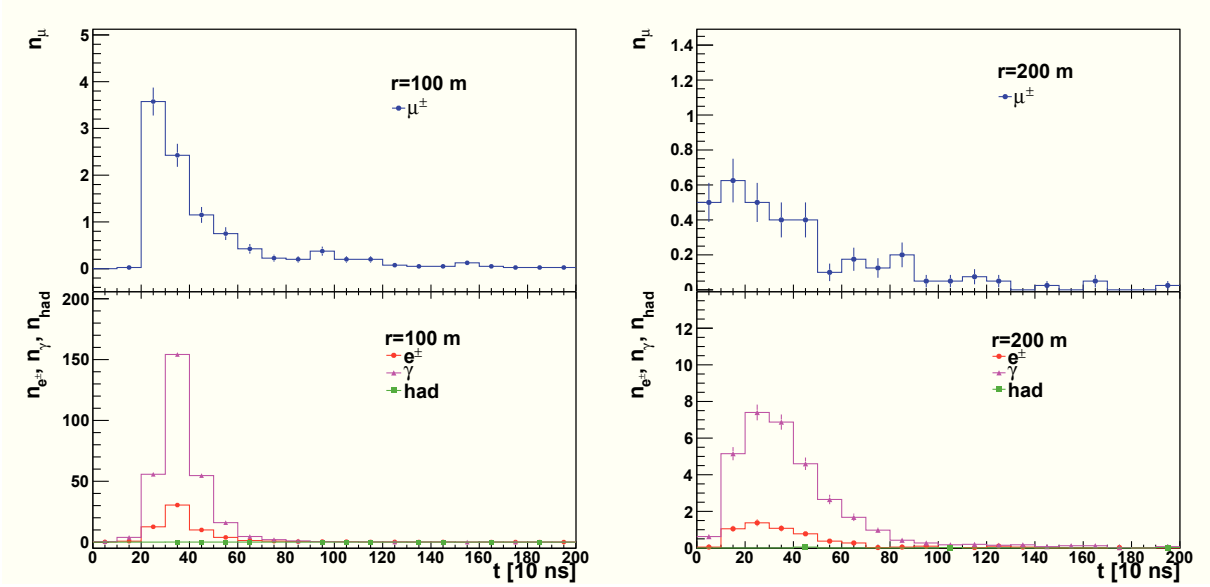

(a) $\log E$=17.0 (b) $\log E$=17.0

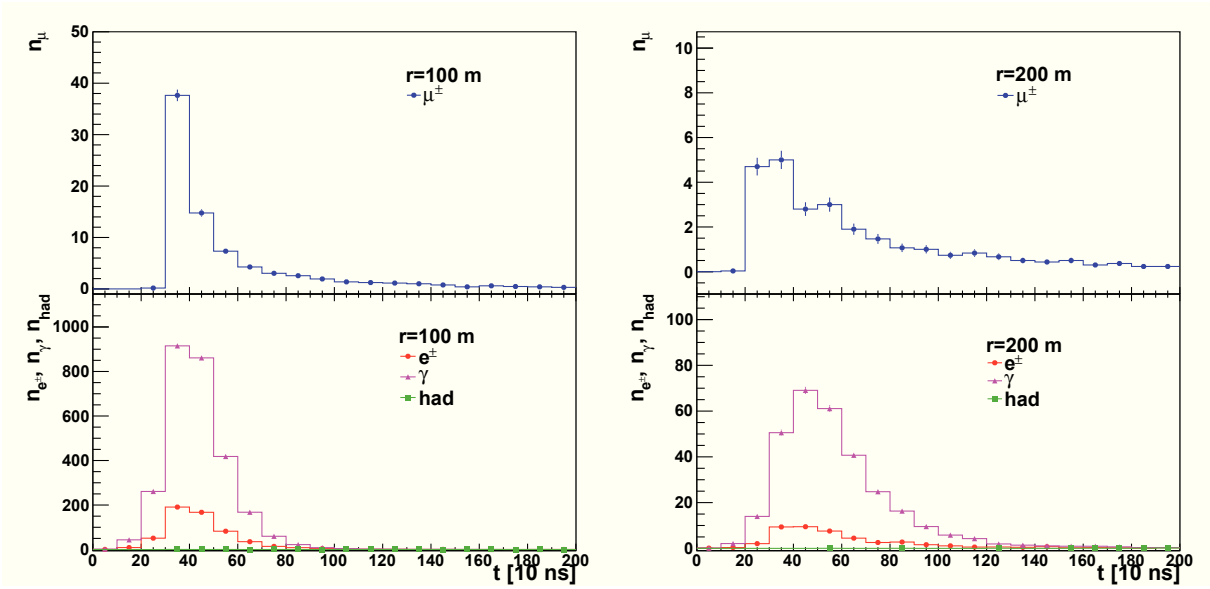

(c) $\log E$=18.0 (d) $\log E$=18.0

Figure 5.13: Number of particles resampled at ground level and injected in the detector in a time interval of 10 ns for two different detector-core distance. Top panel corresponds to $r = 100$ m while bottom panel to $r = 200$ m. We report the results obtained for two different shower energy ranges $\log E$=17 (5.13(a), 5.13(b)), $\log E$=18 (5.13(c), 5.13(d)).

Moreover to compare over all timing bins the expected number of muons with respect to the background, we report in Fig.5.14(a) the number of particles resampled at ground level and injected in the detector as a function of the distance r from the core for different shower energy ranges $\log E$=16-16.2 (green stars), $\log E$=17-17.2 (purple dots), $\log E$=18-18.2 (blue triangles), $\log E$=19-19.2 (red squares). Top panel corresponds to the number of muons while the bottom panel to the electromagnetic component. Fig. 5.14(b) is relative to the number of particles injected and triggering at least 2 detector planes. Due to the radius cut applied in the resampling no data are available below 100 m in the case of shower energies larger than 10^{17} eV and below 50 m in the range 10^{16}-10^{17} eV. We can note that although the number of background particles is larger respect to the muons number at ground, it reduces when we consider only the events that trigger at least 2 planes.

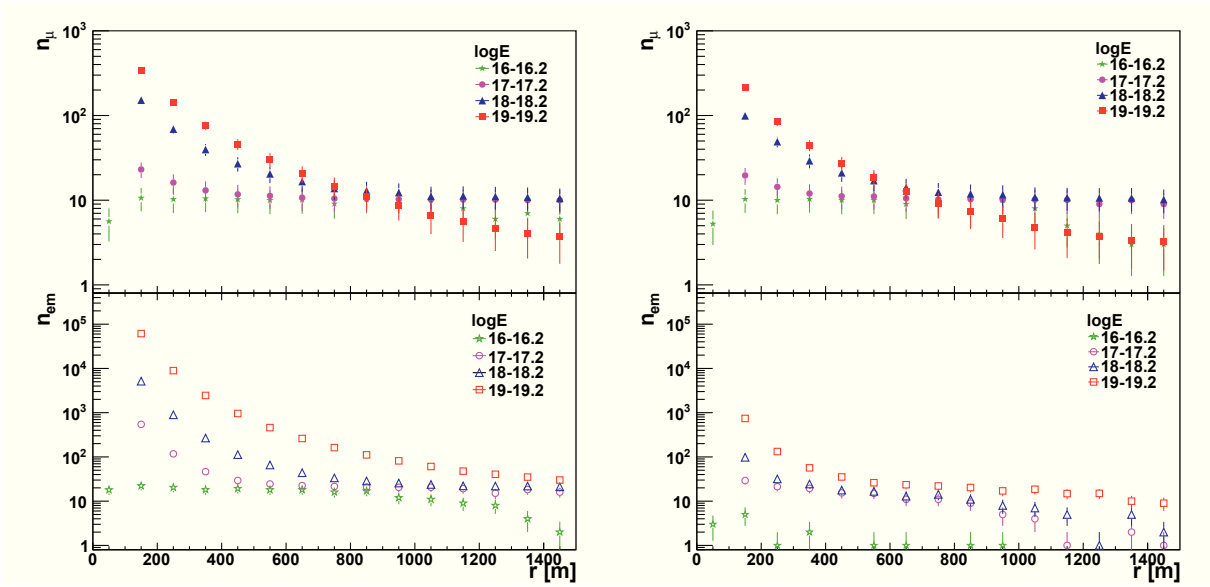

(a) $\log E$=16.0-17.0 (b) $\log E$=17.0-18.0

Figure 5.14: Fig. 5.14(a): Number of particles resampled at ground level and injected in the detector as a function of the distance r from the core for different shower energy ranges: $\log E$=16-16.2 (green stars), $\log E$=17-17.2 (purple dots), $\log E$=18-18.2 (blue triangles), $\log E$=19-19.2 (red squares). Top panel corresponds to the number of muons while the bottom panel to the electromagnetic component; Fig. 5.14(b): Number of particles resampled at ground level and triggering at least 2 detector planes in the detector as a function of the distance r from the core. Same notation of Fig. 5.14(a).

Finally, it is worth to quantify the muon trigger probability as a function of the applied strip threshold. We report in Fig. 5.15 the computed probability for 2-fold and 3-fold muons events, as a function of the strip trigger threshold in number of produced photoelectrons at the cathode or in energy deposit (top horizontal axis). The number of photoelectrons at the cathode is generated from the strip energy deposit dE/dX assuming a poissonian fluctuation with mean $< n_{pe} >= \kappa \times dE/dX$ (κ = 5 pe/MeV). The trigger probability is then calculated taking as reference tracks those having a non null probability to enter the detector and trigger at least two or all three planes. We show the results for two different muon angular range, $0° < \vartheta < 5°$ and $30° < \vartheta < 35°$, representative of vertical and inclined tracks. A threshold of $\sim 500-600$ keV may be eventually applied to reduce the background contamination without affecting considerably the expected muon event rate.

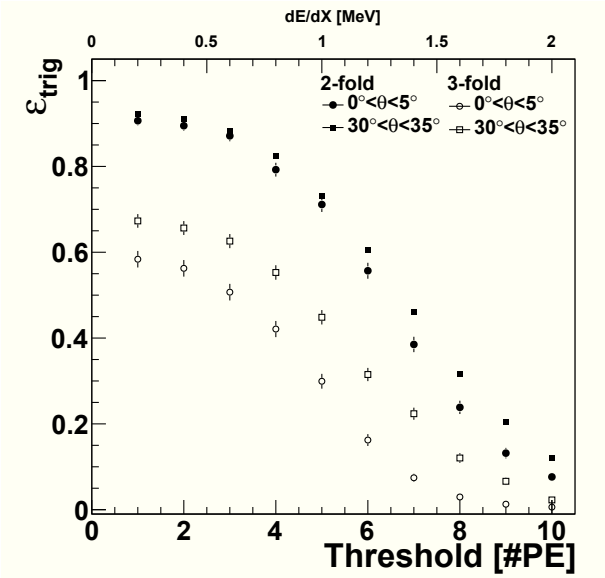

Figure 5.15: 2-fold and 3-fold trigger probabilities for muons as a function of the threshold conditions applied in the strips, in number of photoelectrons. The horizontal axis on top of the panel report the corresponding threshold in energy deposit.

5.4 Muons identification with neural network

The information coming from the simulations is then used to analyze the efficiency of the detector for the discrimination of particle tracks derived from high energy electrons/photons and muons impinging the ground. In this section we present a neural network analysis approach that might be used to disentangle the muonic and electromagnetic signatures in the detector.
Section 5.4.1 describes the set of parameters chosen for the particles identification. Then, section 5.4.2 concerns the description of the constructed Artificial Neural Network capable of associating measurements with known classes or groups, and capable of adjusting itself ('learning') according to situations presented to it.

5.4.1 Discriminating parameters

To identify muons from background we need to define a set of parameters sensitive to the particle identity to be determined on an event-by-event basis. As already pointed out in Section 5.3.1 the different propagation (ballistic vs shower) in the soil may characterize muons from other particles. For this reason we used the following set of observables for the discrimination:

- $m^{X,Y}$: multiplicity of hit strip in $X-$ or $Y-$plane;
- $r^{X,Y} = \frac{m_{X,Y}}{(\max_{x,y} - \min_{x,y} + 1)}$: neightbouring parameter for $X-$ or $Y-$plane;

where $\max_{x,y}$ and $\min_{x,y}$ are the maximum x or y number Id of hit strips. $r^{x,y}$ is a measure of how much the hit strips are found one next to the other. It assumes values equal to 1 for adjacent strips and <1 otherwise. A set of 12 parameters is therefore defined for each event. When a plane is not triggered we obviously have m=0 and r=0.
We report in Fig. 5.16 and 5.17 the distribution of these observables in each detector plane for simulated muons and background particles triggering at least two planes from the air shower data sample. As already mentioned, electromagnetic particles trigger on average more strips

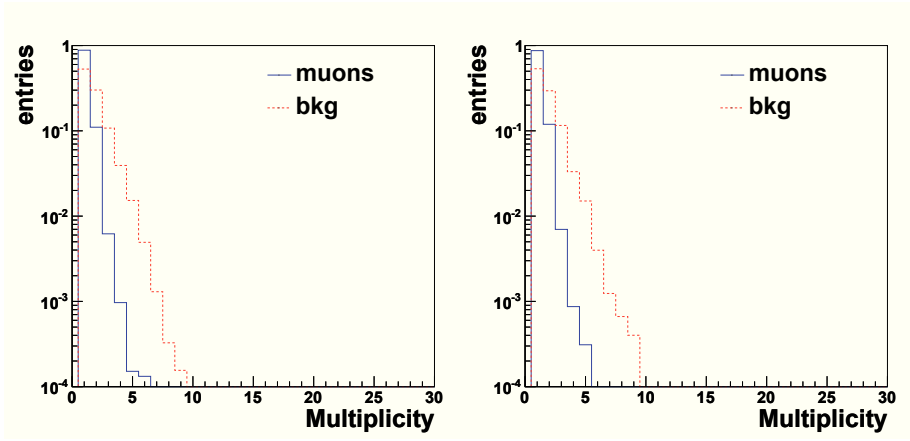

(a) plane 1X (b) plane 1Y

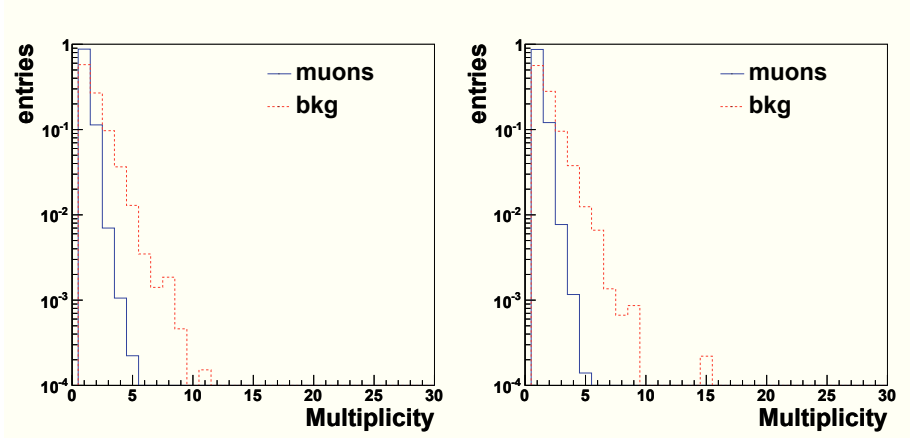

(c) plane 2X (d) plane 2Y

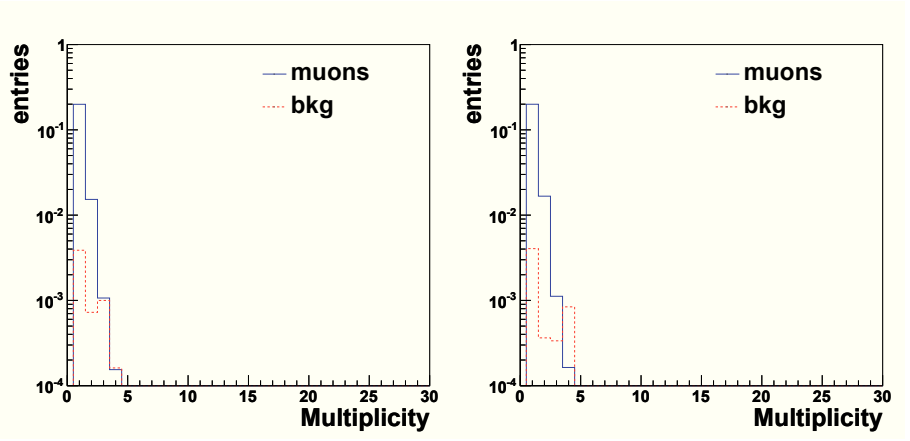

(e) plane 3X (f) plane 3Y

Figure 5.16: Distribution of multiplicity of hit strips for muons (solid lines) and background particles (dashed lines) triggering at least two detector planes from the shower data sample.

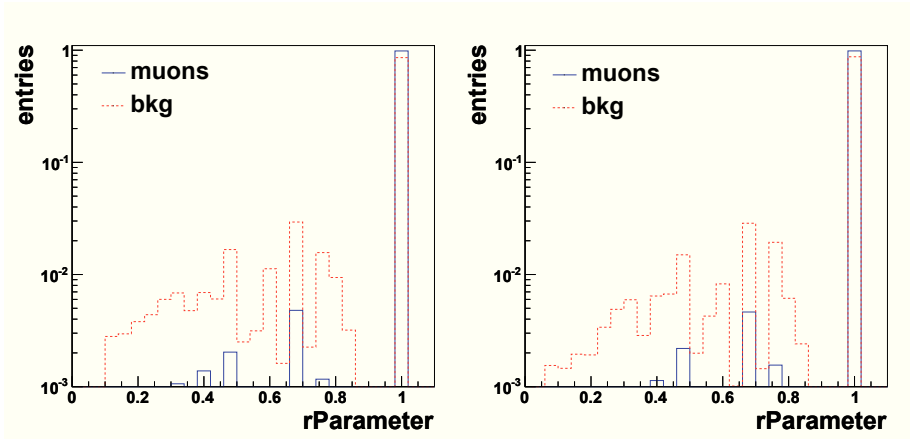

(a) plane 1X (b) plane 1Y

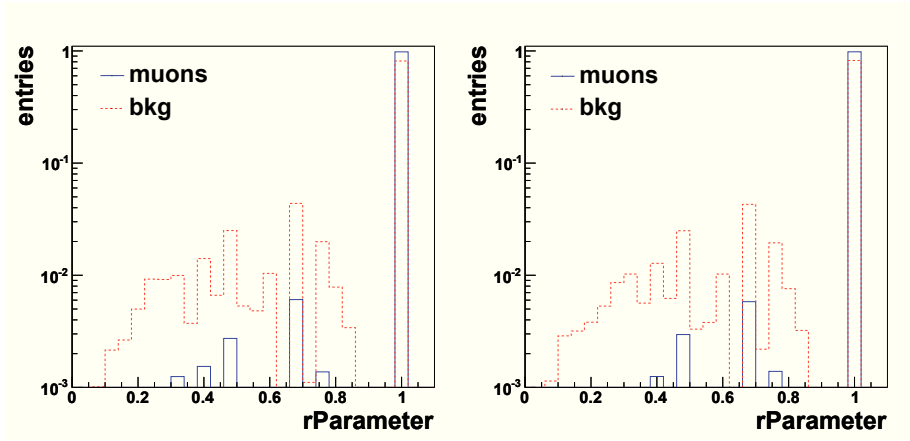

(c) plane 2X (d) plane 2Y

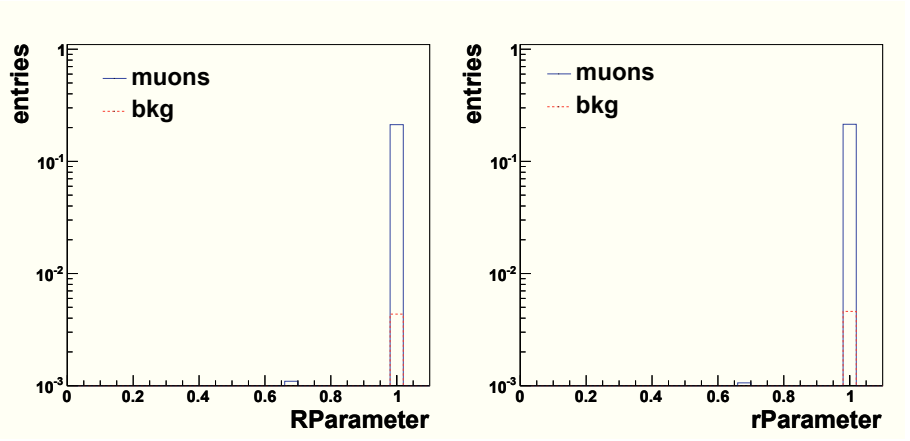

(e) plane 3X (f) plane 3Y

Figure 5.17: Distribution of r parameter for muons (solid lines) and background particles (dashed lines) triggering at least two detector planes from the shower data sample.

than muons resulting in a broader multiplicity distribution. Tipically the hit strips are found one next to the other for muons, with the exception of possible cases when a subshower or an isolated gamma are produced. The r parameter is therefore on average distributed around 1, while smaller values are observed for the background particles.

5.4.2 The neural network method

A feed forward neural network (NN) is structured in parallel layers of neurons, connected to neurons in adjacent layers by weighted connections, indicating the strength of the neuron link. The input layer is connected to the input data vector and an indefinite number of hidden layers process the signal towards the output layer which returns the final response of the network to the presented input data.

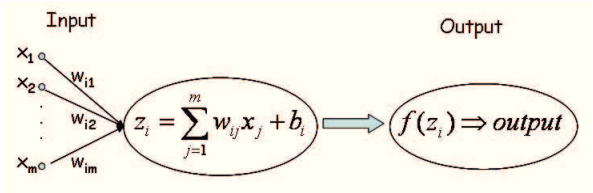

Figure 5.18: A single neuron of index i: the input vector components x_i, the weights w_{ij} (j=1,...m), the biases b_i, the transfer function f and the output signal $f(z_i)$ are showed.

The basic processing unit in the network is the neuron: the input signals x_i $(i = 1, m)$ coming from each input channel are linearly transformed by applying a multiplicative weight w_{ij} and an additive bias b_i to form the net neuron input z_i:

$$z_i = \sum_{j=1}^{m} w_{ij} x_j + b_i \tag{5.4}$$

The neuron output is obtained by applying a transfer function $f(z_i)$ to the net input (see Fig. 5.18). Common forms of such activation functions are the simple linear function $f(z_i) = \alpha z_i + \beta$, or the sigmoidal form functions, as well as the logistic function $f(z_i) = \frac{1}{1+\exp(-\alpha z_i)}$ and the hyperbolic tangent function $f(z_i) = \frac{\exp(z_i)-\exp(-z_i)}{\exp(z_i)+\exp(-z_i)}$.

For what concerns our identification purposes, after testing several network architectures, no significative improvements have been found by choosing a number of neurons considerably larger with respect to the input parameter size, hence we adopted for simplicity the studied architecture with the smallest number of adjustable weights, 12 inputs, 3 hidden layers, each one with 12 neurons, and an output layer with one neuron. The activation functions are hyperbolic tangent in the hidden layers and linear in the output layer.
Next step is the choice of the training algorithm. The training data is a set of N events $(\mathbf{x}_i, y_i)$ $i = 1, ...N$, defined by the 12-dim input vector $\mathbf{x}_i \equiv$($m1X$, $m1Y$, $m2X$, $m2Y$, $m3X$, $m3Y$, $r1X$, $r1Y$, $r2X$, $r2Y$, $r3X$, $r3Y$) and by the desired output vector (1 in the case of muon event, 0 in the case of background event) y_i. The supervised training algorithm minimizes the difference between the desired output y_i and the network computed output t_i, by adjusting iteratively the weights and biases of the net in order to minimize a given error function E. A standard error

function, extensively used in literature, is the square error function E_{MSE}:

$$E_{MSE} = \frac{1}{2}\sum_{i=1}^{N}[y_i(\mathbf{x},\mathbf{w}) - t_i]^2 \tag{5.5}$$

Sometimes it may happen that the presence of large neuron weights deteriorates the network generalization capabilities. In these cases a regularized error function E_{REGMSE} is often introduced to minimize the network weights together with the network performance:

$$E_{REGMSE} = \gamma\, E_{MSE} + (1-\gamma)\sum_{i=1}^{N_W} w_i^2 \tag{5.6}$$

where N_W is the number of weights of the network and γ is a parameter responsible to guarantee a compromise between the network error minimization and the generalization performances of the network. Value of γ close to 1 tend to favor the error minimization and viceversa for values of γ close to zero; a conservative value of 0.5 was therefore fixed.
Several backpropagation training algorithms have been tested (steepest descent, conjugated gradient and quasi-Newton algorithms). We achieved better identification performances with quasi-Newton methods, since other algorithms often return bad or local minima of the error function. We used a quasi-Newton algorithm with the Broyden-Fletcher-Goldfarb-Shanno (BFGS) error minimization formula [241][242].
The identification analysis proceeds as follows:

- *Pattern selection*: we divided the simulated shower set in three independent subsets (learn, validation and test data set, the first used to train the network, the second to stop the training phase and check the net generalization capabilities and the last to evaluate the achieved performances.

- *Feature pre-processing*: we normalized the features in the range [-1,1] to avoid large dynamics among the network inputs;

- *Training phase*: we trained the network to return a value of 0 or 1 in presence of a backgroung or muon event, respectively. The learning phase was stopped at a given epoch when the network began to show a clear overtraining behavior, corresponding to a loss of generalization in the identification procedure, e.g. when the network error calculated over the test sample stopped to fall down and began to increase.

- *Evaluation of the results*: given the distribution of the network outputs $NNout$ in presence of muon and background events, one has to put a cut to separate the particles classes and evaluate the performances of the built network by means of the identification efficiency ε and purity P:

$$\begin{aligned} \varepsilon_\mu(cut) &= \frac{N_\mu(NNout > cut)}{N_p} \\ P_\mu(cut) &= \frac{N_\mu(NNout > cut)}{N_\mu(NNout > cut) + N_{bkg}(NNout > cut)} \end{aligned}$$

  where N_μ, N_{bkg} are the total number of muon and background events in the sample, while $N_\mu(NNout < cut)$, $N_{bkg}(NNout > cut)$ represent the number of muon and background

events for which the output of the net is smaller or higher than the chosen cut. Clearly the efficiency and purity depend on the adopted cut over the net outputs, which should be optimized according to the specific problem under investigation. Eventually the choice of the cut is a compromise between the desired purity and event rejection level.

5.4.3 Results

The trained network was tested with an independent set of simulated particles from EAS. The response of the net is shown in Fig. 5.19 for different energy intervals. Muons are shown in red while the background in black. For better visibility both histograms have been normalized to unity. As can be seen, muons are correctly identified in all energy bins. We also note that a significant background contamination is present, especially for low energies <1-2 GeV, making very difficult or impossible to discriminate the muon signal. As the energy increases the muon events are almost completely separated from the background. This evidence can be explained in terms of particles footprints. In fact at energies larger than 1-2 GeV electromagnetic showers are produced and the background multiplicity significantly differs from the muon one making easier the discrimination.

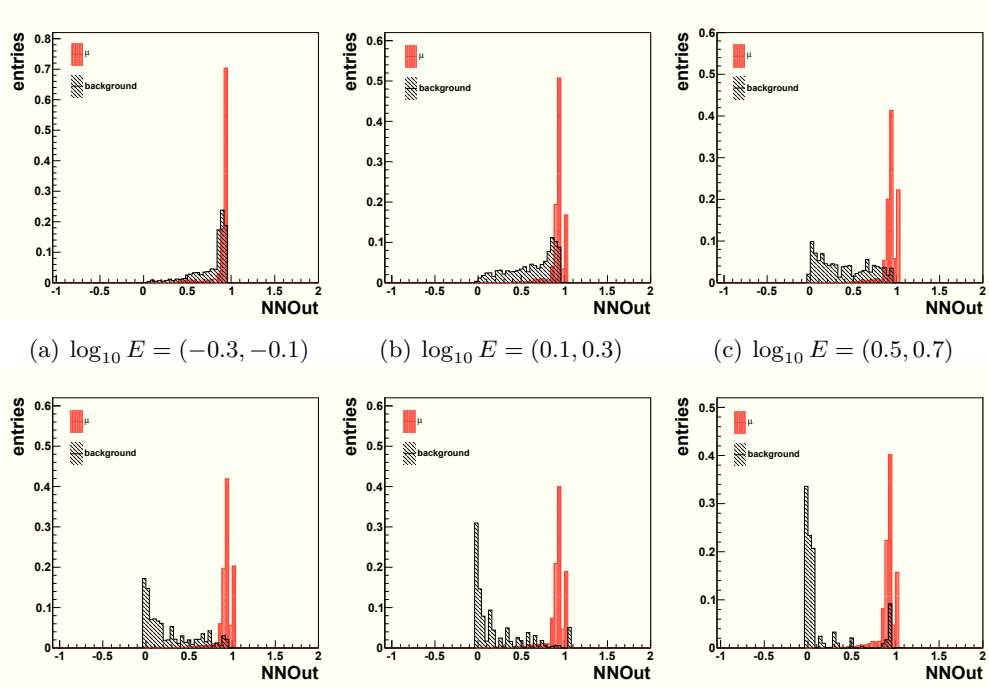

(a) $\log_{10} E = (-0.3, -0.1)$ (b) $\log_{10} E = (0.1, 0.3)$ (c) $\log_{10} E = (0.5, 0.7)$

(d) $\log_{10} E = (0.7, 0.9)$ (e) $\log_{10} E = (0.9, 1.1)$ (f) $\log_{10} E = (1.1, 1.3)$

Figure 5.19: The neural network response for different energy bins. At low energy (up to 1 GeV) the discriminating parameters for muons and background are almost equal, so there is a significant background contamination. Instead at higher energies the two groups are almost completely separated.

Following the steps described in the previous section, we report in Fig. 5.20 the efficiency and purity curves as functions of the adopted cut over the network outputs. Filled dots represent efficiency while empty dots stand for purity. These kind of curves are designed in order to choose the optimum cut according to the needs of the analysis (high purity or high efficiency required, low event rejection factor, ...). From the plots we observe that the choice $NNcut = 0.5$ leads to

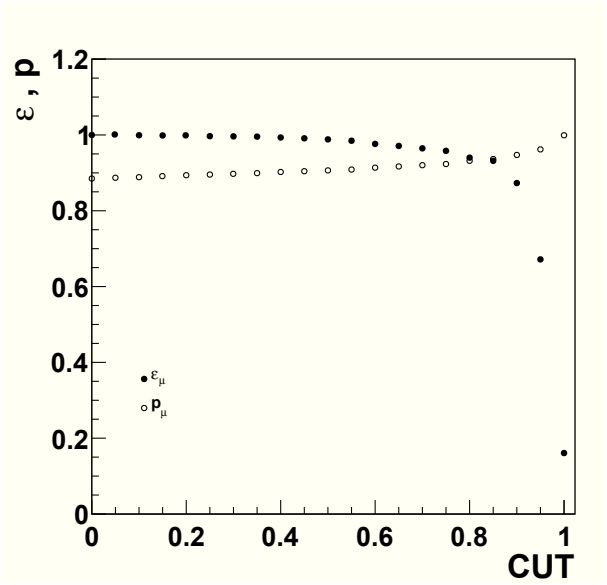

Figure 5.20: Efficiency and purity curves as function of the chosen cut over the network outputs. Filled dots correspond to efficiency while empty dots correspond to purity.

good classification, allowing to reach efficiency and purity over 85%, without rejection of a large number of events.
Fig. 5.21 shows the muon identification efficiency ε_μ and purity p_μ as a function of the particle energy, zenith angle and distance from the core, as obtained by choosing a cut $NNOut$ =0.5 in the network response. The identification efficiency is very good at all energies, larger than 85%. If we normalize the background to the expected signal the average purity is of the order of $\sim$ 60%, increasing above 80% at high energies ($>$ 5 GeV). However, if we consider the realistic muon/background ratio present in our air shower simulations, we obtain a purity >80% for energies above 1 GeV as showed in Fig. 5.21.

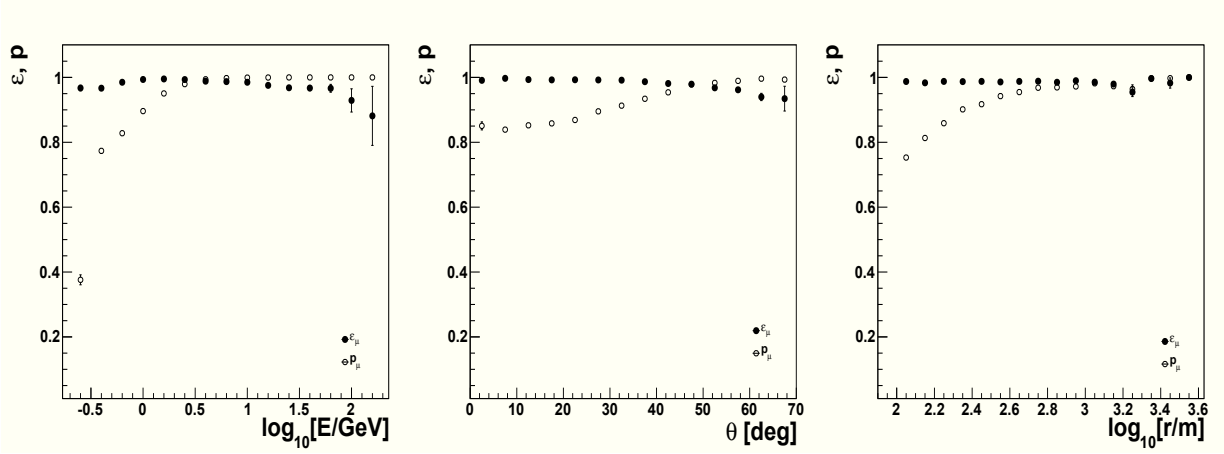

(a) ε_μ, p_μ vs $\log_{10} E$ (b) ε_μ, p_μ vs θ (c) ε_μ, p_μ vs $\log_{10} r$

Figure 5.21: Neural Network efficiency and purity as a function of the particle Energy (a), zenith angle ϑ (b), and distance from the core r (c). The identification efficiency is larger than 85% at all energies and almost indipendent from ϑ and r.

Finally the obtained efficiency for the muon identification over the total data set is $\varepsilon_\mu = 97\%$, while the total purity is $p_\mu = 90\%$. Furthermore, rejecting the event that trigger only 2 planes and accepting only the 3-fold events, a minor number of electromagnetic events are present and we obtain $\varepsilon_\mu = 99\%$ and $p_\mu = 99\%$. However in this case $\sim 40\%$ of muon events do not reach the third plane and would be lost.
As a cross check we compared the identification performance with those obtained by other group within Auger with independent methods and data samples. In [243] *Sanchez et al.* report an efficiency of 88% and purity of 60% accepting 1-fold, 2-fold and 3-fold events, and a purity of 99% accepting only 3-fold events. Such results are in good agreement with the ones reported in this work thus supporting the present analysis.

5.5 Reconstruction of muon tracks

In this section we present a method to reconstruct the muon track direction from the hit points produced in the detector planes. When a particle triggers a strip in both the X, Y planes of a detector module, a track hit is created with coordinates (x_h,y_h,z_h), respectively given by the strip in the $Y-$ and $X-$plane and by the average depth of the detector planes. The spatial resolution is related to the size $s_{x,y} = 4$ cm of the XY pixel and is given by $\sigma_{x,y} = s_{x,y}/\sqrt{12} \sim 1.15$ cm. As final hit point coordinates, we therefore assumed the pixel centers smeared with a gaussian of width corresponding to the spatial resolution.
Two main steps, cluster finding and track fitting, required to determine the track direction are detailed in next sections.

5.5.1 Cluster finding

In this first stage the produced track points in each plane are scanned to identify possible clusters. A cluster is defined by points located in adjacent strips. When a cluster is found, its points are replaced by the cluster baricenter in the track fitting procedure. The patterns to be searched have quadratic or rectangular shape. To study what kind of shapes are the most relevant we report in Fig. 5.22 the hit multiplicity in each detector plane as a function of the primary energy for true and fake hits. The colour map and text labels indicates the probability to have a given multiplicity in each energy bin. An energy threshold of 300 keV is applied. As can be seen, the muons produce mainly single-strip clusters ($\sim 90\%$ of the cases) or double-strip clusters ($< 10\%$). Very rare are the cases when four adjacent strips are triggered. On the contrary, the fake hit distribution have a larger multiplicity tail, due to the presence of electromagnetic showers that can be induced by the muon in the soil. However, apart for low or very high particle energies, the probability to have spurious hits is quite limited: in ∼10-15% of the cases only one fake hit is present, while the probability to have more than one spurious hit is smaller than 5%. The true muon patterns that have to be identified are therefore of the kind 1×1, 1×2 or 2×2. A possible strategy could be rejecting clusters of larger multiplicities (>4), but as we would like to show this may lead to a wrong hit-cluster association.
As an example we report in Fig. 5.23 two sample of simulated muon events, the first relative to a simple hit configuration to deal with, easy to be recognized, the second relative to a more complicated configuration where the cluster search may fail. The hits effectively produced by the muons are shown in red, while the spurious in black. The red line is the projected true track on each plane. The blue crosses indicate the baricenter of a cluster. In Fig. 5.23(a) the muon cluster in the second plane is correctly identified while two clusters appear in the third

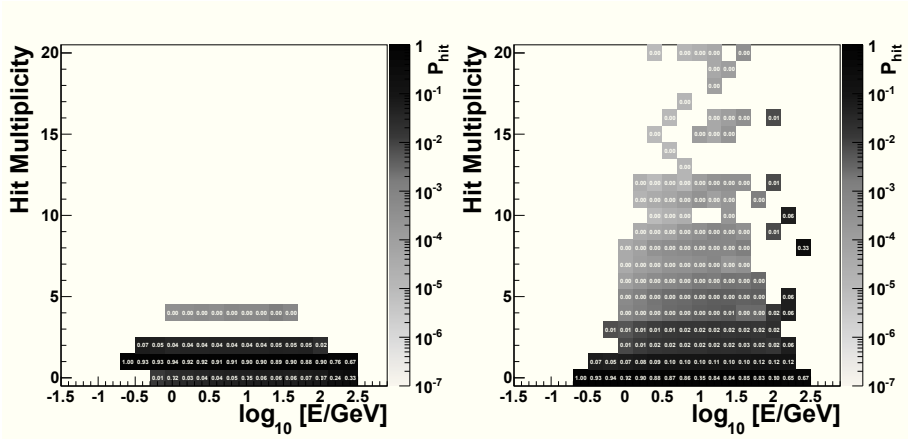

(a) muon, plane 1 (b) background, plane 1

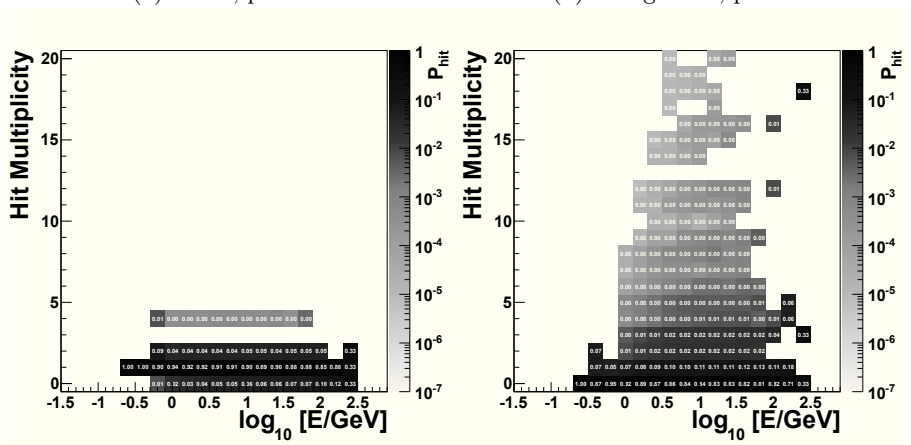

(c) muon, plane 2 (d) background, plane 2

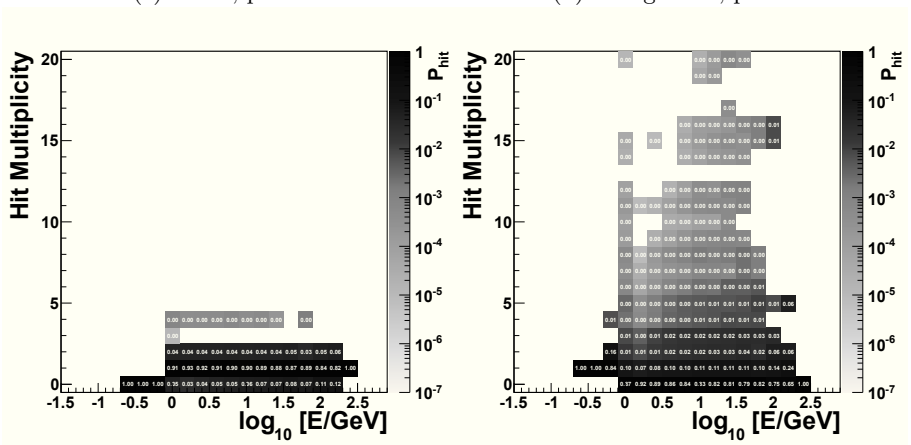

(e) muon, plane 3 (f) background, plane 3

Figure 5.22: Hit multiplicity in each detector plane as a function of the particle energy for muon (left panels) and spurious hits (right panels).

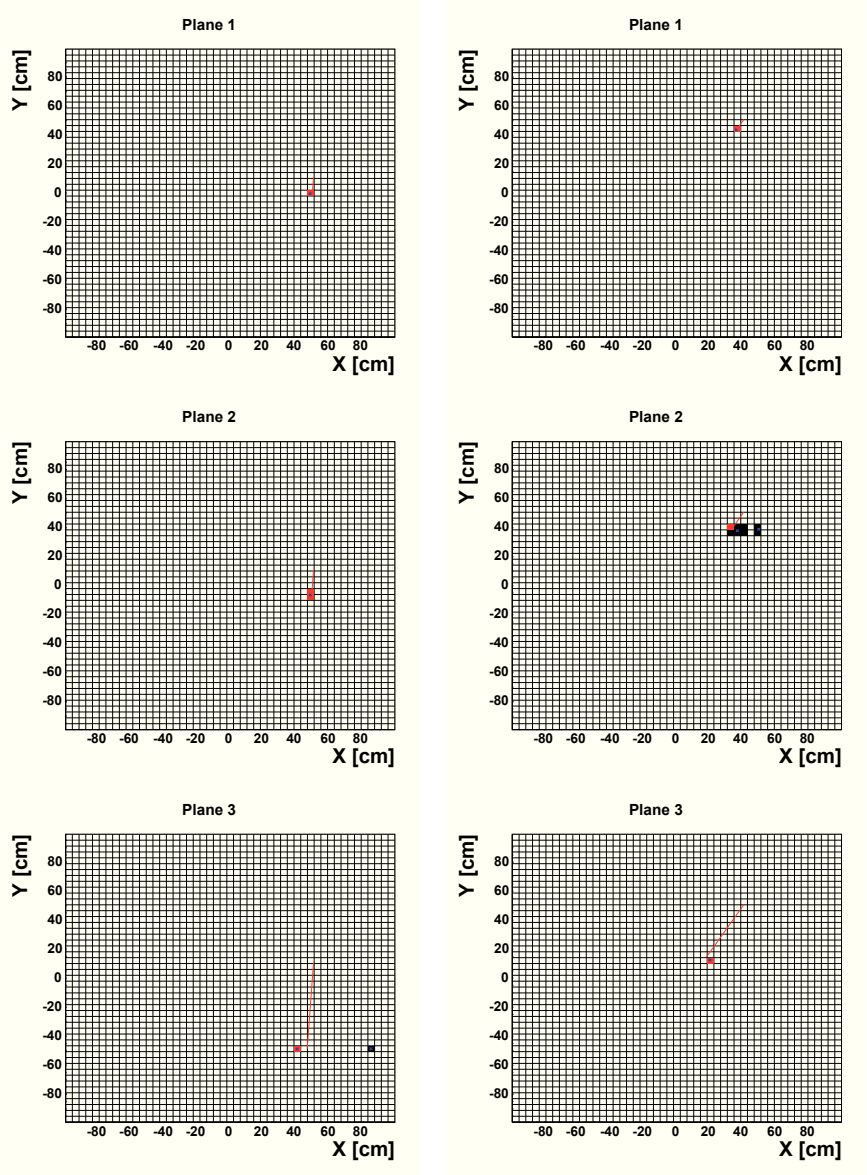

(a) Sample event: a simple configuration

(b) Sample event: a difficult configuration

Figure 5.23: Two sample simulated muon event patterns on each detector plane. Muon hits are shown in red, while spurious in black. The red line is the projected true track on each plane.

plane, one produced by the muon and the other spurious. Two candidate tracks are therefore present. However the two clusters are so separated in space that during the track fitting step the fake track could be rejected according to a minimum χ^2 criterion. The second event is more difficult to be treated. Infact in the second plane the muon hit is englobed in a larger fake cluster. Another spurious cluster is also present. Rejecting the cluster with large multiplicity and keeping the second lead in this case to a hit misclassification resulting in a bad reconstructed track in the final stage. In such situations it is convenient to keep the entire cluster and split it in single hits. These cases could be eventually limited by increasing the applied energy threshold. It is instructive to evaluate the impact of the applied energy deposit threshold and veto in the

hit multiplicity distributions. The choice of the energy deposit threshold applied in the strip is guided by a compromise between having the largest detection efficiency for muons and the need of reducing the noise from spurious hits. To investigate the impact of different thresholds we compare in Fig. 5.24 the probability ε^{μ}_{hit} (filled dots) and P^{fake}_{hit} (empty dots) to have muon and spurious hits in each plane for a given choice of the threshold (E_{thr}=100-300-500 keV) with respect to the case of no threshold applied.
The probabilities are plotted as function of the muon energy (upper panels) and zenith angle (lower panels) with dots for E_{thr}=100 keV, triangles for E_{thr}=300 keV and squares for E_{thr}=500 keV. As observed before, below 10 GeV about 10-20% of the produced hits are not due to the muon. At higher energies the contamination of spurious hits increases at the level of 50-60% for the first two planes and ∼40% for the last plane.
In Fig. 5.25 we report the same plots obtained with a threshold of 300 keV, in one case with a 20 ns veto applied (dots) and in other case (triangles) without any veto condition. In the first case a reduced efficiency and an increased spurious contamination are observed . This is related to the fact that muons tend to travel more confined in time, being in this way more sensitive to a veto timing condition.

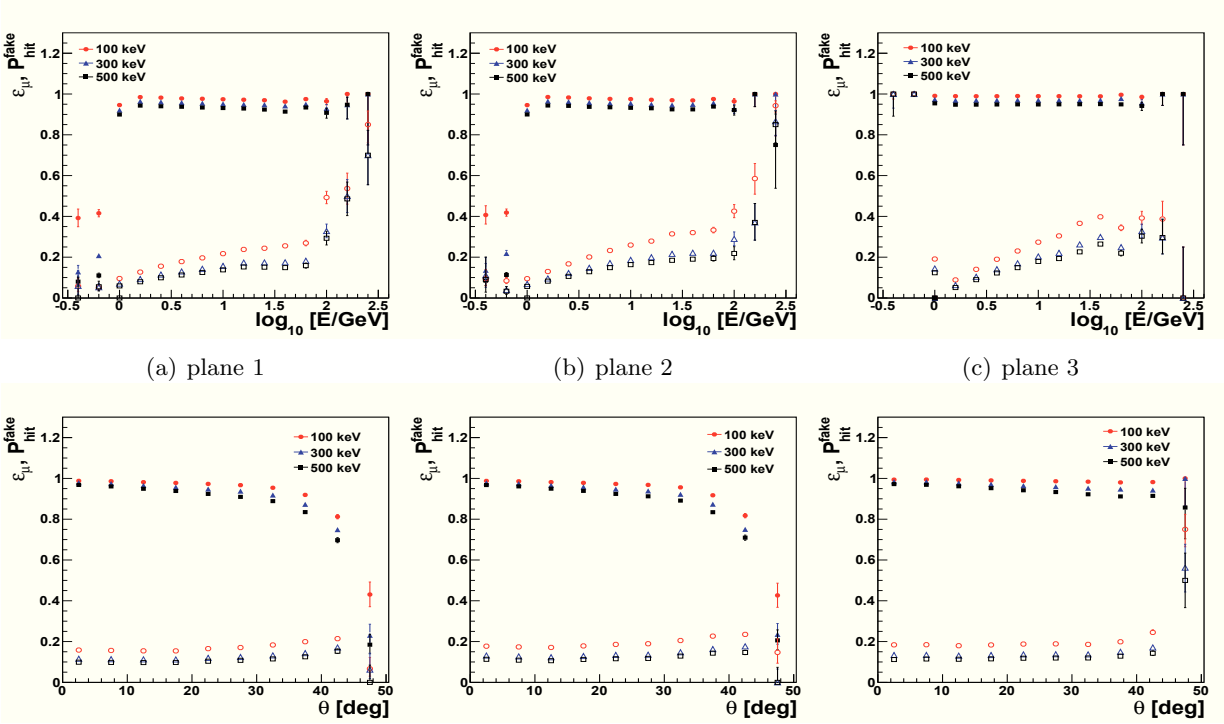

(a) plane 1 (b) plane 2 (c) plane 3

(d) plane 1 (e) plane 2 (f) plane 3

Figure 5.24: Probability to have muon (filled dots) and spurious hits (empty dots) in each plane as a function of the particle energy ((*a*),(*b*),(*c*)) and of theta ((*d*),(*e*),(*f*)) for different choices of the strip trigger threshold energy.

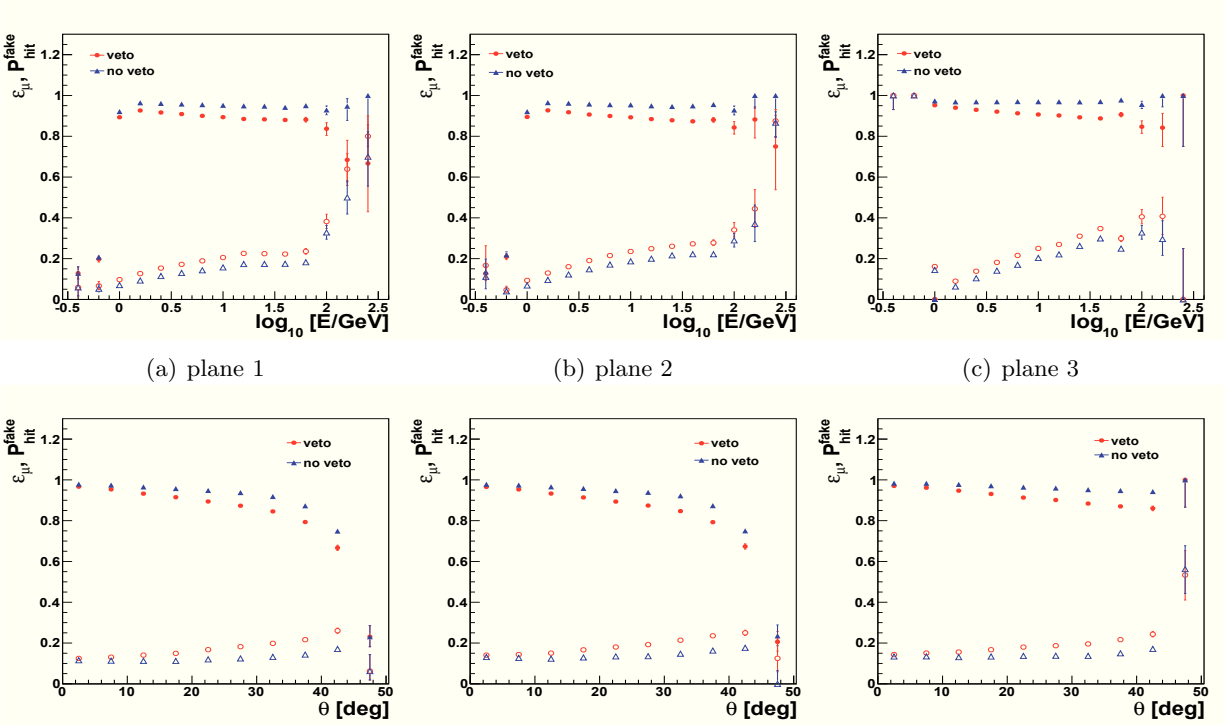

(a) plane 1 (b) plane 2 (c) plane 3

(d) plane 1 (e) plane 2 (f) plane 3

Figure 5.25: Probability to have muon (filled markers) and spurious hits (empty markers) in each plane as a function of the particle energy and theta with (dots) and without (triangles) applying the strip veto condition.

5.5.2 Track fitting

The track seeds are searched in the first detector plane. All available hits are combined to form a list of potential candidate tracks, which are reconstructed as detailed below. A hit in each plane is required to form a candidate track.
The muon track is basically a straight line in space, conventionally described with such equation:

$$\vec{f}(\vec{x}) = \begin{cases} x = x_0 + t_x(z - z_0) \\ y = y_0 + t_y(z - z_0) \end{cases} \tag{5.7}$$

where the four parameters that have to be determined form a track state vector $\vec{x} \equiv (x_0, y_0, t_x, t_y)$ and represents the x, y coordinates at the reference z_0 (i.e. at ground z_0) and the track slopes in the xz and yz planes respectively.
To reconstruct the muon track one could use two alternative methods, one based on a global least-square fit (LS) and the other on the Kalman Filter technique (KF). Both methods have been extensively described in literature, see for instance [244] for a review. In the following we summarize their main features.
In the LS approach, a candidate track is fitted by minimizing the following χ^2:

$$\chi^2 = (\vec{m} - F\vec{x})^T V^{-1} (\vec{m} - F\vec{x}) \tag{5.8}$$

where $\vec{m}$ is the vector of measurements $(x_i, y_i, i = 1, \ldots N)$ with uncertainties σ_i, V is the error matrix of the measurements and $F = \partial f(x_i)/\partial x_j$ is the derivative matrix of f with respect

to the parameters. In the case of a linear problem $\vec{f}=F\vec{x}$ the analytical solution for $\vec{x}$ and its covariance matrix $C_{\vec{x}}$ is given by:

$$\vec{x} = (F^T V^{-1} F)^{-1} F^T V^{-1} \vec{m} \qquad C_{\vec{x}} = (F^T V^{-1} F)^{-1} \tag{5.9}$$

This approach requires the inversion of a covariance matrix of size $N \times N$, which may become problematic when N is large or when the matrix is not diagonal, e.g. when sources of noise are present. In this case the hit multiplicity is sufficiently low to justify the use of this global approach. However the LS framework is not as flexible as the Kalman-Filter for what concerns the treatment of noise effects like multiple scattering or energy losses. In the first case infact one has to look at all measurements at same time and compute a noise matrix to be added to the error matrix of the measurements, see for example [245]. Instead in the KF method only two consecutive states are considered and the noise effects can be included in a more straightforward way, as described below. For this reason we preferred using the KF method in the present analysis, even if it has to be stressed that both approaches lead to a comparable tracking resolution.

In the KF method, the track state vector at the time k, i.e. after inclusion of k measurements, is denoted by x_k and its covariance matrix by C_k. In our case, x_k contains the parameters of the fitted track, given at the position of the kth hit. A propagator matrix F_k describes the propagation of the track parameters from the $(k-1)$th to the kth hit. The coordinate measured by the kth hit is denoted by m_k and the measurement error is described by the covariance matrix V_k. The relation between the track parameters x_k and the predicted measurement is described by a projector matrix H_k. In our case we have:

$$x_k = \begin{pmatrix} x \\ y \\ t_x \\ t_y \end{pmatrix}_k \quad m_k = \begin{pmatrix} x \\ y \end{pmatrix}_k \quad V_k = \begin{pmatrix} \sigma_x & 0 \\ 0 & \sigma_y \end{pmatrix}_k \quad F_k = \begin{pmatrix} 1 & 0 & z_k - z_{k-1} & 0 \\ 0 & 1 & 0 & z_k - z_{k-1} \\ 0 & 0 & 1 & 0 \\ 0 & 0 & 0 & 1 \end{pmatrix} \quad H_k = \begin{pmatrix} 1 & 0 & 0 & 0 \\ 0 & 1 & 0 & 0 \end{pmatrix} \tag{5.10}$$

The KF method is based on a recursive approach made of three phases, *prediction-filtering-smoothing*. The filter has to be initialized by choosing a starting approximation x_0 and C_0 of the track state vector and the covariance matrix. We assumed a vertical initial track direction and vertex (0,0) (with respect to the station coordinate system) and a diagonal covariance matrix, with large diagonal elements[3]. In the prediction step the state vector and its covariance matrix are propagated to the location of the next measurement with the following prediction equations:

$$\tilde{x}_k = F_k x_k \qquad \tilde{C}_k = F_k C_{k-1} F_k^T + Q_k \tag{5.11}$$

where $\tilde{x}_k$ and $\tilde{C}_k$ are the predicted state and covariance at kth location. The predicted residuals are given by $\tilde{r}_k = m_k - H_k \tilde{x}_k$ and $\tilde{R}_k = V_k + H_k \tilde{C}_k H_k^T$.
The Q_k term resumes the additional error introduced by the multiple scattering or energy losses. Infact in the presence of scatterings there are real random deviations from a straight line, correlated from one plane to the next. For example, if a muon scatters to the right at one plane, it is more likely to end up to the right of the original undeviated path than to the left. We followed [244, 246] to express the multiple scattering contribution from thick layers. The

[3] A starting point could be provided by the least square track solution, even performed without taking into account the multiple scattering. However in this case it can be seen that the filtered track parameters tend to converge towards the initial approximation and are influenced by the first measurements, as discussed for instance in [247, 248].

noise matrix Q is given by

$$Q_k = \begin{pmatrix} cov(t_x,t_x)l_k^2/3 & cov(t_x,t_y)l_k^2/3 & cov(t_x,t_x)Dl_k/2 & cov(t_x,t_y)Dl_k/2 \\ ... & cov(t_y,t_y)l_k^2/3 & cov(t_x,t_y)Dl_k/2 & cov(t_y,t_y)Dl_k/2 \\ ... & ... & cov(t_x,t_x) & cov(t_x,t_y) \\ ... & ... & ... & cov(t_y,t_y) \end{pmatrix} \tag{5.12}$$

where l_k is the traversed length of the medium in terms of radiation length, $D = \pm 1$ indicates whether the motion increases (+1) or decreases the z-coordinate, $cov(t_x, t_x)$, $cov(t_y, t_y)$, $cov(t_x, t_y)$ are the covariance matrix contribution from thin scatterers, derived in [246] and given by:

$$\begin{aligned} cov(t_x, t_x) &= (1 + t_x^2)(1 + t_x^2 + t_y^2)\sigma_{ms}^2 \\ cov(t_y, t_y) &= (1 + t_y^2)(1 + t_x^2 + t_y^2)\sigma_{ms}^2 \\ cov(t_x, t_y) &= t_x t_y (1 + t_x^2 + t_y^2)\sigma_{ms}^2 \end{aligned}$$

where $\sigma_{ms}^2 = \left(\frac{13.6\,MeV/c}{p}\right)^2 t_0\sqrt{1 + t_x^2 + t_y^2}\left[1 + 0.038\ln\left(t_0\sqrt{1 + t_x^2 + t_y^2}\right)\right]^2$ is the variance of the multiple scattering angle of a particle of momentum p traversing a thickness t_0 in number of radiation lengths. We assumed a radiation length of 21.997 g/cm^2 for the Malargue soil.
The energy losses due to ionization in each soil layer depends in good approximation on the muon track length l and are could be eventually taken into account by considering an average deposited energy of dE/dX_{ion}= 1.8 MeV/g/cm^2, so that the corrected energy used in each filter step is $E\text{-}dE/dX_{ion} \cdot l$.

In our case the most important scattering contribution comes from the thick soil layers within each detector plane, rather than from the strip themselves or their casings. Eventually, additional contributions can be added to the noise matrix in the same way. In this work we neglected other scatterers and the energy losses contributions.
In the filtering step the state vector and covariance are updated using the information of the kth measurement according to the filter equations:

$$K_k = \tilde{C}_k H_k^T R_k^{-1} \qquad x_k = \tilde{x}_k + K_k r_k \qquad C_k = (1 - K_k H_k)\tilde{C}_k \tag{5.13}$$

where K_k is the gain matrix and the obtained filtered residuals are $r_k = (I - H_k K_k)\tilde{r}_k$, $R_k = (I - H_k K_k)V_k$. The χ_k^2 contribution of the filtered point is then given by $\chi_k^2 = r_k^T R_k^{-1} r_k$. At the last filtered point k=n the track parameters have been calculated using the information from all the preceding hits. However we would like to know the track parameters at the initial step k=0, e.g. before the muon enters the ground, to get the best estimate of the initial direction. For this the smoothing step is applied step by step in the direction opposite to that of the filter, according to these equations:

$$A_k = C_k F_{k+1}^T \tilde{C}_{k+1}^{-1} \qquad x_k^n = x_k + A_k(x_{k+1}^n - \tilde{x}_{k+1}) \qquad C_k^n = C_k + A_k(C_{k+1}^n - \tilde{C}_{k+1})A_k^T \tag{5.14}$$

with the smoothed residuals given by $r_k^n = m_k - H_k x_k^n$, $R_k^n = R_k - H_k A_k(C_{k+1}^n - \tilde{C}_{k+1})A_k^T H_k^T$. The state vector at stage k=0 and its covariance finally gives the desired track parameters and their uncertainties.

5.6 Tracking performances

We applied the tracking algorithm to reconstruct the sample of muons coming from simulated showers triggering the three detector planes.
In a first case we neglected other particles than muons entering the detector as well as the time sampling of the DAQ system. Multi-muon events are therefore excluded in this case. Such situation corresponds to the measurements of "background muons" from very low energy showers, useful for prototype calibration, alignment and testings. In a second case we considered the events from high energy showers and the binary information of each hit strip is collected using a timing sampling of 10 ns. In such time interval more than one particle can produce hits in the detector and therefore multi-tracks events are expected. Typically this situation occurs much more frequently in the first timing bins, when the core is relatively near the station (< 150 m) and for higher shower energies. In both cases we increased the strip energy threshold at $dE/dX_{thr} = 500$ keV to remove as much spurious hits as possible.

5.6.1 Tracking performances of single muon tracks

To study the hit reconstruction accuracy we report in Fig. 5.26 the differences ΔX, ΔY between the true and reconstructed muon hit position for each detector plane. The obtained uncertainty is of the order of 0.5 cm for the first two planes, increasing to ~ 1 cm for the last plane. The misclassification probabilities have been found of the order of 7%.
We report in Fig. 5.27 the obtained resolution for the reconstructed track parameters (θ, ϕ, X_0, Y_0) as a function of the particle energy and zenith angle in two different conditions: Multiple Scattering (MS) correction switched-off (labeled as 'no MS'), and MS correction applied assuming an average energy of 1 GeV (labeled as 'MS')[4]. The upper panels represent the obtained angular resolution in θ and ϕ, while the resolution for the vertex coordinates X_0, Y_0 is shown

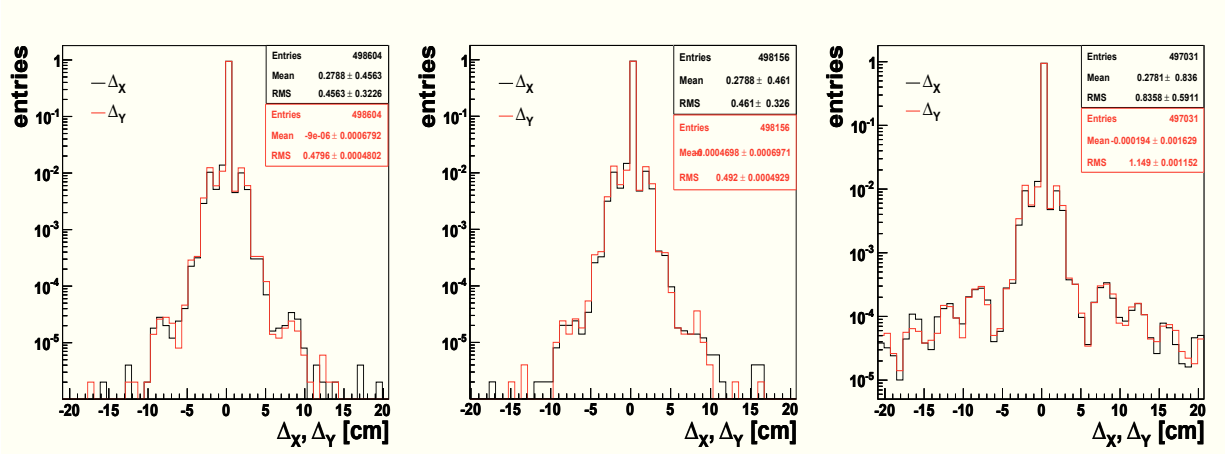

(a) plane 1 (b) plane 2 (c) plane 3

Figure 5.26: Deviation of the reconstructed hit positions (coordinate X in black, Y in red) with respect to the true position for each detector plane.

[4] An assumption must be made for the average track momentum as in our case this information in not experimentally available.

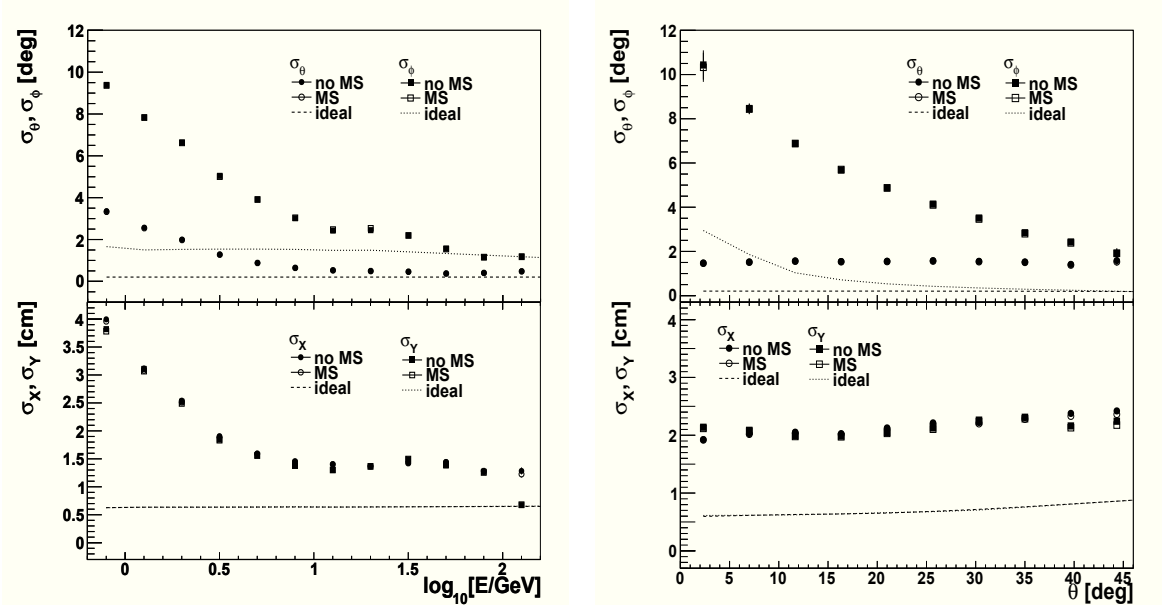

(a) (b)

Figure 5.27: Track angular and vertex resolution as a function of the muon energy (a) and zenith angle (b) in two different conditions: multiple scattering correction switched-off (filled markers, labeled as 'no MS'), multiple scattering correction applied assuming an average energy of 1 GeV (empty markers, labeled as 'MS'). In the top panels the resolution achieved for θ parameter is shown with dots, while for ϕ with squares. In the bottom panels the resolution for the x-coordinate of the vertex is shown with dots, while for the y-coordinate with squares. The dashed and dotted lines represent the ideal resolution calculated in absence of multiple scattering and considering only the pixel resolution.

in the bottom panels. As can be seen, the track reconstruction is better for vertical tracks and is slighly improved when the true MS correction is included, both for vertical and for inclined tracks.
We also computed for comparison (not shown in the plots) the resolution achieved when reconstructing the track with only the first two detector planes. The worst resolution is obtained in such case, thus pointing out that the last plane measurement is somehow relevant for the track reconstruction purpose even if its surrounding thick soil layer introduces a considerable noise in the hit measurement.
As a cross check we also repeated the analysis replacing the Kalman Filter track finding with a least square fit. Both approaches have been found to lead to comparable results for what concerns the track reconstruction accuracy.

5.6.2 Tracking performances in presence of background

In the case of high energy events the obtained hit multiplicity is considerably larger than the previous case especially in the first two planes where the electromagnetic contamination is larger. The hits due to the muons are often found englobed in large spurious clusters, the number of candidate tracks to be searched is increased and consequently the track recognition is more problematic.
To reject fake track candidates and reduce the number of candidate tracks to be fitted, a cut in the space angle among each track segment (i.e. $< 5°$) can be assumed. When the core falls close

to the station the hit multiplicity is so large in the first time bins that it is practically impossible to correctly identify the muon tracks, at least with the current detector design limited to only three tracking layers. Such bins should be considered as saturated. For instance a cut on the number of hits per plane may be introduced.

To evaluate the tracking performances we need to define a set of reference tracks N_{ref}, e.g. a set of tracks that an ideally performing algorithm should find, here defined by all muon tracks hitting the three detector planes in non-saturated sampling bins. We considered as saturated those sampling bins where one of the three detector planes has a number of track points larger than N_p^{sat}. The saturation threshold is chosen as a balance between having a high tracking efficiency and a corresponding low fake track rate. A fitted track was then considered to reconstruct a true track from the reference sample according to a parameter matching criterion $|\theta_{rec} - \theta_{ref}| < 5°$, $|\phi_{rec} - \phi_{ref}| < 20°$, $|X_{rec} - X_{ref}| < 5$ cm, $|Y_{rec} - Y_{ref}| < 5$ cm.

With these choices we can evaluate the following quantities as a function of the particle energy, angle and distance from the core to estimate the quality of tracking:

Track efficiency: $\varepsilon^{track} = \frac{N^{rec}}{N_{ref}}$

Ghost rate: $\nu^{ghost} = \frac{N^{ghost}}{N_{ref}}$

Clone rate: $\nu^{clone} = \frac{\sum_i N_i^{clone}}{N_{ref}}$

where N^{rec} is the number of reconstructed tracks, N^{ghost} is the number of fake tracks reconstructed by the algorithm, N_i^{clone} is the number of tracks reconstructing a reference track i.

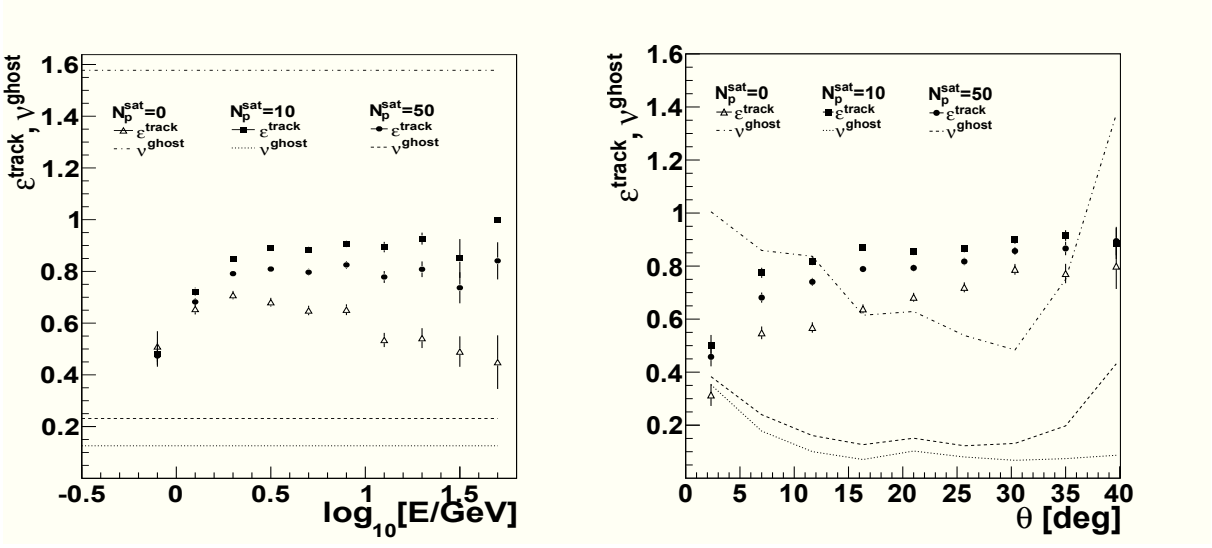

(a) (b)

Figure 5.28: Left: Tracking efficiency (dots) and ghost rate (lines) as a function of the particle energy for different saturation thresholds: N_p^{sat}= 0 (empty triangles), 10 (filled squares), 50 (filled dots); Right: Tracking efficiency (dots) and ghost rate (lines) as a function of the particle zenith angle. Same notation of 5.28(a))

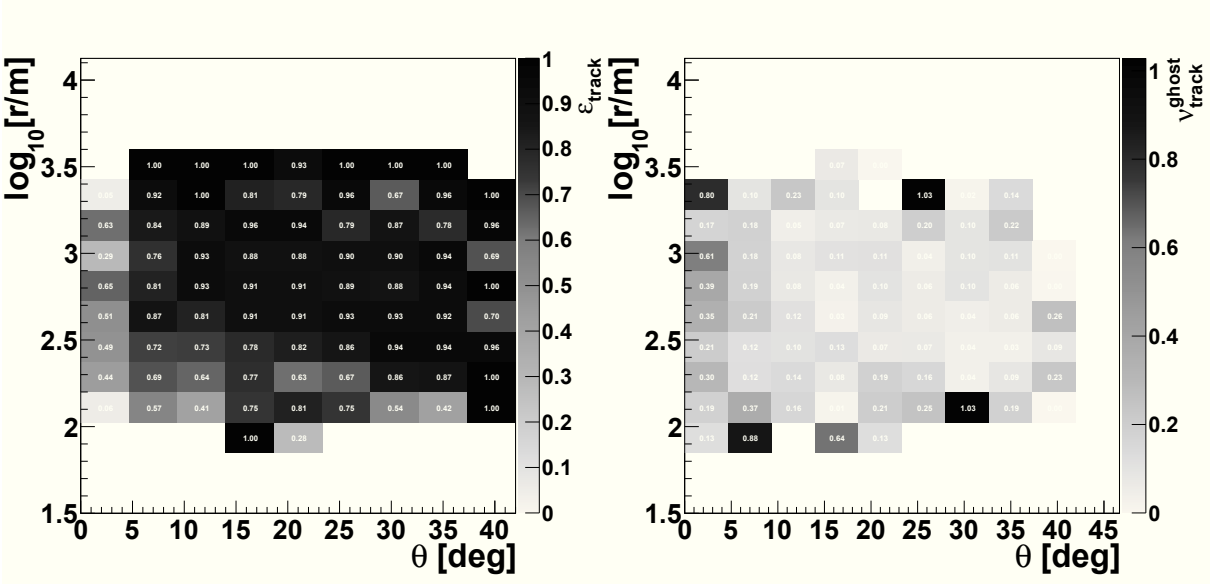

(a) (b)

Figure 5.29: Left: Tracking efficiency (left panel) and ghost rate (right panel) as a function of the muon zenith angle and distance from the core.

Fig.5.28 shows the tracking efficiency and ghost rates as a function of the particle energy (5.28(a)) and zenith angle (5.28(b)) for different saturation conditions: $N_p^{sat} = 0$ (no saturation condition), 10, 50. As we do not reconstruct the track energy we report in the plots an average ghost rate. As can be seen the track efficiency increases with the muon energy and zenith angle, assuming values greater than 80% when the saturation threshold is applied. The use of a saturation cut considerably reduces the ghost rate at the cost of reducing the event rate. The clones track rate, not reported in the plots, has been found smaller than 10^{-3}. A more optimized cut could be derived when first data will allow a comparison of real and simulated multiplicity.
Finally, assuming a cut of $N_p^{sat} = 50$ we report in Fig. 5.29 the tracking efficiency and ghost rate as a function of the muon zenith angle and distance from the core. On average the track efficiency is found to be of the order of 70-80% and the corresponding rate of ghost tracks can be maintained below 0.1-0.2 after applying the saturation threshold cut.

Chapter 6

Summary

The evolution of the Cosmic Rays spectrum through the second knee and the ankle, and corresponding predicted changes in composition, are crucial to understand the end of Galactic confinement and the effects of propagation on the lower energy portion of the extragalactic flux. The latter is strongly related to the cosmological distribution of sources and to the composition of the injected spectrum. To study this energy region the Pierre Auger Collaboration has extended the energy range of its observatory in Argentina for high quality data from 0.1 to 3 EeV. The extensions include three additional fluorescence telescopes with a more elevated field of view (HEAT) and a nested surface array with 750 and 433 m spacing respectively and additional muon detection capabilities (AMIGA).
The BATATA muon counter hodoscope has been designed as an additional prototype with the objective of estimating the electromagnetic contamination expected in the AMIGA muon counters. It consists of three XY planes of 2×2 m^2 of 49 plastic scintillating strips each, buried underground at 0.5, 0.8, 2.80 m depths, roughly at the center of the AMIGA array. Currently BATATA has entered the commissioning phase: the first plane (the deepest one) was buried in July 2011, while the others are planned to be deployed during the first months of 2012.
The subject of the present work has been to perform an end-to-end simulation of the BATATA device. The simulation includes the shower evolution in the atmosphere, the propagation of secondary cascades through the ground, the photon emission inside the scintillators, their propagation in the plastic and eventual absorption by the wavelength shifter inside the optical fibers and emission and propagation inside the fiber and up to the window of the PMT. The information coming from the simulation has been then used to analyze the efficiency of discrimination of particle tracks, derived from high energy electrons/photons and muons impinging the ground. The analysis was principally focused on the study of the reliability of an event-by-event particle identification with the use of pattern recognition methods, like neural networks, working with the multiplicity and closeness of triggered bars as discriminating parameters.
Using these simulations, we demonstrated that a good efficiency can be achieved in separating $\mu^{\pm}$ from $e^{\pm}$ and γ. The main obtained results can be summarized as follows:

- the muons are correctly identified although a significant background contamination is present for low energies;
- in particular up to 1-2 GeV is very difficult or impossible to discriminate the muon signal from the background signal because the discriminating parameters are almost equal for the two species;
- counting the events that trigger at least 2 planes the obtained efficiency for the muon

identification is $\varepsilon_\mu \sim 97\%$, with a purity $p_\mu \sim 90\%$;

- rejecting the events that trigger only 2 planes and accepting only the events that trigger all the three planes, a reduced contamination due to electromagnetic events is present and we obtain $\varepsilon_\mu \sim 99\%$ and $p_\mu \sim 99\%$. However in this case $\sim 40\%$ of muon events do not reach the third plane and would be lost.

These studies have been compared to independent analysis reported by authors within the Auger Collaboration. A very good agreement has been observed, thus representing a valid check of our work.
Although the main goal of BATATA is to quantify the electromagnetic contamination of the muon signal as a function of depth for cosmic ray shower, BATATA offers also the possibility of measuring the incoming direction of muons, including those coming from low-energy showers ('background muons'). Such measurements are indeed interesting, not only for calibration or alignment studies, but also for anisotropy studies, i.e. searches of muon excesses in the sky, or comparison of angular distribution with those predicted by current hadronic models.
To reconstruct the muon track directions we used a Kalman-Filter technique studying different reconstruction strategies. No significant improvements are achieved for the track parameter resolution after including a multiple scattering correction in the track finding procedure. An angular resolution of $2 - 3^\circ$ in zenith is achieved with typical tracking efficiencies around 80%. The accuracy in the vertex reconstruction is found of the order of $\sim 1.5 - 2.0$ cm. Such results have been cross-checked using an alternative least-square method. Both approaches have been found to lead to comparable results for what concerns the track reconstruction accuracy.
The studies carried out in this thesis demonstrate that under the discussed conditions a good reconstruction of the muon component is possible for 3-fold events coming from low energy showers or high energy showers falling sufficiently far from the station. A further validation and optimization of the designed method will come as soon as the first data will be available at the beginning of next year.

Bibliography

[1] V.F.Hess, *Über Beobachtungen der durchdringen Strahlung bei sieben Freiballonfahrten*, Phys. Zeit **13** (1912), 1084.

[2] R.A.Millikan and G.H.Cameron, *The Origin of the Cosmic Rays*, Phys. Rev. **32** (1928), 533.

[3] W.Bothe, W.Kolhörster, *Das Wesen der Höhenstrahlung*, Zeitschrift für Physik A **56** (1929), 751.

[4] Clay, J. Proc. Amsterdam **30** (1927) 1115.

[5] A.H.Compton, *A Geographic Study of Cosmic Rays*, Phys. Rev. **43** (1933), 387.

[6] B.Rossi, *Cosmic Rays*, McGraw Hill (1964).

[7] P.Auger and R.Maze, Comptes rendus de l'Académie des sciences serie B **207** (1938), 228.

[8] J.Linsley, *Evidence for a Primary Cosmic-Ray Particle with Energy 10^{20} eV*, Phys. Rev. Lett. **10** (1962), 146.

[9] J.Linsley, L.Scarsi and B.Rossi, *Extremely Energetic Cosmic-Ray Event*, Phys. Rev. Lett. **6** (1961), 485.

[10] D.M.Edge et al., *The cosmic ray spectrum at energies above 10^{17}*, J. Phys. A **6** (1973), 1612.

[11] C.J.Bell et al., *The upper end of the observed cosmic ray energy spectrum*, J. Phys. A **7** (1974), 990.

[12] D.D.Krasilnikov et al., *Evidence for an anisotropy in the arrival direction of cosmic rays with energies above 10^{19} eV*, J. Phys. A **7** (1974), L176.

[13] N.Chiba et al., *Akeno Giant Air Shower Array (AGASA) covering 100 km^2 area*, Nucl. Instr. Methods A **311** (1992), 338-349

[14] R.M.Baltrusaitis et al., *The Utah Fly's Eye detector*, Nucl. Inst. Methods A **240** (1985), 410.

[190] T.Abu-Zayyad et al., *Status of the High Resolution Fly's Eye Detector: Operation and Installation*, Proc. 26th ICRC (1999).

[16] J.Boyer et al., *FADC-based DAQ for HiRes Fly's Eye*, Nucl. Instr. Meth. A **482** (2002), 457.

[17] J.Abraham et al., *Properties and performance of the prototype instrument for the Pierre Auger Observatory*, Nucl Instr and Meth A **523** (2004), 50.

[18] H.Kawai et al., *Telescope Array Experiment*, Nuclear Physics B (Proc. Suppl.) 175-176 (2008) 221-226.

[19] C.D.Anderson, *The Positive Electron*, Physical Review, **43** (1933), 491-494.

[20] C.D.Anderson and S.Neddermeyer, *Note on the Nature of Cosmic-Ray Particles*, Phys. Rev. **51** (1937), 884.

[21] C.M.G. Lattes, H.Muirhead, G.P.S.Occhialini, and C.F.Powell, *Processes involving charged mesons*, Nature **159** (1947), 694- 697.

[22] G.Rochester and C.Butler, *Evidence for the existence of new unstable elementary particles*, Nature **160** (1947),855.

[23] A.M.Hillas, *Cosmic Rays: Recent Progress and some Current Questions*, arXiv:astro-ph/0607109v2 (2006).

[24] *Particle Data Group*, J. Phys. G 33 (2006), 1.

[25] J. P. Wefel. *The composition of the cosmic rays - an update*, NASA STI/Recon Technical Report A, **93** (1991), 51971.

[26] D.Kazanas, and A.Nicolaidis, astro-ph/0103147.

[27] D.Kazanas, and A.Nicolaidis, *Cosmic Rays and Large Extra Dimensions*, General Relativity and Gravitation **35** (2003), 1117.

[28] A.Dar and A.De Rújula, *A theory of Cosmic Rays*, Phys. Rept. **466** (2008), 179–241.

[29] S.I.Nikolsky, *Break in the cosmic ray spectrum or confinement violation near 10^6 TeV?*, Nucl. Phys. Proc. Suppl., **39A** (1995), 228–234.

[30] A.D.Erlykin and A.W.Wolfendale, *A single source of cosmic rays in the range 10^{15} to 10^{16} eV*, J. Phys. G**23** (1997), 979–989.

[31] M.T.Dova, L.N.Epele, and J.D.Swain, *Massive relic neutrinos in the galactic halo and the knee in the cosmic ray spectrum*, arXiv:0112191.

[32] J.Candia, L.N.Epele and E.Roulet, *Cosmic ray photodisintegration and the knee of the spectrum*, Astroparticle Physics **17** (2002), 1.

[193] A.M.Hillas, *The Origin of Ultra-High-Energy Cosmic Rays*, Ann. Rev. Astron. Astrophys. **22** (1984), 425–444.

[34] V.Berezinsky and S.I.Grigoreva, *The Cosmic Ray Spectrum Black Body Bump*, Bull. Russ. Acad. Sci. Phys., 51N10 (1987), 111–113;

[194] D.Allard, E.Parizot, and A.V.Olinto, *On the transition from galactic to extragalactic cosmic-rays: Spectral and composition features from two opposite scenarios*, Astroparticle Physics **27** (2007), 1.

[36] D.Hooper, S.Sarkar and A.M.Taylor, *The intergalactic propagation of ultra-high energy cosmic ray nuclei*, Astroparticle Physics **27** (2007), 2–3.

[37] T.Abu-Zayyad et al. [HiRes-MIA Collaboration] , Astrophys. J., **557** (2001), 686-699.

[38] R.U.Abbasi et al. [HiRes Collaboration] , Astrophys. J. **622** (2005), 910-926.

[39] P.Sokolsky, *Recent Results from the High Resolution Fly's Eye Experiment*, Nuclear Physics B (Proc.Suppl.) 175-176 (2008), 207–212

[40] J.Bellido for the Auger Collaboration, *Measurement of the average depth of shower maximum and its uctuations with the Pierre Auger Observatory*, Proc. 31st ICRC (2009), arXiv:0906.2319.

[41] S.E.Forbush, *On World-Wide Changes in Cosmic-Ray Intensity*, Phys.Rev. **54** (1938), 975.

[42] T.Antoni et al., *Large-Scale Cosmic-Ray Anisotropy with KASCADE*, ApJ **604** (2004), 687–692.

[43] M.Kachelrieß and P.D.Serpico, *The Compton Getting effect on ultra-high energy cosmic rays of cosmological origin*, Physics Letters B **640** (2006), 225–229.

[44] L.W.Jones, *Cosmic ray studies with the L3-cosmics program at* Cern, Czechoslovak Journal of Physics **56** (2006), A201–A210.

[45] Y.Oyama, *Anisotropy of the primary cosmic-ray flux in Super-Kamiokande*, astro-ph/0605020 (2006);
G.Guillian, *Observation of the Anisotropy of 10 TeV Primary Cosmic Ray Nuclei Flux with the Super-Kamiokande-I Detector*, Proc. 29th ICRC (2005).

[46] G.Guillian et al., *Observation of the anisotropy of 10 TeV primary cosmic ray nuclei flux with the Super-Kamiokande-I detector*, Phys. Rev. D**75** (2007), 062003.

[47] S.Udo for the Tibet Asgamma Collaboration, *Galactic Anisotropy of Multi-TeV Cosmic-Ray Intensity Observed by the Tibet III Air Shower Array*, Proc. 28th ICRC (2003).

[48] M.Amenomori et al., *Observation by an Air-Shower Array in Tibet of the Multi-TeV Cosmic- Ray Anisotropy due to Terrestrial Orbital Motion Around the Sun*, Physical Review Letters **93** (2004), 061101.

[49] N.Hayashida et al., *The anisotropy of cosmic ray arrival directions around* 10^{18} *eV*, Astroparticle Physics **10** (1999), 4;
N.Hayashida et al., *Possible Clustering of the Most Energetic Cosmic Rays within a Limited Space Angle Observed by the Akeno Giant Air Shower Array*, Phys. Rev. Lett. **77** (1996), 1000;
M.Teshima at al., Proc. 27th ICRC (2001).

[50] J.A.Bellido et al., *Southern hemisphere observations of a* 10^{18} *eV cosmic ray source near the direction of the Galactic Centre*, Astroparticle Physics **15** (2001), 2.

[51] J.Abraham et al., *Anisotropy studies around the galactic centre at EeV energies with the Auger Observatory*, Astroparticle Physics **27** (2007), 4.

[52] The Pierre Auger Collaboration, The Pierre Auger Observatory Design Report, Technical Report (1997).

[53] J.Abraham et al., *Correlation of the Highest-Energy Cosmic Rays with Nearby Extragalactic Objects*, Science **318** (2007), 938.

[54] A.A. Penzias, R.W. Wilson, , Ap. J., **142** (1965), 419.

[55] K.Greisen, *End to the Cosmic-Ray Spectrum?*, Phys. Rev. Lett., **16** (1966), 748.

[56] G.T.Zatsepin and V.A.Kuz'min, *Upper limit of the spectrum of cosmic rays*, JETP Letters **4** (1966), 78.

[57] R.Schlickeiser, Cosmic Ray Astrophysics, Springer (2002).

[58] M.J.Chodorowski, A.A.Zdziarski and M.Sikora, *Reaction rate and energy-loss rate for photopair production by relativistic nuclei*,

[59] C.D.Dermer, *On Gamma Ray Burst and Blazar AGN Origins of the Ultra-High Energy Cosmic Rays in Light of First Results from Auger*, Proc. 30th ICRC (2007).

[60] J.W.Cronin, *The highest-energy cosmic rays*, Nucl. Phys. B Proc. Suppl **138** (2005), 465–491.

[61] L.N.Epele and E.Roulet, *On the propagation of the highest energy cosmic ray nuclei*, JHEP **10** (1998), 009.

[62] O.E. Kalashev, V.A. Kuzmin, D.V. Semikoz, I.I. Tkachev, arXiv:astro-ph/0107130.

[63] J.Abraham et al., *Observation of the Suppression of the Flux of Cosmic Rays above* 4×10^{19} *eV*, Phys. Rev. Lett. **101** (2008), 061101.

[64] R.U.Abbasi et al., *First Observation of the Greisen-Zatsepin-Kuzmin Suppression*, Phys. Rev. Lett. **100** (2008), 101101.

[65] F.Aharonian et al., *High-energy particle acceleration in the shell of a supernova remnant*, Nature **432** (2004), 75–77.

[66] E.Fermi, *On the origin of the cosmic radiation*, Phys. Rev. **75** (1949), 1169–1174.

[67] W.Axford et al., Proc. 15th ICRC (1977).

[68] G.Krymsky, Dok. Acad. Nauk USSR **234** (1977), 1306.

[69] A.Bell, *The acceleration of cosmic rays in shock fronts*, I. Mon. Not. R. Astron. Soc. **182** (1978), 147–156.

[70] R.Blanford and J.Ostriker, *Particle acceleration by astrophysical shocks*, Astrophys. J. **221** (1978), L29–L32.

[71] P.Lagage and C.Cesarsky, *The maximum energy of cosmic rays accelerated by supernova shocks*, Astron. Astrophys. **125** (1983), 249–257.

[72] E.Berezhko, *Maximum energy of cosmic rays accelerated by supernova shocks*, Astroparticle Physics **5** (1996), 3–4.

[73] K.Kobayakawa, Y.Sato and T.Samura, *Acceleration of particles by oblique shocks and cosmic ray spectra around the knee region*, Phys. Rev. D**66** (2002), 083004.

[74] L.G.Sveshnikova, *The knee in galactic cosmic ray spectrum and variety in supernovae*, Astron. Astrophys. **409** (2003), 799–808.

[75] L.Anchordoqui et al., *Ultrahigh Energy Cosmic Rays*, Int. J. of Mod. Phys. A **18** (2003), 2229–2366.

[76] H.J.de Vega and N.G.Sánchez, *Decay rates of unstable particles and the extreme energy cosmic rays top-down scenarios*, Phys. Rev. D**67** (2003), 125019.

[77] D.J.H.Chung, E.W.Kolb and A.Riotto, *Production of massive particles during reheating*, Phys. Rev. D**60** (1999), 063504.

[78] V.L.Ginzburg and S.I.Syrovatskii, *The Origin of Cosmic Rays*, Macmillan (1964).

[79] T.K.Gaisser, *Cosmic Rays and Particle Physics*, Cambridge University Press (1990).

[80] A.W.Strong and I.V.Moskalenko, *Propagation of cosmic-ray nucleons in the Galaxy*, ApJ **509** (1998), 212;

[81] B.Rossi, *High Energy Particles*, Prentice-Hall (1952).

[82] K.Greisen, Progress in Cosmic Ray Physics **3** (1956), 1.

[83] W.Heitler, *The Quantum Theory of Radiation*, Oxford University Press (1944);

[84] K.Kamata and J.Nishimura, *The Lateral and the Anglar Structure Functions of Electron Showers*, Prog. Theor. Phys. Suppl **6** (1958) 93.

[85] C.Wong, *Introduction to high-energy heavy-ion collisions*, World Scientific (1994).

[86] R.J.Glauber, *Lectures in Theoretical Physics*, Interscience (1959);

[87] B.Keilhauer et al., *Impact of Varying Atmospheric Profiles on Extensive Air Shower Observation: Fluorescence Light Emission and Energy Reconstruction*, Astroparticle Physics **25** (2006), 4.

[88] H.Haken and H.C.Wolf, Molecular Physics and Elements of Quantum Chemistry, Springer (2004).

[89] B. Keilhauer et al. *Nitrogen fluorescenceyield in dependence on atmospheric conditions.*, Proceedings of the 29th ICRC, Pune, volume **1**,(2005) 101-106.

[90] A.N.Bunner, *Cosmic Ray Detection by Atmospheric Fluorescence*, PhD thesis at the Cornell University (1967).

[91] G.Davidson and R.O'Neil, *Optical Radiation from Nitrogen and Air at High Pressure Excited by Energetic Electrons*, J. Chem. Phys. **41** (1964), 3946.

[92] M.Nagano et al., *New measurement on photon yields from air and the application to the energy estimation of primary cosmic rays*, Astroparticle Physics **22** (2004), 3–4.

[93] F.Kakimoto et al., *A measurement of the air fluorescence yield*, Nucl. Instr. Meth. A**372** (1996), 527–533.

[94] R.U.Abbasi et al., *A Study of the Composition of Ultra-High-Energy Cosmic Rays Using the High-Resolution Fly's Eye*, ApJ **622** (2005), 910–926.

[95] A.Bucholtz, *Rayleigh scattering calculations for the terrestrial atmosphere*, Appl. Optics **34** (1995), 2765–2773.

[96] L. Cazon, R. A. Vazquez and E. Zas, *Depth development of extensive air showers from muon time distributions.*, Astropart. Phys. **23** (2005) 393-409, astro-ph/0412338.

[97] G.A.Askaryan, *Excess Negative Charge of an Electron-Photon Shower And Its Coherent Radio Emission*, Soviet Phys. JETP **14** (1962), 441–443;
G.A.Askaryan, *Coherent Radio Emission from Cosmic Showers in Air and in Dense Media*, Soviet Physics JETP **21** (1965), 658.

[98] J.V.Jelley and J.H.Fruin, *Radio Pulses from Extensive Cosmic-Ray Air Showers*, Nature **205** (1965), 327–328.

[99] T.Huege and H.Falcke, *Radio emission from cosmic ray air showers: Coherent geosynchrotron radiation*, Astronomy and Astrophysics **412** (2003), 19–34;

[100] F.Salamida for the Auger Collaboration, *Update on the measurement of the CR energy spectrum above* 10^{18} *eV made using the Pierre Auger Observatory*, Proc. 32st ICRC, Beijing, (2011).

[101] R.Vazquez for the Auger Collaboration, *The cosmic ray flux observed at zenith angles larger than 60 degrees with the Pierre Auger Observatory*, Proc. 31st ICRC (2009), arXiv:0906.2189.

[102] R.U. Abbasi, et al. (HiRes Collaboration), Astropart. Phys., **32** (2009) 53-60.

[103] The Pierre Auger Collaboration, *Measurement of the energy spectrum of cosmic rays above* 10^{18} *eV using the Pierre Auger Observatory*, Phys. Rev. Letters **104** (2010) 091101, arXiv:1002.0699v1

[104] J.Bellido for the Auger Collaboration, *The distribution of shower maxima of UHECR air showers*, Proc. 32st ICRC, Beijing, (2011)

[105] J.Abraham et al., *Upper limit on the cosmic-ray photon fraction at EeV energies from the Pierre Auger Observatory* Astropart. Phys. **31**, (2009) 399-406.

[106] J.Abraham et al., *Upper limit on the cosmic-ray photon flux above* 10^{19} *eV using the surface detector of the Pierre Auger Observatory*, Astroparticle Physics **29** (2008), 4.

[107] M.Settimo for The Pierre Auger Collaboration *An update on a search for ultra-high energy photons using the Pierre Auger Observatory*, Proc. 32st ICRC, Beijing, (2011).

[108] K.Shinozaki et al., *Upper Limit on Gamma-Ray Flux above 10^{19} eV Estimated by the Akeno Giant Air Shower Array Experiment*, ApJ 571 (2002), L117;

[109] A.V.Glushkov et al., *Constraints on the fraction of primary gamma rays at ultra-high energies from the muon data of the Yakutsk EAS array*, JETP Lett. **85** (2007), 131.

[110] G.Gelmini, O.E.Kalashev, D.V.Semikoz, *GZK Photons as Ultra High Energy Cosmic Rays*, J. Exp. Theor. Phys **106** (2008), 1061–1082.

[111] J.Ellis, V.Mayes, D.V.Nanopoulos, *Ultrahigh-energy cosmic rays particle spectra from crypton decays*, Phys. Rev. D **74** (2006), 115003.

[112] J.Alvarez-Muñiz for the Auger Collaboration, *The sensitivity of the surface detector of the Pierre Auger Observatory to UHE Earth-skimming and down-going neutrinos*, Proc. 30th ICRC (2007).

[113] O.Blanch Bigas for the Auger Collaboration, *Limits to the diffuse flux of UHE tau neutrinos at EeV energies from the Pierre Auger Observatory*, Proc. 30th ICRC (2007).

[114] Y.Guardincerri for The Pierre Auger Collaboration *The Pierre Auger Observatory and ultra-high energy neutrinos: upper limits to the diffuse and point source fluxes* Proc. 32st ICRC, Beijing, (2011)

[115] R.Abbasi et al. *Constraints on the extremely-high energy cosmic neutrino flux with the IceCube 2008-2009 data* Phys. Rev. D **83** (2011), 092003;

[116] P.W.Gorham et al. *Observational constraints on the ultra-high energy cosmic neutrino flux from the second flight of the ANITA experiment*, Phys. Rev. D **82** (2010), 022004,

[117] I.Kravchenko et al., *RICE limits on the diffuse ultrahigh energy neutrino flux*, Phys. Rev. D **73** (2006), 082002.

[118] M. Ahlers et al. *GZK Neutrinos after the Fermi-LAT Diffuse Photon Flux Measurement*, Astropart. Phys. **34** (2010) 106-115.

[119] D. Semikoz, G. Sigl, *Ultra-High Energy Neutrino Fluxes: New Constraints and Implications*, JCAP (2004) 0404:003.

[120] R.U.Abbasi et al., *A Search for Arrival Direction Clustering in the HiRes-I Monocular Data above $10^{19.5}$ eV*, Astroparticle Physics **22** (2004), 2;
R.U.Abbasi et al., *Study of Small-Scale Anisotropy of Ultrahigh Energy Cosmic Rays Observed in Stereo by HiRes*, ApJ **610** (2004), L73;
R.U.Abbasi et al., *Search for Point Sources of Ultra-High Energy Cosmic Rays above 4.0×10^{19} eV using a Maximum Likelihood Ratio Test*, ApJ **623** (2005), 164–170.

[121] T.Stanev et al., *Arrival Directions of the Most Energetic Cosmic Rays*, Phys. Rev. Lett. **75** (1995), 3056;
Y.Uchihori et al., *Cluster analysis of extremely high energy cosmic rays in the northern sky*, Astroparticle Physics **13** (2000), 2–3.

[122] J.Abraham et al., *Correlation of the highest-energy cosmic rays with the positions of nearby active galactic nuclei*, Astroparticle Physics **29** (2008), 3.

[123] J.Abraham et al., Astrophysical Sources of Cosmic Rays and Related Measurements with the Pierre Auger Observatory, Proc. 31st ICRC (2009), arXiv:0906.2347.

[124] M.-P.Véron-Cetty and P.Véron, *A catalogue of quasars and active nuclei: 12th edition*, Astronomy and Astrophysics **455** (2006), 773.

[125] K.Allkofer et al., *The absolute cosmic ray muon spectrum at sea level*, Phys. Lett. B **36** (1971), 425.

[126] H.Jokish et al., *Cosmic-ray muon spectrum up to 1 TeV at* 75^o *zenith angle*, Phys. Rev. D **19** (1979), 1368.

[127] V.Agrawal et al., Phys. Rev. D **53** (1996), 1314.

[128] T.Stanev, *High Energy Cosmic Rays*, Springer Press, (2009).

[129] C.A.Ayre et al., *Precise measurement of the vertical muon spectrum in the range* $20 - 500$ GeV/c, J.Phys. G **1** (1975), 584.

[130] I.P.Ivanenko et al., Proc. 19th. Int. Cosmic Ray Conf. (La Jolla), **8** (1985), 210.

[131] B.C.Rastin, , J.Phys. G **10** (1984), 1609.

[132] M.D.DiPascale et al., J.Geophys. Res. **98** (1993), 350.

[133] M.Boezio et al., Phys. Rev. D **62** (2000), 032007.

[134] M.Motoki et al., Astroparticle Phys. G **19** (2003), 103.

[135] P.Achard et al. (L3 Collaboration), , Phys. Lett. B **598** (2004), 15.

[136] S.Heino et al., Phys. Lett. B **594** (2004), 35.

[137] P.Adamson et al. (MINOS Collaboration), *Measurement of the Atmospheric Muon Charge Ratio at TeV Energies with MINOS*, Phys. Rev. B **76** (2007), 052003.

[138] A.A.Petrukhin, V.V.Shestakov, Can. J.Phys. **46** (1968), S377.

[139] R.P.Kokoulin, A.A.Petrukhin., Proc. 12th. Int. Cosmic Ray Conf. (Hobart) **6** (1971), 2436.

[140] L.B.Bezrukov, E.V.Bugaev, Yad. Phys. **33** (1981), 1195 [Sov. J. Nucl. Phys., **33** (1981) 635].

[141] M.Crouch, Proc. 20th. Int. Cosmic Ray Conf. (Moscow) **6** (1987), 165.

[142] Yu.M.Andreev, V.I.Gurentzov, L.M.Kogai Proc. 20th. Int. Cosmic Ray Conf. (Moscow) **6** (1987), 200.

[143] M.Aglietta et al Astropartcile Phys. **3** (1995), 311.

[144] M.Ambrosio et al, Phys. Rev. D **52** (1995), 3793.

[145] Ch.Berger et al, Phys. Rev. D **40** (1989), 2163.

[146] J.Matthews, Astroparticle Phys. **22** (2005), 387.

[147] J.Alvarez-Muñoz et al. , Phys. Rev. D **66** (2002), 033011.

[148] T.Abu-Zayyad et al *A multi-component measurement of the cosmic ray composition between* 10^{17} *eV and* 10^{18}., Astroparticle Physics (1999).

[149] T.Abu-Zayyad et al., *Measurement of the cosmic ray energy spectrum and composition from* 10^{17} *eV and* $10^{18.3}$ *using a hybrid fluorescence technique.*, Astrophys. J., **557** (1999), 686.

[150] N.Hayashida et al., *Muons* ($>= 1-GeV$) *in large extensive air showers of energies between* $10^{16.5}$ *eV and* $10^{19.5}$ *eV observed at Akeno.*, J. Phys. G **21** (1995), 1101.

[151] N.Inoue for the AGASA Collaboration, *Muon Component in Giant Air Showers with Energy of* $\geq 10^{19}$ *eV Observed by AGASA*, Proc. 27th. Int. Cosmic Ray Conf. (Hamburg) **1** (2001), 345.

[152] D.Fuhrmann et al., *Muonic Component of Air Showers Measured by the KASCADE-Grande Experiment*, Proc. 31th. Int. Cosmic Ray Conf. (ŁÓDŹ) (2009).

[153] M.Nagano et al., *Size dependence of frequency attenuation length of extensive air showers observed at Akeno*, J. Phys. G: Nucl. Phys **10** (1984), L235.

[154] K.Shinozaki, Nuclear Physics B (Proc.Suppl.) **151** (2006), 3–10.

[155] T.Antoni et al., *The Cosmic-Ray Experiment KASCADE*, Nucl. Instr. Meth. A **513** (2003), 490–510.

[156] T.Antoni et al KASCADE Collaboration, *KASCADE measurements of energy spectra for elemental groups of cosmic rays: Results and open problems*, Astroparticle Physics **24** (2005), 1–2.

[157] W.D.Apel et al KASCADE Collaboration, *Energy spectra of elemental groups of cosmic rays: Update on the KASCADE unfolding analysis*, Astroparticle Physics **31** (2009), 2.

[158] W.D.Apel et al KASCADE Collaboration, *Muon production height studies with the air shower experiment KASCADE-Grande*, Astroparticle Physics **34** (2011), 476.

[159] B.R.Dawson et al, *A Comparison of Cosmic Ray Composition Measurements at the Highest Energies*, Astroparticle Physics **9** (1998), 4.

[160] J.Abraham et al., *Operations of and Future Plans for the Pierre Auger Observatory*, Proc. 31st ICRC (2009), arXiv:0906.2354.

[161] J.Abraham et al., *Auger South: The Pierre Auger Cosmic Ray Observatory in Argentina*, Technical paper in preparation for Nucl. Instr. Meth.

[162] I.Allekotte et al., *The Surface Detector System of the Pierre Auger Observatory*, Nucl. Instr. Meth. A**586** (2008), 409–420.

[163] X.Bertou et al., *Calibration of the surface array of the Pierre Auger Observatory*, Nucl. Instr. Meth. A**568** (2006), 839–846.

[164] M.Aglietta For The Pierre Auger Collaboration, Proc. 29th ICRC, Pune, (2005).

[165] P.Ghia, *A compact 3ToT as SD physics trigger for vertical ($\vartheta < 60^o$) showers*, GAP-2004-018.

[166] J.Abraham et al., *The Fluorescence Detector of the Pierre Auger Observatory*, Nucl. Instr. Meth. A**620** (2010) 227

[167] The Pierre Auger Collaboration, *A Study of the Effect of Molecular and Aerosol Conditions on Air Fluorescence Measurements at the Pierre Auger Observatory*, Astroparticle Physics **33** (2010) 108

[168] K.Green et al., *A prototype system for detecting the radio-frequency pulse associated with cosmic ray air showers*, Nucl. Instr. Meth., A**498** (2003), 256–288.

[169] H.Falcke et al., *Detection and imaging of atmospheric radio flashes from cosmic ray air showers*, Nature **435** (2005), 313–316.

[170] D.Ardouin et al., *Radio-Detection Signature of High Energy Cosmic Rays by the CODALEMA Experiment*, Nucl. Instr. Meth. A**555** (2005), 148–163.

[171] H.R.Allan, Progress in Elementary Particle and Cosmic Ray Physics **10** (1971), 171.

[172] H.Falcke et al., LOPES Collaboration Nature **435**, (2005) 313-316.

[173] D.Ardouin et al., CODALEMA Collaboration Nuclear Instruments and Methods in Physics Research, A**555** (2005) 148-163.

[174] D.Veberic and M. Roth GAP-note 2005-035.

[175] Proc. of 29th ICRC, Pune, India, 7 (2005) 291.

[176] M.Roth For The Pierre Auger Collaboration, Proc. 30th ICRC (2007), Merida, Mexico; arXiv:0706.2096.

[177] Phys. Rev. Lett. **101** (2008) 061101.

[178] M.Mostafa For The Pierre Auger Collaboration, Proc. of ICRC (2005), Tsukuba.

[179] M.Nagano, K. Kobayakawa, N. Sakaki, and K. Ando, Astropart. Phys. **20** (2003) 293.

[180] M.Ave et al. (AIRFLY Collaboration) Nucl. Instrum. Meth. A **597** (2008) 41.

[181] P.Privitera et al. (AIRFLY Collaboration) Proc. 30th ICRC (2007).

[182] M.Unger et al., Nucl. Instr. and Methods A**588** (2008) 433.

[183] D.Gora et al., Astropart. Phys. **22** (2004) 29.

[184] B.R.Dawson, M. Giller and G. Wieczorek , Proc. 30th ICRC (2007).

[185] C.Di Giulio, Proc. 31th ICRC (2009), Lodz, Poland; arXiv.0906.2189.

[186] S.Benzvi, Proc. 31th ICRC (2009), Lodz, Poland; arXiv.0906.2358

[187] M.Nagano et al., *Energy spectrum of primary cosmic rays between* $10^{14.5}$ *and* 10^{18} *eV*, J. Phys. G **10**(1984), 1295.

[188] T.Abu-Zayyad et al., *Measurement of the cosmic-ray energy spectrum and composition from* 10^{17} *to* $10^{18.3}$ *eV using a hybrid technique*, Astrophys. J. **557** (2001), 686.

[189] M.I.Pravdin et al., *Energy Spectrum of Primary Cosmic Rays in the Energy Region of* 10^{17} - 10^{20} *eV by Yakutsk Array Data*, Proc. 28th Int. Cosmic Ray Conf.(Tuskuba) (2003), 389.

[190] HiRes Collaboration, *Measurement of the Flux of Ultrahigh Energy Cosmic Rays from Monocular Observations by the High Resolution Fly's Eye Experimen*, Phys. Rev. Letters **92** (2004), 151101.

[191] V.Berezinsky, A.Z.Gazizov, S.I.Grigorieva, *On astrophysical solution to ultrahigh energy cosmic rays*, Phys. Rev. D **74** (2006), 043005.

[192] V.Berezinsky, *Dip in UHECR and Transition from Galactic to Extragalactic Cosmic Rays*, astro-ph/0509069.

[193] A.M.Hillas, *Where do* 10^{19} *eV cosmic rays come from?*, Nucl. Phys. B (Proc.Suppl.) **136** (2004), 139.

[194] D.Allard et al., *UHE nuclei propagation and the interpretation of the ankle in the cosmic-ray spectrum*, astro-ph/0505566.

[195] G.Medina Tanco for the Pierre Auger Collaboration, *Astrophysics motivation behind the Pierre Auger Southern Observatory enhancements*, Proc. 28th Int. Cosmic Ray Conf.(Tuskuba) (2003), 389.

[196] G.Medina et al., *Enhancing the Pierre Auger Observatory to the* $10^{17} - 10^{18.5}$ *eV range: Capabilities of an Infill Surface Array*, Nucl. Inst. Meth. A **566** (2006), 302.

[197] Auger Collaboration, *First estimate of the primary cosmic ray energy spectrum above 3 EeV from the Pierre Auger Observatory*, Proc. 29th Int. Cosmic Ray Conf.(Pune) (2005), astro-ph/0507150.

[198] N.Hayashida et al., , Astrop. Phys. **10** (1999), 3031311.

[199] A.Haungs et al. (KASCADE-Grande Coll.), *Investigating the* 2^{nd} *knee: The KASCADE-Grande experiment*, astro-ph/0508286.

[200] T.Stanev, *IceTop Status in 2004*, astro-ph/0501046.

[201] M.Platino for the Pierre Auger Collaboration, *Auger Muons and Infill for the Ground Array of the Pierre Auger Observatory*, Proc. 31th Int. Cosmic Ray Conf.(Łódź) (2009).

[202] Presentation at Auger meeting (Nov. 2011).

[203] F.Suarez et al., *Multi-pixel PMTs for the AMIGA project: Proposal for the testing facility and first measurements*, Auger Internal note, GAP2008-164.

[204] A.D. Supanitsky, Ph.D thesis, Universidad de Nacional Buenos Aires.

[205] A.Etchegoyen for the Pierre Auger Collaboration, *AMIGA, Auger Muons and Infill for the Ground Array*, Proc. 30th Int. Cosmic Ray Conf.(Merida) (2007).

[206] F.Sanchez for the Pierre Auger Collaboration *The AMIGA detector of the Pierre Auger Observatory: an overview*, Proc. 32nd Int. Cosmic Ray Conf. Beijing (2011).

[207] The MINOS Collaboration, *MINOS Techical Design Report*, FNAL internal document NuMI-L-337 (1998).

[208] F.A.Sanchez et al, *Buried plastic scintillator muon telescope*, Proc. 30th Int. Cosmic Ray Conf.(Mérida) (2007).

[209] D. Supanitsky et al., *Optical fiber characterization and scintillator strip assembly for the BATATA detector*, Auger Internal note, GAP2008-157.

[210] F.A.Sanchez et al, *Testing and quality protocols of 3-folded x-y hodoscope*, Proc. 31th Int. Cosmic Ray Conf.(Łódź) (2009).

[211] EPOXY TECHNOLOGY, INC, http://www.epotek.com.

[212] G.Medina Tanco for the Pierre Auger Collaboration, *BATATA: A device to characterize the punch-through observed in underground muon detectors and to operate as a prototype for AMIGA*, Proc. 31th Int. Cosmic Ray Conf.(Łódź) (2009).

[213] Photonics HAMAMATSU /http://www.hamamatsu.com.

[214] N.Tagg et al., Nucl. Instrum. Meth. A **539** (2009) 668.

[215] F.Sanchez et al., *PMT and scintillator strip system testing and characterization for the BATATA detector: I*, Auger Internal note, GAP2008-158.

[216] R.Alfaro et al., *Buried plasticscintillatormuontelescope(BATATA)*, Nucl. Instrum. Meth. A **617** (2010) 511.

[217] C.Canet et al., *The site of the BATATA detector in Malargüe, Argentina: geological characterization*, Auger Internal note, GAP2008-159.

[218] D.Heck et al., *CORSIKA: A Monte Carlo Code to Simulate Extensive Air Showers*, Report FZKA-6019 (1998).

[219] K.Werner, *Strings, pomerons and the VENUS model of hadronic interactions at ultrarelativistic energies*, Phys. Rep. **232** (1993), 87.

[220] N.N.Kalmykov, S.S.Ostapchenko, *The Nucleus-nucleus interaction, nuclear fragmentation, and fluctuations of extensive air showers*, Yad. Fiz. **56** (1993), 105; Phys. At. Nucl. 56 (1993), 346;
N.N.Kalmykov, S.S.Ostapchenko and A.I.Pavlov, *EAS and a quark - gluon string model with jets*, Bull. Russ. Acad. Sci. Phys. **58** (1994), 1966.

[221] J.Ranft, *Dual parton model at cosmic ray energies*, Phys. Rev. D**51** (1995), 64.

[222] R.S.Fletcher, T.K.Gaisser, P.Lipari and T.Stanev, *Sibyll: An event generator for simulation of high energy cosmic ray cascades*, Phys. Rev. D**50** (1994), 5710.

[223] J.Engel, T.K.Gaisser, P.Lipari and T.Stanev, *Nucleus-nucleus collisions and interpretation of cosmic-ray cascades*, Phys. Rev. D46 (1992) 5013.

[224] K.Werner et al., *The NEXUS model*, Invited talk at International Workshop on the Physics of the Quark Gluon Plasma, Palaiseau (2001), hep-ph/0209198.

[225] K.Werner, *The hadronic interaction model EPOS*, Nucl. Phys. B Proc.Suppl. 175–176 (2008), 81–87.

[226] J.N.Capdevielle, *A Monte Carlo generator for cosmic-ray collisions*, J. Phys. G **15** (1989), 909;
A.Capella and J.Tran Thanh Van, *A new parton model description of soft hadron-nucleus collisions*, Phys. Lett. B**93** (1980), 146–150.

[227] H.Fesefeldt, PITHA 85/02, RWTH Aachen (1985).

[228] G.Battistoni et al., *The FLUKA code: Description and benchmarking*, Proc. of the Hadronic Shower Simulation Workshop (2006), AIP Conference Proceeding **896** (2007), 31–49;

[229] S.A.Bass et al., Microscopic Models for Ultrarelativistic Heavy Ion Collisions, Prog. Part. Nucl. Phys. **41** (1998), 225–370;
M. Bleicher et al., Relativistic Hadron-Hadron Collisions in the Ultra-Relativistic Quantum Molecular Dynamics Model, J. Phys. G **25** (1999), 1859–1896.

[230] W.R.Nelson, H.Hirayama and D.W.O.Rogers, Report SLAC **265** (1985).

[231] D.Heck and J.Knapp, *Upgrade of the Monte Carlo Code CORSIKA to Simulate Extensive Air Showers with Energies* $> 10^{20}$ *eV*, Report FZKA-6097 (1998).

[232] M.Kobal, *A thinning method using weight limitation for air-shower simulations*, Astroparticle Physics **15** (2001), 3.

[233] *http://geant4.web.cern.ch.*

[234] S.Argirï¿½ et al., *The offline software framework of the Pierre Auger Observatory*, Nucl. Instr. and Meth. A **580** (2007), 3.

[235] *http://www.w3.org/XML/*

[236] *http://dev.mysql.com*

[237] *http://xml.apache.org*

[238] P.Billoir, A sampling procedure to regenerate particles in a ground detector

[239] C.De Donato, Private Communication.

[240] F.A. Sanchez and G. Medina-Tanco, Modeling scintillator and WLS fiber signals for fast MonteCarlo simulations, Nucl. Instr. and Meth. A **620** (2010), 182.

[241] C.M.Bishop, *Neural Networks for Pattern Recognition*, Oxford University Press (1995).

[242] H.Demuth, M.Beale, *Neural Network Toolbox - MATLAB - User's Guide* (2006), version 5.

[243] F.Sanchez et al. *Electromagnetic and muon primary discrimination from underground scintillator signatures*, 30th ICRC (2007)

[244] R. Mankel, Pattern recognition and event reconstruction in particle physics experiments, Rep. Prog. Phys. **67** (2004), 553.

[245] P. Avery, Applied Fitting Theory III, Non-Optimal Least Squares Fitting and Multiple Scattering, CBX Note 91-74 (1991).

[246] R. Mankel, Application of the Kalman Filter technique in the HERA-B Track Reconstruction, HERA-B Note 95-239 (1995).
R. Mankel, ranger, a Pattern Recognition Algorithm for the HERA-B Main Tracking System, HERA-B Note 98-079 (1995).

[247] J.A. Hernando, The Kalman Filter Technique applied to Track Fitting in GLAST, SCIPP 98/18 (1998).

[248] B. Jones and B. Tompkins, A Physicist's guide to Kalman Filters.